# PhD Thesis

Anton Kovyakh

# X-ray pair distribution function analysis of transition and noble metals for industrial applications in sensing and catalysis

# Acknowledgements

I would like to express my gratitude to all of my supervisors, both official, Robert Feidenhans'l, Leif Christensen and those picked up along the way, Simon Billinge and Kell Mortensen for excellent guidance and support along the way.

A special thanks goes to all those people involved in the day to day battles. To Solveig R. Madsen for introducing me to the fundamentals of diffraction and continuous support and discussions throughout the whole project. To Martin Søndergaard for all the chemistry discussions and wisdom around the lab. A special thanks to Kirsten Jensen for introducing me to PDF and supporting me whenever help was needed with great advice and discussions. To Soham, Max and Tim from Columbia, who I got the pleasure to meet while in New York and who taught me all of the practical skills in PDF analysis and programming.

And in the end, I would like to express deep gratitude to people close to me in my life and everyone I've met along the way. Both abroad and at home. With you around I felt supported all the way.

# Abstract

Understanding structures and properties of nanoscale materials is increasingly important in contemporary technological development. The presented work investigates the applications of x-ray pair distribution function (PDF) analysis in a number of industrial research projects. The viability of the method is explored in the areas of instrumentation, catalysis, time-resolved measurements and novel data reduction protocols.

Obtaining quantitative structural information efficiently is essential for studying materials synthesized using combinatorial methods. To address this we propose a protocol for measuring and analyzing data from such high-throughput experiments. For this study, a combinatorial array containing catalytic nanoparticles was prepared from liquid precursors, directly on-chip, using an ink-jet liquid handling system. The array was then measured at the x-ray powder diffraction beamline (NSLS-II) and analyzed by the PDF technique using a software implementation of the proposed protocol. The developed protocol software can handle semi-automated data reduction, normalization and modeling. A comprehensive collection of metadata and analysis results is generated from user-defined recipes. By slicing this collection using the included functions it is possible to determine the distribution of material on the array, highlight regions with heterogeneity, and visualize spatially varying structural parameters. The modular design of the software is intended to be transparent and extensible, with potential applications to other experimental techniques.

Copper nanoparticles have the potential to completely replace silver in applications of printed electronics. A cost effective and environmentally-safe method of manufacturing nanoparticles using glucose reduction of copper in an aqueous media is studied in detail using synchrotron x-ray PDF. Nanoparticle growth is observed in-situ, utilizing a new setup for continuous flow characterization. The limiting factor for the reactions is found in the chemical kinetics. Meanwhile, the reducing agent is found to be an effective capping agent. The methodology is successfully tested together with novel data reduction and analysis methods.

Platinum palladium (PtPd) and platinum palladium iron (PtPdFe) nanoparticle catalysts on $\gamma$-$Al_2O_3$ supports are interesting for the applications in diesel oxidation catalysis. In this work, the particles are studied using the PDF analysis. The study concludes that the addition of iron into PtPd leads to a lattice contraction of the alloy improving the temperature for half conversion. In addition, iron doping appears to have an effect on the size of the nanoparticles. The lattice contraction appears systematic, decreasing linearly with the amount of iron added to the synthesis. The findings are confirmed by a control experiment, where catalytic nanoparticles are prepared on graphitized carbon supports.

Molybdenum oxide catalysts on zeolite ZSM-5 supports for methane conversion are studied using the PDF analysis. The catalyst prepared by hydrothermal flow synthesis method contains amorphous molybdenum oxide structures in contrast to the reference sample, which contains nanocrystalline MoO3 and is prepared by impregnation method. The amorphous molybdenum oxide appears to have octahedral coordination and consists of units of several octahedra in a corner share and edge share configurations. The findings indicate that the catalytic material is distributed across the support material with higher concentrations in or around the pores of the zeolite, which might explain its better catalytic activity when compared to the reference.

A series of Atomic Layer Deposition(ALD) grown TiNx thin films is investigated. The material changes its plasmonic properties due to an annealing process. The origins of this change are invesitgated via a thin film PDF method (tf-PDF). It is found that the substrate is changing too significantly. Due to these changes, proper background subtraction could not be achieved. Despite the difficulties in tf-PDF analysis, the x-ray diffraction data was analyzed and the majority phase was determined to be TiN. It is found that during the annealing process the material undergoes a lattice expansion and experiences isotropic domain. In addition, the material has a high degree of preferred orientation in the growth direction.

# Dansk resume

Forståelsen af strukturer og egenskaber af materialer på nanosstørrelser er I stigende grad vigtig for nutidens teknologiske udvikling. Det præsenterede arbejde undersøger røntgen parsdistributionsfunktion (PDF) analyse i en række industrielle forskningsprojekter. Metoden udforskes inden for instrumentering, katalyse, hurtige målinger og nye data reduktionsprotokoller.

At opnå kvantitativ strukturinformation effektivt er afgørende for at studere materialer syntetiseret ved hjælp af kombinatoriske metoder. For at løse dette, foreslår vi en protokol til måling og analyse af data fra eksperimenter med store datamængder. I denne studie blev et kombinatorisk array, der indeholder katalytiske nanopartikler, fremstillet af flydende precursorer direkte på en chip, ved hjælp af ink jet printning. Arrayet blev derefter målt ved røntgen pulverdiffraktions beamlinjen XPD på NSLS-II og analyseret ved PDF-teknikken ved hjælp af en softwareimplementering af den foreslåede protokol. Den udviklede protokolsoftware kan håndtere data reduktion, normalisering og modellering. En omfattende samling af metadata og analyseresultater kan genereres ud fra brugerdefinerede opskrifter. Samlingen kan ved hjælp af de medfølgende funktioner udforskes. For eksempel, er det muligt at bestemme fordelingen af materialet på arrayet, fremhæve regioner med heterogenitet og visualisere rumligt varierende strukturelle parametre. Det modulære design af softwaren er beregnet til at være gennemskuelig og skal kunne udvides med potentielle anvendelser i andre eksperimentelle teknikker.

Kobber nanopartikler har potentialet til helt at erstatte sølv i anvendelser på trykt elektronik. En omkostningseffektiv og miljømæssig sikker metode til fremstilling af nanopartikler, der anvender glucoseduktion af kobber i en opløsning, studeres detaljeret ved hjælp af synkrotron røntgen-PDF. Væksten af nanopartikler observeres in-situ, idet der anvendes en ny opsætning til kontinuerlig flowkarakterisering. Den begrænsende faktor for reaktionerne er fundet til at skyldes af reaktionskinetikken. Samtidigt, er reduktionsmidlet fundet at være et effektivt cappingmiddel. Metoden viser gode resultater med de nye data reduktions- og analysemetoder.

Platin palladium (PtPd) og platin-palladium-jern (PtPdFe) nanopartiklekatalysatorer på $\gamma$-Al$_2$O$_3$ supports er aktuelle indenfor dieseloxidationskatalyse. Disse partikler studeres ved hjælp af PDF-analysen. Undersøgelsen konkluderer, at tilsætningen af jern til PtPd fører til en gittersammentrækning af legeringen, som forbedrer temperaturen til halv omdannelse (T50). Derudover synes jerndoping at have en effekt på nanopartiklernes størrelse. Gittersammentrækningen forekommer systematisk og falder lineært med mængden af jern tilsat til syntesen. Resultaterne bekræftes af et kontrolforsøg, hvor katalytiske nanopartikler fremstilles på grafitiserede carbonunderlag.

Molybdænoxidkatalysatorer på zeolit ZSM-5 underlag til metanomdannelse, studeres ved hjælp af PDF-analysen. Katalysatoren fremstillet ved hydrotermisk flow syntesemetode indeholder amorfe molybdænoxidstrukturer i modsætning til referenceprøven, som indeholder nanokrystallinsk $MoO_3$ og fremstilles ved imprægneringsmetode. Det amorfe molybdænoxid ser ud til at have oktaedrisk ordning og består af enheder af flere oktaedra som deler atomer enten i kanten eller to atomer i siden af en oktaeder. Resultaterne tyder på, at det katalytiske materiale fordeles jævnt over støttematerialet med højere koncentrationer omkring porerne i zeolitten, hvilket kan muligvis forklare prøvens forbedret katalytiske aktivitet, sammenlignet med referencen.

En serie af TiNx film dyrket ved atomarlagspådampning (ALD) er blevet undersøgt. Materialet ændrer sine plasmoniske egenskaber på grund af en annealing proces. Oprindelsen til denne ændring er undersøgt ved hjælp af en tyndfilm PDF-metode (tf-PDF). Der observeres at substratet ændrer sig alt for drastisk. På grund af disse ændringer kunne en ordentlig baggrundssubtraktion ikke opnås. På trods af vanskelighederne ved tf-PDF analysen, blev røntgendiffraktionsdata analyseret, og majoritetsfasen blev bestemt til at være TiN. Det konstateres, at materialet under annealingsprocessen gennemgår en gitterudvidelse og oplever isotropisk vækst af domænerne. Derudover har materialet en høj grad af foretrukket orientering i vækstretningen.

# List of Publications

1. **Anton Kovyakh**, Soham Banerjee, Chia-Hao Liu, Christopher J. Wright, Yuguang C. Li, Thomas E. Mallouk, Robert Feidenhans'l and Simon J. L. Billinge. *"Streamlining data analysis and modelling for high-throughput synchrotron datasets"*, Submitted, May 2018

2. Soham Banerjee, Chia-Hao Liu, Jennifer D. Lee, **Anton Kovyakh**, Viktoria Grasmik, Oleg Prymak, Christopher Koenigsmann, Haiqing Liu, Lei Wang, A. M. Milinda Abeykoon, Stanislaus S. Wong, Matthias Epple, Christopher B. Murray, and Simon J. L. Billinge. *"Improved models for metallic nanoparticle cores from atomic pair distribution function (PDF) analysis "*, Submitted, May 2018

3. Hugo Silva; Patricia Hernandez-Fernandez; Ane Baden; Henrik Hellstern; **Anton Kovyakh**; Erik Wisaeus; Ib Chorkendorff; Leif Christensen; Debasish Chakraborty; Christian Kallesøe. Supercritical Flow Synthesis of Cost-effective PtPdFe nanoparticles for Low-temperature Diesel Oxidation, Submitted, May 2018

4. **Anton Kovyakh**, Espen Z. Eikeland, Solveig R. Madsen, Leif Christensen, Robert Feidenhans'l, Kirsten M.Ø. Jensen, Christian Kallesøe. *Combined Pair Distribution Function (PDF) and EXAFS/XANES study of PtPdFe nanoparticles for Low-temperature Diesel Oxidation*, In preparation

5. Evgeniy Shkondin, **Anton Kovyakh**, Solveig R. Madsen, Kirsten M.Ø. Jensen, A. V. Lavrinenko, Kell Mortensen, *Structural characterization of Atomic Layer Deposition(ALD) grown Titanium Nitride thin films for biosensing applications*, In preparation

6. **Anton Kovyakh**, Morten M. Ley, Troels L. Christiansen, Mikkel Juelsholt, Kell Mortensen, Kirsten M.Ø. Jensen, *High surface area amorphous molybdenum oxides supported on HZSM-5 zeolite for methane valorisation prepared by the supercritical flow method*, In preparation

7. Martin Søndergaard, Solveig R. Madsen, **Anton Kovyakh**, Erik Wisaeus, Leif Christensen, Kisten M.Ø. Jensen, Zachary J. Davis, *Green synthesis of cost effective copper nanoparticle suspensions for applications in printed electronics*, In preparation

# Contents

# Streamlining data analysis and modeling for high-throughput synchrotron datasets   48

# In-situ PXRD and PDF study of the formation of copper nanoparticles for ink jet printable conductive inks   60

# Supercritical Flow Synthesis of Cost-effective PtPdFe Nanoparticles for Low-Temperature Diesel Oxidation   83

## Structure of MoOx catalyst on ZSM-5 Zeolite support for Methane Valorisation

## Characterization of TiNx thin films for plasmonic applications

## Conclusions

## Supercritical Flow Synthesis of Cost-effective PtPdFe Nanoparticles for Low-temperature Diesel Oxidation

# List of Figures

# List of Tables

# 1

## Introduction

Technological progress during the last few decades has been largely carried forward by advances in materials science. Researchers around the world have been making advances in semiconductor design[3, 4], solar cells[5, 6], better construction materials, batteries[7], advances in drug delivery[8] and catalysis[9], just to name a few. As the worlds population grows the burden of human activity on the environment increases drastically; the dwindling deposits of rare metals and fossil fuels and the ever increasing energy demands are tightly coupled with an increase in waste generation by modern societies. These challenges require the technology sector to not only develop completely new solutions, but also to reevaluate the existing production chains and make improvements while allowing the disruptive innovations to mature.

The work carried out for this thesis attempts to do both. Large improvements to already existing technology can be made utilizing the emergent properties of well known materials[10] as their size moves down to the nanoscale. At these sizes the physical and chemical properties often change due to the dominance of quantum[11] and surface effects[12]. For surface critical applications such as heterogeneous catalysis these properties lead to great improvements of activity and efficiency[13, 14, 15]. For industrial applications this also has an additional advantage of producing more surface area per gram of material which in turn increases the commercial interest and boosts industrial efforts within research and large scale production development[16, 17]. In Chapters 6 and 7, pair distribution function (PDF) analysis is employed to characterize new catalytic materials for diesel oxidation and methane valorisation, respectively. Both projects attempt to increase the efficiency of the catalyst by also reducing the cost while keeping up with the demands for large scale production. The ability to integrate PDF analysis into an industrial development process is explored.

Advancing the production methods towards large scale production also greatly influences the amount of experimental data that is collected during characterization. Streamlining and automation are the keywords for modern industry and require new solutions for collecting, storing and visualizing information. Chapter 4 describes the protocol that was developed to address the issue of handling and subsequently analyzing large amounts of

experimental data that can be obtained during a typical experiment.

Increasing global demands for conductive materials in electronics also stimulate the development of new solutions to address the shortage of currently used raw materials such as silver[18]. Copper pastes made from tiny copper nanoparticles are expected to fill the gap, given that robust, cheap and environmentally friendly production processes can be developed. However, large scale production of these tailor-made materials requires an increased understanding of the synthesis process, where the outcome is sensitive to tiny variations in parameters. The attainment of the relation between structure and property has long been the holy grail of materials chemistry. An attempt to aid the development of copper nanoparticle based inks is described in Chapter 5 and is utilizing the latest in-situ monitoring ability together with the new data handling methodology.

The origins of quantum confinement and the changing plasmonic properties of nanoscale materials is investigated in Chapter 8. The material has applications in optics and meta-material lenses, where the desired optical properties of gold films can be replicated by a comparably cheap TiN thin films. The nanoscale thin films are investigated by x-ray diffraction techniques in an attempt to determine relation between its structure and the plasmonic properties of the material.

The chapters are presented in chronological order. This layout ultimately makes sense from a storytelling perspective, yet a lot of the analysis was happening simultaneously due to bottlenecks in available characterization tools, schedules and planning.

## 1.1 Difficulties of characterization on the nanoscale

What unites the seemingly disjointed projects described above is the difficulties in characterization of the materials and understanding of their novel properties. As the materials design complexity increases, so does the difficulty in analyzing them. For the longest time, the most advanced techniques within materials research and characterization have been developed and stayed within the academic environment. This is not surprising, since most of them are expensive, difficult to use and require immense time investments.

Now that societies are transitioning into purely service based economies, scientific knowledge becomes and increasingly valuable commodity. Research institutions with high technical competences rivaling those of an academic department are becoming more and more desirable. The results of these developments are simple: industry is not only hiring the specialists with experience in basic research, it is expressing more interest in being on the forefront[19]. State of the art electron microscopes, automated CT and x-ray diffractometers, gas and optical spectrometers, rheology and surface characterization equipment are commonplace. As a matter of fact, the private sector is often seen using higher quality characterization machines than their academic counterparts[20].

The work in this thesis is mostly focused on the use of x-ray powder diffraction and PDF analysis as a tool for materials research in the confines of tight collaboration with industrial partners. The method has been known for a long time[21], but was difficult to

use due to experimental difficulties. Now with the invention of fast measurement methods such as Rapid Acquisition PDF (RA-PDF)[22], and advances in detector technology and software[23], the PDF analysis is growing rapidly. As of now, numerous studies have been published, studying materials in academic environments[24, 25, 26, 27] and it is an interesting challenge to explore whether the method has an application and more importantly, can keep pace with the tempo of industrial product development.

## Bragg diffraction and its limits

The ability to solve materials structure using x-ray radiation has long been taken for granted since the development of crystallography in the beginning of the 20th century. X-rays are beams of photons with a wavelength on the order of 1Å, similar to the interatomic spacings of the probed materials. When the photons pass through a material they interact with the electron distribution through their electric field leading to the radiation of scattered photons. The low cross section of an electron and high energy of a photon also mean that a measurement is mostly non-destructive. The scattering process leads to interference of the scattered photons essentially using the atomic arrangement of the material as a diffraction grating. If the material is periodic and infinite in all directions, amplified Bragg reflections[28] can be measured at specific angles in space. The geometric arrangement, the degree of periodicity and the scattering power of the atoms would determine the positions and the intensities of these reflections. In crystallography thousands of such reflections can be measured and the structure obtained by solving the inverse problem.

In fact, crystallography often works with such an abundance of information to the number of structural parameters, that even when averaged to 1D, as is the case for a the powder diffraction measurement[29], the structure can still be retrieved. The developments of the powder diffraction technique throughout the last century made routine identifications of phases and their mixtures, unit cell parameters and contents and even structural imperfections possible. And all without the need for preparing a perfect infinite crystal but rather measuring a sufficiently ground powder[30]. The method was revolutionized in 1967 by H. Rietveld[31] who devised a new method for refining crystal structure parameters from the data by optimizing the atomic positions and the shape of their reflections simultaneously. The approach attempts to solve a global optimization problem by iteratively adjusting the model until it matches the experimental diffraction pattern.

Today, powder diffraction measurements are routine, quick and widespread. Modern diffractometers can acquire high quality diffraction data in matter of minutes.The development of robotic sample changers coupled with acquisition and analysis routines lead to an increase in automation allowing for an almost hands-off approach to powder characterization commercially.

Structure solutions by means of a Rietveld refinement relies on measuring "perfect powders" where all possible crystal orientations are equally represented while the size of these crystals fulfills the requirements for translational invariance. The scattering from these powders produces sharp Bragg peaks at specific positions and the analysis is focused

on fitting a number of analytic peak profile shapes that account for various imperfections and limited violations of these requirements.

Nanoparticle powders deviate significantly from crystalline order. At sizes below 50nm the assumption that these domains are infinite no longer applies and sharp Bragg peaks are severely broadened due to crystalline imperfection. The theoretical models describing peak broadening can only go so far. As the structural coherence decreases the classical models that are heavily constrained by symmetry break down completely. In essence, attempting to extract meaningful information from a highly disordered nanoparticle powder is futile, as is illustrated in Fig. 1.1. The simulation here represents the simplest case where the width of the peaks is affected purely by Scherrer broadening equation, assuming a narrow distribution of isotropic particles. As the information content degrades, phase identification becomes problematic, let alone the possibility to disentangle various broadening effects such as strain, structural defects and size non-uniformity.

**Total scattering approach to nanoparticles structure description**

Since the late 1980s the synthesis techniques and applications of nanoparticles has advanced significantly. A lot of effort has been directed at understanding the atomic structure of the nanostructured materials in an attempt to understand why their properties often differ from their bulk crystal structures. One key factor is the effect of their finite size that modifies their electronic structure[32]. The others stem from a large number of atoms being associated with the surface which leads to surface induced strain effects and various new and exotic crystal defects which can lead to them being significantly structurally different to their bulk counterparts[33]. The presence of these imperfections and aperiodic effects lead to the scattered intensity being diffuse. The diffuse scattering intensity contains similar information as the constructively interfering Bragg scattering. The approaches for obtaining a complete picture of the scatterer while treating both the diffuse and the Bragg scattering data equally are commonly called Total Scattering methods.

## 1.2 Pair Distribution Function analysis

One of the two main branches of total scattering analysis is the Pair Distribution Function (PDF) analysis. The technique was originally used to analyze liquids and amorphous materials starting in the 1930s by Warren et al.[21, 34, 35]. The PDF is obtained from the total scattering pattern of an orientationally averaged powder. It gives an expression for a probability of finding pairs of atoms separated by specific distances in real space and is defined as:

$$G(r) = \frac{2}{\pi} \int_{Q_{\min}}^{Q_{\max}} Q[S(Q) - 1] \sin(Qr) \, \mathrm{d}Q, \tag{1.1}$$

and is simply a sine Fourier transform from $Q_{\min}$ to $Q_{\max}$ of a total coherent scattering
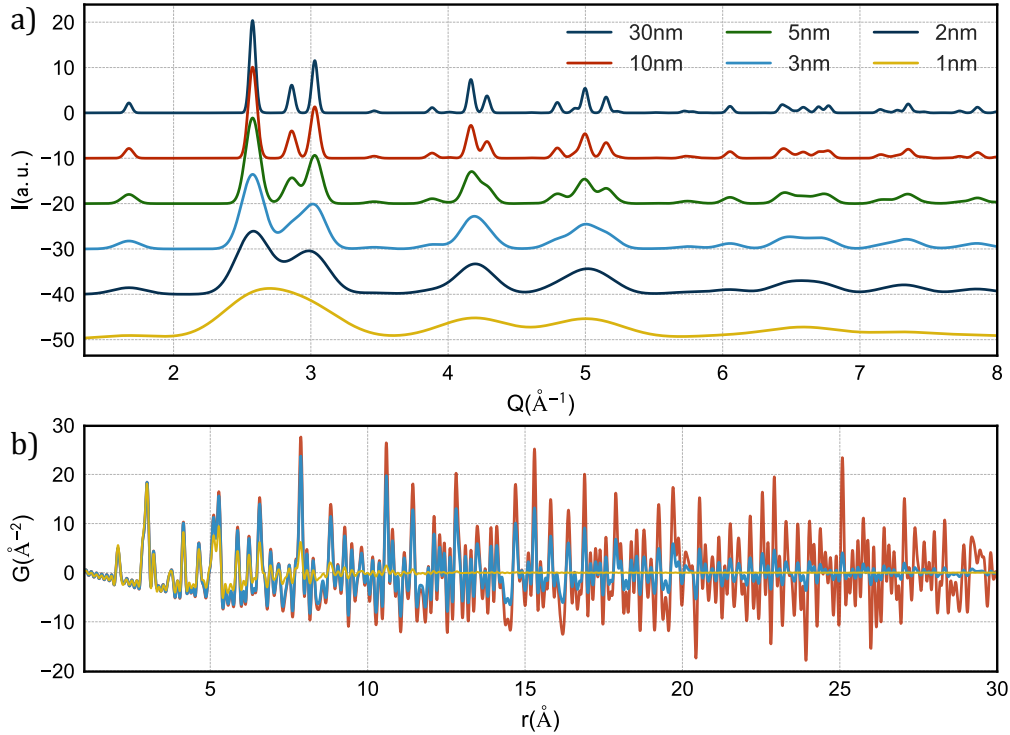
Figure 1.1:   a) Simulated powder diffraction patterns for $Ti_2N$ powder with increasing Scherrer broadening corresponding to crystallites of finite width illustrating the loss of information for nanosized samples. b) The PDF patterns obtained from the powder diffraction patterns above and normalized to the last G(r).

function $S(Q)$, which in turn is obtained by normalizing the experimental data to the total scattering cross-section, i.e. the square of the average atomic scattering factor[36] of the sample. The Fourier transform implies that the powder diffraction pattern is measured for all scattering vectors, i.e. from $Q_{min} = 0$ to infinity. In practice, however, this is impossible, and as such the measurement to as high angles as possible is required. At higher angles the atomic form factors reduce the coherent scattering intensity and counting statistics rapidly deteriorates. Thus, the $Q$ range becomes a trade off between statistical noise and the resolution of the PDF given by $\delta r \approx \pi/Q_{max}$. Typically measuring data with $Q_{max} = 20\text{Å}^{-1}$ to $Q_{max} = 25^{-1}$ is sufficient for most experiments.

PDF analysis works with both the strong Bragg scattering and the weak diffuse scattering simultaneously. As a result, it is very sensitive to a number of factors in the experimental background and the sample environment. It is important to correct for extrinsic contributions to background intensity such as incoherent scattering, fluorescence, absorption, scattering from the sample holder and air scattering and also to normalize by the incident flux[37].

Using the combination of Bragg scattering and the diffuse intensities means that the G(r) contains information about both the long range ordering of the material and the local structure. For bulk crystalline samples the peaks should be visible to an infinitely large $r$ because of the infinitely extending periodicity of the crystal. In reality, however, this is

not the case due to finite instrumental Q resolution. Yet there is a clear difference between large periodic crystals and nanocrystalline samples. The pair correlation peaks for a bulk crystal can be observed in intermediate and long $r$ ranges extending for as long as the measurement resolution can bear. Thus the maximum range for visible correlations serves as a metric for the maximum average size of the measured crystallites without sacrificing the information in the low $r$ ranges. An illustration of this is presented in Fig. 1.1b where the data from Fig.1.1a are directly transformed to G(r). The peaks at low $r$ range are the same for all simulated samples, while the main difference is the range at which they disappear.

### 1.2.1 Obtaining information from PDF

The beauty of the PDF analysis method is the ability to extract large amounts of information from the data in a model independent fashion. This is particularly true in a sequential measurement of several related samples, for example during an in-situ experiment. The PDF provides an intuitive representation of the atomic structure, albeit requiring some experience in analysis due to orientational averaging of three dimensional structures. Being a histogram of interatomic spacings, the PDF is a great tool for exploratory analysis. The observed distances describe bond lengths and can be directly compared to computer models of both crystalline materials and any small structural models. Many bits of information can also be inferred from the width of the peaks in the G(r) such as thermal motion and static disorder. For example, more thermal motion leads to broader peaks, while peak asymmetry can be related to surface induced strain. The integrated peak intensity relates to the coordination number of the atoms, because each peak magnitude is directly proportional to the number of scatterers at those positions and can be extracted provided the contributions from the parasitic effects have been removed. All of these have been successfully used in determining strain[38], local structure transformations[27] and solvation, nucleation and growth mechanisms[39, 26].

For phase identification and more complicated models of disorder, the PDF data can be fitted in real space using a full profile Rietveld refinement approach[40, 41]. Here a PDF model is calculated and the residual is minimized by a least squares method, in the same way as for a crystalline powder.

**Modeling inorganic nanoparticles**

As established previously, the PDF is sensitive to the finite nature of the nanoparticles through the way the signal disappears at long $r$ ranges. This feature is used extensively in modeling via an approach called Virtual Crystal (VC) approximation. This approach assumes that the nanoparticles are similar to their bulk parent crystal structure[42]. The model is then built by applying an attenuation function to the bulk PDF signal that corresponds to the size and shape of the nanoparticles. Analytical expressions for a number simple geometries and distributions for spheres, rods and layered structures exist[43, 44, 45]. These models are efficient and fast as the bulk G(r) is calculated with periodic boundary

conditions from a relatively small unit cell. They can also be fitted and refined with only a few parameters extracting valuable structural information with less danger of over fitting the data.

The software PDFGui[46] and the python suite Diffpy-CMI[47] implement this approach and are routinely used to obtain valuable information from a range of nanocrystalline materials. The Rietveld refinement-like implementation also allows refinement of the structure over a variation of $r$ ranges effectively decoupling the local and average structure or locating range dependence effects such as stacking faults [38, 48], strain [49], phase or core-shell segregation [50, 51] etc. Misfit to these models has also been successfully used to characterize important features such as solvent restructuring and existence of superstructures[52, 53].

Needless to say, the models based on a virtual crystal approximation work only in situations where the nanoparticles actually assume their parent crystal structures. The existence of metastable, amorphous and incommensurate phases, quasicrystals[42] and structural polymorphs[54] means that there is a class of systems for which periodic structures are no longer representative. In this case the PDF can be calculated explicitly using the Debye Scattering Equation(DSE), which for coherent scattering is defined as:

$$I_{coh}(Q) = \sum_{i,j} f_i(\mathbf{Q})f_j^*(\mathbf{Q})\frac{sinQr}{Qr}, \qquad (1.2)$$

where the sum runs over all scattering pairs in the sample. This approach is much more computationally intensive, but allows for a greater degree of flexibility. Any atomic arrangement can be calculated and refined without being constrained by periodicity. Calculating the PDF using the DSE makes it possible to study highly disordered and amorphous materials[55, 56, 57]. Amorphous structures have order on the sub nanometer length scales and are disordered beyond that. Attempting to fit models to such data often results in a number of degenerate solutions with many of them being completely unphysical[58]. But even for physical models it is important to understand that samples are rarely ideal and consist of a single type of particle. While it is possible to model very specific shapes such as pyramids, octaherdra, icosahedra etc. the real sample most likely consists of a statistical distribution of sizes, shapes and a variety of defects.

In many cases additional information is needed to constrain the model. The constraints can be obtained from a variety of sources, such as complementary imaging by Transmission Electron Microscopy (TEM) allowing to constrain the available morphologies, Extended x-ray Absorption Fine Structure(EXAFS) and Raman spectroscopy to constrain the local coordination environment and even Small Angle x-ray Scattering(SAXS) for particle size distributions. The data can be modeled and refined simultaneously in a "complex modeling" framework[59].

## 1.3 Complementary techniques for local structure analysis and complex modeling paradigm

The question of uniqueness of crystal structure solution is an important one in a world where each technique has its strengths, but also significant weaknesses. A typical example would be the difference between local probe techniques vs. bulk probe techniques. Electron microscopy, for example is an excellent and widely available technique for analyzing nanostructured objects. It can be used on both inorganic and organic samples[60] and provides direct and easily understandable information about the material. It is an excellent probe of morphology, size distribution and even atomic arrangements[61]. The main drawback of the technique is typically sample preparation requirements that feeds into its local probe nature. The careful preparation techniques and the incredible spatial resolution mean that only a small area of the sample is examined. Even though it is rare that such a measurement produces an incorrect impression of the sample it is not guaranteed to be representative. The preparation itself can serve as a selector for certain particle sizes or types, the particle counting results might be inaccurate due to difficulties in segmentation and even certain morphologies might be misidentified or missed completely[62]. Despite all this, electron microscopy provides highly complementary information to other measurements such as scattering based techniques. Here I would like to highlight three additional techniques that I have had an opportunity to encounter and that can potentially significantly constrain and improve the models. The additional advantage is that they require, for the most part, minimal effort in terms of sample preparation.

Small Angle X-ray Scattering (SAXS) is an often overlooked scattering regime in a world of total scattering analysis. Due to the way PDF data is acquired, the SAXS signal is filtered out by the beamstop at low angles. The signal contained in the small angle region typically only plays a role in PDF when particle sizes are below 1nm[63]. SAXS is, however, in many ways simply a low resolution limit of the PDF analysis, where whole particles can be considered as the main scatterers. In fact for many years, performing a PDF transform of small angle scattering(SAS) data has been a valuable tool for exploratory analysis of the data.

In reciprocal space, $I(Q)$, a number of parameters can be extracted from SAS data in a model free fashion. When properly normalized, the total number of scatterers is available from the intercept of scattering curve with the intensity axis at $Q = 0$. For dilute systems with no particle-particle interactions, the shape dependent particle form factor and the radius of gyration can be extracted from the long wavelength Guinier[64] region($QR < 1$), while the surface area can be extracted from the short wavelength limit Porod[65] region($QR > 1$). Additional modeling allows to extract particle size distributions[66] and intra-particle interaction mechanisms for studying packing and superstructures[67, 68].

The PDF analysis and small angle scattering can also be performed with neutrons. In fact, much of the theory is exactly the same as it is for x-rays. Neutrons do have a few advantages over x-ray scattering which makes neutron scattering an excellent complemen-

tary technique. Neutrons interact with the atomic nuclei of the sample and their scattering cross section depends on the nuclear structure of the material. This results in different elements, and even their isotopes, having vastly different scattering powers, allowing for a different kind of contrast compared to x-ray diffraction. The differences in scattering power makes it possible to detect light elements, such as lithium and hydrogen, and also in many cases allow for distinguishing elements with adjacent atomic numbers. The contrast can further be manipulated by isotopic substitution, such as in the case for hydrogen and deuterium.

The neutron scattering length is constant in $Q$ and allows for measurements to much higher scattering vectors. In addition, modern instrumentation often allows for both small angle neutron scattering and wide angle neutron scattering data to be collected at the same time using the time of flight method[69]. Neutrons also have magnetic moments and interact with magnetic structures in the material.

Care has to be taken during neutron experiments to avoid incoherent neutron scattering due to differences in spin states of the nucleus, and neutron absorption. Both of these vary across the range of elements and isotopic substitutions must be considered to obtain the best possible data.

X-ray Absorption Spectroscopy(XAS) is another complementary technique fit for augmenting the drawbacks of PDF analysis. Similar to PDF, Extended Xray Absorption Fine Structure (EXAFS) is able to probe bulk samples and provides excellent information about near neighbor distance distribution, coordination numbers and bond angles. It has chemical specificity that PDF throughly lacks and is thus very sensitive to even very dilute species, becoming incredibly important for analyzing supported nanomaterials such as those typically used for catalysis[51, 9]. XANES (X-ray Absorption Near Edge Structure) on the other hand can also reveal the information about the oxidation state of a given chemical species together with the chemical short-range order and magnitudes of local atomic displacements.

All of this provides excellent complementary information providing necessary constraints to the PDF model and can be greatly beneficial for a combined structure solution[9, 26, 50, 51, 24, 70, 71].

# 2

# Materials characterization using x-ray scattering

To understand the contents of the thesis and the work performed during the project, it is important to establish a frame of reference. In this chapter, the most important theoretical basis will be reproduced to the extent which is relevant for understanding the work in the following chapters. A more detailed treatment can be found in a number of excellent sources such as "Elements of Modern x-ray Physics"[72], "Diffraction at the Nanoscale"[73], "Underneath the Bragg Peaks"[74] and "The SAXS Guide"[67].

## 2.1 X-ray scattering basics

X-rays are high energy photons with typical wavelenghs on the order of 1Å. When they pass through the materials they create a strongly varying electric field. The electrons in the material begin to oscillate and, as charged particles experiencing acceleration, emit radiation. This interaction is referred to as Thompson scattering.

For the purpose of this thesis, this interaction is generally considered to be weak. This is known as the kinematic approximation and implies that we can disregard any multiple scattering events. This approximation is valid for several reasons: 1) the scattering cross-section of the electron is extremely small and 2) we are dealing with samples with reduced structural coherence, such as powders.

In the far-field limit, when both the x-ray source and the observer are far from the origin, the incident and the scattered x-rays can be considered plane waves. Here we will only consider elastic scattering, where the incident wave with a wavevector $\mathbf{k}$ results in a scattered intensity wave along a direction $\mathbf{k'}$ and $|\mathbf{k}| = |\mathbf{k'}|$. The difference between the two vectors defines the wavevector transfer $\mathbf{Q}$, and relates to the scattering angle as:

$$Q = |\mathbf{Q}| = 2k \sin \theta = \frac{4\pi}{\lambda} \sin \theta, \tag{2.1}$$

also illustrated in Fig. 2.1.

The scattering amplitude from a single electron is given by the Thomson scattering cross section ($-\mathbf{r}_{th}$) and is independent of $\mathbf{Q}$ as it is emitted in all directions. In a classical picture we consider the atom as surrounded by a charge cloud of electrons with a number density $\rho(r)$. Thus the coherent scattering from an atom is found by integrating over the volume of the charge density weighed by the phase factor:

$$f(\mathbf{Q}) = \int \rho(\mathbf{r}) e^{i\mathbf{Q} \cdot \mathbf{r}} d\mathbf{r} \tag{2.2}$$

Here $f(\mathbf{Q})$ is called the *atomic form factor*. For $\mathbf{Q} \to 0$ the integral evaluates to the total number of electrons in the atom as the phase factor approaches unity. Multiplying Eq. 2.2 by the contribution from each electron($-\mathbf{r}_{th}$) yields the absolute total scattering amplitude from an atom. Thus the total scattering power is proportional to the number(Z) of electrons in the sample with heavier elements scattering more than the light. For $\mathbf{Q} \to \infty$ the atomic form factor and the total coherent *elastic* scattering amplitude approaches 0 due to destructive interference of the waves scattered by different electrons in the atom.

The equation for the atomic form factor can be recognized as a Fourier transform. Thus it becomes clear that the underlying electronic charge distribution can be calculated from the scattered signal. In reality, the quantity measured is the intensity of the scattered signal which is equal to the square of the amplitude function. The implications that arise from this will be discussed in a later section.
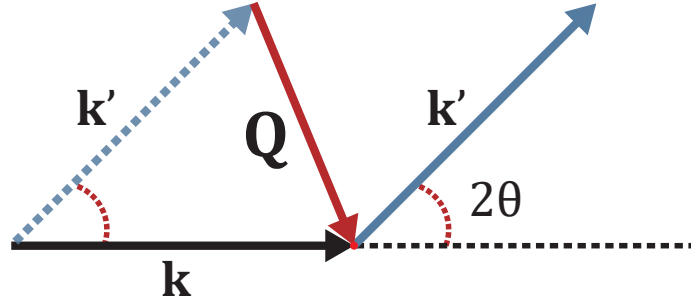
Figure 2.1: The relationship between the scattering vector $\mathbf{Q} = \mathbf{k} - \mathbf{k'}$ and the scattering angle $2\theta$

### 2.1.1 Scattering by a collection of atoms

Now that we have established that scattering from an atom can be described by the Fourier transform of its electron density distribution it is easy to extend this to an ensemble of atoms. We perform a sum over all the atoms $j$ in the sample:

$$\mathcal{F}(\mathbf{Q}) = \sum_j f_j(\mathbf{Q})e^{i\mathbf{Q}\cdot\mathbf{r}_j}, \tag{2.3}$$

and define the molecular form factor. The coherent elastic scattering intensity is the modulus square of the amplitude of the sum of the molecular form factor:

$$I(\mathbf{Q}) = \mathcal{F}(\mathbf{Q})\mathcal{F}(\mathbf{Q})^\star = \sum_i \sum_j f_i(\mathbf{Q})f_j(\mathbf{Q})e^{i\mathbf{Q}\cdot(\mathbf{r}_i-\mathbf{r}_j)} \tag{2.4}$$

In a realistic noncrystalline or nanocrystalline sample like a liquid, gas or a powdered crystalline material the position vector $\mathbf{r}$ is randomly oriented with respect to $\mathbf{Q}$. In addition, due to the fast nature of the x-ray scattering interaction, we can assume that the measured signal is essentially a collection of single scattering events where all spatial orientations are represented with equal probability. Such an isotropic sample can be described by calculating an orientational average of the phase factor, rewriting Eq. 2.4 by evaluating the integral of the phase factor $e^{i\mathbf{Q}\cdot\mathbf{r}_{ij}}$ in spherical coordinates[75]:

$$I(Q)_{coh} = \sum_i \sum_j f_i(Q)f_j(Q)\frac{\sin(Qr_{ij})}{Qr_{ij}}, \tag{2.5}$$

where $\mathbf{r}_{ij}$ is the vector between the atoms $i$ and $j$. Vector $\mathbf{Q}$ is replaced by its magnitude $Q$ as the information from all directions collapses into one due to orientational averaging. Eq. 2.5 is known as the Debye Scattering Equation[76] and states that the coherent

scattering intensity from any collection of atoms is simply a sum of contributions from all atoms in the sample.

The structure factor for a disordered material can then be obtained by separating the self scattering terms where $i = j$ from the double sum and subtracting it, and normalizing by the total number of scatterers.

$$\frac{I(Q)_{coh}}{N} - \langle f^2 \rangle = \frac{1}{N} \sum_{i \neq j} f_i(Q) f_j(Q) \frac{\sin(Qr_{ij})}{Qr_{ij}}, \tag{2.6}$$

and finally normalizing by $\langle f \rangle^2$. Doing all of this accounts for the diffuse Laue monotonic scattering that contributes a monotonically decreasing background due to the destructive interference arising from atomic positions occupied by elements with different scattering power[77], which takes the form $\frac{\langle (f - \langle f \rangle)^2 \rangle}{\langle f \rangle^2}$. The result is the normalized structure factor $S(Q)$:

$$S(Q) = \frac{I(Q)_{coh}}{N\langle f \rangle^2} = 1 + \frac{1}{N\langle f \rangle^2} \sum_{i \neq j} f_i(Q) f_j(Q) \frac{\sin(Qr_{ij})}{Qr_{ij}} \tag{2.7}$$

Rearranging the terms we can define the reduced total scattering structure function:

$$F(Q) = Q[S(Q) - 1] \tag{2.8}$$

## 2.2 Pair distribution functions

Describing the atomic positions of a highly disordered material is often easier in a statistical sense. A commonly used option is the reduced pair distribution function (PDF). It describes the probability of finding an atom separated by the distance $r$ from an arbitrary atom chosen as origin. Thus, this function is a real space weighted histogram of interatomic separations in a material. The PDF is defined as a sine Fourier transform of the normalized total scattering structure function $F(Q)$[36]:

$$G(r) = \frac{2}{\pi} \int_0^\infty F(Q) \sin(Qr) \mathrm{d}Q \tag{2.9}$$

The G(r) is just one of a number of correlation functions that exist in the literature[78] and contains all of the same information about the short and long range structure. The intuitive interpretation of the G(r) can be obtained by examining a closely related Radial Distribution Function (RDF). The RDF is defined as:
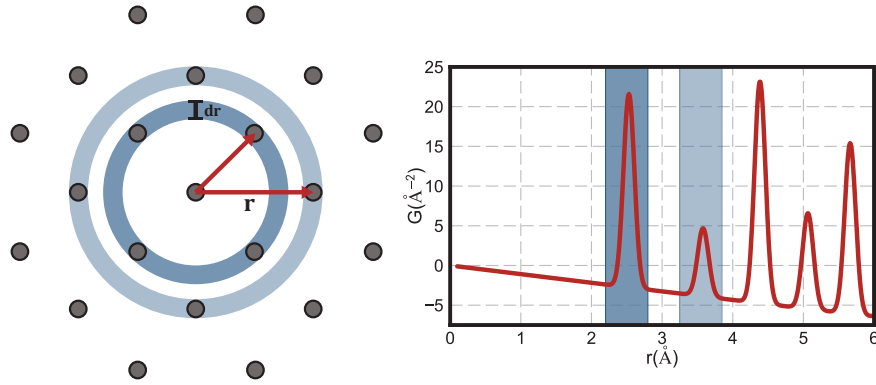
Figure 2.2: PDF construction from a spherical shell of thickness $dr$ at a distance $r$ away from the origin. A cubic face centered (FCC) structure used as an example contains 12 nearest neighbors and 6 next-nearest neighbors (not visible dut to viewing angle).

$$R(r) = 4\pi r^2 \rho(r), \tag{2.10}$$

where the $\rho(r)$ is the local atom-pair density of the material. The RDF is defined in such a way that the number of atoms inside a shell of thickness $dr$ at a distance $r$ away from the origin is given by $R(r)dr$. This is reflected in another description given as a set of delta functions at the atomic positions weighted by their scattering power:

$$R(r) = 4\pi r^2 \rho(r) = \frac{1}{N} \sum_i \sum_j \frac{f_i(Q)f_j(Q)}{\langle f(Q)\rangle^2} \delta(r - r_{ij}), \tag{2.11}$$

again only dependent on the magnitude of vector $Q$, since the three dimensional information is collapsed to one dimension.

Finally, the relation between the RDF and the G(r) is given by:

$$G(r) = \frac{R(r)}{r} - 4\pi r \rho_0 \gamma_0(r) \tag{2.12}$$

Here the $\rho_0$ is the average atomic density of the material and $\gamma_0(r)$ is the characteristic function related to the missing low angle scattering intensity in a typical measurement which modifies the shape of the negatively sloping baseline given by $-4\pi r \rho_0$. It occurs due to the limitations of the experimental methodology where the scattering signal cannot be measured from $Q = 0$, but rather from a finite $Q_{\min}$. For increasing $r$, the value of $\gamma_0(r)$ quickly asymptotes to 1, significantly affecting the analysis only for very small particle sizes, typically below 1nm. A rigorous derivation of this can be found in Farrow et al.[63].

Similarly to the missing information in the range between zero and $Q_{\min}$, the ex-

perimental limitations dictate the maximum magnitude of $Q$ that is accessible during a measurement. In terms of experimental equipment, due to the low energy of the x-rays produced, the copper $K_\alpha$ anode can only reach $Q \approx 8\text{Å}^{-1}$ while Mo $K_\alpha$ can provide up to around $16\text{Å}^{-1}$. The other end of the problem is the asymptotic behavior of the $S(Q)$ itself. For x-rays the coherent intensity in the $S(Q)$ dies out with increasing $Q$, completely disappearing around $30\text{-}50\text{Å}^{-1}$. This means that even when high enough x-ray energies can be accessed via specialized synchrotron facilities, there is a limit as to how far in $Q$ one can measure.

Limiting the integration to a finite value of $Q_{\max}$ has an effect of introducing errors into the data. These appear in terms of oscillations called *termination ripples* which can affect the information that can be extracted from the G(r). This is essentially a convolution of the G(r) by a step function terminating at $Q_{\max}$. The oscillations have a period of $\approx 2\pi/Q_{\max}$ and increase for increased $Q_{\max}$ becoming a negligible factor for $Q_{\max}$ over $30\text{Å}^{-1}$[79].

As a rule of thumb the resolution of the measured PDF is defined as:

$$\Delta r = \frac{\pi}{Q_{\max}} \tag{2.13}$$

Obtaining quality experimental PDF's thus becomes an exercise in optimization of the noise and balancing the $r$ resolution with the degradation of the counting statistics at higher angles. The practical definition of the G(r) thus becomes:

$$G(r) = \frac{2}{\pi} \int_{Q_{\min}}^{Q_{\max}} F(Q) \sin(Qr) \mathrm{d}Q, \tag{2.14}$$

where $Q_{\min}$ is the lowest accessible angle and the $Q_{\max}$ is the highest.

### 2.2.1 Modeling the PDF

The PDF has a number of advantages over the other similar correlation functions. It can be obtained directly from the measured scattering data by a Fourier transform. It tends to zero at $r = 0$ and the negative baseline slope is an expression for the average number density of the material. It also asymptotes to zero at high $r$ values, while oscillating around zero. From the analysis point of view, the main benefit is that the propagated uncertainties on the data are constant in $r$, which means that the difference between the calculated $G_{calc}(r)$ and measured $G_{obs}(r)$ have the same significance for all $r$ values. In addition the amplitude of the oscillations gives a sense of the structural coherence of the sample if the oscillations disappear earlier than dictated by the finite $Q$ resolution of the measurement. And, finally, it is intuitively related to the RDF function which makes the PDF analysis fairly approachable.

## Model free information in the PDF

A number of parameters can be extracted from the G(r) without the need for a structural model despite the heavily averaged representation of the structure. These are unsurprisingly given by peak position, peak intensity and peak width/shape.

The peak position gives the bond distances directly for atom pairs in the sample. Given some knowledge about the system, this allows us to make qualified guesses about the structure of the sample, or structural transformations if these distances are changing. In a real material the peaks will never appear as delta functions, but will be broadened by a Gaussian function due to static or dynamic disorder, such as strain or atomic motion. Given that the data were acquired with a sufficient $r$ resolution, some of these effects may be inferred.

If the G(r) is properly normalized the integrated intensity contains information about the coordination number of a given atom pair:

$$N_C = \int_{r_1}^{r_2} G(r)\mathrm{d}r, \tag{2.15}$$

where $r_1$ and $r_2$ correspond to a range of interest in $r$. This process will work exceptionally well for non overlapping peaks. In case where significant overlap is present, the coordination number can still be retrieved via a structural model or partial PDF analysis[74].

## Structural modeling

For more complicated problems information can be extracted from the PDF via structural modeling. Generally this is done by creating a crystallographic model containing information about the atoms, their positions and dynamics, then calculating the corresponding $G_{calc}(r)$. The $G_{calc}(r)$ is then compared with the data $G_{obs}(r)$ and the goodness of fit residuum, $R_w$, quantifies the similarity:

$$R_w = \sqrt{\frac{\sum_{i=1}^{n} w(r_i)[G_{obs}(r_i) - G_{calc(r_i)}]^2}{\sum_{i=1}^{n} w(r_i)G_{obs}(r_i)}}, \tag{2.16}$$

where $w(r_i) = \frac{1}{\sigma^2(r_i)}$ is the inverse of the estimated standard deviation of each data point. The $R_w$ is then minimized by varying the parameters by a least squares refinement, similar to a full profile Rietveld refinement[41, 80]. Typical refined parameters would be lattice constants, lattice angles, atomic positions, scale parameters, displacement parameters, etc.

The $G_{calc}(r)$ can be calculated from a model using Eq. 2.11 and Eq. 1.1. But since the atomic positions in the real structures are not delta functions, the $\delta$ terms in Eq. 2.11 are convoluted with a Gaussian broadening term $\sigma_{ij}$ given by:

$$\sigma_{ij} = \sigma'_{ij} \sqrt{1 - \frac{\delta_1}{r_{ij}} - \frac{\delta_2}{r_{ij}^2} - Q_{broad}^2 r_{ij}^2} \qquad (2.17)$$

Here the terms $\delta_1$ and $\delta_2$ are the correction parameters describing correlated atomic motion[81] and $\sigma'_{ij}$ is the peak width given by the Atomic Displacement Parameter (ADP) tensors for the atoms. The ability to refine correlated motion parameters is one of the advantages of real space Rietveld refinements over their reciprocal space alternatives[74]. $Q_{broad}$ is the broadening factor as a result of finite experimental $Q$ resolution.

The finite $Q$ resolution of the measurement also leads to a decreasing peak amplitude for larger $r$ values[74]. In principle, the amplitude of the peaks of the PDF should extend infinitely. In practice, however, the PDF attenuates quickly. This attenuation follows a Gaussian shape and is modeled by multiplying the calculated profile by:

$$B(r) = \exp(\frac{rQ_{damp}^2}{2}) \qquad (2.18)$$

Both $Q_{damp}$ and $Q_{broad}$ can be obtained during the calibration step of an assumed perfectly crystalline material.

Nowadays, software that is able to perform these calculations and refinements is freely available. Two programs that were used for this thesis were PDFGui[46] and the python framework Diffpy-CMI[47]. These programs work with a small box modeling approach, where the modeling is attempted by constructing highly constrained models with few parameters. The calculations are made possible by using a crystallographic approach where a periodic unit cell is defined. This significantly reduces the complexity of the calculations by eliminating the need to take a double sum over all the atoms in the crystal according to the Debye equation (Eq. 2.5) and can be done quickly and efficiently. Use of these boundary conditions implies that such an approach is mostly suitable for crystalline materials with low degree of disorder. Some limited deviations from the average can still be modeled by utilizing creative approximations and will be discussed further in Chap. 3. The python suite Diffpy-CMI, also includes an option for calculating the G(r) and performing refinements without the need for periodic approximation, making it possible to model structures of a limited size in an adequate time frame. In this case the scattering is calculated using the Debye equation (Eq. 2.5) and is subsequently Fourier transformed according to Eq. 2.8.

Using the small box modeling approach requires an ability to create a physical model that is a viable representation of the problem. In a situation where this is not possible, either due to the unknown nature of the sample structure or due to the high degrees of disorder, a large box modeling approach may be appropriate. Here, the model is created out of tens of thousands of atoms and is solved by a global optimization method such as Reverse Monte Carlo(RMC)[82], also known as Monte Carlo simulated annealing[83]. Because of the sheer number of atoms, it will be able to reproduce a scattering pattern

close to the experimental one. Using this approach, both the atomic positions and all types of disorder can be simulated and compared to real space and reciprocal space data. Care has to be taken to constrain the model properly as the results are often unphysical[82]. Big box modeling provides exciting options in terms of structure modeling, but is outside the scope of this thesis.

**Shape and size modeling**

In a situation where the amplitude of the peaks in a PDF decays faster than given by the resolution envelope in Eq. 2.13, it becomes possible to perform shape and size analysis of the samples. This intensity decay is typically caused by the loss of structural coherence of the sample as a result of finite size and morphology. An intuitive understanding is gained by imagining a G(r) with the last measured pair correlation at a distance of $r = 30$Å. In a real sample this means that the largest dimension in some direction is given by this distance beyond which no correlations exist. The way the correlation distances disappear compared to the resolution attenuation function tells about the shape of the domain. In mathematical terms this is modeled by multiplying the PDF profile by a characteristic size function, e.g. a spherical shape function:

$$G_{vc}(r) = \gamma_s(r)G(r), \tag{2.19}$$
$$\gamma_s(r) = \left[1 - \frac{3r}{2d} + \frac{1}{2}\left(\frac{r}{d}\right)^3\right]H(d - r),$$

where $d$ is the diameter of the sphere and $H$ is a step function which is equal to 1 when $r \leq d$ and zero otherwise[84].

Functions for other geometrical shapes also exist[44] and can be used in a structural model or refinement in a case where the morphology is known. Notably due to the presence of size and shape distributions, the obtained results can be inaccurate without proper constraints. For more complicated morphologies, the shape profiles can be measured experimentally by small angle scattering experiments.

This type of modeling is sometimes referred to as a Virtual Crystal(VC) approximation[1], since multiplication by a profile function can be conceptually perceived as a cutout from a larger, e.g. perfectly crystalline model. This is in contrast to the Debye Scattering Equation calculation, where the morphology and size of the domains can be calculated exactly.

**Recent developments in VC modeling of Face Centered Cubic (FCC) metals**

Due to its simplicity a lot of simple metal nanoparticle characterization studies using PDF, employ VC modeling. The nanoparticles are assumed to stem from the bulk parent structures and to model this, the data are attenuated by a shape function. For typical Face Centered Cubic (FCC) structures, the typical agreement factor for a good fit of a nanoparticle VC model that is acceptable for publication is in the range of $R_w = 0.22 - 0.25$.
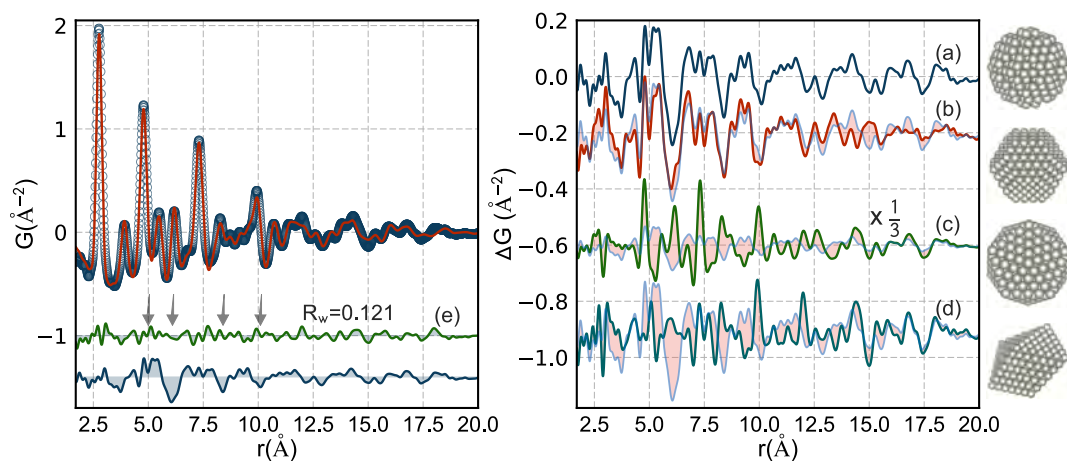
Figure 2.3: Best-fit difference curves for VC and different cluster models and the measured PDF of Pd nanoparticles. The measured PDF (open circles) and calculated (red solid line) from a 3.6 nm decahedron (e). Residuals from a (a) fcc VC sphere (b) truncated fcc octahedron (Wulff) (c) Mackay icosahedron (scaled by factor $\frac{1}{3}$) (d) regular decahedron and the difference as compared to the VC residual is shown in pale blue. Arrows are positioned over characteristic features in the VC residual. The cluster structures are shown to the right in the same order. Reproduced with permission from S. Banerjee et. al[1]

In these cases the generated model accurately describes the major features of the data, perfectly aligning with the major peaks of the PDF pattern. At the same time, it is possible to obtain structure fits an order of magnitude better, in terms of $R_w$, for crystalline materials such as Ni powders that are routinely fit to an $R_w = 0.02$. The logical implication of such a discrepancy has to be the inadequacy of periodic models when describing FCC nanoparticle structures. Indeed, in a case like this, it is only appropriate to assume that part of the structural information that is contained in the data is not being modeled and fit[1].

A metastudy has been performed on a collection of FCC nanoparticles made from different materials and alloys, having different size distributions and morphologies. The VC model captures the average arrangement of the atoms but is incapable of describing the structural defects in these types of materials. Examining the residuals across the collection, it was determined that PDF is sensitive to the [111] type twin plane defects and that these can be modeled using discreet structural models. The presence of the twin defects in the core of the nanoparticles can be successfully refined using polyhedral shapes, as illustrated in Fig. 2.3. Each shape has a different associated twin defect density. The missing features in the fit residual of the typical FCC structure refinement can be significantly improved locally, by fitting a matching polyhedral shape, that corresponds to the correct defect density on the material. This illustrates that poor fit residuals for PDF refinements of nanoparticles should not be considered as a limitation of the method, but rather an incomplete treatment of the data, from which additional useful information can be extracted. In fact, such a significant improvement leaves very little to work with in the residual posing a question whether more complicated models are justified.

**Multicomponent systems**

In the case where the measured sample consists of multiple structural phases the total PDF will be defined as a weighted sum of all of the contributions. In a simplified form this can be expressed in terms of a superposition of the contributions from all PDFs[74], e.g for a system consisting of $a$ and $b$:

$$G(r) = G_{aa} + G_{bb} + G_{ab} \tag{2.20}$$

If the phases are well segregated and the presence of a second component does not affect the structure of the first, the cross terms become small and can be neglected. When the approximation is valid the total reduced pair distribution function becomes the sum of all phases in the sample. This makes it possible to perform phase quantification refinements and manipulations where reference datasets, such as substrates, are measured and subtracted from the scattering pattern of the mixture and allow for analysis of the remaining data[25].

## 2.3  Small Angle Xray Scattering (SAXS)

The previous sections focused on extracting the information from the x-ray scattering for higher $Q$ vectors. The limit where $Q$ is close to zero also contains a lot of information about the sample. The scattering in the small angle region is concerned with small $Q$ values, i.e. large values real space. At this range of $Q$ values, the scattering from individual atoms cannot be resolved anymore, hence the scattering contains information about larger domains/particles and corresponding effects like particle interactions.

### 2.3.1  Small angle scattering basics

The small angle scattering amplitude is given by the Fourier transform of the average electron density of the scattering volume: It follows that the intensity for a sufficiently averaged measurement is given by:

$$I_{SAXS}(Q) = \int_V \rho(r)e^{i\mathbf{Q}\cdot\mathbf{r}_i}\mathrm{d}V_i \int_V \rho(r)e^{-i\mathbf{Q}\cdot\mathbf{r}_j}\mathrm{d}V_j \tag{2.21}$$
$$\approx \left| \int_V \rho(r)e^{i\mathbf{Q}\cdot\mathbf{r}}\mathrm{d}V \right|^2$$

If we can assume that the sample consists of identical particles with a uniform scattering density and that the solution is dilute and particle-particle interactions can be neglected, then we can extract the scattering contribution of the particles by subtracting the scattering contribution of the solvent:

$$I_{SAXS}(Q) = (\rho_p - \rho_s)^2 \left| \int_V e^{i\mathbf{Q}\cdot\mathbf{r}}\mathrm{d}V \right|^2, \tag{2.22}$$
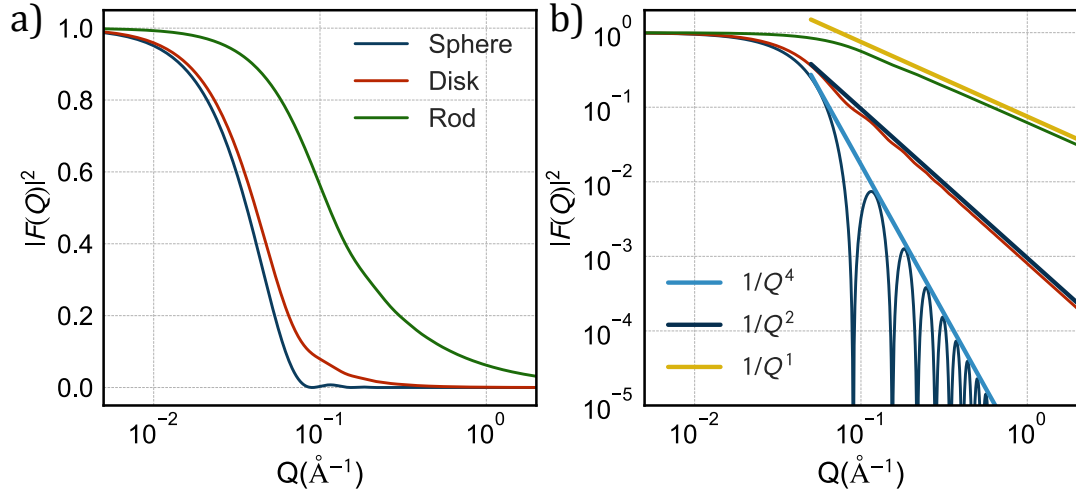
Figure 2.4: a) SAXS form factors for a sphere, disk and a rod. b) The dimensionality can be determined via a linear fit to the medium $Q$ region of the SAXS data.

where $\rho_p$ is the scattering length density of the particles and $\rho_s$ is the scattering length density of the solvent. From here the single particle form factor is defined as:

$$F_{SAXS}(\mathbf{Q}) = \frac{1}{V_p} \int_{V_p} e^{i\mathbf{Q}\cdot\mathbf{r}_j} dV_p, \tag{2.23}$$

and the total intensity simplifies to:

$$I_{SAXS}(Q) = N\Delta\rho^2 V_p^2 P(\mathbf{Q}), \quad P(\mathbf{Q}) = |F_{SAXS}(\mathbf{Q})|^2 \tag{2.24}$$

Several observations can be made here. First, it is clear that for $\mathbf{Q}$ approaching zero, the form factor will approach unity and the intensity from a single particle will be equal to $\Delta\rho^2 V_p^2$. Thus, in an actual measurement the intensity at $Q = 0$ is proportional to the volume squared of the total number of scatterers in the sample. The requirement is, of course, that the intensity has been properly normalized for incident intensity and sample absorption. The scattering at $Q = 0$ usually cannot be measured experimentally, but can typically be extrapolated if a sufficiently low angle data is measured. The second observation is that similarly to the atomic form factor, $F_{SAXS}$ contains information about the shape and size of the electron distribution, or rather in this case the scattering shape and dimensions of the scattering particle. The geometric form factors can in a few cases be determined analytically[72, 85], and otherwise are calculated numerically. Some of the analytically derived form factors are illustrated in Fig. 2.4a).

When working with inorganic nanoparticle suspensions, as was intended for this thesis, a good assumption for the particle shape is a sphere. In the case of a spherical form factor, a number of important sample parameters can be quickly extracted from the measured data. In the low $Q$ region, also called the Guinier region[84], the approximate size of the scattering particles, given by the particle radius $R_p$, and radius of gyration, denoted $R_g$, can be extracted. For a sphere, a linear fit to the data of logarithmic intensity and
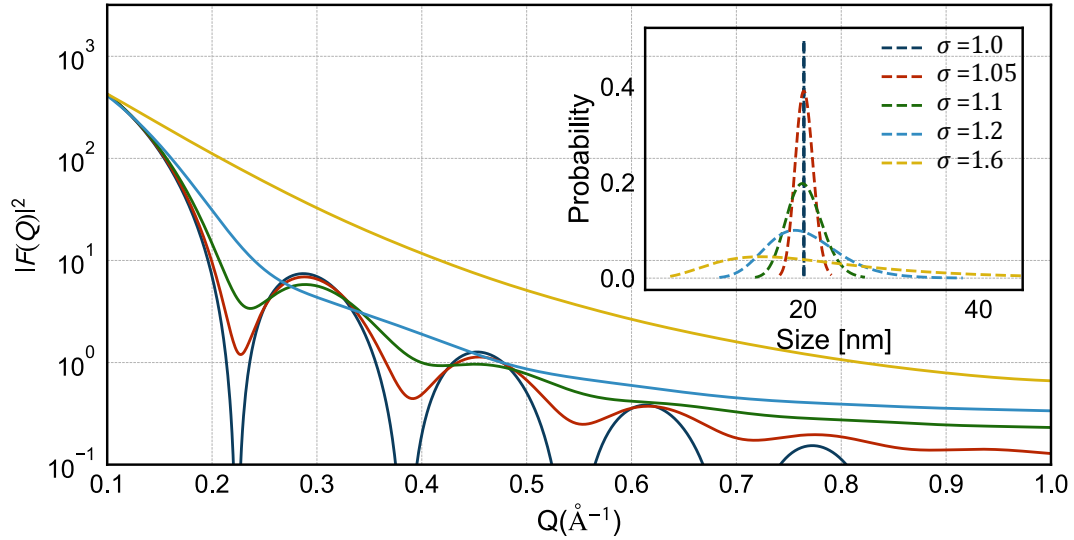
Figure 2.5:   Effects of polydispersity on the SAXS intensity. Lognormal distribution with a mean of 20 and $\sigma = 1,\ 1.05,\ 1.1, 1.2$ and $1.6$.

squared momentum transfer yields the particle radius from a slope of $-R_p^2/5$. Similarly, the radius of gyration would follow $-R_g^2/3$. In the high $Q$ region of small angle scattering the intensity will decay proportionally to the surface area of the spherical particles and inversely proportionally to $Q^{-4}$.

Finally, the particle size distribution can be modeled by multiplying Eq. 2.24 by the characteristic function describing the distribution, similarly to the way it can be modeled from PDF. The expression reads:

$$I_{SAXS}(Q) = \Delta\rho^2 \int_0^\infty D(R)V_p(R)^2 P(Q,R)\mathrm{d}R, \qquad (2.25)$$

where D(R) is the function describing the distribution and the integral over D(R) is normalized to one. The presence of a size distribution will generally smear out the features in the measured scattering intensity introducing a lot of ambiguity into the measurement. This effect is illustrated in Fig. 2.5. For this reason it is important to obtain proper constraints from complementary measurements.

## 2.4   Crystalline materials

The crystal in crystallographic terms is defined as an infinitely extending arrangement of atoms. It consists of a pattern of atoms that repeats in all spatial directions. This periodic pattern is called a *unit cell* and is the minimal building block of a complete crystal. Similarly to a molecule, the unit cell is an arrangement of atoms and we can define a *unit cell form factor* in much the same way, taking a sum of all the scattering

contributions in a unit cell:

$$F_{uc}(\mathbf{Q}) = \sum_j f_j(\mathbf{Q})e^{i\mathbf{Q}\cdot\mathbf{r}_j}, \tag{2.26}$$

The crystal is built up by applying symmetry operations such as translations, rotations, reflections or a combination of these, depending on the symmetry of the crystal. From this, the scattering amplitude from a crystal can be expressed as a product of the sum of the unit cell and the sum of all of the symmetry operations needed to reproduce a certain periodic arrangement:

$$F_C(\mathbf{Q}) = \sum_n e^{i\mathbf{Q}\cdot\mathbf{R}_n} \sum_j f_j(\mathbf{Q})e^{i\mathbf{Q}\cdot\mathbf{r}_j}, \tag{2.27}$$

where $R_n$ denotes the set of vectors in real space that define the characteristic symmetry of the lattice and the sum over n runs over all unit cells in the crystal.

In reciprocal space the lattice is defined by the lattice vector:

$$\mathbf{G} = h\mathbf{a_1}^* + k\mathbf{a_2}^* + l\mathbf{a_3}^*, \tag{2.28}$$

where $\mathbf{a_1}^*$, $\mathbf{a_2}^*$ and $\mathbf{a_3}^*$ are the reciprocal basis vectors and $h$, $k$ and $l$ are integer numbers. The basis vectors are defined such that $a_i \cdot a_j^* = 2\pi\delta_{ij}$. Looking at the sum in Eq. 2.27 it is clear that as the number of terms increases, constructive interference occurs only when the phase factors adds up to multiples of $2\pi$. This happens exactly when $\mathbf{Q} = \mathbf{G}$ and the Laue condition is fulfilled[72]. The integers $h$, $k$ and $l$ are Miller indices and are used to describe a set of planes intersecting the basis vectors at $(a_1^*/h, a_2^*/k, a_3^*/l)$. This means that in one dimension, the Laue condition is equivalent to a well known Bragg's law, where the constructive interference for a crystal occurs whenever the lattice plane spacing is equivalent to the whole number of wavelengths:

$$n\lambda = 2d_{hkl}\sin(\theta), \tag{2.29}$$

where $d_{hkl}$ refers to the spacing between the planes of the family $[hkl]$, $\lambda$ is the wavelength of the incoming light and $\theta$ is the incidence angle.

Calculating the coherent scattering intensity for a crystal is thus relatively simple. The intensity given by the lattice sum is proportional to the total number of unit cells and their volume while the amplitude of any particular reflection corresponding to any $[h, k, l]$ set of lattice planes can be calculated by evaluating the unit cell form factor for a given lattice vector $\mathbf{G} = \mathbf{Q}$ using using Eq. 2.28 and Eq. 2.26. For example, for an FCC lattice with a basis consisting of four atoms:

$$r_1 = 0, \quad r_2 = \frac{1}{2}(a_1 + a_2), \quad r_3 = \frac{1}{2}(a_2 + a_3), \quad r_4 = \frac{1}{2}(a_3 + a_1), \tag{2.30}$$

the unit cell form factor becomes:

$$F_{uc}(\mathbf{G}) = f(\mathbf{G}) \sum_j e^{i\mathbf{G}\cdot\mathbf{r}_j} \qquad (2.31)$$

$$= f(\mathbf{G})(1 + e^{i\pi(h+k)} + e^{i\pi(k+l)} + e^{i\pi(l+h)}),$$

producing a very specific pattern of intensities, where the reflections are only possible for all odd or all even Miller indices.

### 2.4.1 Powder diffraction

One of the incredibly useful methods for analyzing structures of crystalline materials is by means of powder diffraction. Pioneered by Debye and Scherrer[29] and later revolutionized by the invention of the Rietveld refinement method[31], powder diffraction has been a go to method for identifying and studying compounds in a laboratory environment.

In a powder diffraction measurement the sample is assumed to be a perfect powder where all spatial orientations of the crystal are present at the same time. The consequences of this are twofold, first all sample orientations are present, which means that all incidence angles and by extension, the Laue condition, for all available lattice planes is satisfied. The second consequence is that all spatial orientations are also present with *equal probability*, similar to a liquid or amorphous sample. This means that the measured intensity will be spherically averaged and will depend on the magnitude of the vector $Q$.

One of the key strengths of powder diffraction is its ability to quickly identify a pattern of intensities and assign them to a corresponding space group which relates to the atomic arrangement in a unit cell. While this can be done arguably more accurately by measuring scattering from a single crystal, the experimental requirements for powder diffraction are less stringent. The sample can be a finely ground powder, which is usually much easier to obtain than a large and perfect crystal, and as the data are averaged around the azimuth in a powder diffraction experiment, there is no need for crystallographic alignment. The intensity as a function of $Q$ will decay for larger $Q$ vectors due to the atomic form factor comprising the unit cell and the exponential attenuation from atomic motion as accounted for by the Debye-Waller factor and thermal diffuse scattering[72]. As the lattice spacing decreases for larger $Q$, the reflections will also start to overlap significantly reducing the maximum viable measurement range. In practice this means that measurements can be done quickly on relatively inexpensive low energy in-house x-ray diffractometers. The required computational complexity is also considerably less than that required for a full single crystal experiment, when used with a conventional Rietveld refinement method.

In an actual measurement, the incoherent intensity will still be present in much the same way as before, but since all of the structural information is contained within the phase factor of the scattered waves and their interference, it can be safely ignored. Absorption on the other hand is often a useful tool, especially in cases where elemental specificity is required, such as in Extended x-ray Absorption Fine Structure (EXAFS), but is beyond the scope of this thesis.

**Rietveld Refinement**

The Rietveld refinement method[86] is an extremely powerful technique for extracting information from a powder diffraction measurement. The method is based on the ability to constrain a model to a periodic unit cell obtained from the pattern of Bragg reflections in the measured dataset. The intensities can then be calculated from the unit cell form factor, and the unit cell parameters can be refined together with peak broadening parameters at the same time. The small number of parameters in a typical Rietveld refinement makes it possible to compute the scattering patterns quickly and adjust the parameters for the best fit to the data. Sophisticated software such as FullProf[87], GSASII[88] and MAUD[89] are able to compute the form factors for the models and minimize the goodness of fit parameters via efficient least squares algorithms.

When a powder diffraction dataset is measured it includes all of the intensity emanating from a sample hit by a beam of photons. In a Rietveld refinement the incoherent and diffuse scattering present underneath and in between the Bragg peaks can be ignored, focusing instead on the positions and intensities of the strong reflections amplified by the periodicity of the crystal. This is typically done by fitting a polynomial to the background. The information that can be obtained from a powder diffraction pattern thus divides into three categories: the information about the crystal structure and symmetry from the positions of the Bragg peaks, the contents of the unit cell from the peak intensities and the microstructure of the sample from the peak profile.

**Information from a powder diffraction pattern**

The pattern of the positions of the Bragg peaks produces a unique fingerprint that can be matched with a space group that defines the symmetry of the lattice. Once the space group has been correctly established, the positions will give the length of the basis vectors and lattice spacings.

According to Eq. 2.31, the intensities of the Bragg peaks are given by the atomic arrangement weighted by the scattering power of the atoms occupying a given lattice plane. From here follows that the peak intensity contains the information about the contents of the unit cell. Deviations from the ideal arrangement in terms of substitutions by a different atomic species or lattice vacancies will affect the relative intensity in the pattern. The change in intensity could also be an indication of preferred orientation in the sample if the orientation of the crystallites in the powder is not perfectly random, since the total intensity of a Bragg reflection is proportional to the number of unit cells in a given direction parallel to the wavevector transfer.

The peak profile in a powder diffraction pattern carries the information about the microstructure of the sample. A multitude of factors can contribute to the broadening of the Bragg peaks and their shape. Typically two main effects are size broadening due to the finite size of crystalline domains and macrostrain. In addition to the sample related broadening of the peak profile, the instrument also plays a role. Typical sources of instrumental broadening are slit geometry, beam divergence, beam profile, sample size etc.

The broadening effects from the sample can be separated into two groups due to the different angular dependencies of the involved processes. Crystallite size broadening is typically analyzed via the Scherrer equation[90]:

$$\beta = \frac{K\lambda}{\langle D \rangle \cos\theta},$$ (2.32)

where $\beta$ is the FWHM of the peak broadening after subtracting the instrumental contribution, $\langle D \rangle$ is the average domain size and $K$ is constant dependent on the particle morphology. For an isotropic crystallite consisting of cubic unit cells, the value of $K$ was originally derived to 0.88[90].

The average size obtained from Scherrer equation gives a volume weighted average and in practice serves only as an indication of crystallite size rather than an accurate and representative number. It cannot necessarily be compared to size estimates obtained from other techniques, such as PDF or TEM, but is very useful in studying trends, e.g. in an in-situ measurement of particle growth. When comparing to a TEM specifically, it is important to remember that the size obtained from Scherrer's formula relates to the size of coherent crystalline domains, and that particles visible in TEM might consist of several of them. One typical example are a multitude of geometric structures with twin-plane defects, such as decahedral shapes that are typically found in noble metal particles, where every single primary particle consists of 5 sub domains[91]. In addition, the electron microscopy imaging will also include any amorphous volume as part of the particle, which is typically invisible to Scherrer analysis.

Similarly, the macrostrain generally takes the form:

$$\beta \propto \langle \epsilon^2 \rangle^{\frac{1}{2}} \tan\theta,$$ (2.33)

where $\epsilon = \frac{\Delta d}{d}$[92]. Similarly to the size effects in a powder, macrostrain is a convolution of multiple effects such as lattice relaxations and disorder. Peak profiles can give rich information if properly constrained.

In general, the Rietveld refinement procedure does not rely on physical modeling of the peak profile. The Bragg peak shapes are assumed to be a convolution of a Gaussian and a Lorentzian function, i.e. the Voigt profile, that has been shown to work well in practice. The final choice, however is at the user's discretion, depending on the type of analysis one attempts to perform.

## 2.5   Synchrotron light sources

Since their discovery in the end of 19th century, x-rays have been extensively used for science. Their properties make them ideal for imaging and since the formulation of the Braggs Law, the field of crystallography was able to look inside materials and study them on an atomic level. Originally, the x-rays were produced by x-ray tubes, where electrons are accelerated from a cathode onto a metal anode. These sources are very versatile,
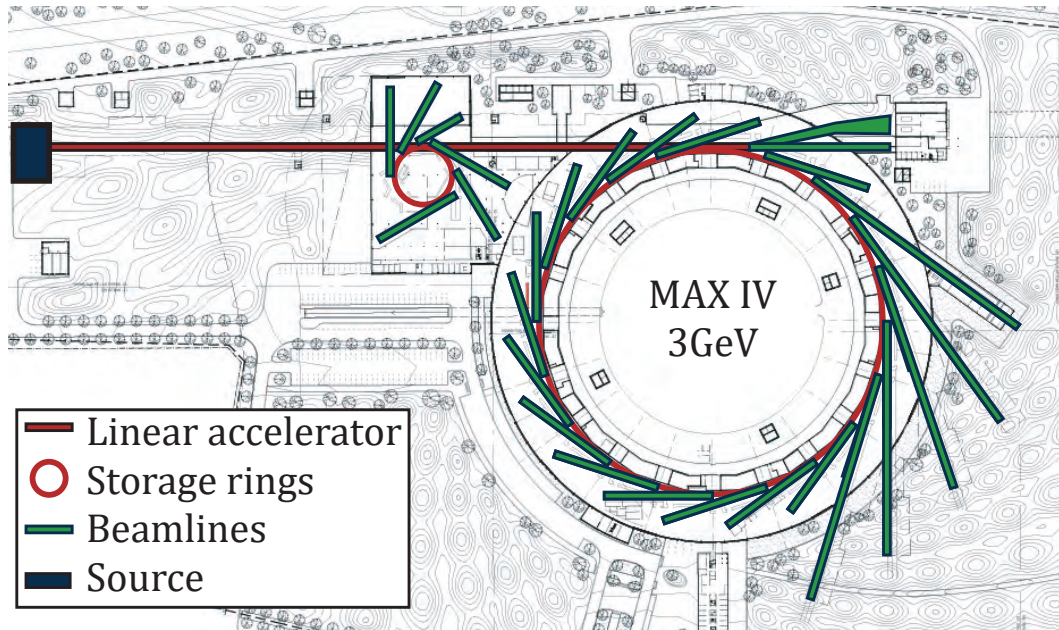
Figure 2.6: The layout of the MAXIV synchrotron. The electrons are accelerated using a linear accelerator and are stored in the storage ring. The beamlines are placed tangentially to the storage rings and are using the radiation produced from keeping the electrons in the circular path.

but produce limited amounts of x-rays on the order of $10^6 - 10^8$ photons per second. Increasing the amount of radiation is impractical in these sources as the currents required would simply evaporate the material and destroy the equipment. As an example, a rotating copper anode can produce the x-rays from its $K_\alpha$ transition at a wavelength of 1.54Å, at a rate of around $10^8$ photons per second. The acceletartion voltage in this case is on the order of $40 - 60$keV with currents of $20$mA$-40$mA producing a large amount of heat that needs to be taken out of the system.

While other complicated anode designs exist nothing can compare to the flux of radiation that can be generated using synchrotron facilities. Originally built as particle colliders, these circular accelerators were quickly recognized as excellent sources of all types of radiation. The principle is simple, electrons are traveling at relativistic speeds in a circular ring contained by strong magnetic fields. As they are accelerated into the circular path, the electrons emit electromagnetic radiation. Using synchrotrons, much higher flux of the order of $10^{18}$ photons per second can be achieved.

Nowadays, the majority of synchrotrons are built for the sole purpose of generating strong x-ray beams for use in science within imaging, crystallography and spectroscopy, and medicine for various cancer treatment procedures. In addition to generating radiation purely from the bending of the electron trajectories, radiation can be generated using specialized devices, such as wigglers and undulators, inserted into the electron paths. For example, the undulators work by introducing an alternating magnetic field along the path of the electron forcing it to oscillate and emit radiation even on straight section of the ring. The energy emitted can be tuned by changing the spacing between the magnets giving an

extra layer of flexibility.

The emitted radiation can then be collected, collimated, monochromatized and focused, sending it to experimental stations to perform experiments. A more detailed description of a typical experimental station used for powder diffraction can be found in Chap. 3.

To overcome the problem of decaying intensity over time as the energy is taken out of the electrons travelling around the ring, modern synchrotrons employ a new scheme for continuous beam injections. While a typical halftime for a synchrotron is on the order of ten hours, new synchrotrons like inject new electrons at a rate of $\approx$100Hz. This reduces the energy spread to 0.1% of total intensity over time or around a factor of 10 compared to older machines[93]. This allows for more consistent measurements without the need of correcting for the decay in intensity.

# 3

## Experimental methods

This chapter outlines the equipment and the experimental procedures that were used in performing the experiments for the various studies in this thesis. It will introduce both the laboratory based equipment and synchrotron based measurement stations. In addition, specialized setups that were developed will be described. The data analysis workflow will be presented, adding a number of personal experiences and guidelines for optimal data processing.

## 3.1  In-house characterization techniques

Most routine investigations using x-ray radiation can easily be performed in a laboratory in-house environment. A number of commercial diffractometers exist that offer ready to use solutions to a customer or a department willing to invest into expanding their characterization tools. These sources are typically compact and easy to use, with very clear guidelines on data acquisition and analysis. The sources are powerful enough that typical measurements, such as phase identification from PXRD or size estimation from SAXS, can be done within half an hour per measurement. These tools also contain a number of automated functions that allow for efficient measurements and analyses.

While not as bright as synchrotrons, they can sometimes rival many beam lines in terms of resolution and convenience. In terms of convenience, their main benefit is that they are readily available at the home institution instead of having to apply for experimental time far in advance via a proposal system. In fact many preparatory studies are carried out on home systems, only applying for specialized synchrotron time when the limit of these in-house machines is reached.

Many samples studied in this thesis were first measured on an in-house system to test whether the characterization could be carried out on the spot. The specialized setup for in-situ measurements was also developed and tested in the lab, before being put to use during time limited experiments at the synchrotron. This section quickly outlines the in-house instruments and their main advantages.

### 3.1.1  PXRD

The in-house powder diffraction experiments were carried out on an PANalytical Empyrean X'Pert Pro diffractometer system. The system uses a custom modular system that allows for easy swapping of the modules such as collimation, filtering, detector and anodes. The diffractometer configuration used with this thesis utilizes a Cu anode to produce x-ray radiation of the wavelength of 1.54Å from the Cu $K_\alpha$ transition. The measurements are performed in Bragg-Brentano geometry. In the case of this diffractometer, it is implemented by mounting both the source and the detector on a moving arm of the goniometer and during the measurement the scan proceeds in a $\theta$-$\theta$ geometry. This is illustrated in Fig. 3.2a). The x-ray beam is collimated by a number of slits along its path and is cut down to fill an area of around 0.25cm$^2$. Similarly, the beam is collimated on its way back from the sample to eliminate excess air scattering and other effects leading to line broadening.

The detector is mounted on the arm opposite to the x-ray source and moves symmetrically to it. This allows the system to access the angles from -111∘ < 2$\theta$ < 168°. It is a hybrid pixel detector with pixel size of 55$\mu$m. The sample to detector distance is 240mm. The detector is able to combine pixels and is continuously moving and utilizes special software which allows it to achieve sub-pixel resolutions in 2$\theta$. It can also perform measurements in 2D mode, producing 2D images of the scattering pattern.

The sample is located in the middle of the goniometer setup and sample preparation
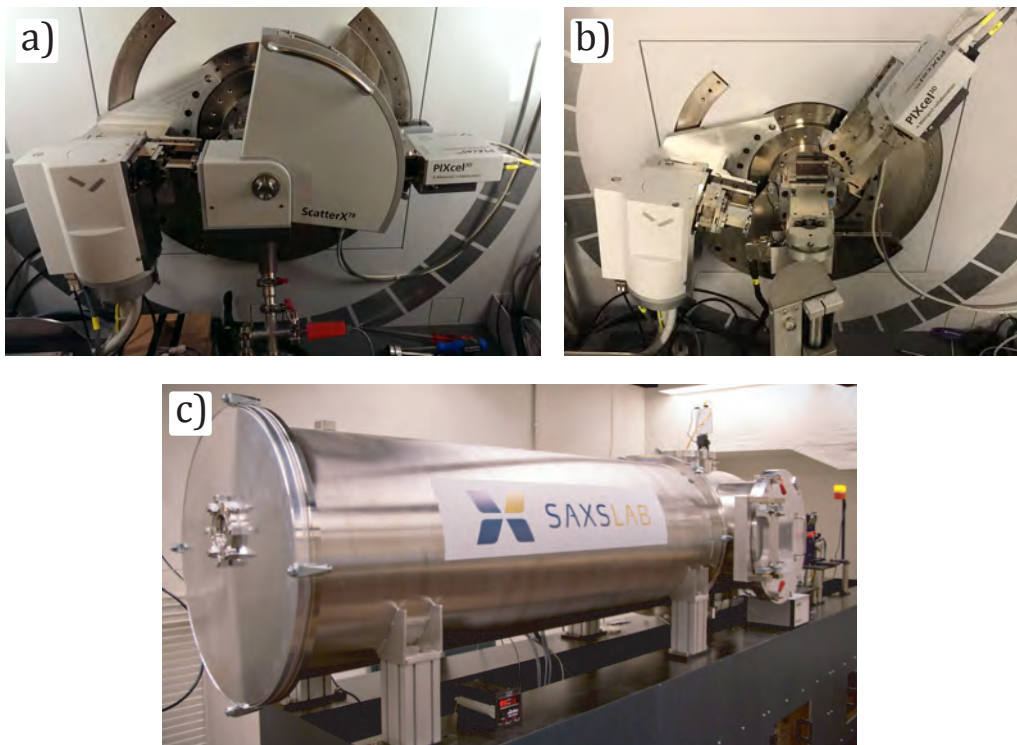
Figure 3.1: a) In-house PANalytical system in SAXS configuration. The vacuum chamber encloses the sample. Detector moves along the goniometer arm. b) In-house PANalytical system set up for powder diffraction. The source and the detector move symmetrically in a $\theta - \theta$, i.e. Bragg Brentano geometry. c) Ganesha SAXSLab system for small angle scattering. The sample and the detector are enclosed by a vacuum chamber that reduces air scattering.

involves spreading the powder in on a special Si plate that is rotated during the measurement to improve the powder average. The modular nature of the system also allows to swap out the rotating plate for capillary holder and also has modules for high temperature or low temperature environments, although neither have been used for the experiments presented in this work.

The instrument is equipped with a robotic sample changer, which allows the user to prepare upwards of 120 samples to be measured. The system is engineered to be extremely robust. The measurements are designed to be reproducible by fixing the sample position in one place and by tight calibration of motor movements. Thus it requires no alignments between measurements, like older diffraction systems might. The peak profile broadening is calibrated by measuring a $LaB_6$ standard and refining the instrumental peak profile, and is typically done monthly.

### 3.1.2 Small Angle X-ray Scattering equipment

SAXS measurements were performed on two separate instruments. Although different visually, they perform quite similarly to each other.

The first instrument was the PANalytical Empyrean X'Pert Pro with the powder diffraction modules swapped out for the vacuum enclosure used for SAXS measurements. The upstream collimation system is additionally augmented to a focusing mirror. In the SAXS configuration, only the detector is moving, with the x-ray source staying stationary. The sample is placed inside the vacuum chamber and can be in either a capillary, for liquid samples, or powder, with a specialized sandwich style powder insert. The goniometer can access angles upwards of 105 degrees in $2\theta$.

The system utilizes a semi-transparent beam stop and is calibrated by positioning the direct beam at zero angle. The system can acquire both the 1D averaged data for the full range of goniometer motion or a 2D image in a smaller area of interest. Figure 3.1 shows both in-house instruments in their utilized configurations.

The second used instrument was the SAXSLab GANESHA originally developed at University of Copenhagen in a collaboration with SAXSLab. In this instrument both the detector and sample holders are situated inside a cylindrical and continuous vacuum chamber. The fully evacuated flight path ensures absence of air scattering after the last collimation slit responsible for the undesired background in the measured data.

To generate x-rays a Rigaku Micro-Max002+ source is used. It is a sealed Cu X-ray tube source producing x-rays at a wavelength of 1.54Å. The beam is focused down to approximately $300\mu m$ in diameter using Kirkpatrick-Baez focusing mirrors and is collimated by four sets of motorized slits. The instrument is equipped with a Pilatus 300K solid-state photon-counting detector, a proprietary noise-reduction algorithm for cosmic background and a real-time automated data-reduction system. The detector can be moved in the chamber relative to the sample position allowing a $Q$ range on the order of up to $0.0025\text{Å}^{-1}$, when the detector is furthest from the sample, to approximately $3.0\text{Å}^{-1}$ when it is at its closest. With the proper specific stages, the GANESHA allows temperature control (-170°C to 300 °C), mechanical solicitation (shear and tensile), controlled light exposition, a sample flow-through setup and diverse mounting plates for films, paste cells, single-use and refillable capillaries.

The $Q$-calibration is performed by scanning a Silver Behenate sample at different sample-detector positions/distances. A correct $Q$-calibration is achieved when the main Bragg peak of Silver Behenate is at it's correct position of $Q = 0.107\text{Å}^{-1}$. The measured peaks for all the different scans will then agree and overlap each other.

## 3.2  Synchrotron X-ray measurements

Although many experiments can be performed by the mean of conventional x-ray home sources, the use of synchrotron facilities can bring numerous advantages. The high brilliance associated to these light sources can in principle decrease data acquisition time from several hours to a few seconds exposure time. The beamline at a synchrotron typically also has better collimation and potentially better $Q$ resolutions. The higher flux would also allows for more sophisticated measurements of the sample under specific conditions
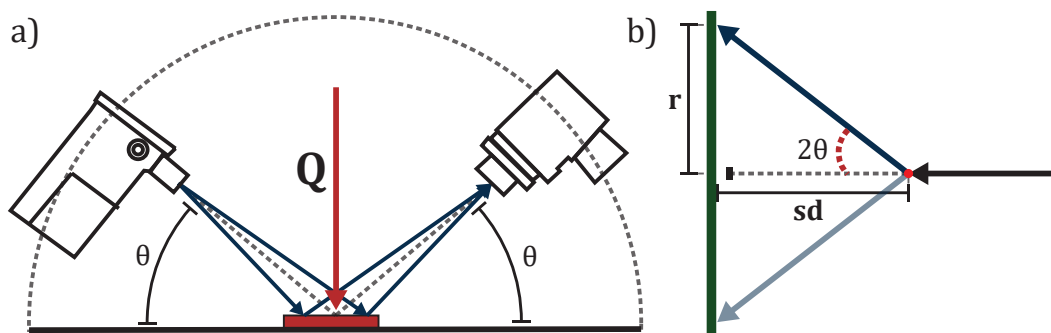
Figure 3.2: Diffraction geometries. a) Bragg brentano geometry, $\theta - \theta$ geometry. Both the source and the detector are moving symmetrically to keep the scattering vector in the downward facing direction at all times. b) Transmission geometry used at most conventional RA-PDF beamlines.
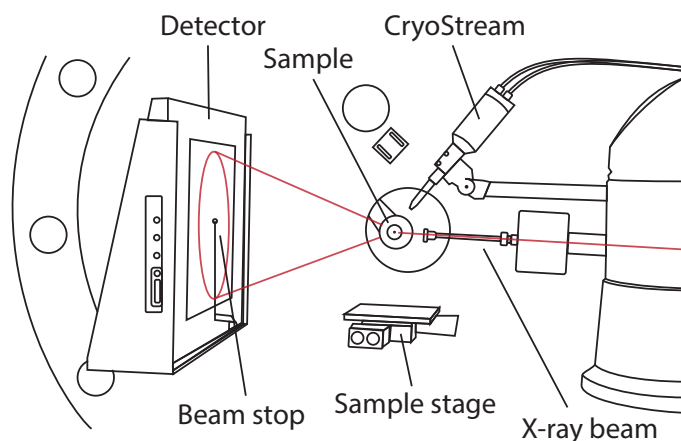


Figure 3.3: Schematic of the 28-ID-2 beamline at NSLS II. The detecto is situated in close proximity to the sample to achieve the best possible $Q_{\mathrm{max}}$. The samples can be cooled or heated by an air jet - Cryostream. Sample stage and other mounting points can be used to attach equipment such as protective cases and sample environments, such as furnaces or pressure chambers.

in-situ, such as thermal transitions or mechanical manipulations.

The use of tuneable/adjustable third-generation synchrotron sources with insertion devices such as wigglers or undulators allows the use of multiple wavelengths, or beam , for various types of experiments, such as studies of the dynamics in the system, while home sources are usually limited to the x-ray properties inherent to the adopted anode.

## 3.2.1 Rapid Acquisition PDF(RA-PDF) techniques

The most common setup for a synchrotron experimental station, or beamline, for performing total scattering measurements for use with PDF analysis follows the main principles outlined in Chupas, et al.[22]

The setup utilizes the readily available beams of high energy photons at modern synchrotron sources. The RA-PDF setup utilizes a flat 2D area detector that is positioned

close to the sample. This positioning allows the detector to capture scattering for sufficiently high angles to reach the required $Q_{max}$. The sample is fixed in place in the beam path and the experiments are done in transmission geometry, also referred to as Debye-Scherrer geometry. The detector is typically placed concentric with the beam, such that it can collect the full extent of the Debye-Scherrer cones for maximum statistics. The direct beam is stopped by a beamstop which is fixed on a thin pole in the center of the detector. The position of the beamstop also defines the $Q_{min}$ as it blocks a portion of the direct scattering alongside the incident x-ray beam.

The accessible $Q$ window is defined by the position of the detector with respect to the sample. The range can be calculated via the maximum angle of $2\theta$ that hits the outer pixels of the detector:

$$\tan(2\theta) = \frac{r}{sd}, \tag{3.1}$$

where $r$ is the distance from the beam center on the detector to the outer pixel and $sd$ is the sample-to-detector distance. The scattering geometry is illustrated in Fig. 3.2b). The $\Delta\theta$ resolution of RA-PDF measurement is generally poor as a trade off for high angular range required for PDF data. As the detector is typically motorized, the $\Delta\theta$ resolution can be improved allowing for high resolution powder diffraction measurements while reducing the $Q_{min}$-$Q_{max}$ window.

The measurements for this thesis were carried out at three different facilities: beamline 28-ID-2 (XPD) at the National Light Source II at Brookhaven National Laboratory in Upton, NY, the beamline 11ID-B at the Advanced Light Source at Argonne National Laboratory in Argonne, IL, and at the beamline P.02 at the PetraIII accelerator located at DESY, Hamburg. Despite their different locations they are configured nearly identically, as seen from the user perspective. They operate in hard x-ray range at wavelengths on the order of 60keV. The high energy allows access to $Q_{max}$ between $25\text{Å}^{-1}$-$30\text{Å}^{-1}$ when the detector is placed in its closest proximity to the sample, around 170mm. All three beamlines use a large 2D Perkin Elmer amorphous silicon detector positioned orthogonally to the beam path. It has an array of 2048x2048 pixels with a pixel size of $200\mu$m. The detector is motorized, which allows it to be moved back to distances of up to 1.5m away from the sample positions, allowing for a high resolution powder diffraction measurements for $0.1\text{Å}^{-1} < Q_{min} - Q_{max} < 10\text{Å}^{-1}$ range. It is also possible to increase the accessible $Q$ range by positioning the detector off-centered with respect to the beam.

The general layout of the 28-ID-2 beamline at NSLSII is shown in Fig. 3.3. The beam is collimated up until the sample position to reduce the amount of air scattering during the measurements. The beam can additionally be reduced by slits to decrease the instrumental broadening effects from photons scattering in parallel from different positions along the sample. For routine PDF measurements this is rarely necessary, as the instrumental broadening from the $\Delta\theta$ resolution is greater than the smearing effect from the beam profile, but could improve a measurement for a complementary powder diffraction experiment.

The beam lines are generally set up for samples packed inside capillaries. The capillaries

used are typically low scattering kapton capillaries, or quartz or borosilicate glass capillaries for more sensitive samples. The capillaries are mounted onto goniometer heads or fixed sample holders and can be rotated for additional powder averaging. For multiple capillaries, some beamlines also provide an option to use motorized sample changers to increase the efficiency. At a typical photon flux of a PDF beamline, good quality measurements can be taken in a matter of several minutes.

The experimental stations are not limited to just capillary measurements and can be adjusted with the help of the beamline staff to accommodate exotic sample holders and environments. The setups are routinely augmented by flow cells and specialized equipment.

## 3.3 Specialized setups for material characterization

As part of the collaboration with XPD beamline as NSLSII a setup for PDF measurements of combinatorial arrays has been developed. The setup uses a machined bracket designed to accept standard combinatorial array prepared by collaborators at UC Berkeley and the Pennsylvania State University. The arrays are 62x62mm and can be attached to the goniometer head and can be moved in the $xy$-plane(detector plane) in a pre-programmed pattern to cover all of the 25 deposition wells. The data analysis workflow for this type of measurements has been developed and is described in detail in Chap. 4. In short, the beamline is configured to output a complete metadata file, which can be loaded into a collection database. The collection can then be analyzed by a semi-automated script, which can generate an overview of the measurement, combined with structural analysis information.

### 3.3.1 In-situ synthesis setups

For the in-situ studies of growth kinetics a modified version of the Aarhus supercritical cell was used. The Aarhus supercritical reactor[70] was developed at Aarhus university specifically to study the supercritical syntheses in-situ.

The reactor consists of a machined capillary holder that can be mounted to the goniometer head mount or onto the sample stage. This allows it to be positioned and moved using the motorized equipment of the beamline. The setup utilizes fused silica capillaries, that can tolerate pressures upwards of 400bar and temperatures up to 600°C. Being a supercritical reactor, the capillary can be pressurized by an HPLC pump, which is connected to the capillary via Swagelok fittings. To properly connect the capillary to the pressurization system, graphite ferrules are employed instead of standard stainless steel. The graphite is much more malleable, which makes it better at creating a tight seal against a fragile capillary without shattering it.

The heating is achieved by a hot air jet positioned underneath the capillary. Due to the offset between the air jet and the capillary, the temperature needs to be calibrated by inserting a submerged thermocouple into the capillary before the measurements and sweeping the temperature presets.

### 3.3.2 Flow cell mixing setups

A specialized setup was developed to study the earliest stages of nanoparticle nucleation and growth. This setup also incorporates design elements needed for the industrial flow synthesis and in-line characterization[94].

The main idea is to use a dynamic liquid flow through the system to increase the time resolution of the instrument. Time sensitive processes, like nucleation and growth, can then be studies by measuring at a certain point of the reaction as if frozen in time.

To achieve this, the Aarhus supercritical setup was modified keeping its ability to attach to the goniometer head with a robust and leak proof capillary and a heating system. This essentially turns the setup into a flow cell.

The reaction mixture can be separated into multiple parts, that when mixed would initiate a chemical reduction. The direct application of this setup will be discussed in detail in Chap. 5. The precursors are then connected to pumps that can provide a steady flow of reactants. The measurement is performed at a fixed distance away from a specifically designed mixing point. The time between the mixing and the measurement is controlled by adjusting the flow rates or changing the length of tubing. The diagram of the setup can be seen in Fig. 3.4.

The setup was first developed using an Anton Paar flow cell with the Ganesha SAXSlab instrument. The precursor solutions were supplied using two Harvard Instruments syringe pumps, which could supply a flow rate between 100 nanoliters per minute to 50mL per minute. It utilized 1mm silicone tubing that matches the capillary and a microfluidic Y-junction turbulent mixer. The mixing rate was calibrated by measuring the conductivity of a mixture of water and saline solution at different points after the mixer. The tests established that the Y-junction microfluidic mixer, where two inlets are angled at 90°with respect to eachother work best for low flow rates, while for flow rates over 0.5ml/min, the more common T-junctions are sufficient. For tubing larger than 1mm internal diameter and spiral insert can be added to increase the mixing efficiency. Ultimately, for a Y-junction mixer and flow rates on the order of 0.1ml/min reliable measurements could be done already 1s after the mixing. In the end we achieved a 1s time resolution for 30minute measurements on an in-house system.

Apart from increasing the time resolution of measurement, the flow setup allows to eliminate the risk of beam damage to the sample. An example is seen in Fig. 3.5, where a solution of polyvinylpyrrolidone (PVP) was measured at an in-house system for around 1 hour and exhibits a visible color change in the part of the capillary which is hit by the x-ray beam.

In the end, we never ended up developing a synthesis that would benefit from this setup, due to massive agglomeration which is intrinsic to syntheses with high concentrations of copper and silver precursors. However, the ability to avoid beam damage on sensitive organic solutions were successfully used at a synchrotron to measure background solutions for mixtures with PVP, glucose and sodium dodecyl sulfate(SDS). More details about the experiments will be presented in Chap. 5.
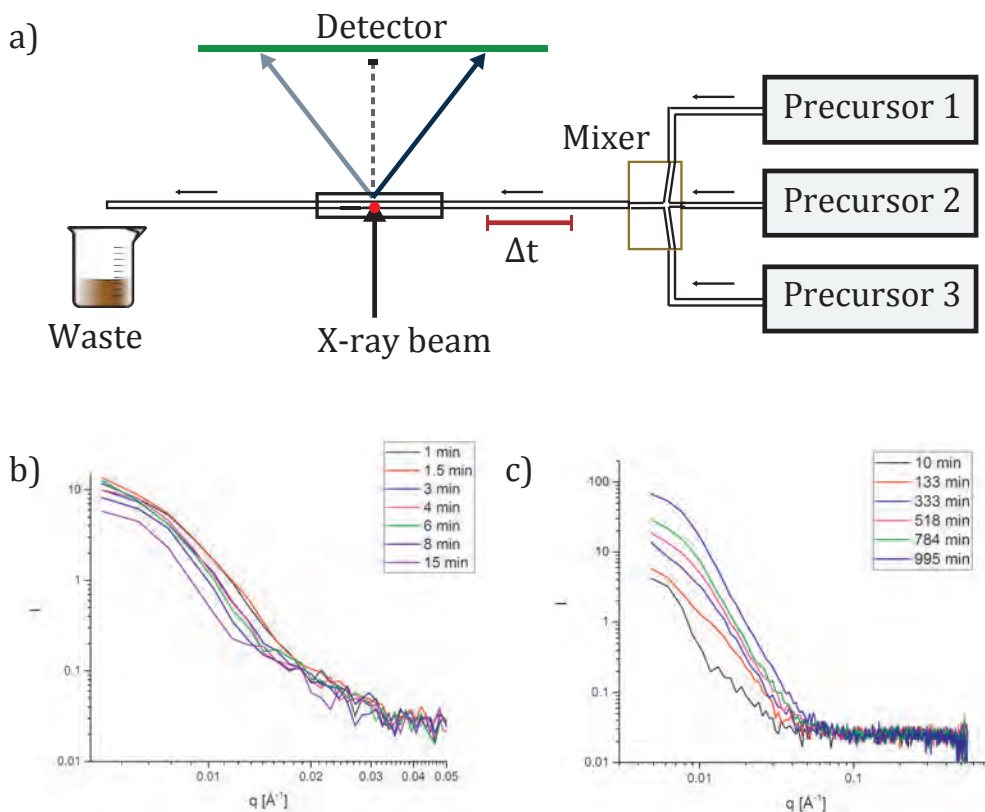
Figure 3.4: a) A diagram of the flow setup. The precursors are mixed in the Mixer and travel towards the capillary, hitting the beam at time defined by the tubing length and pump speed. b) Agglomeration of silver spheres. Using the setup it was possible to achieve sub minute time resolution for measurements of $\sim$30 min. c) Flow measurements help avoid beam damage. The data is from measurements of agglomeration of PVP in aqueous solution, which is normally sensitive to beam damage. Here the agglomeration can still be seen.
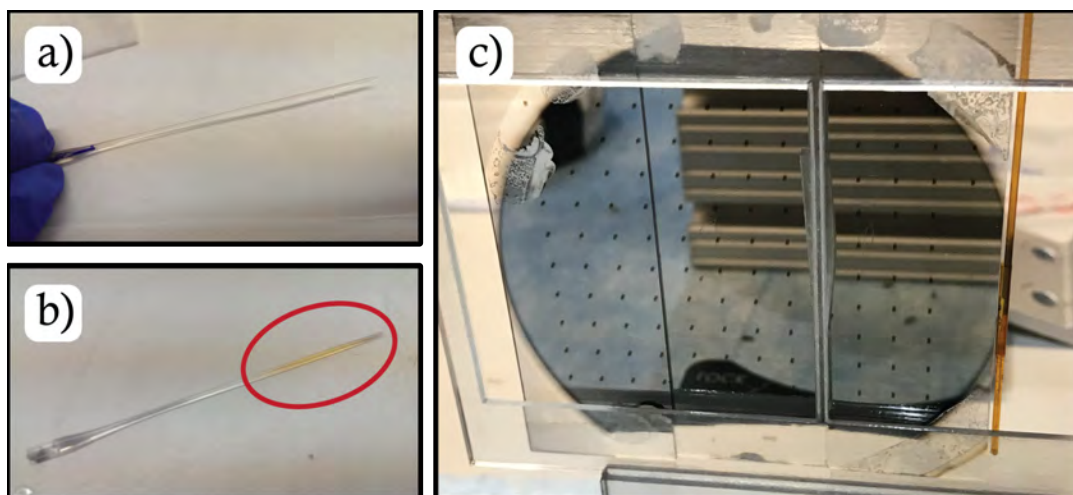
Figure 3.5: Beam damage can occur during x-ray experiments. a), b) Capillary with glucose+ PVP solution before and after a 1 hour in-house measurement respectively. The yellow ting of the liquid is a clear sign of beam damage. c) Beam damage(squares) on metallic glass alloys on a quartz wafer. Measurements performed at a high intensity synchrotron source at beam line ID11-B at APS, ANL.

### 3.3.3 Remote controlled equipment

As the x-ray shutters open and the x-rays are allowed into the experimental hutch, the access to measurement equipment is restricted for safety reasons. All control is thus performed remotely through the computers at the beamline.

The setups described in this section are not integrated into any of the beamlines used. For this reason it is important to be able to operate the reactors remotely from the safety of the experimental station.

The Aarhus supercritical reactor uses HPLC pumps that are positioned outside of the experimental hutch and connects to the experiment via pressurize tubing. The pumps used for the mixing flow reactor are capable of communicating through an RS232 serial ports and can be controlled remotely. To achieve this, a custom Python script was developed using the pySerial package. The script sends commands over a USB to RS232 connection and is able to start, stop, set and change flow rates for each pump independently. The commands used for communicating with the instrument can be found in the operation manual.

## 3.4 Requirements for ink jet printing of nanoparticle based inks

One of the goals of the experiments studied in the thesis was the ability to use the nanoparticle suspensions in ink-jet systems for deposition of conductive electrodes for sensors, solar cells or printed electronics[95][96][6].

The printer works by letting tiny droplets of ink pass through the nozzle and hit
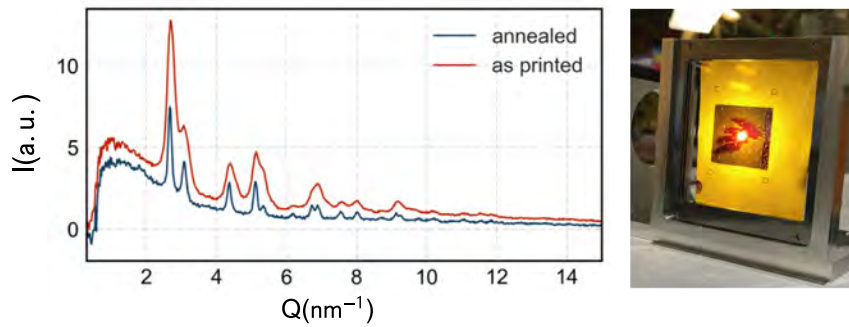
Figure 3.6: A example of nano-ink printing. A thin layer of nanoparticle suspension is deposited onto the surface using a specialized ink jet printer. The measurement before and after sintering shows change in crystallinity via changing peak width.

the printing media in a controlled fashion. This warrants specific requirements to the nanoparticle primary size, i.e. size of agglomerates and viscosity. For ink-jet printing, the nanoparticle agglomerates must be less than 100nm. The aerosol jet printing requires nanoparticle agglomerates under $1\mu$m in size.

After deposition, the nanoparticles are sintered by means of hot press, laser sintering or photonic sintering techniques. All of these have a common property of applying heat to the surface to burn off the organic ligands and make the nanoparticle layer conductive. A viability study was performed at XPD beamline at NSLSII which attempted to measure the change happening in the printed layers of Pt and Au nanoparticle inks. The printer deposits a continuous spray of 15pL droplets that spread out to a surface area of around 170nm. The total thickness after four passes is estimated to be under 100nm and appears semi-transparent to visible light. The printed area was annealed by a near infrared-lamp, an Adphos NIR 42-250 5,4 kW, set at full power and passing at a speed of 90mm/s, which should give $\approx$0,5 W/cm$^2$. The excerpt of the experiment is illustrated in Fig. 3.6. The powder diffraction pattern illustrates significant growth of crystallites in the ink, even though the sintering temperature is far below the melting temperature of both Pt and Au, at around 300°C.

## 3.5 Data reduction

The typical format for the raw data coming from the detector when performing RA-PDF measurements is 2D .tiff images. Each pixel on the image corresponds to a particular $Q$ value and the intensity corresponds to the number of photons scattered at that particular angle.

While it is possible to perform data analysis on 2D images directly[97] it is typically much easier to do on 1 dimensional intensity curves. Before the images can be converted to 1D scattering patterns, each pixel needs to be assigned to the correct value of scattering

vector by means of calibration. Calibration procedure relies on measuring a well known standard material like certified lanthanum hexaboride, silicon or nickel powders just to name a few. The software can then find the Debye Scherrer rings in the image, fit a series of concentric ellipses and assign the correct scattering angles to each ring. The beam center and the tilt of the detector is then calculated from the ellipse geometry.

In this thesis, several software packages have been used: Fit2D[98], Dioptas[99] and pyFAI[100]. Several pieces of information are required in order to perform proper calibration, like pixel size, wavelength, beamline polarization factor and sample to detector distance. Notably, detector distance and wavelength are almost linearly correlated in the typical PDF energy range. The wavelength is typically fixed, as it should normally be well known, and the sample to detector distance is allowed to refine such that the pattern corresponds to the measured standards list of pre-defined spacings.

When each pixel has been assigned a correct $Q$ value, they are typically binned along the azimuth and normalized by their number to get the correct intensity. For proper data analysis, outlier pixels need to be removed from the image. These can be caused due to cosmic rays or other kinds of improper shielding and produce pixels with extremely high counts or be defective counting too small, too large or nothing at all. The outliers might significantly distort the integrated and averaged intensity of the azimuth if not removed from the image by means of masking.

After proper calibration and masking, the azimuthally integrated one dimensional intensity data is ready for analysis.

### 3.5.1 Data treatment with PDFGETX3

The integrated intensity data can be in value of instrumental angle, or wavevector transfer $Q$. This is sufficient to start reciprocal space analysis by means of Rietveld refinement or Total Scattering analysis in reciprocal space.

The PDF is a Fourier transform of the coherent scattering intensity of the sample as described in Sec. 2.2. From there, it will be possible to find the structure factor $S(Q)$, then the reduced total scattering structure factor $F(Q)$ and finally the reduced pair distribution function $G(r)$.

The first step in obtaining the PDF is to remove all sources of incoherent and parasitic scattering such Compton scattering, absorption and multiple scattering, air scattering and scattering from sample holder, detector response etc. Any additional scattering which is not directly related to the sample can be removed simply by subtracting a reference measurement including all additional effects like empty capillary and sample holders. This is always done as the first step after integration and is described in greater detail in Sec. 3.5.2.

For this thesis a software PDFGETX3 [101] has been used for all data reduction beyond azimuthal integration. PDFGETX3 uses *ad hoc* data corrections that have been shown to work equally well[102] to the conventional process of calculating all corrections explicitly[103]. This approach made total scattering studies much more accessible and fast.

The physics behind these corrections is well understood[74], and can be broken down into additive and multiplicative correction to the total measured intensity. For example, there is a good separation in frequency between the scattering signal of the sample and other parasitic contributions such as Compton scattering and multiple scattering. These evolve slower than structural information and by fitting and subtracting an arbitrary function to the total intensity with no frequencies higher than $\approx 2\pi/r_{nn}$, where $r_{nn}$ is the nearest neighbor distance, these contributions can be removed.

Similarly, to obtain the corrected $S(Q)$ the program utilizes well known asymptotic behavior of the structure function. It is approximately zero for $Q = 0$ and asymptotes to unity at high $Q$. The normalization utilizes the fact that one of the normalization steps is to divide Eq. 2.6 by the square of the mean scattering power $\langle f \rangle^2$. The structure factor is corrected such that $S(Q = 0) = 1 - \langle f^2 \rangle / \langle f \rangle^2 \approx 0$, where $f(Q = 0) \to Z$, where $Z$ is the atomic number(charge) of the scatterers in the sample, in addition to $S(Q \to \infty) \to 1$[69].

Inside the PDFGETX3 the parameters for $Q_{\min}$ should be chosen as to eliminate any stepping artifacts from the azimuthal integration around the beam stop. $Q_{\max}$ should be set to the highest available value before the unphysical kink in the detector intensity that originates from the integration of the corners. It might then be necessary to adjust it to eliminate experimental noise from the low counting statistics at these high values of $Q$. The $r_{poly}$ parameter defines the $r_{nn}$ in the PDFGETX3 software and should generally be left at it's standard value of 0.9. The correct sample composition should also be entered.

Needless to say, using the *ad hoc* corrections does not yield a PDF on the absolute scale necessary for determining accurate coordination numbers. If accurate absolute intensity is required, then all corrections should be done manually[104]. The data should be normalized for incident intensity, sample volume, packing density and so on. For general analysis this is generally not a problem, since an absolute scaling factor can be applied during modeling or comparison between datasets. In fact, observations indicate that data measured at the same time and processed identically using PDFGETX3 are directly comparable[69].

### 3.5.2 The art of background subtraction

Nowadays, if one is working with PDF analysis it is likely that the materials of interest are hard to detect. Typically this is because they are small nanoparticles or clusters, layered structures and the like which are notoriously hard to work with with typical x-ray diffraction techniques. In addition, for the purpose of measurement they would typically be in solution or a powder, packed in a capillary or deposited onto a substrate and on top of that on a nanocrystalline support. All of this means that getting the pure signal from the material of interest is incredibly difficult.

A way of doing it is by subtracting the scattering pattern for the corresponding support. In theory, when measuring a nanoparticle dispersed in a solution, one would prepare the solvent itself in an identical capillary as a reference measurement. Then one would measure it for an equal amount of time in the same sample holder and then subtract the resulting pattern when doing the data reduction.

In practice, this rarely works to the full extent. There is a number of factors that would contribute to the issue:

1. The capillaries used to measure the sample vs the support are not necessarily identical even if they are from the same batch. Reusing the same capillary or using kapton tubes usually minimizes this problem.

2. Beam intensity can fluctuate during the measurement resulting in a different total collected counts for sample and reference. This is especially common when synchrotron is not running in continuous injection mode. A similar issue originates from the liquid moving inside the capillary during in-situ experiments, resulting in different local concentration of the sample at any given time.

3. Small changes in experimental geometry as a result of equipment moving or otherwise changing will lead to different amounts of air scattering and upstream scattering from said equipment. For example, a common issue is bending of a capillary due to high pressure and temperature, which is common in in-situ experiments. Using a single capillary static setup for sensitive samples would usually minimize the problem.

4. Substrate chemically changing as a result of deposition of material of interest.

A number of solutions exists to there issues. They are by no means perfect and need to be evaluated on a case by case basis.

### Extensive masking and image-to-image background subtraction

A common issue found on all beamlines used for this thesis is presence of air scattering shadows coming from the equipment at or upstream from the sample even when collimation is present. Despite being weak they still make a contribution to the total scattering signal. This can be seen in Fig. 3.8. The dataset has been integrated using three different masks: a mask that only covers the beamstop region, a small mask covering just the region with the worst perceived artifact and a full mask covering the majority of the artifacts, illustrated in Fig. 3.7 as a), b) and c) respectively. From the residuals it is apparent that there is a lot of signal originating from the shadows and that using a smaller mask that is blocking the most visually apparent region does not necessarily remove it. It is also seen that the shadows typically manifest themselves at high Q regions in F(Q) and low r regions of G(r), since they are not overshadowed by the scattering intensity originating from the sample to the same degree.

These shadows, in turn, rarely make or break a dataset and more often than not performing any kind of background subtraction would remove the majority of the negative effects. In case of static experiments the best way to do it is to perform an image-to-image background subtraction before azimuthal integration. This would provide the most accurate elimination of scattering artifacts. Care has to be taken however, whenever any pieces of equipment are moving as this might introduce more anomalous signal to the intensity pattern than when doing so after averaging. There are also currently no reliable ways of properly scale the intensity of the background image, which makes image-to-image subtraction problematic when dealing with changing beam intensity or different sample
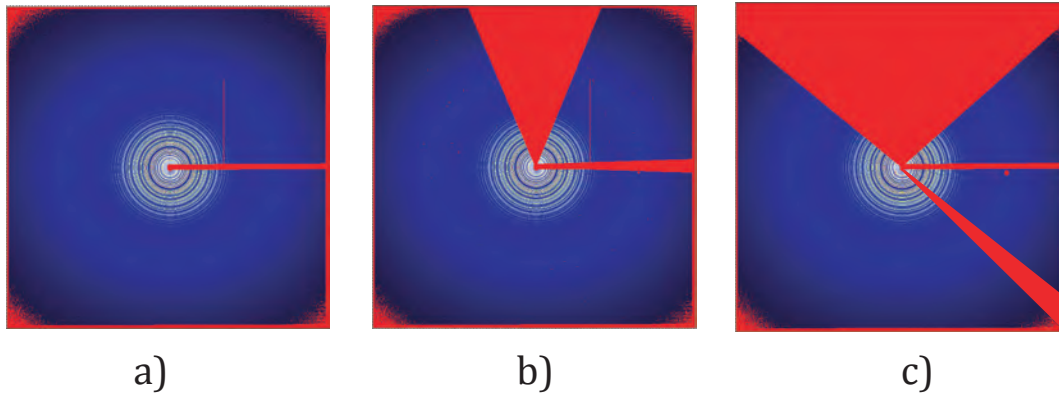
Figure 3.7: Different extents of masking. a) typical mask covering the beamstop. b) A mask covering the worst shadow region. c) Full mask covering all shadow signal.

quantities.

**Scaling the background intensity and reciprocal space background subtraction**

Varying beam intensity or varying sample absorption typically results in the background that does not correspond to the sample at default scaling. A common practice is therefore to scale the background by an arbitrary factor through visual inspection. A good rule of thumb is to maximize the background intensity without exceeding the counts of the sample anywhere along the pattern. By identifying the region of the integrated pattern where background intensity matches the sample intensity can be used for automatic and dynamic background scaling in a series, for example in-situ measurements.

When a background measurement consists of several phases, for example, kapton capillary and a powder support, purely scaling the background would not be the best solution. While the powder signal in the capillary can be packed differently, the capillary stays constant. A good solution would be to separate the components and subtract them separately, starting with the capillary.

This approach is illustrated in Fig. 3.9. A simple scaling and subtraction of the reference still leaves a good portion of the structural information of the support in the scattering pattern, which then gets transformed to G(r). By subtracting the capillary signal from both the reference and the sample first and then using the kapton subtracted datasets to perform the final background subtraction, a better scaling can be achieved. This results in a clean G(r) containing just the Mo signal and allows for a much better structural refinement.

**Real space background subtraction**

The inverse Fourier transform used to obtain the G(r) from the F(q) preserves all of the information in the scattering pattern. It is therefore not surprising that a reliable background subtraction can be performed in r-space just as well as in Q-space. However, due to the way structural information manifests itself in these two representations there are
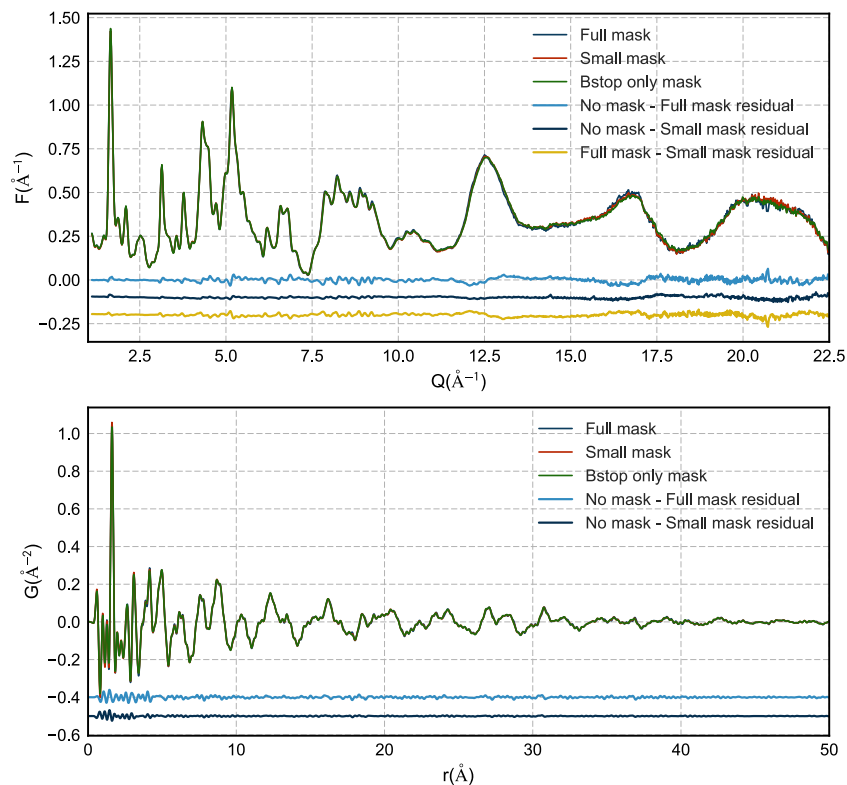
Figure 3.8: Integrated intensity of a $MoO_x$ on ZSM50 measured at beamline P.02 at PETRAIII. The signal coming from the shadows of the air scattering is present in the image and manifests itself across the F(q) and the G(r). It is important to evaluate where the largest portion of the unrelated to the sample signal is located, and then decide on the most effective masking method.

some advantages to attempt the background subtraction in real space instead of reciprocal space. When working with supported nanoparticles, the scattering signal from the support appears often less crystalline. This broadens the Bragg peaks of the support material in the sample and makes it difficult to obtain a matching background measurement that will not result in subtraction artifacts. In real space however, the crystallite size effects appear as an attenuation of the PDF signal beyond a certain range corresponding to the size of the crystals. PDF also quickly loses the sensitivity to size effects once the crystals become large where the attenuation would be given by the instrumental broadening parameter. Assuming the nanoparticles are small, their signal would not be visible past a certain r range. Thus, the G(r) of the support material and the support material decorated with nanoparticles would be identical over that r range. By scaling the support material to match the sample at a mid to long range it is possible to extract only the contribution from the nanoparticles.This approach is successfully used in Chapter 7 for extraction of the amorphous signal of molybdenum oxides. The zeolite structures are matched at high r region and subtracted, revealing the intensity corresponding to the deposited material in the low $r$ range of the PDF.
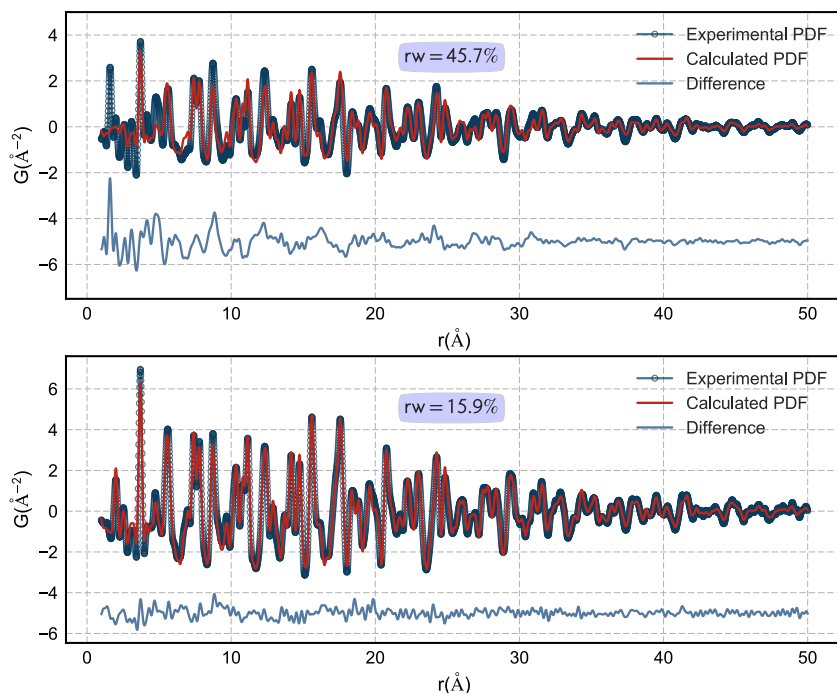
Figure 3.9: Refinements for $MoO_2$ phase of Zeolite ZSM5 support. (top) Reference background was scaled and subtracted. Refinement yields an $R_w$ value of 45%. A keen eye will see a zeolite resemblance in the residual. (bottom) Refinement to the G(r) after subtracting the capillary first from reference and sample before performing the final background subtraction. The agreement factor for the model has improved dramatically.

## 3.6 Structural refinement guidelines

There exist a multitude of software to perform structural refinements to the normalized and properly transformed data for both powder diffraction and PDF analysis. An excellent choice for powder diffraction would be the FullProf suite[87] and GSAS-II[105], while for PDF analysis PDFGui[46] is probably the most commonly used one.

In general, it is advisable to follow the tutorials that accompany each of these software packages. This section is not intended to provide a complete guide on how to use them, but rather a collection experience for how to start with a task of refining a structure.

Fist step is to evaluate whether a model is even remotely appropriate for the dataset at hand. To do this, a good idea is to remove all unnecessary effects that might add to the broadening of the Bragg peaks in PXRD or peaks in the PDF, and calculate the model. These typically include atomic motion for PDF, size and strain broadening for PXRD. The resulting calculation should produce a simulation with very sharp, non overlapping peak pattern that can be used as a fingerprint for comparison.

The next step is to adjust the scale factor for the model. Letting it refine is typically sufficient if the data quality is good and the model in question is correct, but can be tricky if the model that is being tested is not exactly on point due to variations in lattice parameters or when dealing with a mixed phase sample. In the latter case, the scale parameter can be

adjusted by hand until the calculated model more or less scales correctly to the data set.

From here, one should be able to see whether the model resembles the dataset or if it is in any way close. The main strategy is to match the peak positions first, then deal with intensities and profile. Something to consider at this point is whether the model can match the peak positions of the data by simple stretch operations. Introducing isotropic stretch parameters or refining the lattice cell proportionally (like it would be in a cubic lattice) should always be tried first, before anything more complex.

Once the positions are fixed, the next step should be to introduce the broadening effects. For PDF, isotropic displacement parameters are the obvious choice. For powder diffraction that would be size broadening, then strain. For PDF, if the signal attenuates significantly faster than dictated by the instrumental resolution, introducing a spherical attenuation function might help reach the convergence quicker.

From this point the residual should be the guiding force behind qualified guesses to the correct model parameters. Angular dependence of certain broadening effects such as Scherrer broadening in Eq. 8.5 and strain given by Eq. 2.33 is different, and should be adjusted according to the misfit in the residual. For PDF analysis the typical parameters of interest are $\delta_1$ and $\delta_2$ correlated motion parameters, which contribute to the peak broadening in PDF differently, according to Eq. 2.17.

More complicated modeling should only be attempted once the "easy" options have been depleted, in which case it is always helpful to add complementary constraints from other techniques.

### 3.6.1 Time series refinements

There are two fundamentally different ways of approaching time-series data. The time-series can be treated as a collection of separate events or as a continuous and sequential evolution of the system. While this sounds quite obvious, treating the data where each measurement is being analyzed independently of all others is the least biased, but typically most time consuming way of analysis. When all datasets are treated independently and the results converge to a continuous evolution, one can be sure that the model is a useful description of the process.

The most common way is typically to treat the data as a continuous process and assume that each following time step is a uninterrupted evolution. In this case, the starting parameters from one step would carry over to the next significantly speeding up the computational time. The risk here is obvious again, the minimization problem could have been sitting in a local minimum all the way through the refinement process.

In my experience, a combination of the two typically works best and ensures that the results are as unbiased as they can get. Before tackling a dataset with several thousand time frames, a good idea is to take out a random number of samples evenly distributed across the time axis and analyze them independently and outside of order. In addition to creating a set of guides for the sequential refinements, this approach also gives a quick overview of the process without being incredibly time consuming.

Another helpful realization for dealing with sequential time-series refinements is that time is just a measurement axis. The analysis can be done in any direction on this axis that suits the problem at hand. This becomes especially useful when attempting to locate a phase transition or an appearance of the secondary phase. Oftentimes it is easier to start the sequential process at the frame where all structural phases are equally represented. Then proceed with the sequential analysis in the direction of it disappearance. While in theory this should not make a difference on the result, the way software typically works is that multiplication by a scale factor of zero oftentimes leads to instabilities in the minimization process. Thus it is easier to start from the middle and then find the instability which can be adjusted by hand, rather than slowly advance ahead hoping that the fit would pick up the vanishing minority phase on it's own.

# 4

# Streamlining data analysis and modeling for high-throughput synchrotron datasets

The following chapter describes a new software protocol, called mapPDF, developed for analysis of data from high throughput experiments, such as in-situ experiments or spatial mapping. The software is intended for use by a novel python programmer who wants more flexibility than provided by standard analysis software. mapPDF is utilized throughout the thesis, whenever sequential data analysis is needed. The protocol integrates seamlessly with the XPD beamline at NSLS-II, where specialized mounting hardware for combinatorial arrays was designed. The work presented here has been submitted for review under the name:

**Anton Kovyakh**, Soham Banerjee, Chia-Hao Liu, Christopher J. Wright, Yuguang C. Li, Thomas E. Mallouk, Robert Feidenhans'l and Simon J. L. Billinge. *"Streamlining data analysis and modelling for high-throughput synchrotron datasets"*, Submitted, May 2018

The text in the chapter is presented in the exact same way as in the manuscript. For completeness, the manuscript is also included in the appendix.

# Streamlining data analysis and modelling for high-throughput synchrotron datasets

Anton Kovyakh[1], Soham Banerjee[2], Chia-Hao Liu[2], Christopher J. Wright[2], Yuguang C. Li[3], Thomas E. Mallouk[3], Robert Feidenhans'l[1] and Simon J. L. Billinge[2,4].

[1]Niels Bohr Institute, University of Copenhagen, Universitetsparken 5, DK-2100 Copenhagen, Denmark

[2]Department of Applied Physics and Applied Mathematics, Columbia University, New York, NY 10027

[3]Department of Engineering Science and Mechanics, Department of Chemistry, and Department of Biochemistry and Molecular Biology and Department of Physics, The Pennsylvania State University, University Park, Pennsylvania 16802, United States

[4]Condensed Matter Physics and Materials Science Department, Brookhaven National Laboratory, Upton, NY 11973

## 4.1 Introduction

The traditional approach to novel material engineering is based on rigorous theoretical and experimental analysis for predicting materials properties. This is inherently inefficient in a world where the materials synthesis is often unpredictable and suffers from lack of control[106]. As a result there has been a major push towards high throughput (HT) operations and combinatorial studies[107, 108].

The approach of experimental trial and error has become a widely accepted industry standard in many fields including heterogeneous catalysis, pharmaceuticals, biomaterials, optics and multi-principal element alloys[109, 110, 111, 112, 113, 114].

Obtaining quantitative structural information is essential when studying new materials. For inorganic compounds, x-ray diffraction (XRD) has been a dominant tool for retrieving average structural and phase information since the development of the Rietveld method[80]. The technique can be extended to non-crystalline materials and the ability to resolve the local structure through the use of Pair Distribution Function (PDF) analysis[115].

Several strategies exist for increasing the throughput of x-ray diffraction measurements like employing robotic sample makers[116], *in-situ* ion beam sputtering deposition[117] or by operando studies[118]. Recently, a spatially resolved XRD experiment in reflection geometry was able to map the phase composition of sputtered Bi, V, Fe alloy on a $Si/SiO_2$ substrate[119] One of the more promising methods is analyzing combinatorial arrays of thin film libraries on a chip.

Advances in ink-jet printing technologies allow for deposition of hundreds to thousands of distinct compositions on a single substrate[120]. Analysis of such arrays is possible using the recently demonstrated normal incidence thin film diffraction method and PDF analysis[121].

Such high throughput (HT) measurements challenge existing powder diffraction workflows at synchrotron sources. Even when the data may be collected rapidly using large area 2D detectors [122] the complex data reduction and modelling steps are not currently automated resulting in many datasets that must be processed manually, which is time-consuming and error-prone. This becomes extremely challenging when the library sizes
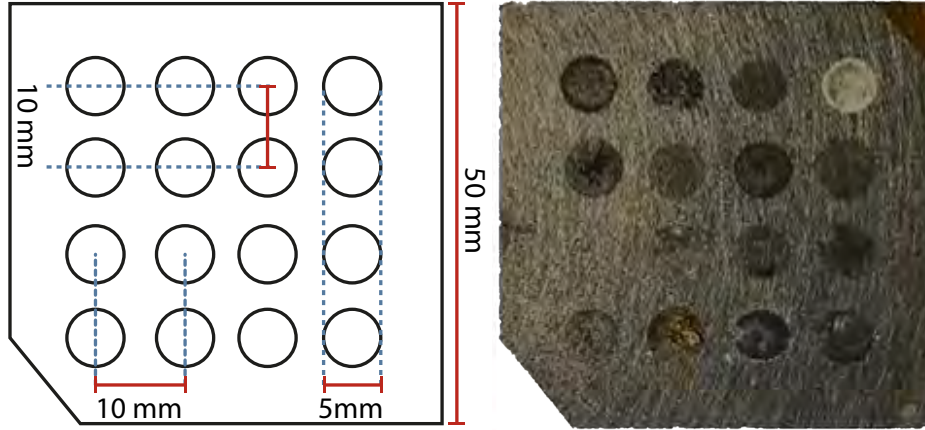
Figure 4.1: A typical sample layout for combinatorial studies (left) and the tested array or catalytic material(right). A square piece of carbon paper was used as a substrate for the ink-jet printed material in a 4x4 configuration

increase past $\sim 10^2$ measurement points. In the lab-on-a-chip experiment one of the key steps is to relate positional information (where the beam hits the sample) with measured data in the form of diffraction images and any prior information from the sample preparation such as target composition. Automation is a priority at modern x-ray synchrotron beamlines where metadata about the instrument configuration, such as motor positions, is available electronically.

Here we describe a protocol for handling this type of analysis, including data acquisition at the XPD powder diffraction instrument at NSLS-II, data reduction that tolerates sample heterogeneity, and subsequent data analysis using the pair distribution function (PDF) technique. The accompanying software allows the data to be reduced and analyzed in a highly automated fashion, and the extracted material specific properties to be easily visualized as 2D parameter maps. As a demonstration we consider an array of catalytic nanoparticles. This supports a major goal in HT nanostructure characterization for situations with hundreds of measurements per hour and analysis times on the same order of magnitude as the measurement time [114].

The protocol is developed for screening spatially resolved PDF data and is modular in design. This allows the protocol to be extended to a wide variety high throughput experiments, such as in-situ synthesis experiments, as well as other experimental techniques.

## 4.2 The PDF method

The experimental PDF, denoted $G(r)$, is the truncated Fourier transform of the total scattering structure function, $F(Q) = Q[S(Q) - 1]$:[36]

$$G(r) = \frac{2}{\pi} \int_{Q_{\min}}^{Q_{\max}} F(Q) \sin(Qr) \, dQ, \tag{4.1}$$

where $Q$ is the magnitude of the scattering momentum. The structure function, $S(Q)$, is extracted from the Bragg and diffuse components of x-ray, neutron or electron powder diffraction intensity. For elastic scattering, $Q = 4\pi\sin(\theta)/\lambda$, where $\lambda$ is the scattering wavelength and $2\theta$ is the scattering angle. In practice, values of $Q_{\min}$ and $Q_{\max}$ are determined by the experimental setup and $Q_{\max}$ is often reduced below the experimental maximum to eliminate noisy data from the PDF since the signal to noise ratio becomes unfavorable in the high-$Q$ region.

The PDF gives the scaled probability of finding two atoms in a material a distance $r$ apart and is related to the density of atom pairs in the material.[74] For a macroscopic scatterer, $G(r)$ can be calculated from a known structure model according to

$$G(r) = 4\pi r \left[\rho(r) - \rho_0\right], \tag{4.2}$$
$$\rho(r) = \frac{1}{4\pi r^2 N} \sum_i \sum_{j \neq i} \frac{b_i b_j}{\langle b \rangle^2} \delta(r - r_{ij}).$$

Here, $\rho_0$ is the atomic number density of the material and $\rho(r)$ is the atomic pair density, which is the mean weighted density of neighbor atoms at distance $r$ from an atom at the origin. The sums in $\rho(r)$ run over all atoms in the sample, $b_i$ is the scattering factor of atom $i$, $\langle b \rangle$ is the average scattering factor and $r_{ij}$ is the distance between atoms $i$ and $j$.

In practice, we use Eqs. 4.2 is used to fit the PDF generated from a structure model to a PDF determined from experiment. For this purpose, the delta functions in Eqs. 4.2 are Gaussian-broadened and the equation is modified to account for experimental effects. PDF modelling , is performed by adjusting the parameters of the structure model , such as the lattice constants, atom positions and anisotropic atomic displacement parameters, to maximize the agreement between the theoretical and an experimental PDF, described by the weighted agreement factor parameter $R_w$.

## 4.3 Experiment

The combinatorial catalyst library was deposited using a Pipetmax automated liquid handling system on semicrystalline carbon paper (Toray 120, from FuelCellStore) in a $4 \times 4$ grid giving 16 circular deposition sites ("wells") 5 mm in diameter and with a center to center spacing of 10 mm. Transition metal nitrate solutions at 0.1 M were used for deposition, except for the Au well where $HAuCl_4$ was used. The precursor solutions were mixed onto the carbon paper and reduced with excess hydrazine solution. The sample was then vacuum dried over night in a 60 degree oven and washed with DI water to create the different alloyed metal samples as shown in Fig. 4.1. The choice of chemicals, size, number of samples and pattern are programmable from the liquid handling system for future implementations of this protocol.

The experiments were carried out at the 28-ID-II (XPD) beamline (NSLS-II; Brookhaven National Laboratory) using the normal incidence thin film PDF (tfPDF) method [123]. The combinatorial array was mounted perpendicular to the x-ray beam direction using a 3D
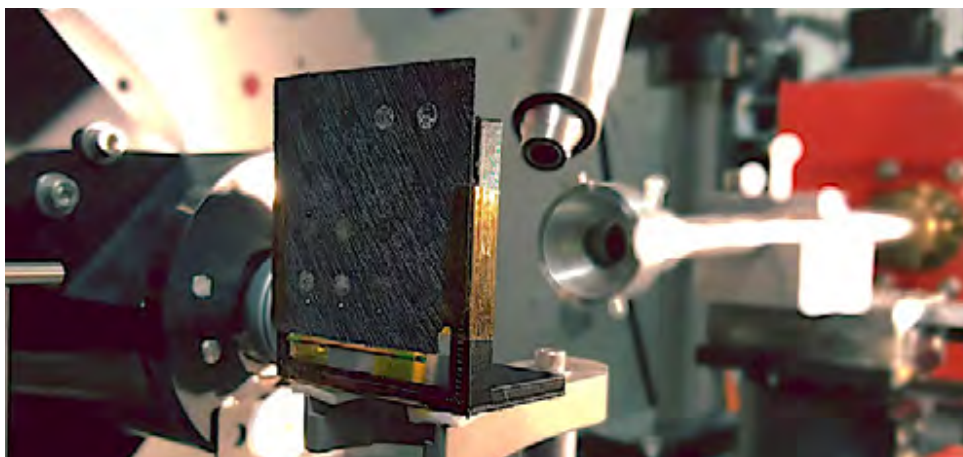
Figure 4.2: The combinatorial library mounted on a 3D printed bracket in front of the x-ray beam. The array is mounted to the goniometer which allows measurement access to all deposition sites.

printed bracket. The measurements were performed in a transmission geometry as shown in Fig. 4.2. The array was moved relative to the beam position using goniometer motors in an $xy$-plane perpendicular to the incident beam direction, with a fixed sample to detector distance. A 2D detector was placed behind the sample at a distance of 203.4 mm, which gave an effective instrumental $Q$ range, where $Q = 4\pi \sin\theta/\lambda$, of $0.12 \leq Q \leq 32$ Å$^{-1}$. The incident wavelength of the x-rays was $\lambda = 0.183983$ Å with a beam cross section at the sample of $250 \times 300$ $\mu$m in the vertical and horizontal directions, respectively.

The sample wells are much larger than the beam, and the sample distribution within the wells is not uniform (see the Results section). We therefore sought a measurement protocol that scanned over large areas of the sample in order to find both the best measurement conditions for sample determination, and also to assess the heterogeneity of the sample. A zoomed-in measurement area of 9 mm by 15 mm was chosen over which the beam was scanned in a meandering array of points. The chosen scan pattern encompassed two catalyst "wells" containing AuAg and AgCu nanocrystalline material, respectively, as shown in Fig. 4.1.

A coarse alignment was done to set the position of the first measurement point by using a laser coaxially aligned with the incoming x-ray beam. The meandering measurement pattern was then executed with a series of 1 mm steps vertically followed by 1 mm horizontal offsets rastering back in the vertical direction, repeated to cover the full measurement area. Exposure time was selected, based on signal quality, and set to $5s$ per point achieving measurement throughput of over 6000 measurements per hour.

The sample-detector distance, $Q$ range and the geometric orientation of the detector were calibrated by measuring a crystalline Ni powder mounted on the same bracket that holds the sample chip prior to data collection. The experimental geometry parameters were refined using the Fit2D program [98]. A mask was created to remove outlier pixels and applied to the 2D images from the measurement series before azimuthal integration to 1D diffraction patterns.

The carbon sheet produces a significant background in this experimental geometry, but the background signal can be subtracted from the data leaving only the structural information of the deposited material. Background subtraction is not trivial for these samples and is described in greater detail in the results section. The total scattering structure function, $F(Q)$, was then obtained after standard corrections and normalizations of the data and Fourier transformed to obtain the PDF, using PDFgetX3 [101] within xPDFsuite [124]. The maximum range of data used in the Fourier transform ($Q_{max}$) was chosen to be 21 Å$^{-1}$ in the current case, which was the best compromise between resolution and noise.

## 4.4 Results

### 4.4.1 Protocol automation software

The main goal of the protocol is to address the large number of measured data-points that are generated during high throughput experiments. We have written a set of Python scripts that are intended to be highly flexible and customizable allowing for efficient data collection, curation, reduction and analysis. The software is intended to be accessible and user friendly. The code can be executed using IPython[125] and Jupyter notebook.

The overall approach builds a collection of information about the experiment, associating reduced data, user inputs based on prior knowledge of the material, and analysis results. The collection can then be sliced and visualized easily by the user to interrogate and draw conclusions from the entire dataset. A schematic of the overall layout is shown in Fig. 4.3 showing all of the modules and the general workflow.

The data analysis protocol is currently optimized for the XPD beamline at NSLS-II. After a measurement, the xpdAcq[] acquisition software at the beamline outputs a log file containing the metadata, such as motor positions, measurement times and unique identifiers for each diffraction image.

In the first step the protocol software interrogates the log file and converts each measurement entry into an event. Each event then contains links to positional and other measurement metadata and the corresponding image files. The main benefit of the approach is manageability of the contents of the collection which are easy to visualize for the user using standard python plotting packages such as matplotlib[126] in conventional 1D or heatmap plots by simple iteration and filtering of the corresponding keywords. In addition we have prepared a few custom plotting functions that produce the figures presented.

Any pre existing knowledge can be appended to the corresponding event entries using simple macros, such as python for loops and conditional statements. For example, we can add composition information based on our prior knowledge of the layout of the sample:

```python
for event in collection():
    if event['x_motor'] < 1:
        event['composition'] = 'AgCu'
```
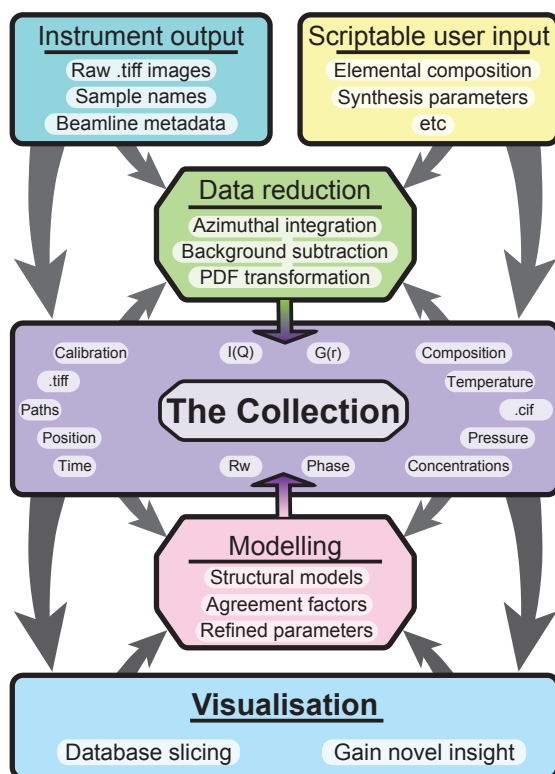
Figure 4.3: A flowchart illustrating the core of the mapPDF protocol and current implementation. Instrumental output, such as links to images and metadata, is combined with user created metadata to perform data reduction. Every step of the process is saved in the collection which can be sliced and visualized for screening and advanced analysis.

This way, any useful information which is absent in the metadata can be added on a per entry basis.

Experimental geometry calibration information is obtained from a Ni standard material measured at the same time as the array (Fig. 4.2). Calibration parameters are used when the images are azimuthally integrated to one dimensional $I(Q)$ patterns using Fit2D. The integrated patterns are then linked alongside the other information in the collection to the correct events as data arrays.

### 4.4.2 Background subtraction

The tfPDF measurement requires careful subtraction of the substrate scattering because the substrate signal (background) was significant compared to the small signal from the deposited nanoparticles. In the case of the samples presented, the total intensity of the material is on the order of 2-4% of the total scattering intensity.

Background images were acquired from a sample region with no nanomaterial and integrated to $I(Q)$ in the same way as the images containing the material. A different background measurement can be assigned to each entry in the collection. This is particularly useful when substrate properties vary as a function of position and a background measurement in proximity to the material of interest is optimal for signal extraction. In

the present case a single background dataset was collected from the center of the array and assigned to all images.

The background subtraction is performed after interpolating the background dataset onto the $Q$ grid of the target pattern. In most cases a scaling factor of 1 should be used for all backgrounds in a dataset, but a global scale factor may be defined by the user if needed. This is usefull since the real experimental conditions, such as beam intensity and packing/deposition densities can vary and result in a deviation from the ideal scale. Additionally, a utility function has been provided to optimize the background subtraction per entry in the collection, by minimizing the difference between sample and background signal intensity, over a user defined $Q$-range[127]. The background subtracted diffraction patterns are then appended to the collection as data arrays.

### 4.4.3 PDF transformation and model fitting

The background subtracted $I(Q)$ data is Fourier transformed to the PDF using PDFgetX3 [101] using parameters such as $Q_{max}$ and elemental compositions that are stored in the collection. The output PDF data, $G(r)$, is again appended to the main collection. A representative example of data at each step of the process is shown in Fig. 4.4. These transformation steps can be performed on all database entries or a subset.

In the combinatorial array experiment presented, each well contained different metallic nanoparticles. We used an virtual crystal fcc model to refine the experimental PDFs and extract structural parameters for each event in the collection. A sperical attenuation function was added in order to simulate the size effects for crystallites or nanoparticles within the material. The PDFs, relevant metadata entries and initial guesses for the structural parameters are fed into the model to perform structural refinement using the DIFFPY-CMI [47] - Complex modelling Infrastructure software available at `diffpy.org`. A representative example from the combinatorial array experiment may be seen in Fig. 4.5. The primary parameters of interest from the output of the refinement for this dataset, namely the crystallite size and lattice parameter, and weighted agreement factor $R_w$, are associated with the correct event in the collection, as shown in Fig. 4.3.

### 4.4.4 Visualizing combinatorial data

Good visualization tools are essential for HT experiments. The approach outlined above results in a comprehensive collection of measured data and data analysis results. Presenting this data in a manageable way is usually a major challenge. The main philosophy we have taken is to make spatial maps of scalar quantities that are associated with some aspect of the components in the collection, for example, goodness of fit or lattice parameter. Figure 4.6 illustrates a usecase where position of the quantity on the plot corresponds to the physical position on the chip where the data were measured, as viewed along the direction of travel of the x-rays. Fig. 4.6 a) shows the $R_w$ from fits of the fcc model to the background subtracted data from our array of catalytic material as a function of position
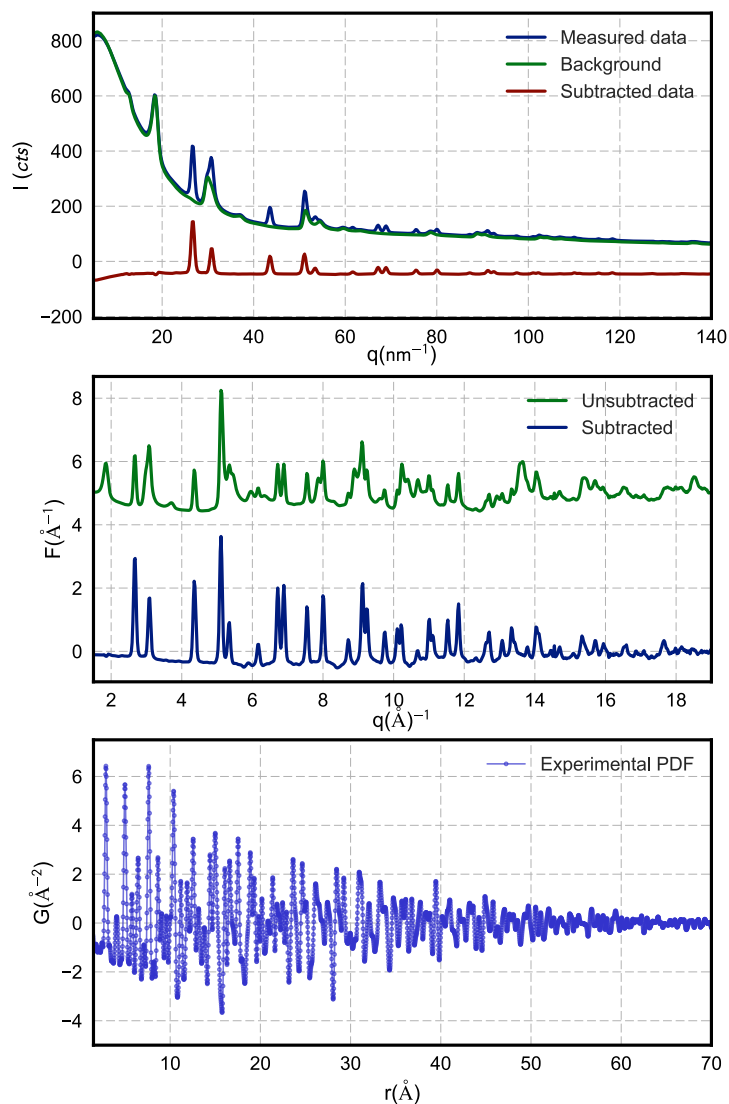
Figure 4.4:    An example of data processing from a single event in the collection.  The background signal is subtracted following normalization in order to better resolve scattered intensity from the nanoparticle sample.

on the array.  The plot can be generated from a complete collection using a simple plotting function:

```
slice_2D('x_motor','y_motor','rw')
```

this function loops over the collection, extracts the parameter of interest, sets the correct boundaries, and provides colorscale.

The color of the squares indicates the model fit quality at the measured position, where dark red indicates minimal or no agreement to the candidate structure, and dark blue for good agreement.  In theory, after the background subtraction step, the areas where all of the signal is from the substrate would contain nothing but noise.  Since we are fitting the fcc model, these regions will result in poor $R_w$ values and good fits are an indication of where the catalytic material is located, and indirectly, how much is there.  For more
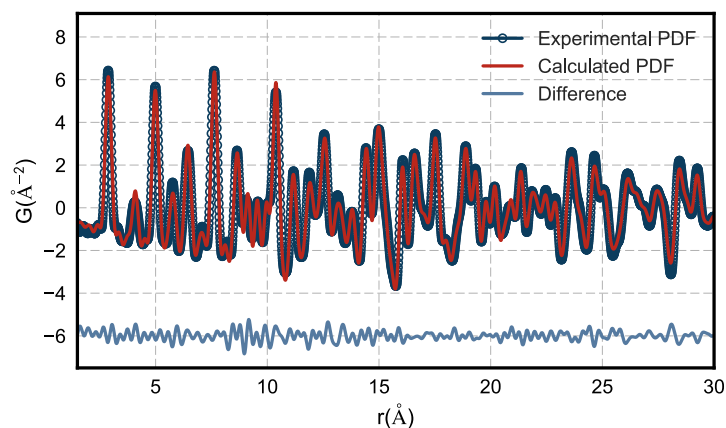
Figure 4.5: An example of a single PDF fit using a bimetallic FCC model to one of the datafiles in the collection. Blue illustrate the experimental data. The refinement score $(R_w)$ is 12.3%.

complicated materials, where the relationship between $R_w$ and snr aren't trivial, one could locate the material of interest by using a different metric, such as scattering intensity after background subtraction, selected bragg peak intensity, absolue maximum counts, etc. through the software in exactly the same way. We can then return to the locations with the material to do more careful structural analyses.

In a similar fashion to the figure above, it is possible to generate maps of any quantity in the collection with multiple filters by using simple python for loops, conditional statements and built in matplotlib functions like the one presented in Figure. 4.6 b):

```python
for i in collection:
    if i['rw']<0.3:
        plt.scatter(i['x'], i['y'], c=i['psize'])
```

The code snippet above generates the spatial map of nanoparticle size vs. position, refined from the virtual crystal fcc model after filtering for acceptable $R_w$. In the current case, it was apparent that the material is only present within the deposition sites.From the figure it is also clear that the particle size distributions differ within the wells with the AgAu well being much more uniform and smaller on average.

### 4.4.5 Software flexibility, modularity and availability

The software that implements the protocol can be divided into several key parts as presented in figure 4.3 are initial data treatment, transformation of the data and model fitting and refinement. All three can be modified, replaced or omitted by the user depending on the use-case and user preferences.

Although originally intended for tracking positional information about the sample, the protocol can be extended to keeping track of any scalar quantity and has been found extremely useful for time-series datasets. Structural parameter evolution as a function
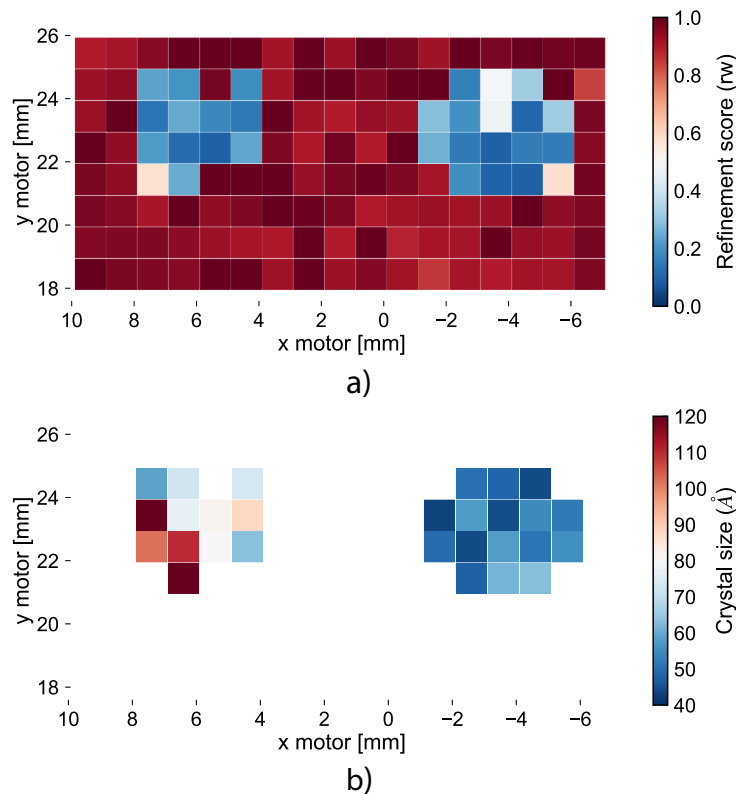
Figure 4.6: **a)** Map of refinement scores vs. position for the array. Red squares indicate a measurement area with a poor refinement score, while blue squares indicate areas with good refinement scores, and thus presence of the fcc phase. There are two distinct regions with nanomaterial surrounded by measurements of nothing but the background. The refinement scores for this dataset are highly correlated with signal to noise ratio and give an indirect metric for the amount of material in a given area. **b)** Map of particle size vs. position on the array filtered to only display good model refinement scores. The colorscale indicates spherical particle diameter parameter from smaller (blue) to larger (red) crystallite size estimates. The figures are generated using simple conditional statements to slice the collection.

of time, instead of being a function of motor positions, can be visualized using the protocol software and helps streamline systematic analyses of large in-situ datasets. The methodology has also been extended for studying nanocluster formation in a wet synthesis environment as a function measured at the P.02 beamline at PetraIII, Hamburg, Germany as described in Chapter. 5. Considering each measurement in sequence as separate events with time as a parameter of interest allows for quick and systematic analysis of large in-situ datasets.

The software is free and distributed under a BSD license at `http://www.diffpy.org`. The latest source code is available on GitHub as part of the diffpy organization at `https://github.com/diffpy/mappdf` as well as an example dataset used to generate the figures above.

## 4.5  Conclusion

An analysis protocol and a set of scripts for treating a wide variety of combinatorial high-throughput materials characterization data is presented. The protocol software is flexible and can be modified and expanded by the user. An example of a combinatorial catalyst library analyzed using the PDF technique has been demonstrated, highlighting the power of the approach. The ability keep track of and analyze large volumes of data and additionally parametrize the dataset allow for quick analysis that is necessary for high throughput experiments.

## 4.6  Acknowledgements

# 5

# In-situ PXRD and PDF study of the formation of copper nanoparticles for ink jet printable conductive inks

This chapter describes the process development for copper nanoparticles over a period of 3 years. Both the chemistry and the characterization techniques have undergone major changes in the pursuit of sustainable and profitable large scale synthesis. Thus the chapter outlines this development through the eyes of the synchrotron characterization techniques, often lagging behind the main development process. Through these techniques we attempt to collect our knowledge of the system and suggest a methodology for both characterizing future products and helping guide further development. Several experiments observing the reduction of copper are performed in-situ. New continuous flow setup for synchrotron measurement is employed, testing both the viability of the method and attempting to map the reaction in greater detail.

Due to the sensitive nature of the process, the exact recipes for the production of nanoparticle suspensions are omitted, but can be found in the publication summarizing the process that will follow the thesis in the near future.

## 5.1 Introduction

The market for printed electronics using ink jet printing techniques has experienced significant growth in the recent years. With applications in displays, sensors, Radio Frequency IDentification (RFID) tags, smart packaging, battery technologies, automotive and 3D printing[128], it is forecast to surpass the US $70 billion world annual revenue[129] within the next decade.

In terms of manufacturing, the ability to print with conductive material is generally considered to be environmentally friendly. Compared to traditional fabrication techniques based on photolithography and wet etching of substrates covered in conductive material, direct printing generates less waste and requires less harmful substances[130]. In addition, conductive inks can be directly applied to numerous substrates which are not limited to silicon or glass and include flexible polymers and fabrics[131].

The majority of conductive inks are based on silver as the filler material. While not as good as other noble metals at resisting oxidation it is cheaper and malleable, yet still comprises a significant portion of the cost of many devices where it is used[132]. Recent market reports also indicate that peak production of silver, where only a third comes from primary sources, has been reached[18] forecasting a surge in pricing moving forward. Compared to silver, metallic copper is just 6% less conductive and roughly 3 orders of magnitude more abundant which makes the commodity prices around 2 orders of magnitude lower than those of silver. Therefore the possibility to replace Ag based inks by copper based alternatives is a very attractive option.

To compete with silver based conductive inks, copper based products need to fulfill a number of requirements. The nanoparticles need to be well dispersed, have low sintering temperature, have high conductivity and be resistant to oxidation[133]. The first two can be achieved by preparing dispersions of small nanoparticles[134]. The downside, however, is that this makes copper particles more active and prone to oxidation forming the insulating $Cu_2O$ layer on the surface. For this reason, the synthesis and sintering of copper pastes typically had to be performed in inert atmosphere and used strong capping agents, such as thiols and oleic acid, that had negative effects on the conductivity of the sintered material[135, 136, 137, 96].

Recently a number of synthesis methods have been developed that utilize weaker bound capping agents or capping agents that can be burnt off during the sintering process[138]. These methods include vacuum vapor deposition[139] gas-phase plasma processes and thermal decomposition[140], microemulsion [141], thermal and chemical reduction[142, 134, 143, 144, 145]. What all these have in common, however, is the rather low loadings of nanoparticles in the produced ink resulting in poor production rates making most reported recipes unfeasible economically. Many also utilize fairly hazardous reduction agents such as hydrazine that put an additional strain on handling the chemicals and chemical waste in an industrial capacity.

In an industrial process where commodity prices are low, waste treatment suddenly

becomes a significant portion of the production costs. Utilizing less harmful chemicals and environmentally friendly production technologies becomes increasingly valuable. Recently demonstrated reduction processes of copper by glucose appear particularly interesting from an industrial standpoint[143][138]. The reactions appear to have good yields of over 95% material recovery and produce fairly harmless waste products consisting mostly of a mixture of sulfates, ammonia and carboxylic acids.

The following study examines a number of variations of the synthesis with glucose as the reducing agent. The capping agents and concentrations are optimized to produce as little waste as possible while performing complete reduction of the Cu content. These reportedly "facile" reactions prove to be more complex and are difficult to study in the lab. Most existing studies attempt to characterize the final product by means of x-ray diffraction and electron microscopy, while the observations during the synthesis are mostly performed by observing the colors[146, 134, 147, 148, 149, 138]. An additional layer of information can be obtained by following the reduction process as it happens in-situ. The characterization in the following study is performed in-situ using synchrotron powder diffraction and PDF techniques looking into both the earliest stages of the formation of the copper particles and following them as they are reduced and grow. The chapter will describe the ideas, experiments, trouble and results of the in-situ copper formation studies.

### 5.1.1 Copper reduction overview

Most copper is contained in various oxidized copper forms. Some of these are the byproducts of other industrial processes making it cheap and readily available. Thus it is logical to attempt to produce metallic copper nanoparticles in solution starting from these readily available bi-products of other industrial activities. In this study we have used $CuSO_4 \cdot 5\,H_2O$, $Cu(OH)_2$ and $Cu_2O$ precursors. In aqueous media the first two can be dissolved and in an oversimplification exist as a $Cu^{2+}$ ion. From our observation, the reduction process to metallic zero valent Cu goes through following steps[138]:

$$Cu^{2+} \longrightarrow CuO \longrightarrow Cu_2O \longrightarrow Cu \tag{5.1}$$
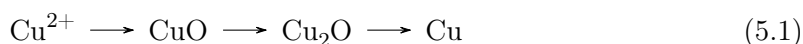
Typically, in order for the reduction process to happen quickly and to completion, strong and toxic reducing agents like hydrazine are used[134]. This is impractical and expensive in industrial setting. In order to keep the process as environmentally friendly and economic as possible, the reducing agent was chosen to be D-glucose[143]. The original reports state that D-glucose would be unable to carry out the reduction of copper to completion[145]. Nowadays, it is recognized that full reduction is indeed possible at high pH and after proper optimization of concentrations and temperatures during the reaction[138]. In proper conditions the simplified reaction is happening via oxidation of D-glucose and formation of gluconic acid, which is summarized as:
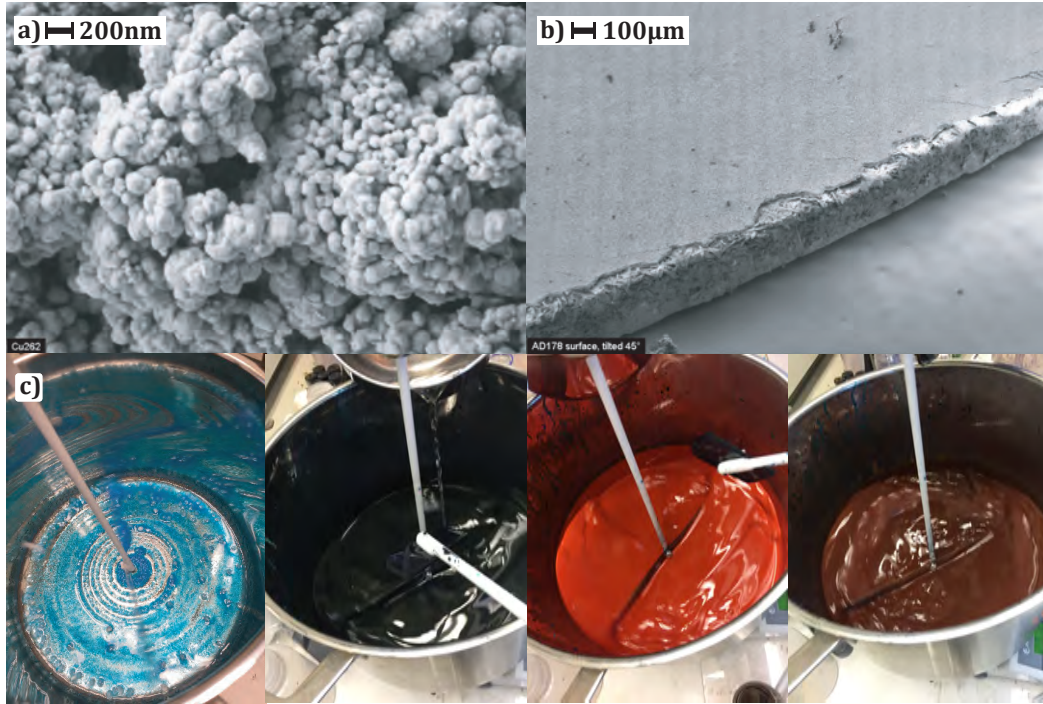
Figure 5.1: a) Copper nanoparticles produced from the $Cu(OH)_2$ precursor b) Conductive pad printed by the aerosol print method using the ink containing copper nanoparticles and after photonic sintering. c) Prototype batch production of copper nano-ink using the recipe with lactic acid as a capping agent. Left to right: $CuSO_4 \cdot 5\,H_2O$ dissolved in water, CuO formation after addition of NaOH, reduction to $Cu_2O$ after addition of glucose, final reduction to $Cu^0$.

$$Cu^{2+}_{(aq)} + C_6H_{12}O_{6(aq)} + 3\,OH^-_{(aq)} \longrightarrow Cu^0_{(s)} + C_6H_{11}O^-_{7(aq)} + 2\,H_2O_{(l)} \qquad (5.2)$$

Notably, the full reaction is likely much more complex due to the many bi-products of glucose oxidation and the likely recombination of these products[150].

All chemicals are sourced from Sigma-Aldrich in powder form. For batch synthesis all powders are added directly into the reactor vessel containing water. For in-situ synthesis, the reactants are dissolved in water and then mixed right before the measurement.

In total four systems were studied. Attempts were made to vary the parameters where possible. Lactic acid (LA) and Sodium Dodecyl Sulfate(SDS) were used as capping agents. These are summarized in Table 5.1. Details about the recipes will be given as appropriate.

## 5.2 Experimental methods

Powder diffraction measurements were performed during two separate beamtimes at the beamline P.02-2 at PetraIII, DESY, Hamburg. The wavelength for the measurement was

| Name | Reducing agent | Precursor | Surfactant |
|------|----------------|-----------|------------|
| Cu_1_a,b | Glucose | $CuSO_4$ | lactic acid |
| Cu_2 | Glucose | $CuSO_4$ | SDS |
| Cu_3 | Glucose | $Cu_2O$ | – |
| Cu_4 | Glucose | $Cu(OH)_2$ | – |

Table 5.1: An overview of the different synthesis parameters studied in-situ. Cu_1_a was synthesized at 78°C and Cu_1_b at 92°C

0.2072Å. The measurements were performed in transmission geometry in PDF configuration, meaning the sample was positioned in close proximity to the detector. The calibrated sample to detector distance for the first beamtime was 238.4mm giving an effective $Q_{max}$ = 20Å$^{-1}$, while for the second the distance was set to 201mm, giving an effective range of $Q_{max}$ = 22Å$^{-1}$.

The in-situ synchrotron measurements were performed using the modified Aarhus supercritical flow reactor[70]. The modifications are described in detail in Sec. 3.3. The precursor and the reducing solutions were prepared separately and then pumped through a turbulent mixer attached to the capillary assembly. During the setup procedure the flow was maintained to avoid the reaction starting. When the experimental hutch was properly sealed, the x-ray beam was allowed onto the sample and the heat gun reached its set point temperature, the flow was terminated and the reaction observed. The data were acquired by summing up 50 exposures of 0.1 second for the first beamtime( Cu1a,b and Cu2 samples) and 20 exposures 0.1 seconds for the second beam time. The resulting time resolution was respectively 5s and 2s.

### 5.2.1 Data reduction and structural refinements

For calibration and testing purposes some of the data ware azimuthally integrated using Fit2D program[98] and the structural refinements of the calibrant were carried out using PDFGui[46] to obtain the reference $Q_{damp}$ and $Q_{broad}$. For complete analysis and visualization most the data were handled by the software mapPDF which is described in Chapter 4. In the latter case the integration was done using pyFAI[100] library integrated into the software. The masking was done using a total mask method, where all images were summed and outlier pixels for the stack were removed. While not a perfect masking method, it yields a sufficiently good result for the purpose of the analysis. The structural refinements were performed as part of the mapPDF workflow using the PDFCalculator module for the crystalline structures and DebyePDFCalculator for the evaluation of solvation clusters.

A subset of the refinements for the crystalline products were done in PDFGui using $r$ range of 1−85Å at Nyquist sampling frequency[151]. The refined parameters for all datasets were the co-constrained scale factors, lattice parameters, isotropic atomic displacement parameters (ADP $U_{iso}$), $\delta_2$ sharpening parameter which is shared by all phases and spherical particle diameter (SPD).

Metallic Cu, space group $Fm3m$, and $Cu_2O$, space group $Pn\bar{3}m$, are both face cen-
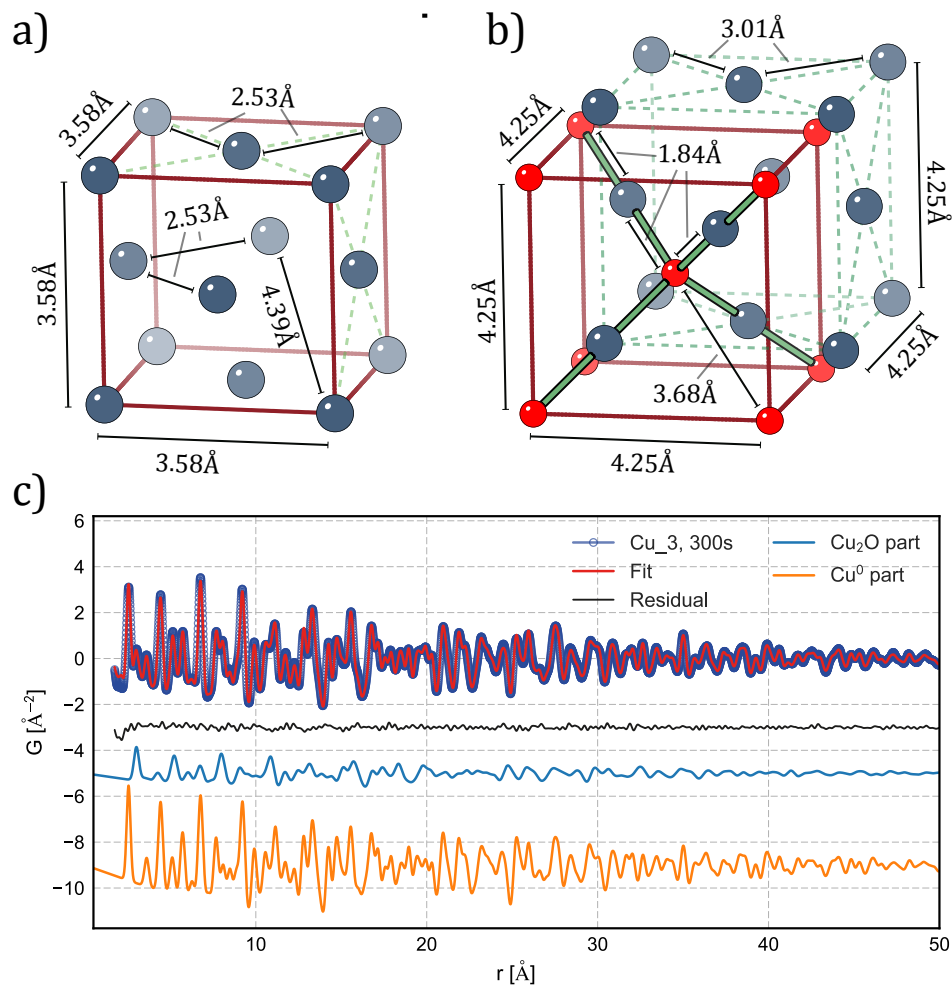
Figure 5.2: a) Structure of $Cu^0$ metal(blue), space group Fm3m, FCC arrangement. The unit cell is highlighted in dark red. b) Structure of $Cu_2O$, space group $Pn\bar{3}m$. A body centered cubic(BCC) oxygen(red) sublattice intertwined with an FCC copper(blue) sublattice. The unit cell is highlighted in dark red. c) Typical PDF fit for a mixed phase copper and cuprite dataset. The model consisting of crystalline $Cu_2O$ and Cu is sufficient to describe all features in the data. The PDFs of each phase in the fit are presented below the combined fit. Model agreement score $R_w$= 11.5%.

tered cubic (FCC) from the perspective of the Cu atoms. In cuprite the oxygen creates a body centered cubic sublattice, while copper has an FCC arrangement shifted a quarter diagonally with respect to the oxygen sublattice. The unit cells of both compounds are illustrated in Fig. 5.2. Cuprite and copper metal have very different lattice constants of around 3.6Å and 4.26Å respectively. This means that the peaks in their PDFs have limited overlap and can be distinguished even for fairly imbalanced mixtures, for example, the nearest neighbor peaks in an FCC lattice are at $\sqrt{2}/2 \cdot a$ and are at 2.54Å for Cu and 3.01Å for $Cu_2O$. The $r$ resolution is important to be able to accurately quantify the two phases in the early stages of the reduction process, and a $Q_{max}$ close to $20Å^{-1}$ is preferred.

For crystalline material, the FCC models are used to describe all of the datasets apart from the initial solvation structure. Model agreement scores are of the order of $R_w$= $10\% - 25\%$, which ranges from very good to good for the technique. Most importantly, the models are sufficient to describe all of the features in the data, and as seen in fig. 5.2c), the residual contains little room for improvement. In the datasets containing sulfate groups, the main areas of misfit are below $r = 5$Å and can be improved simply by adding a sulfate cluster to the fit or by cutting out the low $r$ portion of the refinement. For consistency, this was not done, and all results presented in this chapter are obtained from fitting just the crystalline models. From this point of view, the choice of the model is deemed adequate.

## 5.3 Results

The main challenge when attempting to reproduce the batch reactions at a synchrotron is the "industrial" nature of the process. Due to the requirements for reducing waste and maximizing yields, highest possible concentrations are used. While having high concentrations is good for a synchrotron measurement owing to better diffraction signals, having these high concentrations comes at a cost of higher x-ray absorption and solutions being viscous, thus limiting the diffusion in confined volumes of a typical capillary. The low diffusion in the capillary might introduce uncertainties due to local concentration differences compared to the batch process. Another factor is that many reagents are at or above their solubility limit at room temperature and require the reaction to start before they dissolve, introducing uncertainties into the measurement and a degree of unpredictability. These issues are irrelevant during industrial productions. Both of these issues are alleviated by having a large container with constant mixing and continuous addition of reagents during the synthesis. As a result the syntheses performed at the synchrotron were modified slightly, typically by adding enough water as to be able to dissolve the reactants.

### 5.3.1 Cu 1(a,b) synthesis: lactic acid (LA) capping

In this synthesis, the copper ions from dissolved copper sulfate are reduced to metallic copper by glucose in strongly alkaline conditions according to Eq. 5.2. lactic acid is added both to stabilize the pH and to act as a capping layer to protect the metallic nanoparticles from oxidation and controlling the size of the product by inhibiting nanoparticle growth[152].

**Preparation**

Precursor solutions of glucose and NaOH, and copper sulfate pentahydrate and lactic acid were prepared in two separate beakers. The amount of glucose required lies at the solubility limit of glucose in water at room temperature. For this reason the mixture was heated up slightly to allow all of the powder to dissolve and then brought back to room temperature. Glucose can stay in solution for a few hours before crystallizing giving enough time to prepare the rest of the experiment. To complete the first part of the recipe, NaOH is added to glucose.

$CuSO_4 \cdot 5\,H_2O$ stays as a powder when mixed with lactic acid and requires additional water to dissolve. As the water is added the mixture begins to heat up slightly and the sulfate dissolves. This second part of the recipe is also sufficiently stable before the rest of the experiment can be prepared.

The synthesis is initiated by mixing the two parts described above. To be able to see the early stages of the reaction at the synchrotron a mixing setup was employed as described in Sec. 3.3. The flow rates on the pumps were adjusted to deliver the correct stoichiometry to the capillary. As the experimental hutch is closed, the liquid is allowed to flow through the reactor, essentially keeping the reaction time at zero. When the heat gun reaches target temperature, the flow on the pumps stops and the reaction is observed until completion.

The experimental backgrounds for PDF analysis were measured in a similar fashion, stopping the flow during the measurement at target temperatures. The background solutions appeared stable over the course of $3-5$ minutes of the measurements.

**In-situ synthesis**

The reduction of copper with lactic acid as capping agent was examined at room temperature, 78°C and 92 °C. The overview is presented in Fig. 5.3.

The diffraction data is visualized as a waterfall plot comparing the course of the reaction in Fig. 5.3 a) and b). The intensity is on the logarithmic axis. As the heat is turned on after 25s, following a short delay, the rapid formation of crystalline $Cu_2O$ is observed. Cuprite phase growth, as observed via the refined scale factor, persists throughout the whole reaction. Following a delay of $50-75$s a small amount of metallic Cu phase is formed as is seen from the appearance of Cu [0 0 2] peak at $Q = 3.5 Å^{-1}$ and the asymmetric broadening of the strong $Cu_2O$ [0 0 2] peak at $2.94^{-1}$ by the appearance of the [1 1 1] peak of FCC copper. The metallic copper phase slowly grows up to a refined phase fraction of 10% over the course of the reaction.

Extracting accurate absolute crystallite sizes in the case of copper reduction by glucose is impossible, however, the trends obtained from the refinements should be reliable regardless of the inaccuracies on the absolute scale. The reactants were examined in-situ using PDF analysis. The background subtraction was handled by mapPDF as described in Chapter 4 by scaling the background file to match the data around $15 Å^{-1}$. The refinements for the crystalline products were done using PDFGui using $r$ range of $1-85 Å$ at Nyquist
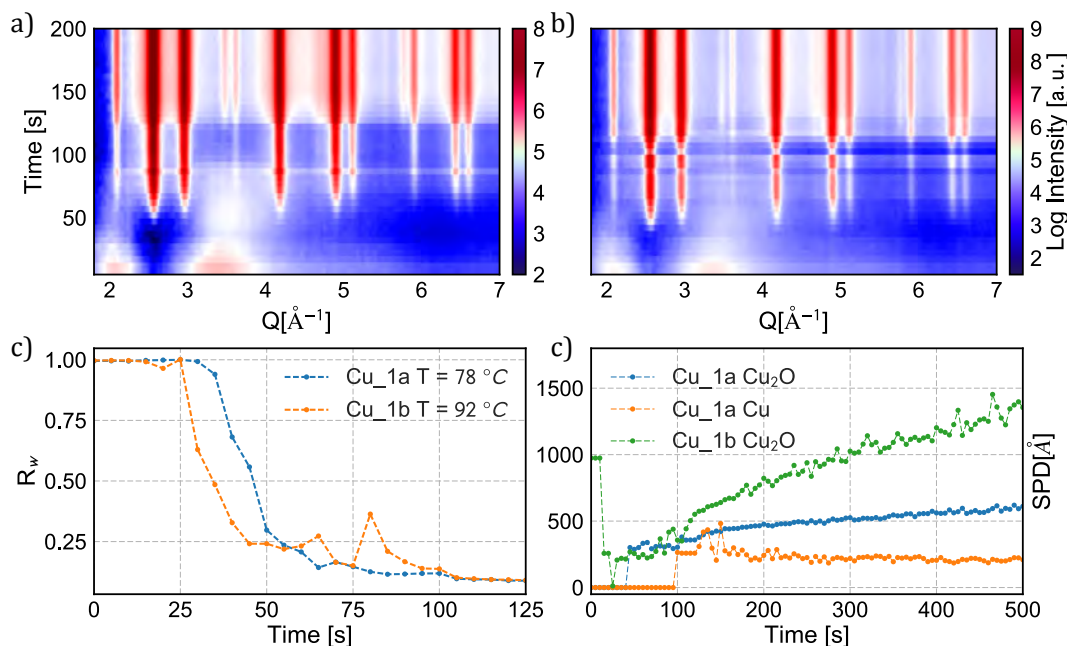
Figure 5.3: Overview of the reaction Cu_1. a) 78 °C and b) 92°C waterfall plots of in-situ reduction of copper sulfate by glucose and lactic acid on logarithmic intensity scale. c) Model agreement score $R_w$ used as a proxy metric to detect the $Cu_2O$ phase growth as a function of time. d) Refined SPD parameters of $Cu_2O$ and copper phases during the first 500s of the reaction for the two temperatures.

sampling frequency[151]. The refined parameters were the co-constrained scale factors, lattice parameters, isotropic atomic displacement parameters (ADP $U_{iso}$), $\delta_2$ sharpening parameter which is shared by all phases and spherical particle diameter (SPD). Total conversion to metallic copper was impossible as the pH drops during the reaction and needs to be adjusted for glucose to be able to reduce the remaining $Cu_2O$[134].

**Effects of temperature**

The effects of temperature on the reduction of copper are seen in Fig. 5.3. Upon heating up the mixture a rapid formation of $Cu_2O$ begins. The formation of the oxide phase starts around 10s earlier in the sample at higher temperature of 92°C. The $R_w$ value can be used as a proxy for this effect. As soon as the oxide phase can be detected in the G(r) the agreement factor improves. This is illustrated in Fig. 5.3 c). Only the $Cu_2O$ phase is refined and the improvement is seen around 2 frames (10s) earlier than for the low temperature. In addition, comparing the PDFs directly as seen in Fig. 5.4 show the same effect as distances associated with the oxide phase start to appear and are highlighted in green.

As expected the high temperature synthesis also leads to a much faster growth of $Cu_2O$ crystals(Fig. 5.3 d)). While the absolute values refined from PDF analysis cannot be trusted, the relative change appears reliable and the refinements themselves were stable.

Unfortunately, it was impossible to quantify the FCC Cu phase fraction in the high
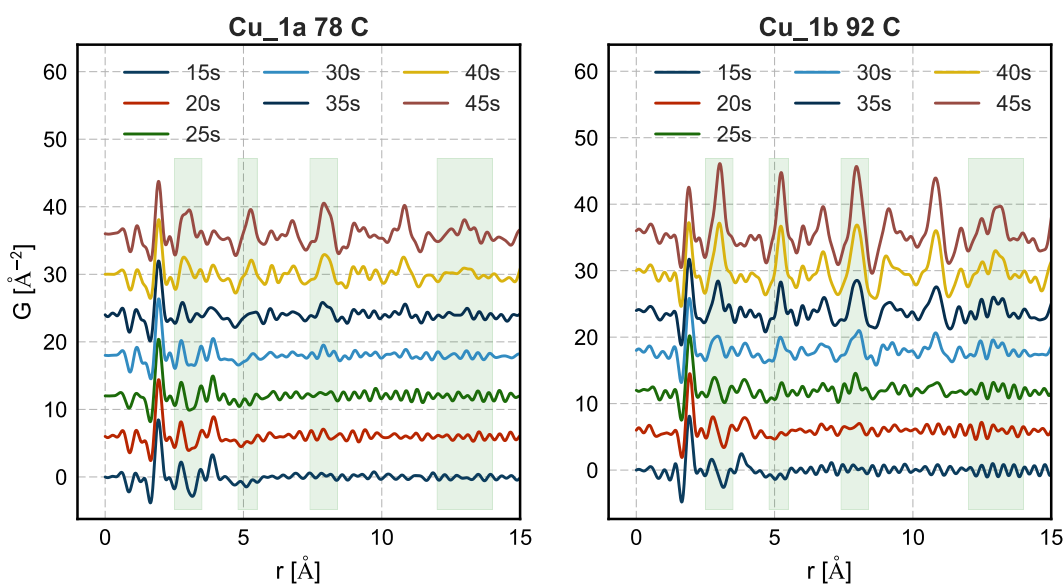
Figure 5.4:   Comparison of the nucleation of $Cu_2O$ from the PDF data for Cu_1_a and Cu_1_b syntheses.  Highlighted in green are some of the features that can be associated with the oxide phase appearing as the time progresses.  PDF curves are offset for clarity.

temperature synthesis due to the overwhelming signal from very large crystallites of $Cu_2O$ and vanishingly small intensity of metallic copper.

For the complete reduction process to take place the pH has to be kept alkaline past pH = 9.  Initially the pH is adjusted by adding large amounts of NaOH, but it will decrease during the reaction as glucose is slowly oxidized.  In a batch synthesis the pH can be regulated by continuously adding NaOH which is not feasible in a flow reactor. Unsurprisingly this lead to a continuous growth of $Cu_2O$ and only a slow increase in the metallic copper phase fraction.

**Local structure of the CuSO4 in solution**

G(r) curves seen in Fig. 5.4 show the nucleation of the Cu nanoparticles at the earliest stages of the synthesis.  As the time progresses the Cu−Cu distances associated with $Cu_2O$ can be seen at 3.0Å, 4.25Å, 5.2Å, 6.0Å and larger $r$ values.

Before the crystallization of the copper oxide the copper ion is present in solution as a $Cu^{2+}$ ion.  Its exact coordination in aqueous solution has previously been reported as distorted octahedron surrounded by six water molecules[39][153].  Our system includes other species and as such the copper ion could be coordinated to more than just water.  For the rest of this section, it will be referred to as an oxygen containing ligand O* Examining the first datasets in both reactions we can discern the planar Cu−O* distances at 1.9Å followed by the small peak at around 2.34Å coming from the elongated Cu−O* from the distorted oxygen position above and below the plane caused by Jahn-Teller effect.  These are followed by a peak around 2.8Å which would correspond to O*−O* distances along the edges.  For a single free floating octahedron no additional well defined pair correlation

peaks are expected. In the data, however, there are 2 more peaks at 3.4Å and 3.9Å. One arrangement where these would be possible are arrangements of multiple octahedra sharing one or more oxygen atoms in corner share or edge-share coordination[154][155]. In this case the additional $Cu-Cu$ distances would appear at 3.9Å if sharing one oxygen atom at the corner of the octahedra and 3.6Å corresponding to sharing two.

The main challenge in attributing pair correlation distances to specific atomic species lies in the chaotic nature of the system. The mixture contains species of $OH^-$, $SO_4{}^{2-}$, carboxylic acids(lactic acid and gluconic acid) and glucose with its likely degradation bi-products due to harsh alkaline conditions. Instead of $Cu^{2+}$ ion coordinating to other $Cu^{2+}$ octahedra via an oxygen atom or a water molecule, it might just as well coordinate to sulfate groups or bi-products of glucose oxidation. The sulfate ion specifically and the deprotonated end groups of carboxylic acids are primary candidates for attracting more than one $Cu^{2+}$ ion. Five fold pyramidal arrangements due to Jahn-Teller destabilization of the octahedral complex have also been reported from EXAFS measurements[156][157] and theoretical calculations[158].

Ultimately, more work is needed for determining the exact structure of the $Cu^{2+}$ solvation cluster in the synthesis mixture. The data quality is excellent to support this effort. The nucleation mechanism on the other hand is hard to establish due to insufficient time resolution. Nucleation appears to happen at much faster timescales than the best time resolution currently available at the PDF beamlines. Perhaps the flow mixing setup could be modified, by moving the mixing point closer to the beam, decreasing the temperature and increasing the flow rates to obtain sub-second time resolutions. In this case, the uncertainties from the mixing dynamics would have to be taken into account.

### 5.3.2 Cu 2 synthesis: sodium dodecyl sulfate (SDS) capping

Sodium dodecyl sulfate was previously reported as a good capping agent during the reduction of Cu in solution[143]. It is cheap and non toxic, does not introduce any exotic chemistry to the mix and is reported to protect the particles from agglomerating and and re oxidizing. It utilizes the natural affinity of sulfur to bind to metallic atoms in solution creating a uniform capping layer that should interfere with the naturally occurring Ostwald ripening process.

**Experimental issues and solutions**

The mixture of $CuSO_4$ and SDS is once again at the solubility limit and was prepared in a liquid form by slight heating. When pumped into the tubes of the flow reactor, the mixture solidified which lead to the clogging of the reactor tubing, preventing any flow. Attempting to reduce the concentrations and thus increase the fluidity of the precursor were unsuccessful and the synthesis was performed in "batch" mode by mixing the precursors in a beaker and injecting into the reactor using a syringe and a short piece of tubing. Despite the initial heat-up the reaction appeared stable in the beginning allowing for measurements of the state of the mixture at room temperature. As the heat was turned on and set to
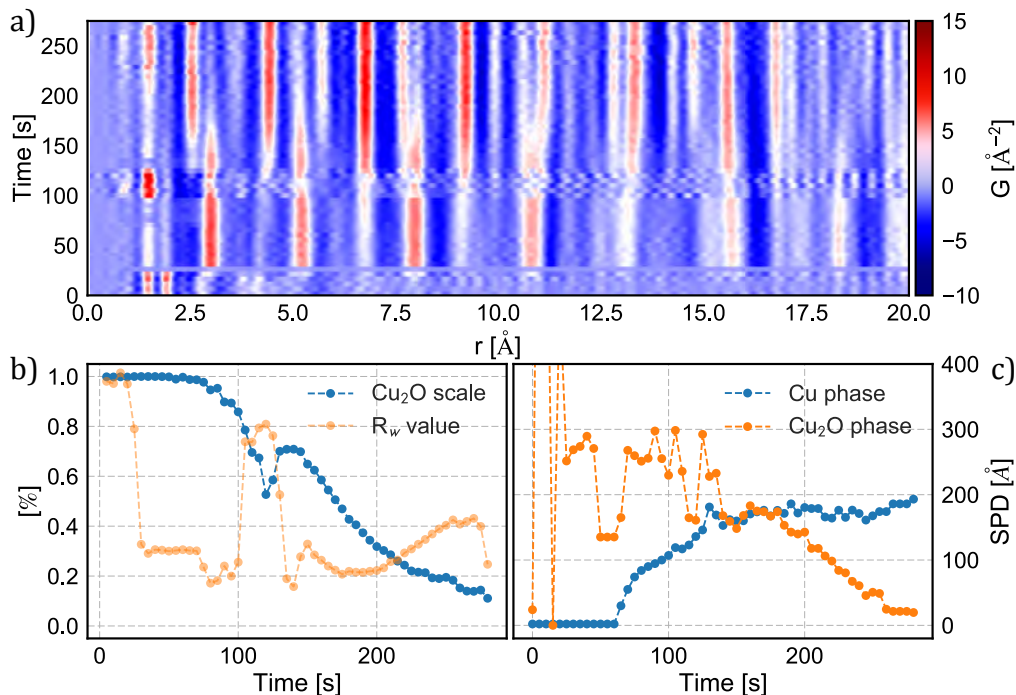
Figure 5.5: Overview of the reaction Cu_2. a) waterfall plot of the background subtracted $G(r)$ patterns showing the growth and the reduction of $Cu_2O$ to metallic Cu. b) The scale parameters for the cuprite phase and associated $R_w$ values from model refinements. The instability is seen as an air bubble moves through the beam due to the liquid boiling. c) Size estimates for the two phases in the reaction as a function of time.

target temperature, the liquid began to boil, the effects of which are seen in Fig. 5.5a) in the varying intensity and unstable refinement parameters Fig. 5.5b).

**Diffraction analysis**

Before the start of the reaction, the copper cluster is similar to the cluster seen in the lactic acid synthesis. The peak at approximately 1.5Å in the $G(r)$ of the cold mixture likely corresponds to a higher concentration of the sulfate ions from the dissolved SDS. Presence of the additional distances corresponding to small cuprite nanoparticles indicates that the reduction process happens upon mixing and a small fraction of cuprite has already formed during the initial heating due to the exothermic nature of the reaction. The assumption for having a similar solvation cluster in this case is reasonable considering the only difference compared to the solution from before is the presence of SDS instead of LA.

As the heat is turned on after 25s, the reduction process takes place. At this concentration it takes less than a minute for the FCC copper phase to appear. The refinements on the PDF data are performed in the same fashion as for the lactic acid synthesis as they were measured during the same beam time. Following a rapid growth of the $Cu_2O$ phase during the first few dozens of seconds of the reaction, the reduction process caps the maximum size of the oxide at around 300Å. The maximum refined SPD size of copper oxide coincides with the appearance of the metallic copper phase. This suggests that

the reduction to $Cu_2O$ is a favorable process and the further reduction of Cu atoms only proceeds once all of the $Cu^{2+}$ atoms are converted to $Cu^+$. The possible mechanisms for this transformation are discussed further is Sec. 5.3.6. The reaction ultimately leads to an almost complete reduction of copper into a metallic form in under 5 minutes.

### 5.3.3 Glucose as capping agent

Apart from being a capable reducing agent for reduction of Cu to metallic state, there have been reports of D-glucose having a positive effect on the nanoparticle size as the concentration increases. These effects have been attributed to the increased local concentrations of the reducing agent in the solution, effectively increasing the number of nucleation sites for Cu nanoparticles[143, 138]. At the same time, the positive effect of higher concentrations of D-glucose on the stability of copper nanoparticles has also been reported and explained by D-glucose acting as an oxygen scavenger in solution[146]. The potential of oxidation products of glucose to act as a surfactant appears to have been overlooked, as most approaches focus on characterizing the effects of the many capping agents such as PVP[159][160], SDS[143] and a number of carboxylic acids by coordinating to copper through an available O atom[134][161][152][94]. Glucose is known to have a large number of oxidation products when put into harsh environments[150] with many of these products used as surfactants in combination with a strong reducing agent.

In our experience, the reaction conditions can be optimized to create stable nanoparticle suspensions without any additional surfactants other than bi-products of glucose oxidation. The following two approaches are an evolution of this idea and an attempt to optimize the complexity, energy and material costs and reduce waste by reducing the number of reactants to just glucose, water, NaOH and the copper precursor.

### 5.3.4 Cu 3 synthesis: using $Cu_2O$ as precursor

Since $Cu_2O$ is clearly an intermediary stage during all syntheses so far and a common contaminant in the final product, it is tempting to forgo the reduction of $Cu^{2+}$ in its ionic form to $Cu^+$ in cuprite. This approach allows to reduce the cost both in terms of material and energy. $Cu_2O$ is a typical waste product from mining nickel and silver and it is already partly reduced. It is also extensively used as a filler in marine paints as an anti-fouling coating of the hull[162]. The process also reduces the environmental impact by reducing the amount of waste water for the synthesis by allowing to start from higher Cu loadings due to the absence of sulfate. The change in copper loadings improves from 20% for $CuSO_4 \cdot 5\,H_2O$ to around $50\%-60\%$ for $Cu_2O$. This makes the whole process more productive and increases its industrial attractiveness. The resulting synthesis is also beautifully simple containing just four ingredients: cuprite, NaOH, glucose and water.

## Preparation

Glucose acts as a reducing agent in this reaction and its solution is prepared separately. The recipe works at the solubility limit for glucose at room temperature and thus the mixture is heated slightly on a hotplate while being stirred. Following complete dissolution of glucose in water the solution can be cooled down to room temperature without glucose precipitating for some time. During this time the solution of NaOH is prepared while continuously being stirred and cooled down to avoid boiling. NaOH is then mixed with $Cu_2O$ powder. Cuprite has very low solubility in water at room temperature, but changes dramatically as the pH and temperature increase[163]. As we are trying to work at as low temperature as possible to avoid triggering the reduction process, most of the powder would stay as crystalline oxide until mixed.

Due to the poor solubility of the precursors, the flow mixing setup was avoided. The reaction is highly exothermic and the reduction process will start as soon as the glucose solution is added to concentrated NaOH and $Cu_2O$ mixture. To avoid exothermic heating of the NaOH and $Cu_2O$, the mixture is contained in a narrow syringe and the glucose solution is quickly pulled in for best turbulent mixing. Upon mixing the contents of the syringe will start to heat up rapidly. This can be avoided by dropping the syringe into a bowl of ice water. When cool the mixture is stable enough to inject it into the measurement setup.

## Diffraction analysis

Using glucose as a reducing agent and $Cu_2O$ as the metallic precursor the reaction is examined in-situ using synchrotron PXRD. The overview is summarized in Fig. 5.6. Because of the low solubility of $Cu_2O$ at room temperature the initial state of the system contains large crystallites of copper oxide. These are seen from strong single crystal reflections on the 2D detector. The heating is turned on at around 100s mark where a rapid reduction of the oxide begins.

The XRD patterns are analyzed using PDF analysis and are transformed to G(r) with a $Q_{max} = 19.9\text{Å}^{-1}$ and instrumental $Q_{max}$ of $22.5\text{Å}^{-1}$. This optimizes the quality while maintaining the highest possible resolution. $Q_{min}$ is chosen as to avoid the masking artifacts, typically around $0.8\text{Å}^{-1}$.

Fig. 5.6 shows the overview of the in-situ reduction of $Cu_2O$ precursor to metallic copper. The diffuse scattering of water changes with increasing temperature. For this reason, the background is measured at the same temperature and for the same temperature ramp consisting of a mixture of glucose and NaOH at correct concentrations while excluding $Cu_2O$. The background subtraction is handled by mapPDF as described in Chap. 4 by mapping both the background series and the data series onto a time axis and subtracting the closest dataset through scaling in the region around $15\text{Å}^{-1}$-$20\text{Å}^{-1}$ in Q space before Fourier transforming to G(r). Due to high crystallinity of the products structural refinements on the background subtracted G(r) were performed in PDFGui[46] as it is significantly faster than the corresponding diffpy.CMI module PDFGenerator(). The refinements
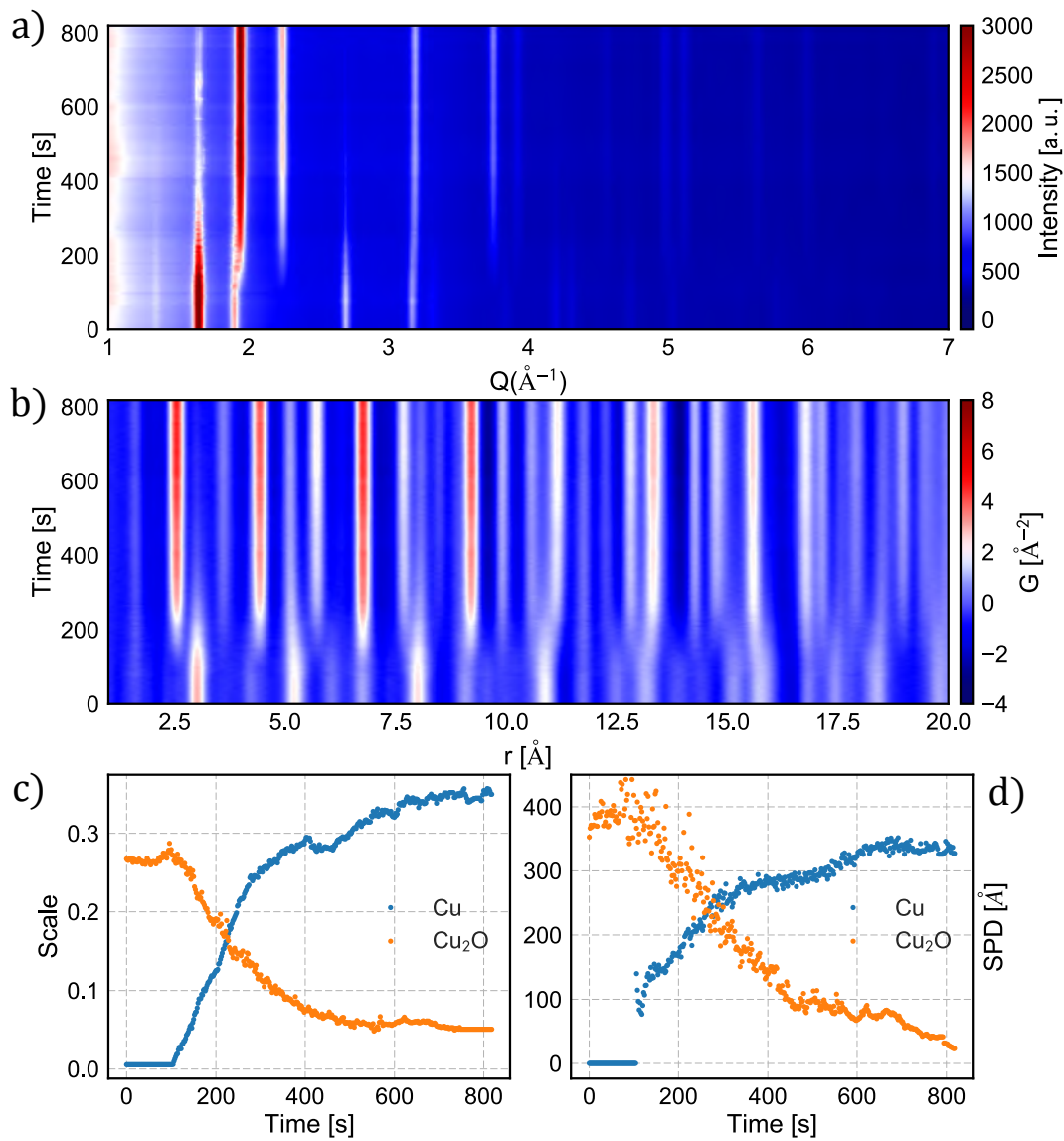
Figure 5.6: Overview of the reaction Cu_3 a) waterfall plot of the PXRD patterns from the reduction of $Cu_2O$. As the heat is turned on around 100s mark, the $Cu_2O$ phase rapidly transitions to metallic Cu phase, as can also be seen in the b) waterfall plot of the PDF's, where the two phases are easily distinguishable. The color scale is adjusted as to best highlight the phase transition and does not clearly show the growth in individual peak intensities after the point of a phase transition. c) The unconstrained scale parameters for Cu and $Cu_2O$ phases. The phase fractions are ratios of each scale parameter and the sum of the two at every given point. d) Spherical particle diameter values during the reduction.

were done with a Nyquist sampling for 1Å-75Å. The $Q_{damp}$ and $Q_{broad}$ parameters were obtained by refining a $CeO_2$ standard. The refinements were initiated in two parts at around frame 100, corresponding to 200s from the beginning of the measurement. The first part was then allowed to run down the frame index from 100 to 1 and the second was similarly allowed to run up until index 403. This ensures a good and stable starting point for both sets of structural refinements as both Cu and $Cu_2O$ phases are roughly equal, as seen in Fig. 5.6 c). The program can then run the macro smoothly until encountering an instability typically associated with trace amount of one of the phases and can be tweaked manually at that point.

Upon mixing, the reaction is highly exothermic and thus the initial temperature was lukewarm estimated around 30°C-35°C. The large crystals of copper oxide can be seen dissolving following the unconstrained scale parameter of copper oxide in Fig. 5.6c). The total intensity increase appears due to dissolution of large crystals and their contribution to the powder average. As they dissolve, they will contribute to the total integrated intensity, as the strong single crystal reflections are masked during data reduction. The similar strategy is used to see the growth of the metallic copper phase in the end of the reaction, when the scale parameter for cuprite becomes unstable, but the growth for copper phase can still be seen. Similarly, the slow growth of the $Cu_2O$ crystals for the first $100s-150s$ from the beginning of the measurement can be observed. The size estimates here should be taken with a grain of salt as they are on the limit of the sensitivity that can be achieved from PDF. While the absolute values should not be trusted at face value, the trends obtained from the refinements should be reliable. In addition, the crystallite sizes of the product are close to the crystallite size estimates of the products produced in batch reactions in the lab and measured at the in-house source.

The refinement macro reaches an instability when approaching the start of the reaction when the crystallite size of Cu phase drops below 100Å as the signal is dominated by very strong peaks of $Cu_2O$. By removing the SPD as a parameter at that stage, the phase fractions can still be estimated through local refinements.

Using Rietveld refinement on the reciprocal space powder diffraction data for size estimation instead of PDF proved impossible. In the PDF configuration, i.e. with detector in close proximity to the sample, the instrumental broadening is too large and is dominating the peak width at the crystallite sizes involved.

### 5.3.5 $Cu(OH)_2$ synthesis

Findings in the lab and during the in-situ experiments indicate that the final particle size of the product copper nanoparticles depends on the sizes of $Cu_2O$. Commercially available $Cu_2O$ typically comes in sub micrometer particle size powders. There is no need for the oxide particles to re-form during the reduction and this is mirrored in the product having larger particles and agglomerates. $Cu(OH)_2$ on the other hand can be found in nanometer sizes likely due to it's much lower solubility in water in ambient conditions. Copper hydroxide can be dissolved at high pH and at raised temperatures, which means

that it's solubility is less of a problem. Using $Cu(OH)_2$ as a precursor appears to have a positive effect on the nanoparticle sizes without significant changes to the recipe making it a more attractive alternative for applications where particle size is critical, such as ink-jet printing.

### Preparation

The sample was prepared similarly to the one described in Sec. 5.3.4. At normal conditions the $Cu(OH)_2$ is insoluble in water. The powder is dissolved as highly concentrated NaOH is added changing the copper hydroxide to $[Cu(OH)_4]_2^-$ The powder did not dissolve completely however until the heat was turned on during the reaction, as it reaches the solubility limit in the amount of water used for preparation of the precursor. The background data was measured as a mixture of right concentrations of NaOH and glucose heated at the exact same temperature ramp for 800s. No changes were observed in the background after around 400s, and thus in the remaining part of the dataset, the last background file was used.

### Diffraction analysis

The data reduction and structural refinements were performed in a similar fashion as described in Sec. 5.3.4. Similarly to previous datasets, the nucleation time for copper oxide is much faster than the time resolution of the experiment. At the beginning of the measurement $Cu_2O$ particles are already around $8-10$nm in size and growing.

The reaction was observed at three temperatures during the synthesis. In the beginning the mixture was kept at room temperature until 400s (frame 200) at which point the heat was turned up to 60°C. After 800 frames, at 1600 seconds, the temperature was further raised to 76 °C.

At room temperature the reduction process is slow as expected. Copper oxide nanoparticles grow as the copper hydroxide is dissolved. As the heat is turned on, the $Cu(OH)_2$ rapidly dissolves followed by a fast growth of the cuprite nanoparticles. At this stage the reduction favors $Cu^{2+}$ to $Cu^+$ reduction until all copper is in the $Cu_2O$ phase. Due to the dominating oxide signal, reliable metallic copper size estimates could not be obtained for the first seconds of the reaction. The metallic phase detection coincides with the halting growth of $Cu_2O$. As the metallic nanoparticles develop, the oxide phase seems to become smaller. The size for the Cu phase can be refined a few minutes from the first detection of the phase starting at around 20nm.

Copper nanoparticle sizes stabilize around 30nm, which is consistent with previous syntheses and in-house XRD measurements for the product of the same recipe. After 1600s, the temperature is raised to 76C in an attempt to speed up the reaction. This in turn leads to a faster reduction of $Cu^+$ as expected.
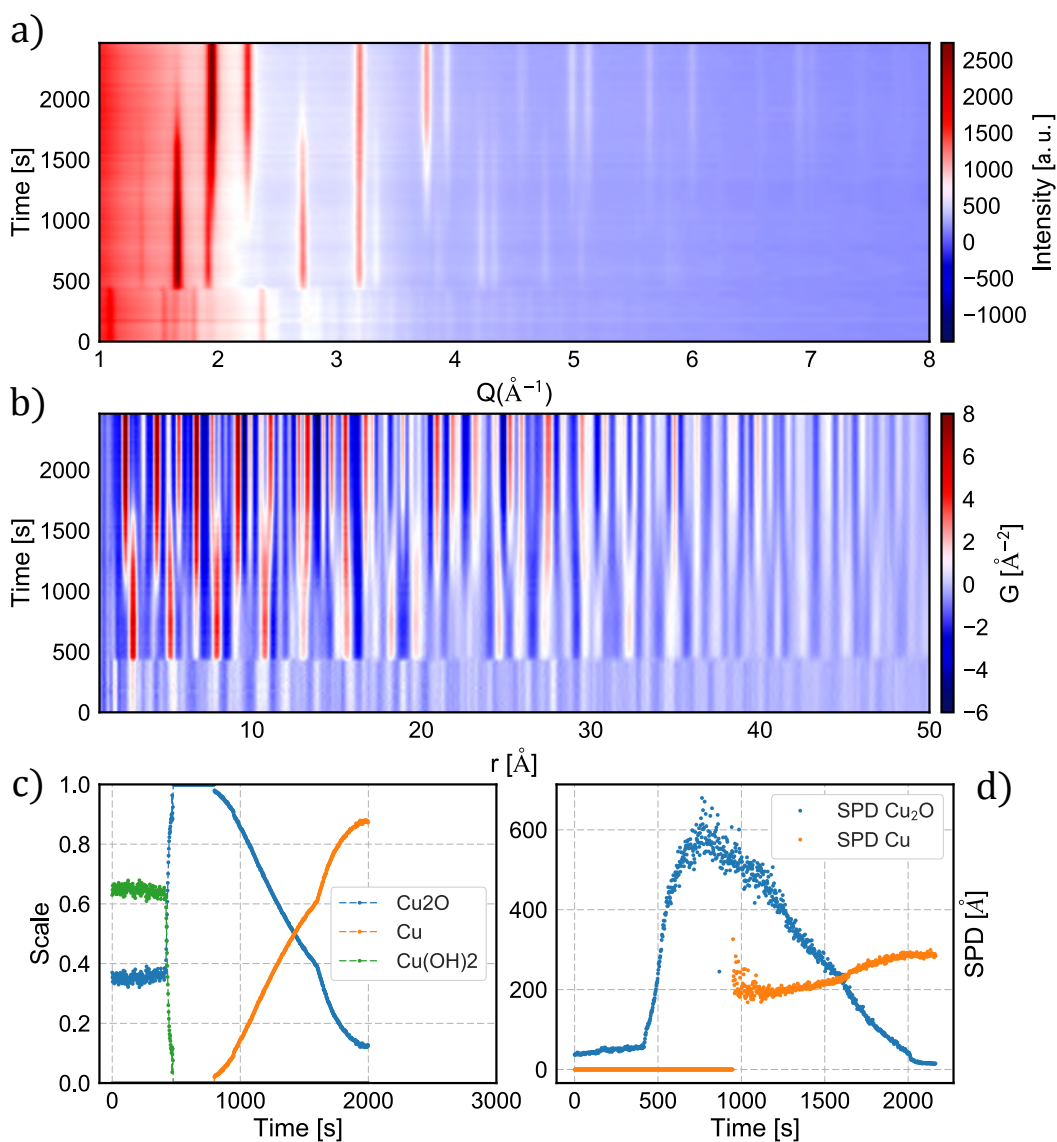
Figure 5.7: Cu 4 reduction synthesis from Cu(OH)$_2$ precursor. a) Waterfall plot of the powder diffraction signal. Cu(OH)$_2$ phase is seen initially, turning into Cu$_2$O and subsequently Cu. b) Waterfall plot of the PDF signal. Changing crystallite sizes can be seen in the extent of the long range order of the G(r). c) Refined scale parameter as a function of time. d) Refined SP diameter as a function of time. Effects of changing temperature are clearly seen in the changing conversion and growth rates.

### 5.3.6   Particle growth and cuprite reduction mechanism

One of the important questions to answer and one of the key reasons for performing the in-situ reduction measurements is to be able to map the mechanism for the conversion from copper oxide to metallic copper.

One way of examining the growth dynamics of the nanoparticles in solution is through the use of Lifshitz-Slyozov-Wagner(LSW) theory[164]. Here we assume that the growth of spherical particles is described by an equation, where the nanoparticles size $D(t)$ at time $t$ is:

$$D(t) = D_0 + K(t - t_0)^{1/x} \tag{5.3}$$

where $D_0$ is the initial particle size, $t_0$ is the time for the initial observation and $K$ is a collection of system specific parameters such as free energy, temperature, liquid properties etc. For a system where the limiting factor for the growth is the availability of the reducing agent near the surface due to diffusion in the mixture, the volume of the particles should increase linearly with time and exponent would be equal to 1/3[165], i.e. $x = 3$. Whereas when the particle growth is limited by the kinetics at the surface, the surface is expected to increase linearly with time, hence $x = 2$[166].

The theory was applied to the measured data for Cu and $Cu_2O$. The results are summarized in Fig. 5.8. The $x$ in the exponent of Eq. 5.3 was fitted to the most stable growing phase of each dataset.

The fit parameter for Cu reduction appears to be close to 2 indicating that the process is limited by the reaction itself and not the diffusion inside the mixture. This is further illustrated in the case for Cu 1 a,b. The growing phase here is the $Cu_2O$. As the temperature is increased, the $x$ value drops. This means that the dynamics shift even further from the diffusion limit. One plausible explanation could be the availability of the reducing agent, i.e. deprotonated glucose. This would become especially relevant in a situation where the reduction or capping processes require one of the oxidized glucose bi-products[150]. The reduction of $Cu_2O$ to Cu appears to follow a similar trend, apart from the case where the initial growth dynamics of appear to be diffusion limited which is seen in Fig. 5.8c). This could potentially be explained by an increased concentration of deprotonated glucose species that are forming while the measurement is being prepared at low temperatures.

One has to be careful in interpreting the results of the LSW model treatment of the data. The constant $K$ is an aggregate of many different phenomena in the reaction an is ultimately an oversimplification of the real system. Particle growth mechanics are very system dependent and thus one should be careful not to use the result as anything more than an indication of where to look when designing a follow up study.

### $Cu_2O$ reduction mechanics

One interesting question which is useful to understand when designing a process is how the reduction of $Cu_2O$ and the formation of Cu particles happens. One could imagine two distinct ways the reaction could happen. A solid state reaction, where the $Cu^+$ atoms are
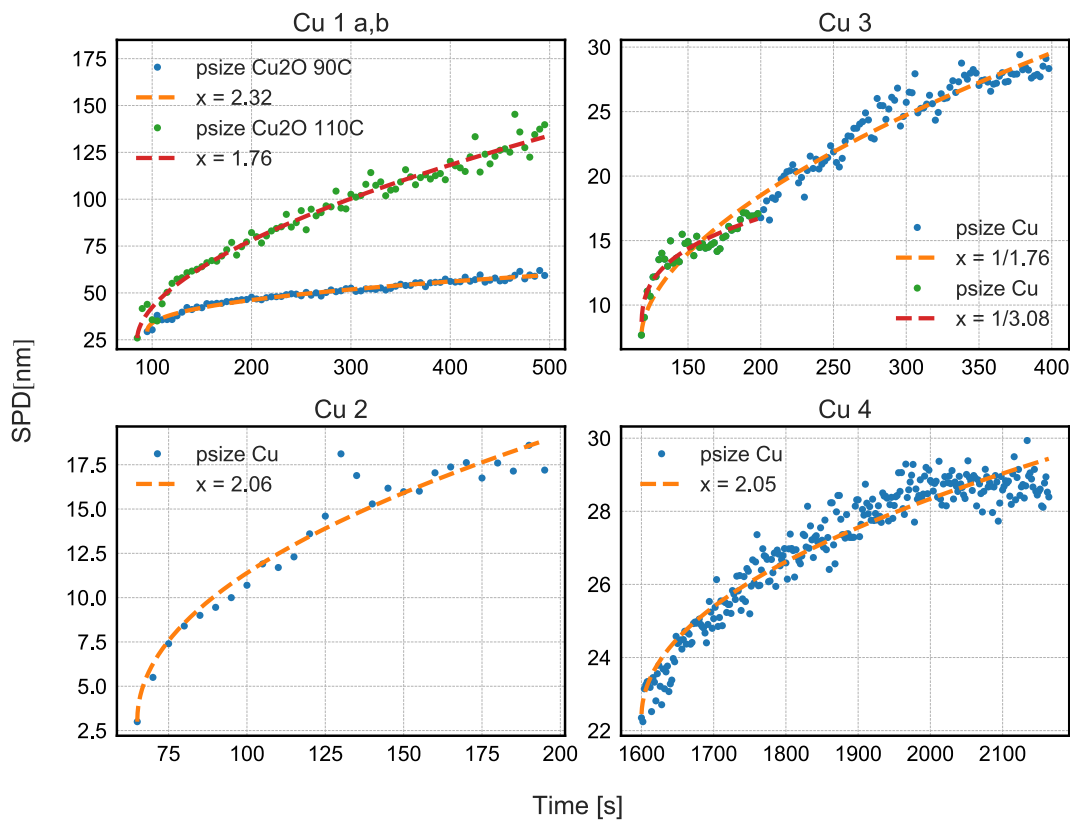
Figure 5.8: Ostwald ripening treatment according to LSW theory for reduction of copper. The findings indicate that the slowest process is related to the reduction itself and could be the reduction rate, oxygen transport or the availability of oxidized glucose species.

reduced to $Cu^0$ and oxygen is simultaneously removed from the system or a dissolution-recrystallization reaction where the large $Cu_2O$ particles dissolve and the freed copper atoms are re-formed into new particles of metallic copper. The solid state reduction is most likely as it is known that copper can be reduced and re oxidized in powder form by flowing Oxygen/Hydrogen gas or when irradiated by UV light[167]. The solid state reduction can also be imagined to happen in two ways. The fist involves the reduction of surface copper atoms which serves as a nucleation site as the oxide nanoparticle is slowly broken down into multiple Cu particles. The other is the reduction and subsequent shuttling of charge into the core and oxygen out of the core of the oxide nanoparticle. In this case the intermediate state would be a core-shell $Cu-Cu_2O$ nanoparticle.

The existing data can't reliably determine the undergoing mechanism based purely on size and phase fraction information. To do this would require very high statistics data with a very high time resolution. If the mechanism goes through a dissolution process, the $Cu_0$ cluster would show up in the residual, provided it is sufficiently different from the oxide phase. Obtaining data of this quality would be difficult.

A more reasonable approach would be to use the sensitivity of PDF to core-shell phenomena[168]. Using the flow-mixing setup one can fix on a certain residence time as the reduction begins to take place, e.g. around 100s from the beginning of the Cu_2

SDS capped synthesis. After obtaining a high quality dataset of that time snapshot, the range dependent refinement would show the two phases existing as either a phase mixture, where pair correlations are only present at the low $r$ range or a core-shell where $Cu_2O$ phase would contain low $r$ and high $r$ correlation while exhibiting a lack of medium range pair correlations. It is important to be aware though that a certain degree of monodispersity is required for the results to be reliable, as a polydisperse mixture will effectively smear out the results across multiple particle sizes.

Notably, the $Cu_2^+ \longrightarrow Cu^+$ reduction appears to be the favorable process in cases where full reduction is possible, i.e. Cu_2, Cu_3 and Cu_4. In each case the growth of the cuprite continues all the way until the appearance of the metallic copper phase, after which the cuprite sizes appear to decrease. If this is indeed the case and the reduction happens as a core-shell solid state reduction then one would expect the final nanoparticle sizes for Cu particles to be roughly equivalent to 3/4 of the oxide nanoparticles due only to the loss of oxygen. The final Cu crystallite sizes in most syntheses appear to be between 1/3 and 1/4 lower than the oxide. Regardless, it would be difficult to imply either mechanism from this fact alone as the particles tend to agglomerate and growth processes such as Ostwald ripening should still take place.

## 5.4 Summary

A synthesis method for well dispersed ink-jettable copper nanoparticles was developed at Danish Technological Institute. The nanoparticles can be obtained from a number of copper oxide compounds using just glucose as a reducing agent. The reaction was optimized extensively such that glucose could completely reduce the $Cu^{2+}$ to the metallic state. The main goals for the optimization were yields and loadings, since higher loadings and high metal recovery rate make the process economical and environmentally friendly. In the end just 4-13 liters of waste water per kilogram of copper nanoparticles are needed, compared to hundreds of liters for previously reported recipes if those were to be scaled up[139, 140, 141, 142, 134, 143, 144, 145].

The reactions were investigated in-situ at a synchrotron facility. A specialized setup was constructed and successfully used, creating a protocol to follow for future studies. Similarly, the analysis pipeline has been developed capable of on the fly visualization. The mapPDF protocol has been customized to work with the copper reduction system and can be effectively used to make fast analysis at the place of experiment in the future.

Metallic Cu nanoparticles need protection from oxidation, otherwise the conductive copper metal turns into an insulating oxide. Lactic acid (LA) was able to protect the particles from agglomerating and oxidizing in the lab, however, because of its acidity, the pH had to be adjusted throughout the reaction. Without the constant adjustment, the reduction to a metallic state stops on $Cu_2O$ phase and this ultimately meant that using LA in a flow synthesis system was impractical.

Using SDS as the capping agent worked reasonably well, however due to it's physical

properties it would have to be significantly diluted or the reaction would have to be performed at high temperatures such that the liquid would not solidify. The dilution increases the amounts of waste water which makes the process less economical and too different from the industrially relevant process.

The realization that the reducing agent or its oxidation byproducts[150] by themselves can serve as just as good surface capping agents allowed us to make the synthesis much more elegant and simple. After significant optimization in the lab, the particles are stable for several months after the synthesis in the native liquid.

The nanoparticle growth for all four recipe iterations was investigated using the LSW theory for Ostwald ripening. The results from all four appear to indicate a reaction limiting effect on growth. It is important to remember that the LSW theory is a very approximate model of the nanoparticle growth and that in the case of the investigated systems includes several phenomena bundled into one fit parameter. The similarity of the result between different capping agents might indicate that the reaction is indeed limited by the reduction mechanics and that the capping agent plays a lesser role in determining the final size of the products in the limit where there is enough capping agent stoichiometrically. Some suggestions for the limiting step could be the deprotonation of glucose in solution or access of the reducing agent to the surface while competing with the capping agent. It would be interesting to determine what oxidation products are present in the solution. One possibility would be to perform a mass spectroscopy study. The mixture of NaOH and glucose was measured as the background solution for the reaction, however, due to the organic nature of the elements present, extracting any useful information is challenging. No obvious changes were detected in the data as it is.

By replacing the $CuSO_4 \cdot 5 H_2O$ precursor it was possible to simplify the reaction while significantly increasing the metal loading. Together with the simplification of the recipe this made the synthesis even more economical and green.

An interesting question still remaining is the mechanism of the reduction process and the degree to which the capping agent and the precursor has the dominating effect on the final nanoparticle sizes. It appears that the formation of $Cu_2O$ happens rapidly upon the initiation of the reaction and it is a more favorable process than the further reduction to a metallic state. The metallic $Cu^0$ presence is only detected after the oxide phase stops growing and after all of the precursors have been converted to $Cu_2O$.

The mechanism of this transformation is unclear. Two possibilities can be suggested. The oxide can be reduced to metallic state through a solid state reaction or by dissolution of the $Cu_2O$ particles and re-formation of the metallic nanoparticles. In lab trials indicate that the size of the precursor powder has an effect on the particle sizes. $Cu_2O$ precursor is typically obtained having larger crystallites and the corresponding agglomerates are typically larger than those formed from the ionic $Cu^{2+}$ form. To clarify this, a set of experiments could be performed where the precursor can be ground by ball milling to a variety of sizes and the synthesis repeated comparing the product.

The question about the structure of the solvation clusters of different precursors remain

and needs further analysis. The data from the $CuSO_4 \cdot 5\,H_2O$ indicates a six fold coordination structure that consists of extending units judging from the extent of the pair distances in PDF. The data quality justifies additional efforts into the solution of the cluster structure, however, due to a large degeneracy when dealing with cluster structures, additional constraints are needed. Raman of NMR experiments should be considered in addition to performing a series of control experiments with other copper salts and different ligands. The models for four fold and five fold coordination geometries should also be tested.

In the end, the equipment and analysis work flows for future experiments was successfully developed. PDF analysis can be of great help to guide the optimization of the large scale synthesis. However it suffers from the availability of the experimental time and would typically require a large time investment for analyzing the data. This in turn makes the analysis lag behind the process development, where progress can be achieved by trial and error. The automation of the data analysis helps these issues a great deal, however, using this type of analysis as a primary tool for process development might be unwise. In-situ studies are much better used for gaining a deeper understanding of the process once optimization phase has been reached.

# 6

## Supercritical Flow Synthesis of Cost-effective PtPdFe Nanoparticles for Low-Temperature Diesel Oxidation

This chapter will present the results from characterization of the PtPdFe nanoparticles some of which are about to be published in H. Silva, et al.[2]. The study presents a novel cost efficient and green synthesis method for large scale production of Fe doped PtPd nanoparticles that have a higher catalytic activity than conventional PtPd catalyst. The nanoparticles are synthesized on $\gamma$-Al$_2$O$_3$ support, which is notorious for its structural disorder. The nanoparticles are around 2nm in diameter and the total loading on the support is around 1%$wt$, which makes the structure of the catalytic material difficult to analyze using in-house equipment. Through indirect means, we are able to show that Fe doping creates an alloy with PtPd leading to lattice compression, which in turn affects the catalytic properties of the material.

The text will explain the conclusions of the study in greater detail, and in addition, outline further analysis that never made it into the original manuscript. The findings support the original conclusions, while still leaving some questions unanswered. The strategy for how to address the arising questions and avoid the limitations of the employed methods is also suggested.

## 6.1 Motivation

The push towards improving the diesel oxidation catalyst (DOC) is highly motivated by the increasing emission standards for diesel vehicles. Strict limits on nitrogen oxides (NOx), carbon monoxide (CO), unburned hydrocarbons (HC, e.g. propene) and particulate matter concentration levels require the DOC to perform in a wide range of operating conditions. These include cold-start phase for low temperature operation under 200 °C, through to high temperature stability of around 750 °C for particulate matter regeneration cycles. The presence of water and an oxygen rich atmosphere complicates the process even further as it accelerates the sintering rate of the well dispersed nanoparticles through Ostwald ripening mechanism as the temperatures increase beyond 300 °C [169],[170]. This limits the number of materials that would meet specifications essentially constricting the choice to noble metals for active phase composition, as their resistance to oxidation and thermal stability play a key role in creating a long-term durable DOC.

Platinum (Pt) and its bimetallic combinations with other metals such as palladium (Pd) are already used commercially[171],[172]. Maximizing the surface area, they are produced as fine nanoparticles on high surface area metal oxide washcoats such as γ-Al2O3[173]. The alloy of PtPd is created as PdO is formed on the surface of the Pt nanoparticles in oxygen rich environments. The mobile atomic species of platinum are subsequently trapped forming the alloy[174][175]. Due to the presence of oxide at the surface, the alloy nanoparticles are less susceptible to sintering as compared to pure platinum[176][177]. Ward et al[178] also reported on a real road-aged DOC, where the formation of PtPd alloyed nanoparticles with random composition and a minor fraction with core-shell structures had a higher retention of spherical particles. Another positive effect of incorporating Pd into the catalyst is the improved activity for HC and CO oxidation compared to a monometallic Pt system, even before aging[171],[179],[180].

Originally, the advantages of using Pd in the DOC also came with an economic advantage of reducing Pt costs. However nowadays, due to an increase in demand in the recent years the price for both metals is largely the same[181]. The discovery of novel catalytic systems that live up to the ever increasing demands in terms of performance while decreasing the cost is of high industrial relevance.

From an economic perspective, iron (Fe) is attractive to incorporate into the DOC and has been tested previously[182][183]. Despite the improved thermal stability explained by the formation of $Fe_2O_3$ layer on the particles, these have shown lower activity when compared to pure Pt systems[184]. The temperature at HC half conversion (T50) of a catalyst with 1.1 wt.% Fe and 3.7 wt.% Pt was ca. 300 °C, after aging in 7.5 % O2 at 800 °C/5 h, far from the low-temperature targets recommended by the U.S. department of energy (DOE): T50 < 150 °C [185].

PtFe alloys have also been reported outside the DOC applications. For CO oxidation, cluster structures of PtFe on $SiO_2$ supports have been reported[186], as well as bimetallic alloys[187] and metal-oxide mixtures[188]. Additionally, iron oxide can help protect the
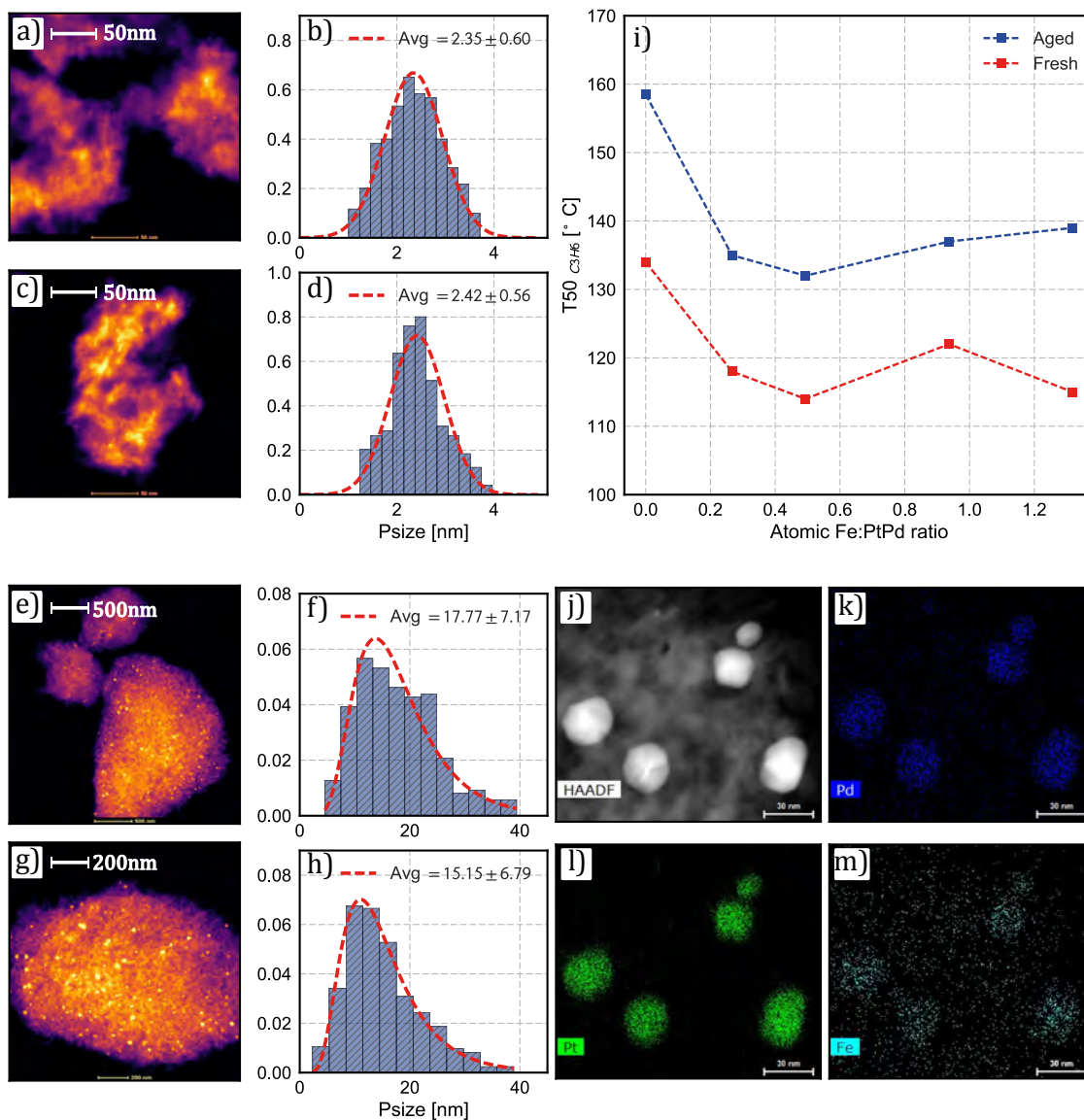
Figure 6.1: HAADF STEM imaging of the PtPd and PtPdFe material. a),b) PtPd fresh, c),d) PtPdFe fresh, e),f) PtPd aged, g),h) PtPdFe aged. Particle size estimation through particle counting. Fe doped samples appear to have a lower average particle size. i) Half conversion (T50) temperature of the catalytic material from the cost series. j)-m) HAADF STEM EDX mapping showing the concentration of Pt, Pd and Fe across the measured sample area. Pt and Pd are localized on the nanoparticles, Fe is mostly localized on the nanoparticles with a portion of iron in the support material.

active metal sites by oxidizing $SO_2$[189][190] which serves as a poisoning agent.

Highly active and stable PtPd/$\gamma$-Al2O3 and PtPdFe/$\gamma$-Al2O3 catalysts for diesel oxidation applications was produced using supercritical flow technology at the Danish Technological Institute[2, 191]. The process allows the productions of well dispersed nanoparticles with a narrow size distribution around 2-3nm and at high throughput rates. This type of product is notoriously difficult to obtain using conventional laboratory methods such as impregnation and is significantly cheaper than comparable techniques that allow for precise control of nanoparticle size[192][193].

The catalyst was characterized for HC oxidation and showed an improvement in the temperature of half conversion of 115°C compared to 135°C for reference PtPd catalyst. In addition, by replacing the PtPd content by iron, the use of precious metals can be reduced by up to 33% while improving the activity. The exact structural effects of the Fe addition into the catalyst are not known, however. This study attempts to address that by examining the material in its fresh and aged states, using the Pair Distribution Ffunction(PDF) analysis, which is an especially strong method for characterizing nanomaterial of this scale[194]. The catalyst is characterized both in the production form on $\gamma$-$Al_2O_3$ support and later a model system on graphitized carbon.

## 6.2   Synthesis of catalyst materials

PtPd and PtPdFe nanoparticles were synthesized using a pulsed flow reactor designed and built at the Danish Technological Institute, shown in Fig.6.2. The system is automated and allows for precise control of the reaction conditions during the synthesis. A multitude of sensors monitor temperatures, pressures and flow rates at all critical points in the system allowing for high degree of reproducibility from one synthesis to another.

PtPd and PtPdFe nanoparticles were synthesized through a reduction of $FeCl_3\cdot 6H_2O$ and $H_2PtCl_2\cdot 6H_2O$ metal salt precursors on $\gamma$-$Al_2O_3$ or graphitized Carbon powders acting as the support material in supercritical ethanol. The precursor mixture which contains the metal salts and support material is continuously stirred during the synthesis in a vessel at the intake of one of the pumps. The mixture is then pumped into the reactor at ambient temperature. Inside the reactor, the precursor mixture meets supercritical ethanol, which then acts both as a solvent and as a reduction agent. Because of the rapid mixing and rapid heating of the reactants, the nucleation of the nanomaterial is instant and homogeneous. The resulting nanoparticles are well dispersed on the support material and are highly crystalline.

To obtain a particular size for the nanoparticles, the material travels through the reactor while being kept at a consistent temperature and pressure before being cooled down where the growth is mostly quenched at the end of the run. The residence times for these reactions are typically on the order of few seconds to a couple minutes.

The PtPd and PtPdFe nanoparticles were allowed to mature inside the reactor at 280bar at a temperature of 300°$C$. The products were then collected and washed with water by
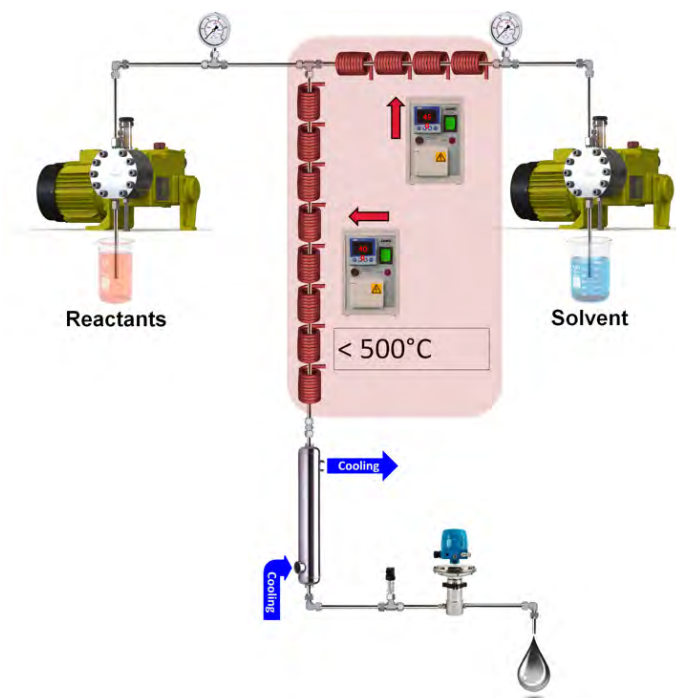
Figure 6.2: The supercritical reactor. The layout allows for separate pumping of the precursor mixtures and the solvents. The system is automated and can be precisely controlled. Reproduced from [2]

means of centrifugation and dried at ambient or close to ambient conditions inside an oven.

Two sets of samples on $\gamma$-$Al_2O_3$ were produced. The first set attempts to optimize the use of precious metals and is replacing the content of the PtPd by Fe, codenamed "Cost optimization series" or "cost series" short. The results from the study of this set are published in H. Silva, et al.[2]. The second set of samples on $\gamma$-$Al_2O_3$ was produced as control and simply adds Fe into the system and is referred to as "doping series". Both sets have metal loadings on the order of $1\%wt$. These are summarized in Table. **??**. The samples produced on $\gamma-Al_2O_3$ were additionally aged in the static oven in an oxygen rich atmosphere at 750°C to simulate aging as in real applications.

## 6.3 Experimental methods

The synchrotron x-ray powder diffraction measurements for the "cost series" were performed at P02.1 beamline at PETRAIII, DESY, Germany. The diffraction experiments were performed in transmission geometry using the Rapid Acquisition PDF method[122], where the diffracted signal was collected using a 2D Perkin-Elmer detector at a distance of 200mm. The incidence wavelength of the x-ray beam was 0.2072Å with a beam cross-section at the sample of 0.5mm in the vertical and the horizontal direction. A reference background measurement was collected alongside the other samples in the series. All measurements were performed at room temperature. The experimental geometry parameters were calibrated before data reduction using $LaB_6$ powder diffraction standard.

The "doping series" and the model system on carbon supports were measured at 11ID-B beamline at Advanced Photon Source at ANL, Chicago, USA. The measurements were performed in transmission geometry while packed into capillaries at a sample to detector distance of around 177mm. The wavelength for the experiment was 0.2113Å giving an effective $Q_{\max} = 25$Å$^{-1}$. The beam size was 0.5 mm in both horizontal and vertical direction. Calibration was obtained using $Ce_2O$ and NIST Si powder.

## Difficulties in background subtraction and background subtraction optimization

$\gamma$-$Al_2O_3$ is notoriously difficult to work with in PDF analysis. It has a disordered local structure[195] and a nanocrystalline microstructure[196]. In addition chemical modification of this support material is likely. A number of structural models has been proposed, for both local[197] and average structures[198]. The subtraction of the alumina signal from the total scattering pattern is therefore problematic and several strategies were employed and their results compared.

Upon deposition of the alloy the perceived crystallite size of the alumina support changes, and the reference material appears more crystalline. For the fresh catalyst this means that the optimal background subtraction would be done in real space, where the coherence length of the support is greater than that of the nanomaterial. On the other hand, for the aged samples, the best background subtraction is achieved by fitting the support data to the material in reciprocal space, since the signal emanating from the nanoparticles is much stronger and provides a clear visual guide for background scaling.

| Name | (Pt) (wt%) | (Pd) (wt%) | (Fe) (wt%) | PtPd:Fe ratio (atomic) |
|---|---|---|---|---|
| Cost series, $(PtPd)_{x-y}Fe_y /\gamma Al_2O_3$ | | | | |
| $PtPd_{0.75}$ | 0.65±0.07 | 0.10±0.01 | - | 0 |
| $PtPd_{0.70}Fe_{0.05}$ | 0.58±0.02 | 0.13±0.03 | 0.06±0.02 | 0.266 |
| $PtPd_{0.65}Fe_{0.10}$ | 0.51±0.02 | 0.13±0.03 | 0.11±0.01 | 0.49 |
| $PtPd_{0.55}Fe_{0.20}$ | 0.45±0.05 | 0.11±0.03 | 0.18±0.02 | 0.93 |
| $PtPd_{0.50}Fe_{0.25}$ | 0.40±0.02 | 0.05±0.02 | 0.19±0.02 | 1.31 |
| Doping series, $(PtPd)_x Fe_y /\gamma Al_2O_3$ | | | | |
| $PtPd_{0.75}$ | 0.71±0.04 | 0.10±+.02 | - | - |
| $PtPd_{0.70}Fe_{0.05}$ | 0.58±0.03 | 0.066±0.05 | 0.12±0.01 | 0.59 |
| $PtPd_{0.65}Fe_{0.10}$ | 0.68±0.04 | 0.08±0.01 | 0.19±0.1 | 0.79 |
| $PtPd_{0.55}Fe_{0.20}$ | 0.71±0.04 | 0.053±0.04 | 0.31±0.02 | 1.33 |
| $PtPd_{0.50}Fe_{0.25}$ | 0.67±0.03 | 0.063±0.04 | 0.70±0.00 | 3.09 |

Table 6.1: Overview of the samples measured together with SEM EDX information. All samples were measured in both fresh and calcined states. All samples are on $\gamma-Al_2O_3$
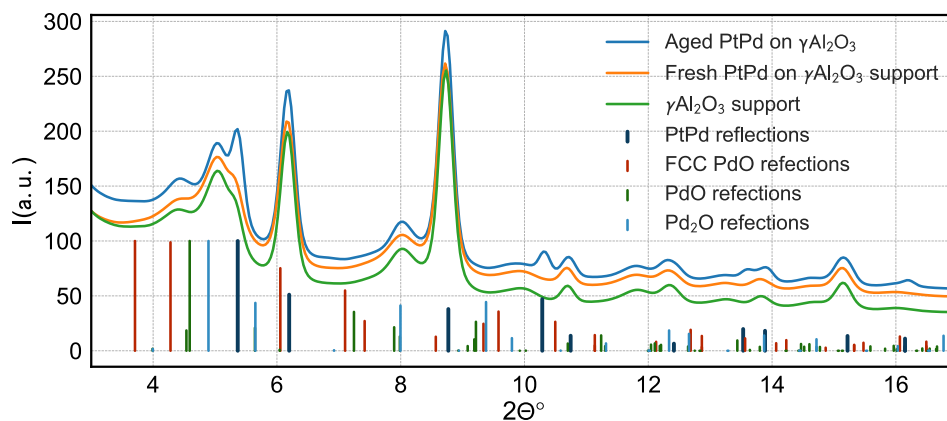
Figure 6.3: X-ray diffraction data from the fresh and the aged PtPd$_{0.75}$ sample overlayed with the scattering signal from the $\gamma-Al_2O_3$ and the simulated phases for common PdO and PtPd alloy. Scattering from the PtPd particles can clearly be seen in the aged sample and aligns well with the expected PtPd alloy.

## 6.4 Effects of Fe doping

A total of 19 synthesis products were studied, including the six on carbon support. To examine the effects of Fe addition into the system, the samples were examined using a combination of complementary techniques. The results of propene oxidation measurements shown in Fig. 6.1i) are a sign of a modification that can be attributed to the Fe doping. First, the the elemental compositions were confirmed using STEM-EDX and the results are summarized in Table. **??**. The results were in line with expectations and are within the tolerated variability of the synthesis and without presence of contaminants that might introduce uncertainties into the interpretation of mechanics of the system.

### 6.4.1 X-ray diffraction

All samples were measured at a synchrotron source with data collected appropriately for both Rietveld refinement study and PDF analysis.

No signs of PdO was found despite the aging procedure happening in the presence of oxygen. The Bragg peaks of the aged material aligns well with PtPd, indicating presence of the expected alloy. This is illustrated in Fig. 6.3. From Rietveld refinements of the PtPd phase the crystallite sizes for aged particles were found to be around 16nm and are consistent with the HAADF-STEM imaging of the samples, shown in Fig. 6.1.

In addition, as shown in Fig. 6.3, the fresh nanoparticles are too small to be reliably quantified by a Rietveld refinement. The small nanoparticles can be instead studied using PDF analysis.

For the samples containing Fe, no diffraction signal that can be attributed to a iron containing phase was observed. This suggests that iron exists in the system as either an amorphous or nanocrystalline phase, or could exist as an alloy with Platinum and Palladium, as observed previously by V.I.Kovalchuk, et al.[199].
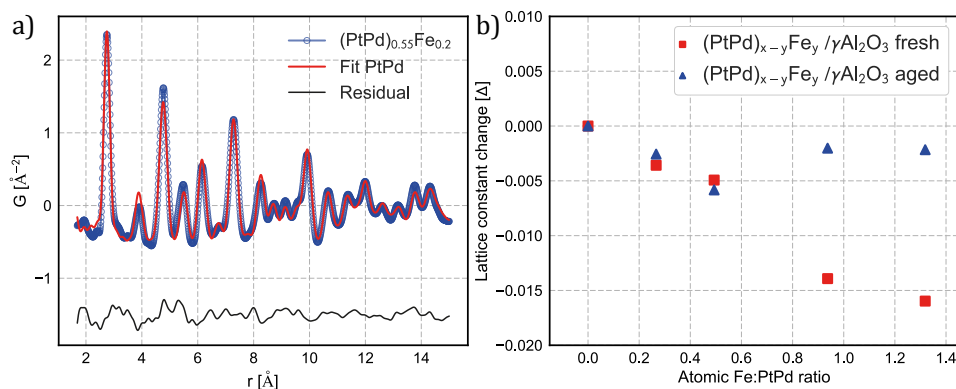
Figure 6.4: a) PDF fit of a spherically attenuated FCC model with agreement factor $R_w = 17\%$. b) Lattice parameters from the background subtracted datasets for PtPd and PtPd:Fe revealing a trend of lattice contraction as result of Fe incorporation. Surprisingly, the lattice constant of the aged samples appears to expand back for Fe doping ratios close to one and above, possibly due to formation of iron oxide.

### 6.4.2 PDF analysis of the fresh PtPd and PtPdFe catalysts on $\gamma Al_2O_3$

The fresh PtPd$_{x-y}$Fe$_y$ /$\gamma$Al$_2$O$_3$ catalysts from the cost series are analysed using PDF analysis[200]. The diffraction signal due to $\gamma-$Al$_2$O$_3$ was subtracted from the total scattering pattern leaving only the scattering intensity from the catalytic nanoparticles as described in Section. 6.3. Azimuthally integrated intensity data were transformed to G(r) with $Q_{\min} = 0.46$Å$^{-1}$ and $Q_{\max} = 20$Å$^{-1}$ for the data obtained at P02.1, PETRA III ensuring the best compromise between resolution and noise. A spherically attenuated FCC bulk model of space group $Fm-3m$ for PtPd alloy and PtPdFe alloy were refined constraining the chemical composition to the stoichiometry obtained by STEM-EDX. The weighted agreement factors were typical for this type of analysis of $R_w$= 0.16 to 0.21.

For the fresh alloys the refinement results also show that the simple model was sufficient to describe all of the major features present in the data as shown in Figure 6.4a). Lattice parameters extracted from the refined models are summarized in Figure 6.4b) and reveal a decreasing trend as the amount of Fe in the system increases. As no features indicating oxide phases were observed, the decreasing lattice parameter trend suggests alloying of Fe into the PtPd lattice by dissolution or substitution, and is a result of the smaller atomic radius of Fe[201][184]. Notably, the decrease of the lattice constant is significantly smaller than expected for an alloy where all of the Fe is substituted into the lattice based on Vegard's law[202]. Nanoparticle crystallite sizes were extracted from the spherical particle attenuation function and were around 2nm which is consistent with HAADF-STEM imaging results, as seen in Fig. 6.1. As a consequence of imperfect background subtraction, the crystallite sizes cannot be determined with a higher reliability to compare the samples within the set.

Due to difficulties when examining highly scattering supported nanomaterial with x-rays, the presence of an additional Fe phase cannot be completely ruled out, yet the findings suggest that the nanoparticles consist of a majority nanocrystalline FCC phase.
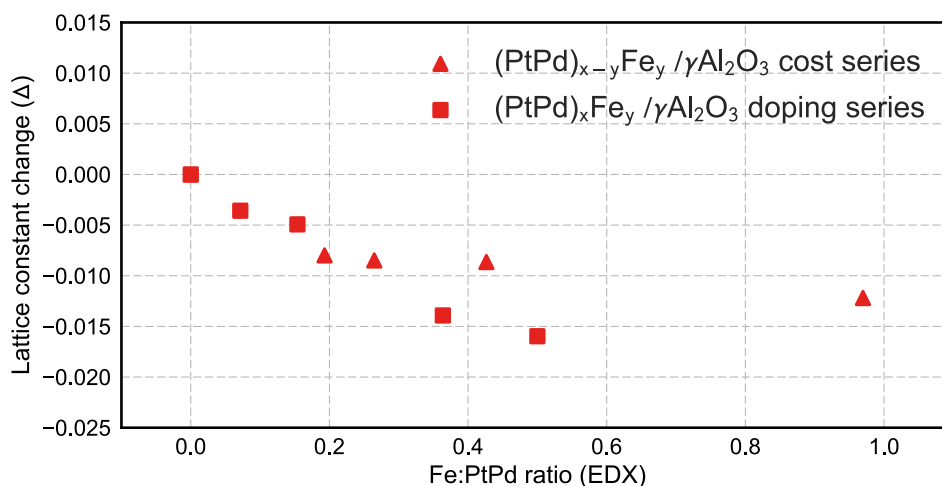
Figure 6.5:   A combined plot of the change of lattice parameter as a result of increasing the content of Fe. The two sample sets line up, supporting the argument that adding iron into the system leads to lattice contraction.

Following the analysis of the cost series, the remaining fresh samples on $\gamma-Al_2O_3$ from the doping series were analyzed using the same approach and the results were combined in Fig. 6.5. The lattice parameters from both experiments were normalized to a pure PtPd sample of the each set and collated as shown in figure 6.5. The lattice shift trends from both datasets fit together well indicating once again the likely formation of an alloy. It is important to note, however, that nanoparticle with sizes under 10nm experience lattice contraction due to the increasing surface area of each particle[203]. Thus possibility that the lattice contraction is happening due to overall smaller sizes because of iron doping needs to be considered.

### 6.4.3   Effects of Fe doping on aged catalysts on $\gamma$-Al$_2$O$_3$

The aged samples of $(PtPd)_{x-y}Fe_y$ are remarkable as they do not preform worse than the similarly aged conventional PtPd alloy, as opposed for PtFe alloys after aging[184]. The PDF treatment of the aged samples was performed similarly to the procedure used for the fresh samples as is summarized for the cost series in Fig. 6.6. Initially, they exhibit the same trend during the addition of iron into the system, indicating alloying in the same way as for the fresh particles. The last two data points deviate significantly from the trend, and that is also reflected in the catalytic activity as shown in Fig. 6.1. Whether this effect is a variation during synthesis and aging process or an effect of iron content reaching a critical limit and segregating into a $Fe_2O_3$ phase is difficult to establish[184]. It is, however, noticeable that the lattice constant shifts to a lower value for all samples with iron doping. Extracting the spherical particle diameter from the model also gives an indication of the crystallite sizes within the system. These results are summarized in Fig. 6.6 and show a systematic decrease in the crystallite size as soon as Fe is added to the system, which is consistent with both the Rietveld refinement results and the HAADF-STEM estimates
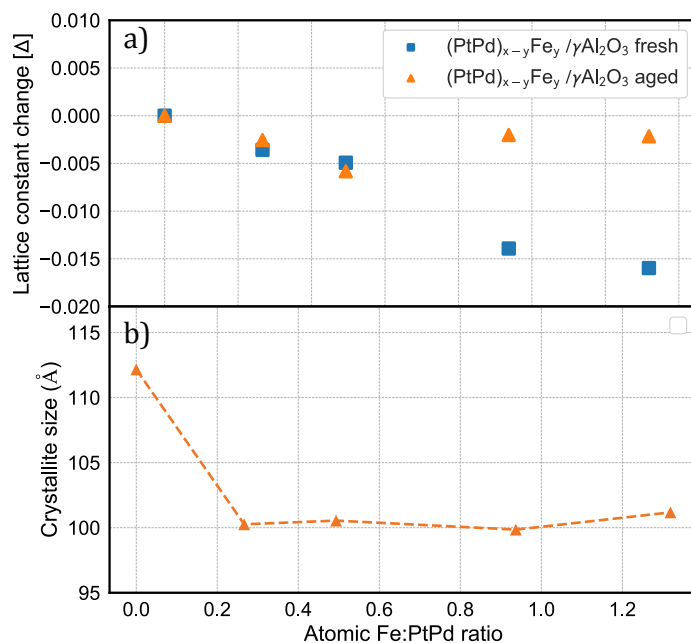
Figure 6.6: a) The lattice constant extracted from an FCC model of a PtPdFe alloy refined to the aged samples datasets and overlayed with the fresh. b) SP Diameters extracted from the models for the aged samples.

shown in Fig. 6.1. The Fe appears to inhibit crystallite growth during the aging process. The obtained crystallite sizes are slightly lower than those obtained from Rietveld and TEM. This is typical for PDF analysis and is usually a result of surface disorder and shape dependent properties of the particles[74].

Examining the G(r) can provide some additional insight into the system. The aged particles are much larger than the fresh, and as such have a much higher signal to noise ratio when subtracting the support. As a result, it is possible to look for the presence of undescribed features in the data and see if any of them correlate with a potential Fe phase. Fig. 6.7a shows the raw G(r) for all samples in the set scaled to pure PtPd on $\gamma-Al_2O_3$. Seen at around 1.9Å, 3.3Å and 4.6Å are features that appear to change as a function of the amount of Fe in the system. These distances can be traced back to a number of Fe oxides. Segregation of hematite ($Fe_2O_3$) phase during aging was previously reported for PtFe alloys as small particles or a thin layer on the surface of the nanoparticles[184]. The pair correlations seen in the data are consistent with many of the nearest neighbor Fe-O distances within a hematite unit cell. No Fe oxide phase could be successfully refined to the data, ruling out any hematite nanoparticles of significant size forming on the support. The features themselves are a somewhat questionable indicator of an iron phase component as it is possible to find irregularities as the r increases. The irregularities could be a good indicator of the features originating due to residual noise from the alumina subtraction, i.e. a change in the structure of the alumina that is unaccounted for by the background measurement or the formation of the $Fe/Al_2O_3$, which would also fit with the distances for hematite.
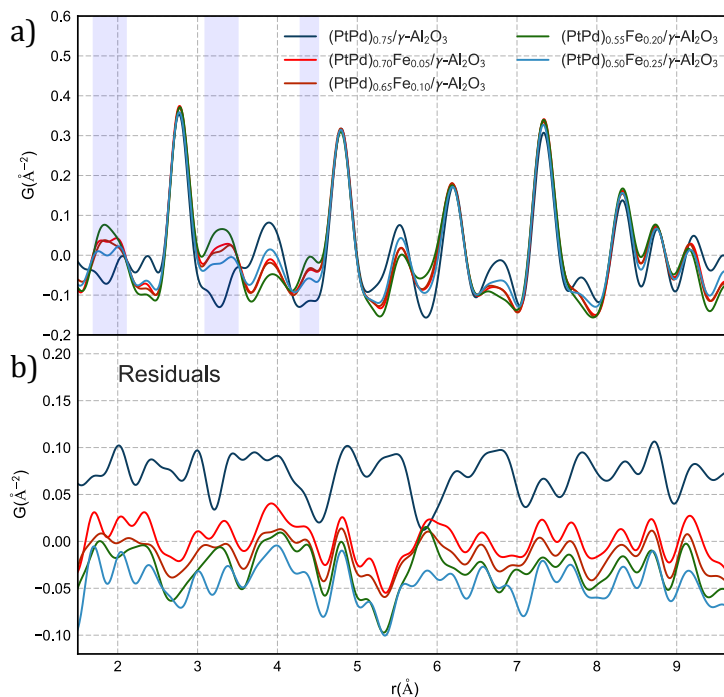
Figure 6.7: a) Raw background subtracted G(r) from the aged cost series. Highlighted regions show correlations that could be attributed to an iron phase. b) Residuals from an FCC model fit to the G(r) above. The residual from the PtPd sample is significantly different to those from PtPdFe samples.

The iron doped samples are clearly systematically different to the samples with pure PtPd. Such systematic difference can be seen when comparing the residual of the pure PtPd sample to the ones with Fe doping. As is seen in Fig. 6.7b), the PtPd residual is significantly different to the ones from the iron doped samples. The residuals were tested through structural refinements for Fe and its oxide phases. None of the tested structures gave a positive match again ruling out a formation of a significant amount of iron containing phase. This is not unexpected, as the original models used to obtain the residual are refined to best fit the data and would scale and stretch the simulated G(r) to optimize the $R_w$. This observation is not necessarily expected to explain the cause behind the difference in catalytic activity and the size distributions within the material.

The addition of iron is the most significant difference between the samples. As a result, to find answers to the questions posed above more research into the Fe content itself is needed. The problem with PDF analysis of this type of material is an inherent property of any x-ray diffraction technique, namely x-ray interaction with matter and the resulting contrast. In this system the amount of material of interest is extremely low on the order of 1%wt. In addition, the scattering power from Pt and Pd is much higher than that of Fe. This means that most reliable results from x-ray diffraction are those seen indirectly through shape, size or crystallographic changes within the material. For further study, spectroscopy type techniques such as EXAFS and XANES would be needed due to their elemental specificity. The ability to determine the coordination environment of the Fe

atoms and its oxidation state would help to clarify whether it is present as part of an alloy or as an oxide. The main difficulty in this case would be the presence of $FeAl_2O_3$[183], indications of which are seen in Fig. 6.1m), which is likely to dominate the iron signal. In this case looking for signatures of metallic iron would be the easiest way to confirm the formation of an alloy. If the iron is present as an oxide layer on the larger particles after aging, as is possibly the case with the aged particles with the highest doping, a state of the art XPS measurement could be performed. Though it might be incredibly difficult due to low loadings and presence of alumina support.

## 6.5   Model system - PtPd Fe on graphitized carbon supports

The biggest difficulty in studying the $(PtPd)_{x-y}Fe_y$ /$\gamma Al_2O_3$ system has consistently been the presence of the $\gamma Al_2O_3$ support. Due to the support material chemically changing during synthesis and due to its similarity to iron oxide, it has been difficult to isolate the effects of Fe doping on the system without fighting the experimental noise. This problem can be addressed by attempting to replicate the material on a substrate that is much easier to work with and then use that as a model system for the commercial material.

Carbon black materials are known to be excellent supports for catalytic materials[204] as they possess high surface area, good electrical conductivity, form porous networks and are sufficiently corrosion resistant in a typical catalysis environment. They are also low cost and are widely available[205]. Most importantly, they have been used extensively for well dispersed Pt based fuel cell catalysts[206][207]. Unfortunately, carbon supports cannot survive the upper operation range of the DOC which only allows to study the fresh catalyst. The decision was made to make a series of samples on carbon black support materials. For the model system a sample of the best performing composition was chosen.

### 6.5.1   PDF measurements

Similarly to the previous samples in this chapter, the samples on carbon supports were measured packed in kapton capillaries in transmission geometry using the RAPDF method[22] at beamline ID11-B at APS, ANL. Measurements were done in close proximity to the detector at the energy of 59.6KeV, giving a maximum resolution of $Q_{\mathrm{max}} = 24 \text{Å}^{-1}$.

### 6.5.2   Carbon supports

The samples were synthesized on three different commercially available support materials: Vulcan X72, Ketjenblack KB300 and Ketjenblack KB600 with a surface area of $787 \mathrm{m}^2/g$, $1270 \mathrm{m}^2/g$ and $1530 \mathrm{m}^2/g$ respectively, as measured by BET. The synthesis was carried out as described in section 6.2. The carbon powders were measured as background supports for studying PtPd nanoparticles. Their $I(Q)$ patterns are similar, with the main difference being the width and intensity of the [002] reflection at $Q = 1.75 \mathrm{nm}^{-1}$. The three $I(Q)$ scattering profiles normalized in the $Q > 2.5 \mathrm{nm}^{-1}$ region and the G(r) patterns can be seen in Fig. 6.8b) and Fig. 6.8a) respectively. The specifications for these supports state
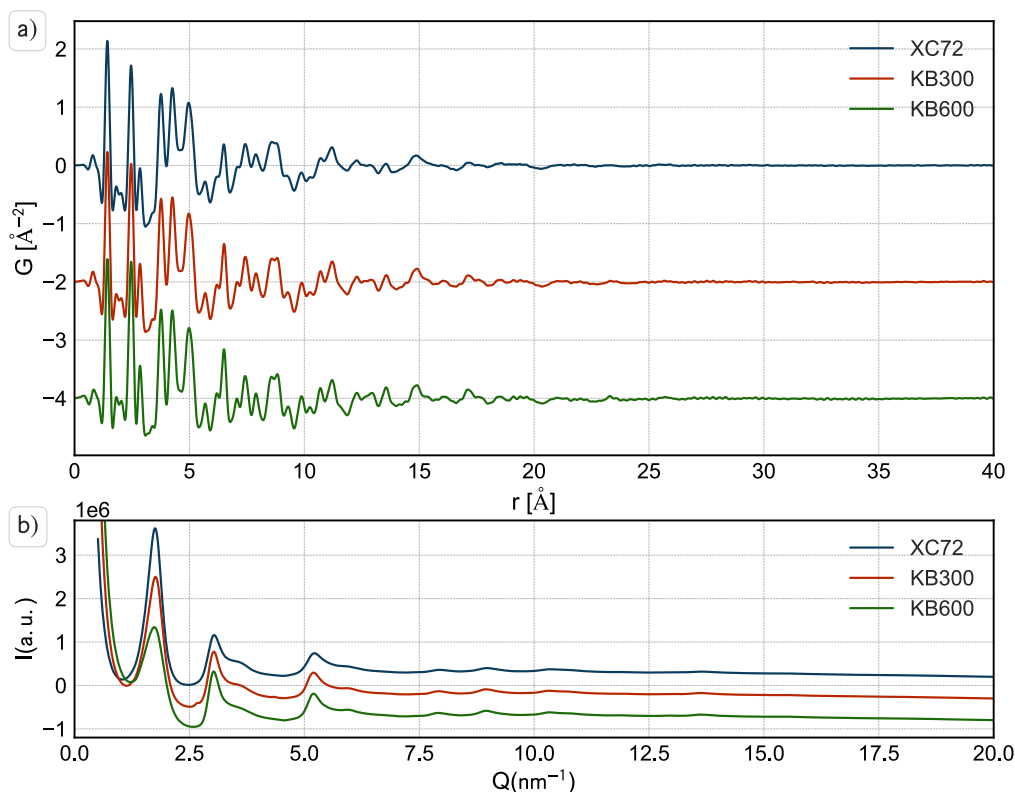
Figure 6.8: Vulcan X72, Ketjenblack KB300 and Ketjenblack KB600 carbon substrates. a) The G(r) of capillary subtracted support. b) I(q) of capillary subtracted support, normalized for $Q > 2.5nm^{-1}$. Low scattering cross section and wide features of these supports make the material ideal for working with PDF studies of supported nanomaterials.

different density and surface area, yet in PDF it is clear that all three are built up of the largely identical carbon subunits of around 2nm in size.

The wide features and low scattering cross section of these supports makes them ideal for studying supported nanoparticles using PDF techniques. The background subtraction even for very small nanoparticles yields a very clear signal of the material of interest.

### 6.5.3 Initial data analysis

Eight samples were made total. Four on on Vulcan X72, samplesD46 and D47, D53 and D54, two on Ketjenblack KB300, samples D49 and D50 and two on Ketjenblack KB600, D51 and D52. The syntheses were aimed for a stoichiometric atomic ratio of PtPd to Fe of 0.5, i.e. $Pt_{0.56}Pd_{0.14}Fe_{0.30}$ in terms of wight fractions with a total metal loading of 1wt%. Iron doped samples are D47, D50, D52 and D54. Samples D46, D49, D51 and D53 contain 1wt% $Pt_{0.8}Pd_{0.2}$ at a ratio of 1:5.

The presence of PtPd alloy was confirmed using powder diffraction spectra as can be seen in Fig. 6.9. The alloy appears nanocrystalline and can be clearly seen on the raw XRD spectrum as opposed to similar datasets of fresh catalyst material on $\gamma Al_2O_3$ as shown previously in Fig. 6.3. The low scattering cross section of carbon support allows for a clear identification of the PtPd phase even on an in-house XRD system, shown in Fig. 6.9.
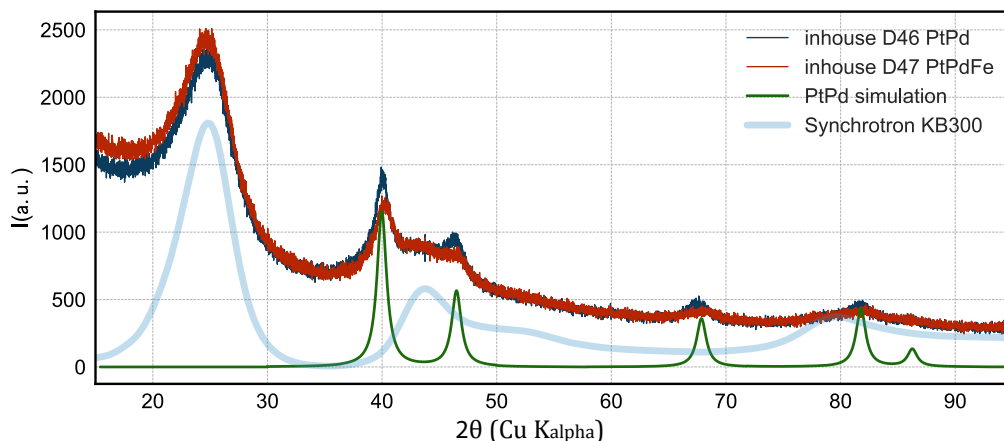
Figure 6.9: XRD patterns for sample D46 and D47 overlayed with KB300 and a simulation of an FCC PtPd crystal. Clear FCC peaks are seen in the datasets with nanomaterial.

The crystallite size for these nanoparticles from Rietveld refinements of the in-house data appears to be around 3.3±0.5nm, but cannot be relied upon as this type of refinement is inadequate for nanoparticles of this size. A more accurate estimation can be obtained from PDF technique.

### 6.5.4 Virtual crystal refinements for PtPd and PtPdFe on carbon supports

The scattering signal from the capillary enclosure and the support was subtracted from the data and the structural refinements resulting to the G(r) were performed using PDFGui program. The results are summarized in Fig. 6.10. A single phase FCC model would provide the simplest description of the system. However, it only described the data up to around 30Å, after which it broke down. Interestingly, the SPD estimate from a 1 phase model is between 40Å-25Å and is very close to the ones obtained by Rietveld refinement for the same dataset.

A more accurate description was obtained by refining a two phase mixture of FCC PtPd alloys where one is refined from 15Å to 75Å and the other for the local structure from 1Å to around 20Å. After the initial refinements the two phases were left unconstrained and allowed to reach a common minimum. The nanoparticles sizes obtained from a two phase model were around 22Å for the local phase and between 80-90Å for the long range average phase.

The validity of the two phase model is confirmed from the TEM imaging of the samples and reveals a bi-modal size distribution with the majority of material existing as 2-3nm nanoparticles with some particles of larger sizes typically around 8-10nm. Thus the PDF size estimates are close to the sizes obtained from TEM measurements. A better description could potentially be obtained by fitting a size distribution attenuation function such as a LogNormal[45], rather than the spherical attenuation function that gives an excellent size estimate only for monodisperse spheres. Care has to be taken when discussing lattice
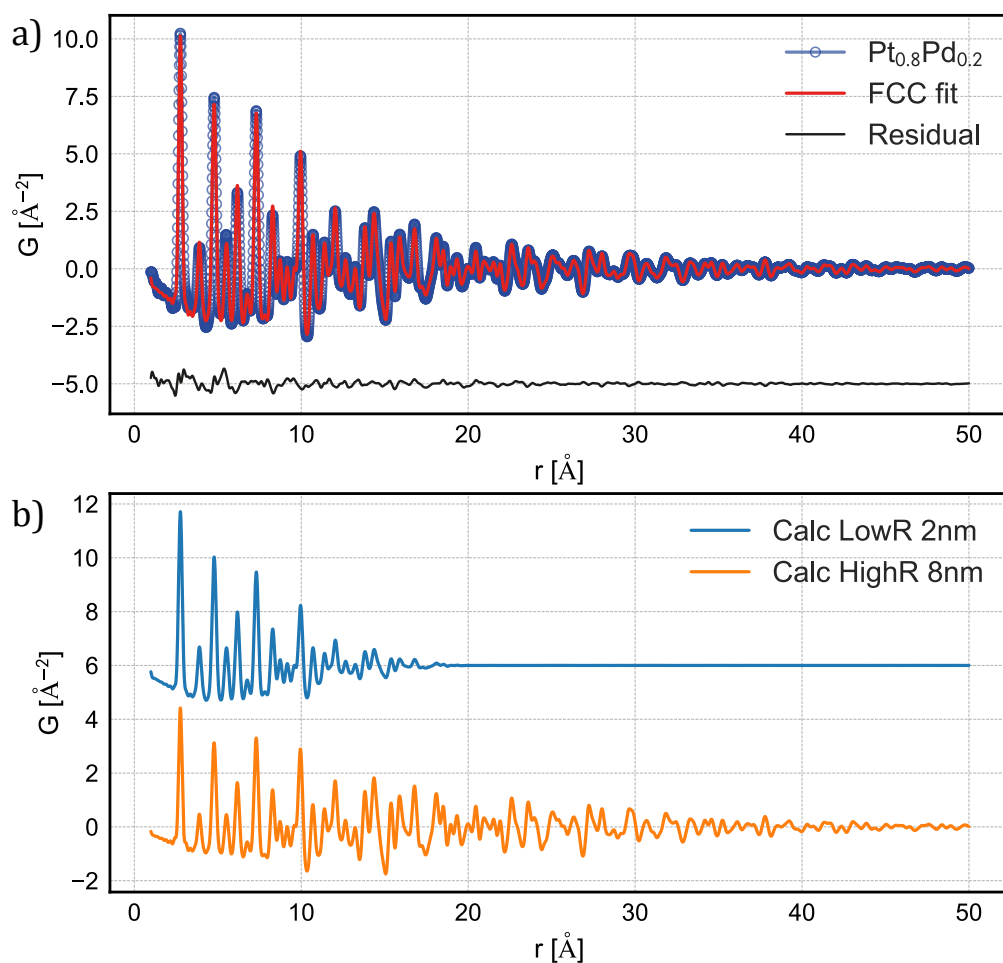
Figure 6.10:   a) Result of a 2 phase FCC model fit to the carbon supported data illustrating exceptional agreement with the data across the full r range. b) Two components of the 2 phase structural refinement, the sum of which constitutes the model.

constants and lattice constant changes for tiny nanoparticles. It is known that the lattice constant changes as the size[203] and shape of the nanopartices varies. Smaller nanoparticles typically result in a smaller lattice parameter and these effects could contribute or even be responsible for the changes attributed to Fe doping. Regardless of the cause, the findings suggest a strong correlation between iron content and nanoparticle size and lattice compression. An interesting analysis to do would be to evaluate the twin defect density using the approach outline in S. Banerjee et al.[1] and test the PtPd against iron doped samples.

The refined parameter values for lattice and crystallite size are extracted from the model and are summarized for the two approaches to size determination in Fig. 6.10. The addition of iron into the system affects the lattice through incorporation of Fe atoms into platinum or platinum-palladium alloy. The effect is systematic for all samples synthesized on carbon supports. The variations in magnitude are expected to stem from a combination of different surface area of the 3 support materials and the variation of the experimental conditions in the synthesis. Remarkably, the lattice compression appears much more significant for
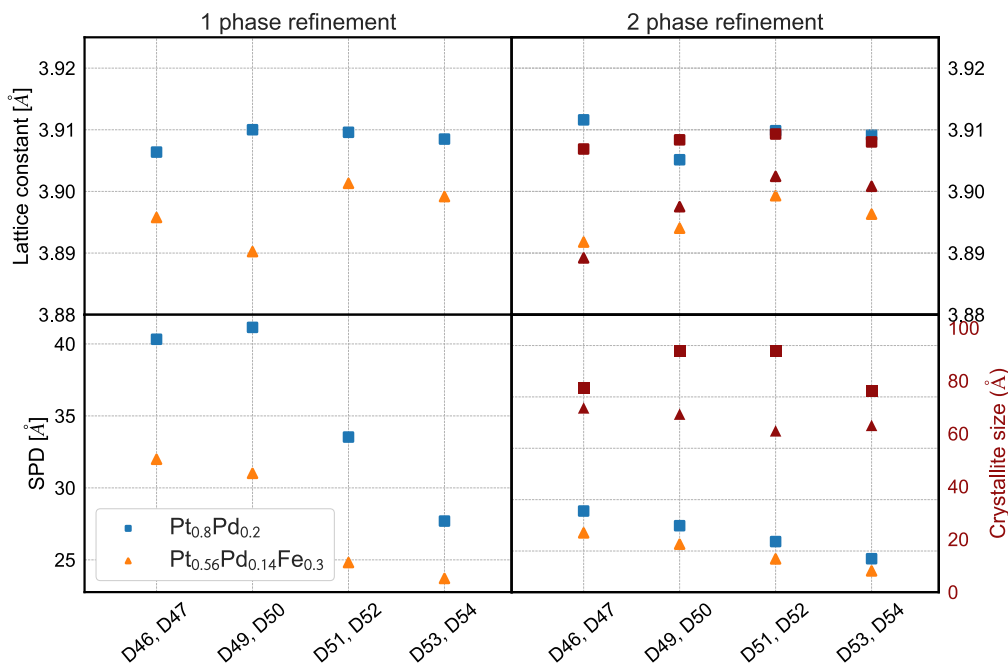
Figure 6.11: a-b) Lattice constants extracted from the 1 phase vs 2 phase model refinements. For two phase refinements, the phase accounting for large particles is indicated in dark red. Refined lattice constants decrease with presence of iron. c-d) Spherical particle diameters extracted from one phase and two phase FCC refinements. Refined SPD decreases with addition of Fe.

samples on carbon as compared to those on $\gamma$-$Al_2O_3$. A likely explanation for this is seen on the TEM elemental map of Fig. 6.1 m). Fe is mostly concentrated inside the nanoparticles, yet a significant portion is also found all around incorporated into the support. Due to similarity between Fe compounds and alumina, it is not unexpected that a significant portion would diffuse into the $\gamma Al_2O_3$ support forming $FeAl_2O_3$ and lowering the surface area of the support[183]. This would effectively lower the amount of iron available for alloying with the PtPd nanoparticles. By removing a chemically similar support, we are effectively increasing the Fe concentration and are alloying a much higher atomic ratio into the catalyst. This should in turn increase the change in the lattice constant of the resulting alloy.

Confirming the location of iron in the samples made on carbon support is the EDX trace measurements shown in Fig. 6.12. The trace signal is corrected for background signal by subtracting a signal of a false positive element from the total signal, in this case Ti. This is important as the signal intensity scales with the amount of material that is exposed to the electron beam. While the figure does not illustrate the correct proportion of elements in the target area, it gives a clear indication that Fe is absent outside of the nanoparticles. This measurement does not rule out a possibility of Fe oxide formation, but coupled together with the changing lattice constant obtained from PDF, supports the argument for alloying. The absence of iron in the support material also means that the samples can be used as a reference measurement in a spectroscopic study. These model
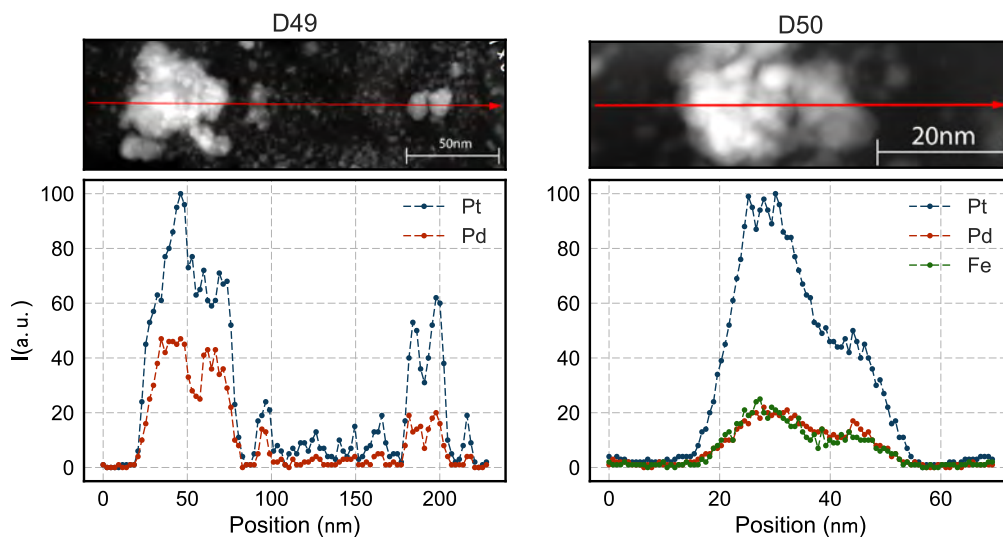
Figure 6.12: EDS trace of the PtPd and PtPdFe systems of samples D49 and D50 respectively. Fe doped nanoparticles show presence of Fe in the nanoparticles evenly spread across the particle and absent on the support.

system samples would provide the necessary complementary information to the samples on $\gamma-Al_2O_3$ supports in helping to constrain the analysis.

## 6.6 Summary

A novel catalyst containing an alloy of PtPd and doped with Fe is synthesized using a supercritical flow reactor. The Fe doping in the system improves the catalytic activity of the material compared to the reference PtPd alloy synthesized alongside the doped samples and is able to beat the (DOE): T50 < 150 °C target[185]. The Fe appears to reduce the sintering of the the nanoparticles when aged at 750°C.

The fresh catalyst was investigated using PDF analysis. The addition of iron appears to affect the lattice constant of the nanoparticles in a linear fashion for the studied compositions. No traces of Fe oxides could be reliably detected in the samples on $\gamma$-Al$_2$O$_3$ support despite the likely formation of FeAl$_2$O$_3$[183].

The aged samples follow the same trend for lattice compression for iron content under atomic ratio of 0.8. Upon incorporation of iron, PDF analysis of the aged samples confirms the decrease in particle size as seen from TEM. No signatures of the nanocrystalline iron phase was found in the aged samples, eliminating the possibility of segregation of the crystalline Fe$_2$O$_3$. Some features of the G(r) could be attributed to a number of iron oxide phases and have also shown a systematic difference in the residual. These features could be an effect of the improper background subtraction due to the alumina support changing chemically.

The x-ray contrast is insufficient to reliably detect all of the effects of the iron doping in the system. A follow up study would require spectroscopy to obtain complementary information. Determining the oxidation state and the coordination environment of Fe

atoms in the system would add constraints and added certainty to the PDF study. A main problem of a potential spectroscopic study is expected to be the presence of $FeAl_2O_3$ in the support.

To avoid the problems that stem from the presence of $\gamma-Al_2O_3$, a model system for the most catalytically active catalyst composition was synthesized on graphitized carbon support. Graphitized carbon was found to be an excellent substrate for PDF analysis resulting in very high quality data for studying the metallic nanoparticles.

The first attempt at a model system synthesis yielded a bimodal nanoparticle size distribution, with the majority of the nanoparticles being around 2-3nm as originally intended. The effects of iron on the lattice and nanoparticle size is larger than in the case of samples supported on $\gamma-Al_2O_3$. As no iron phase signal was found, together with the increased effects from the iron doping, this suggests complete annealing of iron into the FCC lattice of Pt and Pd. These samples would be invaluable to a follow up spectroscopic study as any detected Fe should only be present in direct contact with the PtPd alloy.

With modern synchrotron sources, good beamlines and capable analysis software, analysis of complicated industrially relevant samples appears possible. Despite minute nanoparticle content, useful information can be extracted, given enough care is put into data collection and analysis. Ultimately, for a complete understanding of the system, complementary information is crucial in order to constrain the model parameters. A follow study would greatly benefit from the data described in this chapter and increase the understanding of a complicated system.

# 7

# Structure of MoOx catalyst on ZSM-5 Zeolite support for Methane Valorisation

The following chapter describes the study of amorphous molybdenum oxide species (MoO$_x$) on zeolite ZSM-5 supports. These are synthesized by a supercritical flow method as part of the ADREM project at the Danish Technological Institute. The projects attempts to optimize the production of MoO$_3$/ZSM-5 catalyst used for conversion of methane into higher hydrocarbons. The catalyst produced by supercritical flow method exhibits better catalytic activity than conventional MoO$_3$/ZSM-5 catalyst prepared by impregnation. The study employs PDF analysis to characterize the heavily disordered structures. Using meticulous background subtraction procedures, the signal from the amorphous molybdenum oxide can be extracted and analyzed. The results indicate that the catalyst consists of arrangements of octahedrally coordinated molybdenum atoms across the surface of the zeolite, which leads to a high surface area available to the methane conversion reactions. The results of the study are currently being prepared for publication.

## 7.1 Introduction

With the dwindling oil reserves per capita[208] finding an alternative energy source is crucial for maintaining and improving the global standards of living worldwide. Renewable energy has seen a massive influx of research funding and yet the technology is ultimately not ready to step up to the demands of the growing populations and economies[209]. For now a more efficient use of the available hydrocarbon resources could provide a potential, albeit temporary, solution to the worlds energy crisis. Recent advances in the advanced extraction technologies coupled with the discovery of massive reserves of natural gas[210] could make it the best mid term solution until the renewable industry is ready to take its place.

Methane is the main component of natural gas and has the highest carbon to hydrogen ratio of all hydrocarbons. As a result it is mainly used for heating and electrical generation with just a tiny amounts of it being used as fuel in vehicles[211]. This is in part due to its high transportation and storage costs compared to liquid fuels[212]. The currently available solution is the production of syn-gas which is expensive and energy demanding[213]. It requires the use of high temperatures of over 970K and produces a mixture of CO and hydrogen. At the right conditions the syn-gas can be converted to a range of useful chemicals that are easier to handle, like the latest methanol-to-gasoline (MTG) process. The multiple step techniques are, however, far from being able to exploit the full potential of natural gas[214].

Research into direct conversion of methane into liquid aromatic hydrocarbons in a single step is currently underway and has been seeing massive advances[215][216][217]. The use of molybdenum nanostructures embedded in zeolites has seen an influx of interest because of the two key advantages. The runaway explosive combustion of methane is impossible owing to the absence of $O_2$. The catalyst is also stable and requires no additional reagents to work[218]. This in turn allows for the exploitation of methane in remote conditions. For example to collect and use the methane extracted at remote sources during oil extraction, which is currently being simply vented into the atmosphere and burnt off.

To improve the efficiency, selectivity and conversion and to create a commercially viable catalyst a deeper understanding of the nanostructure of the catalyst at the molecular level is required. Through use of spectroscopy and theoretical modeling it was possible to identify the likely reaction pathways and catalytic sites[219][220][221][222] from model systems, as well as the model systems interaction with the support material[218].

Production of such catalysts on industrial scale provides its own set of challenges. Previous studies suggest that the optimal molybdenum loading in zeolite supported catalysts for methane conversion should be at 2-3%. For higher loadings the material becomes crystalline and starts to lose surface area. As a result, its methane conversion effectiveness drops. A critical point of 5% is reported. At this stage the pores of the zeolite fill up and large crystals are formed[223].

The ADREM project currently underway at the Danish Technological Institute at-

tempts to improve the production of a promising $MoO_3$/ZSM-5 catalyst. Currently, state of the art production methods use impregnation to add molybdenum to the zeolite[224][217]. The use of hydrothermal flow method allows for cost efficient and fast production of the catalytic material and has never yet been attempted. Another advantage of flow synthesis is the precise control of the product with the possibility for automation and large scale production.

Using the synthesis method developed for the ADREM project, synthesis of nanostructured Mo oxides is possible. The material exhibits lower crystallinity and higher surface area at similar metal loading compared to conventional impregnation techniques, which in turn leads to higher overall surface area and better activity and selectivity.

Typically available characterization tools are having difficulties in extracting information from the catalyst material. The product produced by state of the art impregnation and flow synthesis forms structures undetectable by conventional in-house powder diffraction due to the size of the domains. Raman spectroscopy measurements were performed, identifying the nanocrystalline molybdenum oxide produced by impregnation method and heavily disordered material produced by via flow synthesis method. PDF analysis is sensitive to the local structure of materials and as such is able to characterize the heavily disordered amorphous $MoO_3$/ZSM-5. The zeolite support can be subtracted, and PDF analysis is able to investigate the structures of the catalyst on the real samples from the production environment. The majority of the samples prepared by supercritical flow method appear to be amorphous and are made up of networks of octahedrally coordinated molybdenum species. These are likely situated on the surface of the zeolite[224], with some proportion situated in the pores of the zeolite. In addition, it appears that much higher loadings than the reported 5% limit can be produced. These exhibit a mixture of nanocrystalline and amorphous molybdenum oxide.

## 7.2 Experimental methods

### 7.2.1 Synthesis

The reference material is synthesized using an impregnation technique, where $MoO_3$ is physically mixed with the zeolite support. The mixture is then heated and kept at 500°C for six hours, leading to $MoO_3$ diffusing into the support.

The DTI samples were synthesized via a continuous hydrothermal flow method in a self-built reactor[225][226]. Here, a Mo precursor is dissolved in ethanol and the zeolite is added forming a very thin suspension with Mo dissolved. As the suspension is pumped into the reactor, the precursor (Mo + ZSM-5) meets the hot solvent ($H_2O$) in a mixing point. The high temperature reaction that follows is complex with different components decomposing (ethanol into $H_2$/CO/$H_2O$) and oxidized ($H_2$/CO acting as reducing agents) and reduced (Mo(VI) precursor reduced to Mo(IV) and hydrolyzed (Mo(IV) reacting with $H_2O$ forming $MoO_2$). In general, Mo(VI) is reduced and hydrolyzed in a fast reaction forming $MoO_2$, which, owing to the flow aspect of the reaction, does not have time to grow

| Sample name | Mo loading (wt) | Support | SC Temp | Calcination |
|---|---|---|---|---|
| $MoO_x$ 1 | 5.3% | Zeolyst ZSM5 SAR50 | 450 | N/A |
| $MoO_x$ 2 | 5.3% | Zeolyst ZSM5 SAR50 | 450 | 500°C |
| $MoO_x$ 3 | 4.2% | Zeolyst ZSM5 SAR23 | 450 | 500°C |
| $MoO_x$ 4 | 3% | Zeolyst ZSM5 SAR50 | 450 | 500°C |
| $MoO_x$ 5 | 2.8% | Alfa Aesar ZSM5 SAR23 | 450 | 500°C |
| $MoO_x$ 6 | 8% | Zeolyst ZSM5 SAR23 | 450 | 500°C |
| $MoO_x$ 7 | 5% | Zeolyst ZSM5 SAR23 | N/A | 500°C |
| $MoO_x$ 8 | 4.8% | Alfa Aesar ZSM5 SAR50 | 250 | 500°C |

Table 7.1: A subset of the studied samples. Calcination was carried out at 500C for 6 hours. Mo loadings were measured using STEM-EDX.

into larger particles. Some of the $MoO_2$ is attached to the zeolite, while some remains in the solution. In the present synthesis, water was selected as solvent. The precursor solution was made from molybdenum acetylacetonate (99.9%, Sigma Aldrich), NH4-ZSM-5 (SAR = 23) (Zeolyst), PVP40K (99.99%, Sigma Aldrich) and absolute ethanol (99.9%) and ethylene glycol (99.9%, Alfa Aesar). The precursor was mixed to give a total product of m = 10g, taking into account both the support and the precipitated metal oxide and the desired loading 5 wt% Mo/ZSM-5. Molybdenum oxide may dissolve in $H_2O$ and the precursor was prepared with an excess of molybdenum precursor(7 wt% Mo/ZSM-5). The ethylene glycol amount was up to 5% of the total volume of the precursor. The precursor solution was kept under constant stirring at all times before the synthesis. The solvent was pre-heated to 250 °C or 450 °C. The vertical section of the reactor was kept at 375 °C and a pressure of $\approx$ 210 bar was maintained through-out the reaction. During collection of the product, 1 ml of product was discarded in the beginning and in the end. The product has a tendency to get stuck in the reactor tubing due to the zeolite being difficult to maintain in suspension during the synthesis. The product suspension was centrifuged at 10000 rpm for 5 min in 200mL canisters to collect the solid. The supernatant had a dark blue/green colour, while the solid product had a dark blue/violet colour. After collection, the product was washed in absolute ethanol to remove organic residues and dried at room temperature for 24 h. Finally, the samples were calcined in air for 6 h at 500 °C.

The full overview of the samples studied can be found in Table 7.2.1. The reference material prepared by impregnation is $MoO_x$ 7.

### 7.2.2 Synchrotron powder diffraction

Zeolite powders were measured at three synchrotron facilities using the standard RA-PDF[22] acquisition method. The powders were ground to eliminate large agglomerates and then sealed inside 1mm quartz and kapton capillaries. The packed capillaries were then measured at a powder diffraction beamline in transmission geometry in either close proximity to the detector for PDF measurements or at a distance for high resolution powder diffraction. The measurement times were appropriate for each beamline to obtain the best possible data quality.

The measurements performed at XPD beamline, at NSLSII at BNL were done at a wavelength of 0.1847Å at a distance of 205.49mm. This gave an effective $Q_{\max} = 24\text{Å}^1$. The powders were sealed inside 1mm quartz capillaries. The experimental geometry was calibrated using a standard Ni powder. The measurements were performed in a static geometry, as sample changers were unavailable.

For diffraction measurements performed at P.02 at PetraIII, DESY, Hamburg, at a wavelength of 0.2072Å at a detector distance of 199.45mm, giving an effective $Q_{\max} = 22\text{Å}^{-1}$. The powders were sealed inside kapton capillaries. Calibrations were performed by using $CeO_2$ calibrants at each end of the sample change and a $LaB_6$ calibrant as a control. The tilt of the sample changer was calculated and the integration distance was adjusted for each position on the sample changer.

The diffraction measurements done at ID11B at APS, ANL used a wavelength of 0.2113Å at a detector distance of 177mm giving an effective $Q_{\max} = 24\text{Å}^{-1}$. The powders were sealed inside kapton capillaries. The geometry and detector parameters were calibrated using a NIST SRM640a Si powder mounted onto the sample changer. The sample changer was calibrated separately by the beamline staff and had an insignificant amount of tilt, thus the calibration distance was kept at the value obtained from the experimental standard.

The resulting diffraction images were azimuthally integated to 1D diffraction patterns using Fit2D[98] program after masking out the defective and erroneous pixels. Structural refinements were carried out using PDFGui[46] program for bulk crystalline models and diffpy-CMI[47] Python modules combined with custom routines for discrete models.

### 7.2.3 Background subtraction methodology

From the results of electron microscopy and powder diffraction, the zeolite materials appear to be highly ordered. While true at the long scale average structure level, this quickly becomes false when looking at the local structure of a typical zeolite. The local disorder in zeolites are most commonly occurring due to local environment differences of the Al atoms in the Si-O network and have been shown both theoretically[227] and experimentally[228] employing EXAFS and EXANES. In addition, the local structure of the zeolite might change with acidity through presence of other elements[229][228].

This slightly changing support material means that finding a proper background scaling is incredibly difficult in $Q$ space. In $r$ space, this is a different story. Powder diffraction data shows that the average structure of the zeolite does not change when adding $MoO_x$. Thus, we can normalize the PDFs in real space to match them at an average to long range order, typically 25-50Å and perform the subtraction from the normalized datasets. Using the approach described in Section 3.5.2, it is possible to fit the support material to the data, after removing the scattering signal from the capillary. The residual then contains purely the signal from the material of interest. A typical $r$ space subtraction result is shown in Fig. 7.5.
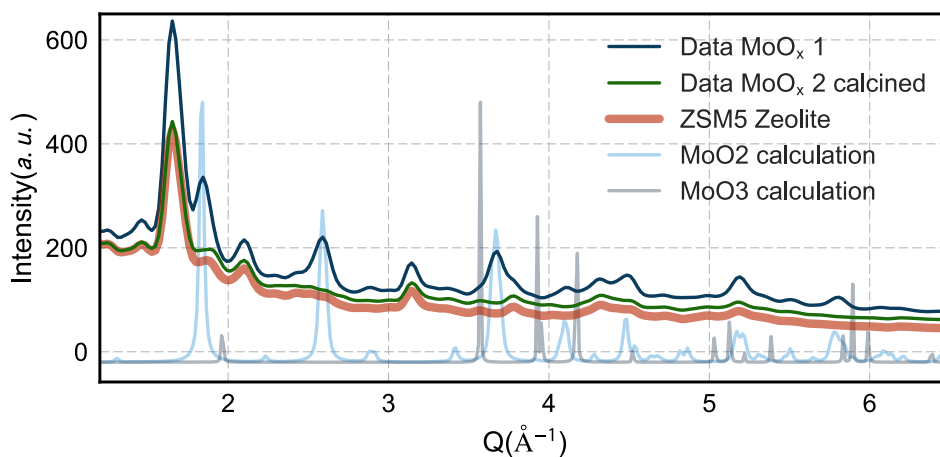
Figure 7.1: X ray diffraction patterns from $MoO_x$ 1 and $MoO_x$ 2 samples overlayed with Zeolite ZSM5 support and calculated diffraction patterns for $MoO_2$ and $MoO_3$ crystals. During calcination a crystalline $MoO_2$ phase is oxidized to $MoO_3$-like phase which can no longer be reliably quantified using Rietveld refinement.

## 7.3 Phase identification of $MoO_x$ on ZSM-5 zeolites

The dry powder of the $MoO_x$ 1 sample prepared by the hydrothermal flow method on zeolite was analyzed using powder diffraction both before and after calcination. Before calcination particles of $MoO_2$ can be identified by their clear Bragg reflections. This is shown in Fig. 7.1 which illustrates the effects of calcination during sample synthesis.

The DTI supercritical synthesis results in large $MoO_2$ nanoparticles being deposited across the surface of the support. During calcination at 500°C in the presence of oxygen, most of the $Mo^{4+}$ in a crystalline $MoO_2$ phase is oxidized to a phase containing $Mo^{6+}$[230]. The temperature is low enough to prevent a significant molybdenum loss due to the volatility of $MoO_3$ at temperatures above 600°C[231].

As seen from the diffraction pattern of the calcined $MoO_x$ 2 sample in Fig. 7.1, the crystalline phase disappears leaving only the diffuse scattering signal, indicating formation of an amorphous phase containing $MoO_3$ or similar phases[232]. The calcination step might be the most crucial part of the synthesis performed at DTI and might be the reason for very good dispersions across the zeolite owing to the mobility of the $MoO_3$. The absence of any clear Bragg peaks from $MoO_3$ phase makes this a perfect candidate for PDF analysis.

### 7.3.1 Combined Rietveld and PDF analysis of non-calcined sample $MoO_x$ 1

A model of $MoO_2$ has been refined using a standard Rietveld refinement procedure using Maud software[89]. To avoid a mixed phase refinement, the diffraction pattern of the zeolite was measured alongside the sample and then added as a background term into the refinement program. Only the scale parameter has been refined for the background dataset. In addition, to take the diffuse scattering into account, a polynomial background term was added.

106 of 183
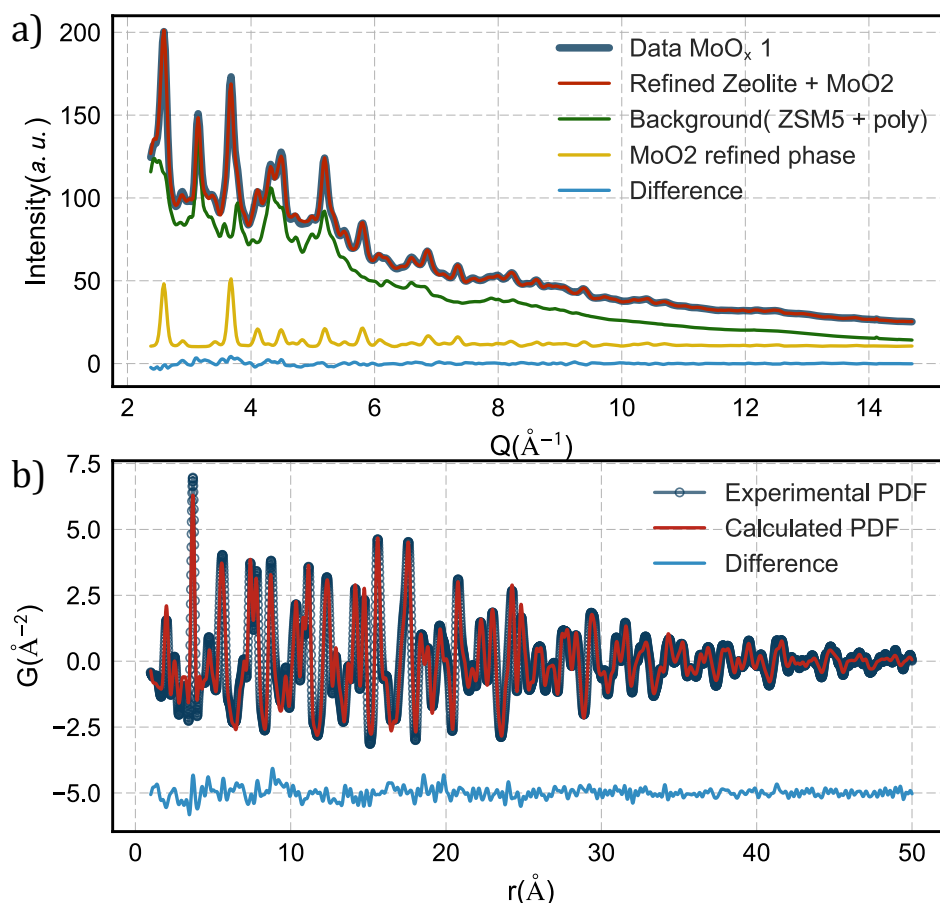
Figure 7.2: Structural refinements of $MoO_x$ 1 sample. a) $MoO_2$ phase is easily refined using both Rietveld refinement method in $Q$ space and b) through PDF analysis in $r$ space.

A model of crystalline $MoO_2$ was then refined as the main phase. Refining the unit cell parameters and the crystallite size via Scherrer broadening was enough to describe the data with sufficient accuracy. The fit is presented in Fig. 7.2 and the refinement score is $R_w$= 1.31%. The refined crystallite size was $45 \pm 3$nm(XRD).

Good agreement factor does not mean that a complete description of the system is achieved. In fact, given the instrumental broadening while acquiring data in PDF mode and poor $Q$ resolution, a good fit is expected. To double check the stability of the structural solution the data was analyzed using PDF analysis. A crystal model of $MoO_2$ was refined in PDFGui obtaining an agreement score $R_w$= 15.9%. This was obtained by refining the unit cell parameters, isotropic B factors and the $\delta2$ sharpening term. The crystallite size was obtained by adding a spherical attenuation function and was around 11.2nm.

The unit cell parameters obtained from PDF agree with the Rietveld refinement. The crystallite size estimate obtained by PDF are typically lower than those obtained from XRD. Additionally, the accuracy of size estimation through PDF is poor when looking at crystals larger than 8-10nm. A likely explanation of the discrepancy could be a wide size distribution. The estimation from PDF will yield an average and skewed down result of crystalline sizes across the sample, while in XRD the size estimate is dominated by
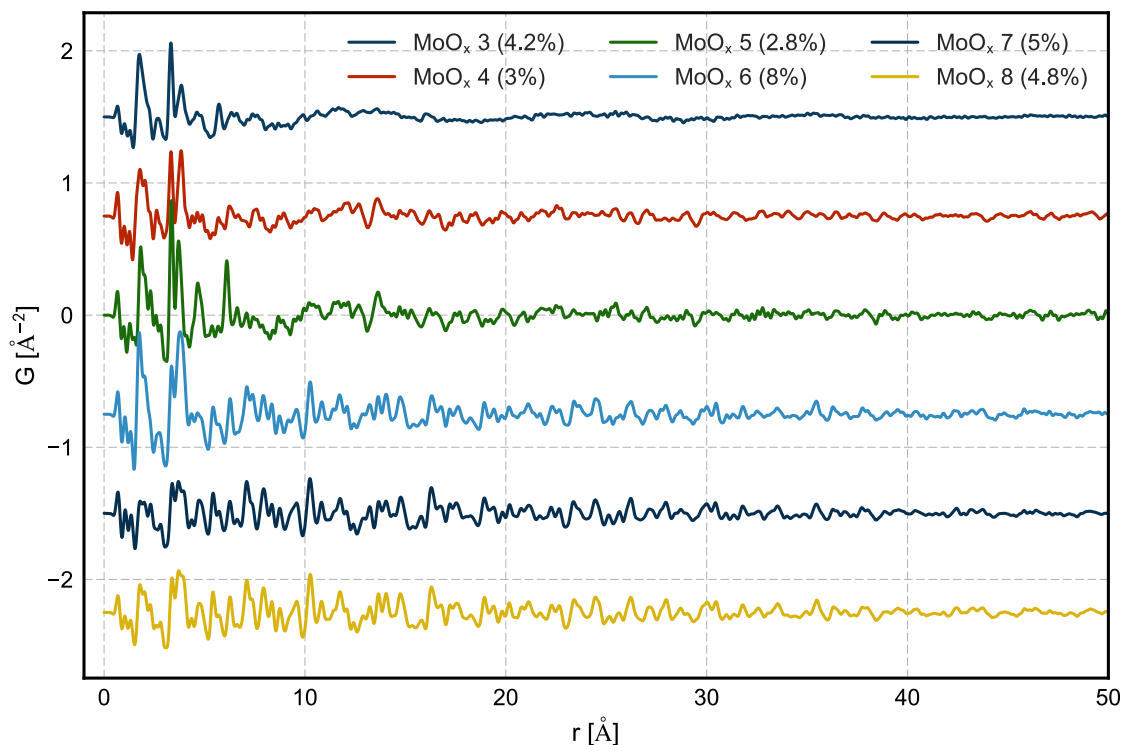
Figure 7.3: Zeolite subtracted PDFs of all samples ordered in terms of increasing crystallinity top to bottom. The data show a number of amorphous as well as nanocrystalline phases.

the larger crystallites producing the majority of Bragg scattering. The diffuse portion of the scattering is ignored while performing Rietveld refinement, skewing the results in the opposite direction towards larger sizes.

## 7.4 Local structure of calcined samples by PDF analysis

In the absence of clear Bragg peaks in the diffraction pattern, an obvious choice for structural analysis of the $MoO_x$ material is PDF. Using the methodology described in Section 7.2.3 the difference PDF's of the calcined samples were extracted. This was done by fitting the kapton subtracted datasets to the target dataset in the region above 25Å. The lower fit boundary has been determined empirically by optimizing the G(r) for quality, i.e. lowest noise and eliminating over-subtraction. Results are summarized in Fig. 7.3 and show a wealth of interesting structures.

The datasets in Fig. 7.3 were sorted in order of perceived crystallinity, descending from least to most crystalline. The figure shows the first 50Å of the G(r), as any correlation beyond that point would be difficult to discern and are dominated by noise. Surprisingly, the majority of samples prepared using the supercritical method results in an amorphous phase judging by the extent of pair correlation distances.

The total loading of Mo in the samples presented appears to have a lesser effect, as all of the measured samples Mo loading was measured to be close to 5% using SEM EDX. This is

expected for the total Mo loading studied here, as the crystallization into larger structures with clearly pronounced Bragg reflections has been reported to happen at loadings over 5%[223].

Notably, the crystalline samples appear to have nearly identical structures, despite being synthesized by different methods. Additional details about the samples can be found in Table 7.2.1.

### 7.4.1 Nanocrystalline Molybdenum oxides

The reference material used in this study is the catalyst $MoO_x$ 7(5%Mo wt) prepared by impregnation. Through Raman spectroscopy it has been shown that this material contains crystalline $MoO_3$ nanoparticles. The PDF refinements of this sample also indicates a high degree of crystallinity.

The ideal structure of $MoO_3$ can be described as an arrangement of infinitely extending layers of distorted octahedra that are joined at the edges[233]. In practice, lattice defects in these structures are common. A whole family of $ReO_3$-type structures can exist[234] differing by arrangements of octahedra and the corresponding ratio of corner shared to edge shared units.

The validity of the $MoO_3$ model can be tested by attempting to fit a spherically attenuated bulk $MoO_3$ model to the G(r) using PDFGui. The refinement results can be seen in Fig. 7.4. Most features of the data are present in the model, while the agreement factor is not perfect. This indicates the similarity between the model and the actual material structure. This is expected for molybdenum oxides as they are known to crystallize as permutations of an ideal $MoO_3$ lattice with a variety of shear plane lattice defects. These defects change the arrangement and ratios of corner or edge-shared octahedra that the $MoO_3$ lattice is made of[234]. This results in a number stoichiometric molybdenum to oxygen ratios close to that of $MoO_3$.

The model can be further improved by focusing on the long range correlation order, by refining the model from 15Å and up as seen of Fig. 7.4 b). The agreement to the average structure improves significantly, as is reflected in the residual. After the refinement the model is calculated back down towards 1Å to assess the agreement at low $r$ region. The residual for the local order between 1Å-10Å becomes significantly worse than when the model was refined across the full range, as seen in Fig. 7.4a). This illustrates that even though the material has a degree of crystallinity and ordered periodicity, it still has a significant local structure component as either a separate phase or a concentration of lattice defects.

The local structure can be described using the same crystalline $MoO_3$ model if we ignore the average structure, i.e. perform the refinement from 1Å to 12Å. By doing this, the residual from the local structure is significantly improved and model now describes the local structure much better as seen from the insert in Fig. 7.4 b).

The remaining nanocrystalline molybdenum oxide samples($MoO_x$ 6 and $MoO_x$ 8) exhibit the same behavior, as is expected from the visual similarity of their G(r).
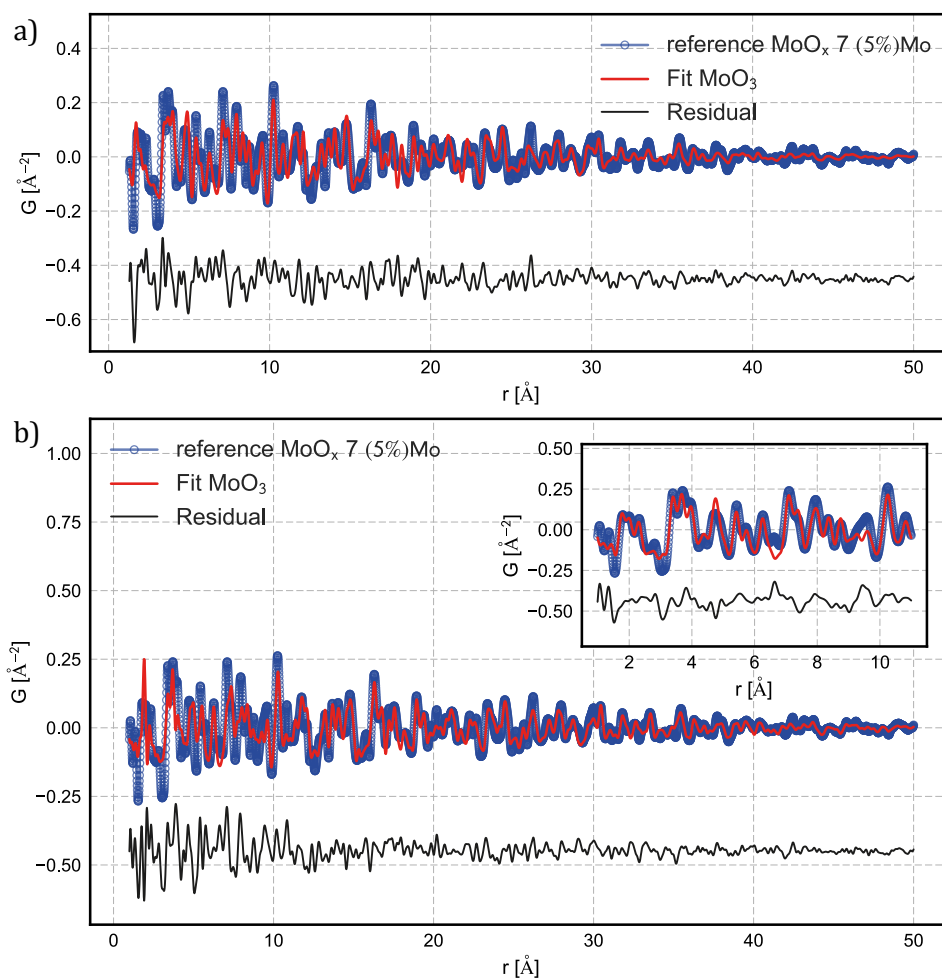
Figure 7.4: a) A PDF refinement of a $MoO_3$ structure to a reference sample refined across the full $r$ range. While the model accounts for the presence of most pair correlations it is clear that it does not describe the data with a high enough degree of accuracy. b) Structural refinement of the $MoO_3$ model to the average structure (over $r > 10$Å) reveals local disorder in the low $r$ region. b) Insert: the local structure can be refined separately, i.e. refined only for $r < 12$, which significantly improves the model agreement in the low $r$ region.

### 7.4.2 Supercritical temperature effect on synthesis

The temperature of the supercritical solvent and the conditions in the reaction column of the reactor have a crucial role in the outcome of the synthesis.

Fig. 7.5 shows the G(r) of $MoO_x$ on zeolite made at two different reactor/solvent temperatures of 250°C and 450°C respectively. The support is subtracted in accordance with the methodology described earlier. The low temperature synthesis product appears nanocrystalline, while the material produced at high temperature is amorphous. The samples were prepared in a single run with the only difference being the reactor temperature. The surface area of the calcined product was measured by Brunauer–Emmett–Teller

| Support | Surface Area (m2/g) | % surface area | Structure |
|---|---|---|---|
| Alfa Aesar NH4-ZSM5 | 369.2106 | | |
| $MoO_x$ 5 | 363.9541 | 98.58 | amorphous |
| $MoO_x$ 8 | 318.8226 | 86.35 | nanocrystalline |

Table 7.2: Surface area comparison for samples prepared at 250°C and 450°C

method(BET) and the results are summarized in table 7.2.

The amorphous sample surface area is proportionally much greater than that of the nanocrystalline, suggesting better coverage of the zeolite surface by the amorphous molybdenum oxide. The reduction of the surface area compared to the pure support is expected due to deposition of the material. Previous reports suggest that after preparation, large portions of the material would concentrate in the pores of the zeolite[218][223]. From this point of view, the large surface area difference could be an effect of the size of Mo oxide particles that are blocking the pores.

Previous studies suggest a threshold for Mo loading of 5% for the formation of a well dispersed $MoO_x$ surface on HZSM-5 zeolite[223] when prepared by the impregnation method. At and above the threshold, the selectivity towards benzene and conversion amount of methane drops off dramatically due to the formation of large crystalline species of $MoO_3$. This threshold can be bypassed with the catalysts prepared by the supercritical flow method. The sample $MoO_x$ 6 sample with 8%wt Mo exhibits better overall catalytic activity towards production of benzene as the reference sample prepared by impregnation.[235]. Our findings show that $MoO_x$ 6 sample with 8%wt Mo consists of a mixture of nanocrystalline and amorphous parts. The amorphous component can be revealed by fitting a $MoO_3$ model to the average structure component, i.e. starting at any r value over 8Å. Afterwards, the parameters are fixed and the model is calculated for the full range of interest. A clear signal corresponding to the amorphous component is clearly present in the residual upon subtraction of the nanocrystalline signal. The results of this treatment are shown in Fig. 7.6. Judging by the relative magnitudes of the peaks in G(r) the amorphous component comprises a significant portion of the sample. The structural features of the amorphous residual are also similar to the rest of the pure amorphous samples, while the nanocrystalline phase is similar to that of the nanocrystalline Molybdenum oxides as shown in Fig. 7.3. The implications of this discovery needs to be studied further,
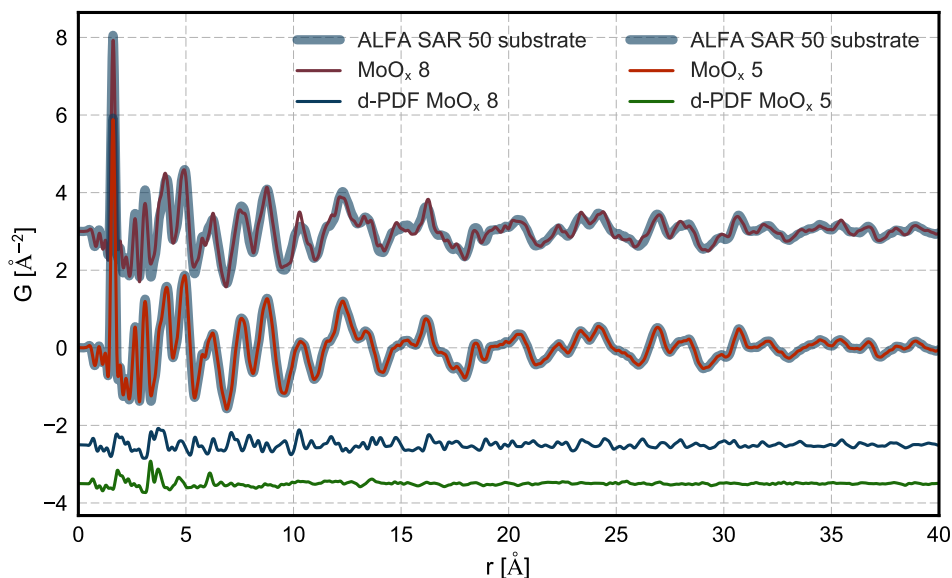
Figure 7.5: Zeolite support subtraction in r-space of $MoO_x$ samples synthesized at 250°C and 450°C. The G(r) from the support material is "fit" to the target G(r) dataset in the region between 25-50Å. The difference PDFs contain only the signal from the nanocrystalline Mo phase and an amorphous Mo phase for the two temperatures respectively. The residuals have been scaled for visual clarity.
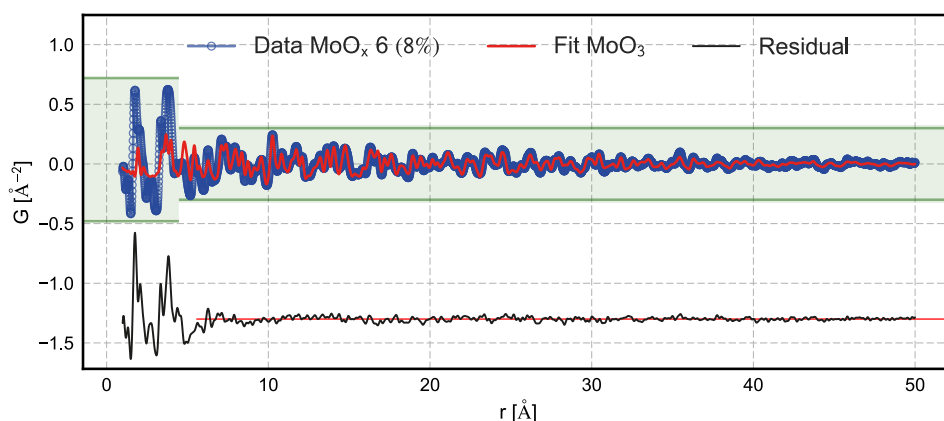


Figure 7.6: PDF fit of the $MoO_x$ 6 sample containing a phase mixture of amorphous $MoO_x$ and crystalline $MoO_3$. By subtracting a refined medium range ($r > 8$Å) model of crystalline $MoO_3$ from the total G(r), the signal from the amorphous phase is revealed in the residual. The red line through the residual is added to highlight the loose ordering of the amorphous phase.

in particular in terms of catalysis. One interesting angle to investigate would be whether increasing the molybdenum loading even further will keep improving the conversion rates.

### 7.4.3 Common trends in the structure of amorphous $MoO_x$

A good place to start while attempting to develop a model for an amorphous material is its typical crystalline state. As described previously, the structures of the $MoO_3$-type compounds consist of distorted $MoO_6$ octahedra joined at the corners or at the edges. The Mo-O distances inside an octahedron are typically 1.6-1.9Å 1.8-2.1Å and 2.1-2.3Å depending on the corresponding lattice distortions and the local environment of the Mo atom with respect to the neighboring Mo atoms[234]. The nearest neighbor Mo-Mo distances for edge-shared octahedra are typically around 3.2-3.4Å while those for corner shared octahedra are typically between 3.7-3.95Å. It is therefore clear that we are able distinguish between the two types of arrangements and their corresponding ratios.

To start constructing a representative model of the remaining samples we start by examining the data shown in Fig. 7.3. From the number of pair correlations on the G(r) curves we know that the maximum size for any model should be around 0.8nm. We can thus construct arrangements of $MoO_6$ octahedra in a mix of corner and edge share configurations of up to four units across. Taking inspiration in the different crystalline "parent" structures of $MoO_3$[234] a number of "cutout" cluster structures are generated. A Python script is used to randomly remove outer Mo octahedra from the structure one by one and the resulting structures are compared to the data. The scattering pattern for each generated structure is calculated using the Debye calculator module from diffpy.CMI[47] refining the arbitrary scale factors, anisotropic displacement factors and the zoomscale, i.e. isotropic stretch of the structure.

A subset of the results is presented in Fig. 7.7. Using the described approach it was possible to obtain a decent description for the main features of all datasets. Attempting to define an exact structure makes little sense in the present case, since the samples are highly disordered. By combining the observations from all of the refined structures it is possible to see the structural similarities across all of the samples.

The assumption that the amorphous structures are built up of block of $MoO_6$ octahedra is sufficient and provides a good description of the main features of the data. One typical feature which is present in all created structures with a good agreement score $R_w$ is an arrangement of three octahedra that are sharing two sides with two neighboring octahedra.The presence of this arrangement is necessary to attain a good description of the local structure up to 6Å. This structural unit is then connected to other similar units or a tail. It is likely that the tail is an artifact of the inability of the model to account for different orientations of the neighboring units due to the amorphous nature of the material. In this case the correct interpretation would be to spread the scattering contribution from a tail to a multitude of eligible sites all around the "core" of the structure.

The semi periodic arrangement of the "core" octahedra is further supported by the presence of a slowly varying electron density distribution beyond the correlation range of
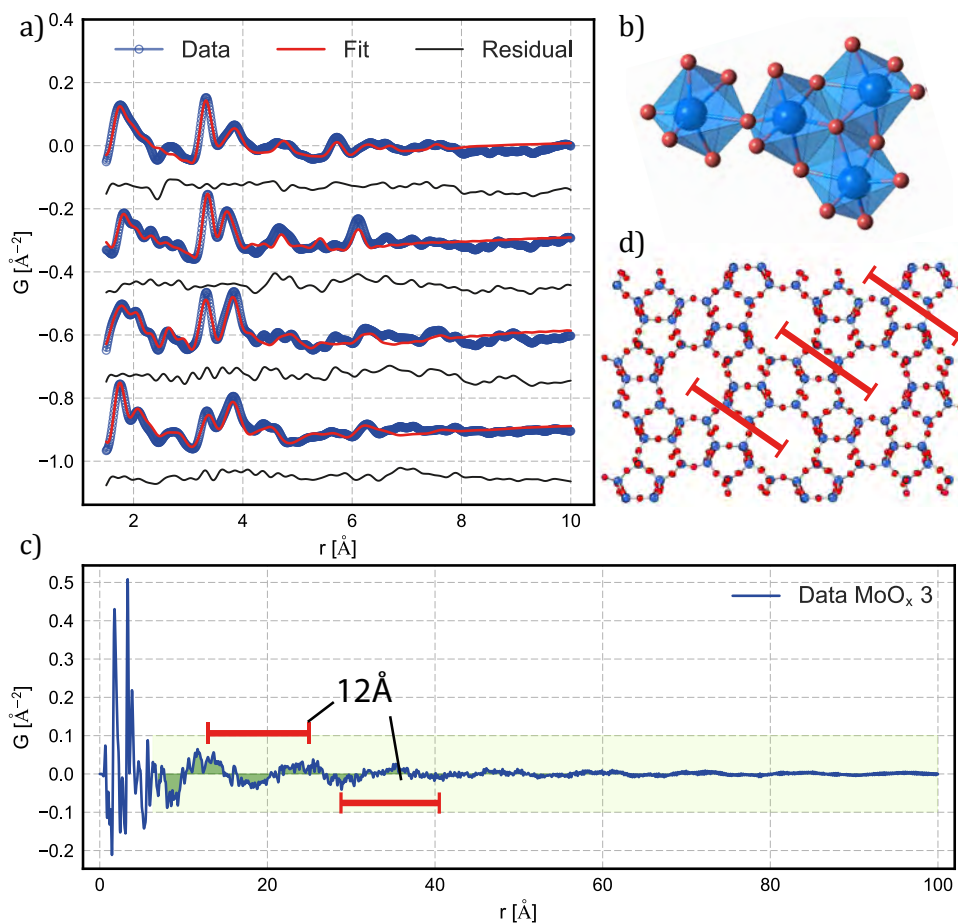
Figure 7.7: a) Local structure refinements of the amorphous $MoO_x$ data in order: $MoO_x$ 1, $MoO_x$ 5, $MoO_x$ 4, residual of $MoO_x$ 6. b) The typical "core" arrangement of three octahedra is present in all structures as likely building blocks, with a random tail. c) The highlighted region shows the slowly varying electron density distribution with a periodicity of around 12Å. This suggests a periodic ordering of the "core" units of amorphous molybdenum structures either due to networking or due to packing into the pores of the zeolite.d) The structure of the zeolite ZSM-5. The pores are arranged in a tetragonal fashion 12Å apart.

the core and its immediate neighbors[236]. The broad features appear in the G(r) at $\sim$12Å, $\sim$24Å, $\sim$36Å and so on, suggesting a square or concentric arrangement. The region is highlighted in Fig. 7.7 d). The periodicity of $\sim$12Å also corresponds to the arrangement of the pores in the zeolite structure which are arranged in the tetragonal fashion. The feature is present in all datasets with amorphous $MoO_x$ structures. There are two ways this can be achieved: as a semi-periodic network of $MoO_x$ "core" units that are joined together at random orientations or as additional units of molybdenum oxide structures packed into pores of the zeolite. We know that at low loadings the $MoO_x$ is expected to reside inside the pores of the zeolite[223][45] as opposed to less favorable positions on the surface of the support[218], when prepared by impregnation. The portion that resides on the surface was reported as nanocrystalline by Li.et al[237] and chainlike $Mo_5O_{12}$ in the pores of the zeolite. An earlier electron paramagnetic resonance (EPR) study by D. Ma, et al.[224] suggests that there exist up to four different types of $MoO_x$, depending on preparation method and the location of the molybdenum oxide on the zeolite. The species present at the surface of the zeolite are expected to have octahedral or square pyramidal coordination. Those in the pores are expected to have a tetrahedral coordination environment in association with aluminum atoms and are found to be very mobile inside the nanoporous zeolite structure.

It is logical to assume that the amorphous structures seen in the data are indeed either octahedral or pyramidal coordinated units at the surface of the zeolite. During calcination procedure the $MoO_2$ is oxidized leading to the creation of mobile species of $Mo^{6+}$. Some of those, like the mobile tetrahedrally coordinated $Mo^{6+}$ species, would naturally find their way into the pores, while the rest will reside close to their origin, at the surface. More analysis is needed to conclude which, of the predicted arrangements is correct. A combination of all three seems the most likely option.

The ratio of the peaks at $\sim$3.3Å and $\sim$3.7Å tells us about the relative number of edge share and corner shared octahedron units. The reasons for the variation of this ratio across the samples are still unexplained, but could be related to the Mo loading or differences during calcination procedure. For future studies a comparison of the state of the samples before calcination would be very useful.

### 7.4.4 Advantages of methane activation and transformation on amorphous Molybdenum oxide based catalyst

The samples with an amorphous $MoO_x$ proved to be more efficient catalysts for the conversion of methane. According to a number of studies, the active surface of a $MoO_3$ catalyst is the [0 1 0] surface in the $ac$ plane of the crystal. Fig. 7.8 shows a cross section of the bulk $MoO_3$ crystal. The [0 1 0] plane separates the layers of octahedra joined by edges and is the typical termination plane for the crystal. This surface contains three types of oxygen atoms where the reaction with carbohydrates can take place: a terminal oxo-oxygen bound to one Mo atom, a stabilized oxo-oxygen bound to two Mo atoms as a corner in two corner shared octahedra and a briding-oxygen bound to three Mo atoms, positions inbetween two corner shared octahedra edge shared to the third[222]. The strength of the
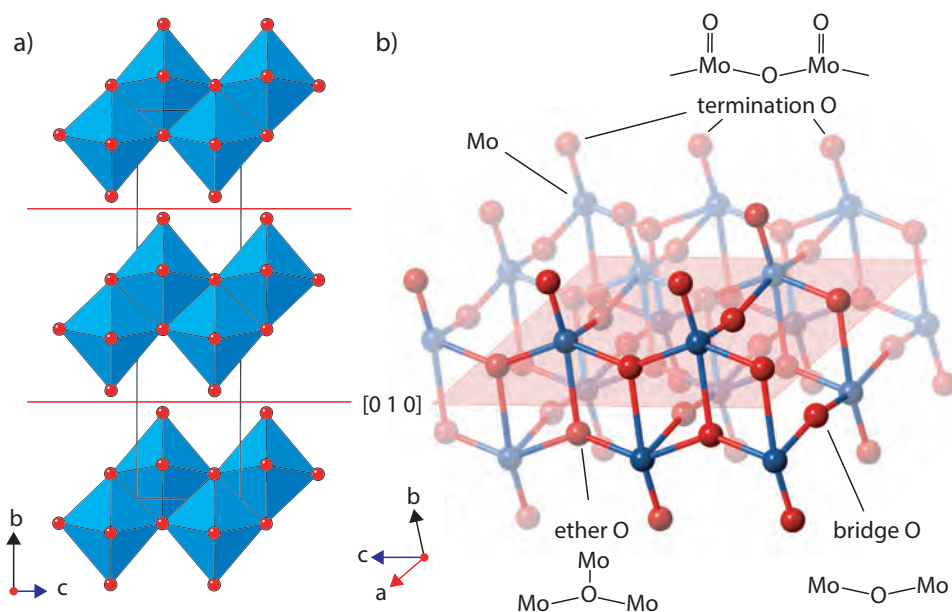
Figure 7.8: a) Structure of $MoO_3$ represented as infinite layers of $MoO_6$ polyhedra stacked along the [0 1 0] plane (red). b) There are three types of catalytically active oxygen sites in the lattice - ether oxygens between three Mo atoms, bridge oxygens between two Mo atoms and termination oxygens bound to one. The termination oxygen sites are the most active towards methane conversion.

metal-oxygen bond is the determining factor in the kinetics of the reaction. A combination of studies have shown that a terminal oxygen site is a much more favorable reaction site for methane conversion[219] requiring just one electron in an H-abstraction process reducing the Mo from VI to V as opposed to a so called (2+2) process involving two electrons and a reduction of Mo from VI to IV[220].

The availability of the oxygen sites is the rate limiting factor in these reactions and thus a higher surface to bulk ratio of the supercritically prepared catalyst possesses a natural advantage. The structural motifs for the amorphous $MoO_x$ also suggests a higher number of termination oxygen atoms on the surface of the catalyst than those of a crystalline $MoO_3$. The presence of two termination oxygens in close proximity promote the (5+2) reaction pathways leading to a production of hydroxyl and alkoxy directly[221]. This suggests the material would posses better selectivity for the production of useful species, while initially suffering from a higher coke production[237].

## 7.5 Summary

Here we report a series of molybdenum oxide based catalysts that have been synthesized using a supercritical flow method. The resulting $MoO_x$ has much lower crystallinity and as a result a much higher surface area than those produced by state of the art impregnation techniques. The first step of the synthesis deposits small $MoO_2$ nanoparticles on the surface, that are oxidized during calcination in an oxygen rich atmosphere. The oxidation

process might make a key difference as the $Mo^{6+}$ oxide is highly mobile[230] and leads to a good distribution of the oxide across the surface.

Neither $MoO_3$ made by impregnation or supercritical synthesis forms large nanoparticles, as is seen from the absence of diffraction peaks on the on top of the substrate. PDF analysis reveals that low temperature flow reactor synthesis and the impregnation method create material with high degree of crystallinity consistent with the $MoO_3$ phase. The local structure of the amorphous oxides consists of loosely arranged $MoO_6$ octahedra in a series of edge to corner sharing ratios reminiscent of the crystalline $MoO_3$-like lattices[234]. This allows for a higher number of double bonded termination oxo-oxygen sites to be available to the methane conversion reactions[222]. These sites have been shown to have a higher activity towards conversion of methane through H-abstraction mechanism than the bridging-oxygen or ether oxygen sites[220] and have better selectivity. In addition, it appears that the previously reported molybdenum loading limit of 5wt% before large crystals of $MoO_3$ are formed can be surpassed[223]. In those catalysts a mixture of nanocrystalline and amorphous phase will be present.

To better understand the origin of the amorphous $MoO_x$, it would be a good idea to test more of the intermediate products, i.e. as prepared $MoO_2$ on zeolite samples. Originally, the middle stage samples were not deemed to be worth keeping. This study changes that assessment and samples before calcination are being prepared for future measurements. Ultimately, some work is needed to assess the degeneracy of the octahedral vs. pyramidal vs. tetrahedral models in an effort to report the results accurately.

# 8

# Characterization of TiNx thin films for plasmonic applications

The chapter describes a study of nanocrystalline thin films grown by atomic layer deposition process. The results of the study are a collaboration on the investigation of properties of $TiN_x$ films together with DTU Photonics. The films change their optical response as they undergo a treatments at various high temperatures. The annealing process happens in a highly controlled environment close to vacuum, which indicates a likely structural transformation within the film as the main reason for the changing optical properties. The films are measured and analysis is attempted using the recently demonstrated tf-PDF method. The analysis turned out to be significantly more complicated than anticipated for practical reasons. Despite the difficulties in analyzing the data, some structural information was extracted. In the following chapet, the analysis is presented, together with suggested strategies for further investigation.

## 8.1 Introduction

Surface Plasmons (SP) and the Surface Plasmon Resonance (SPR) phenomena have been known for over four decades merging the fields of optics and nanophotonics. Light interaction with nanoscale materials with negative real permittivity, such as metals and doped semiconductors, creates waves that propagate along the surface. These waves interact with the surface free electrons that start to oscillate in resonance with the incident wave. The effect leads to tight confinement and significant amplification of the light waves propagating along the material.[238]. These unusual properties have found a range of application in areas like photo catalysis[239], telecommunications[240, 241], therapeutics[242] and information processing[243], through the ability to concentrate and channel light using sub wavelength nanoscale structures.

One the most promising application areas for SP is in the field of biosensing[244, 245]. Here the ability to trace small amounts of analytes by amplifying the signal in tightly confined spaces allows for designing novel point-of-care diagnostic devices that are fast, precise and inexpensive[246]. Engineering arrays of periodic nanoscale structures makes multiplexing of sensing units possible, leading to implementations of sophisticated lab-on-a-chip systems[247].

Traditional metals of choice for plasmonic applications are silver and gold. These metals are expensive and fail in the key requirements for application in biosensing devices, namely stability and robustness. Silver is prone to oxidation, which ruins its plasmonic response, and gold films have a fairly low melting point. This makes both metals unusable for refractory sensing. They are also incompatible with CMOS processing due to their mobility.

Bypassing these limits has been a major goal within research into new metamaterials. Among these, transition metal nitrides offer particularly interesting properties in the near infrared (NIR) range[248, 249]. Titanium nitride in particular is a promising material. It has optical properties similar to gold while having a significantly higher melting temperature. It is mechanically stable and CMOS compatible[250] allowing for a wide range of microstructuring.

Recently a study by E. Shkondin et al.[251] reported on fabrication of high aspect ratio $TiN_x$ structures with high sensitivity towards refractive indices of various ambient liquids for applications in biosensing. The films optical response changes with annealing temperatures, changing from silver colored film as deposited at 500°C, to copper coloured, to golden, as the annealing temperature is increased. The films are annealed in a tightly controlled oxygen free near vacuum environment. This suggests that the change in optical response is due to a structural modification. The changing color of the film is shown in Fig. 8.1c). This follow up study attempts to investigate the origins of the changing optical response due to processing conditions. The recently demonstrated thin film PDF technique[123] is an ideal candidate to investigate the material. The films appear highly nanocrystalline and the PDF analysis technique is ideal for examining the local changes within the material at
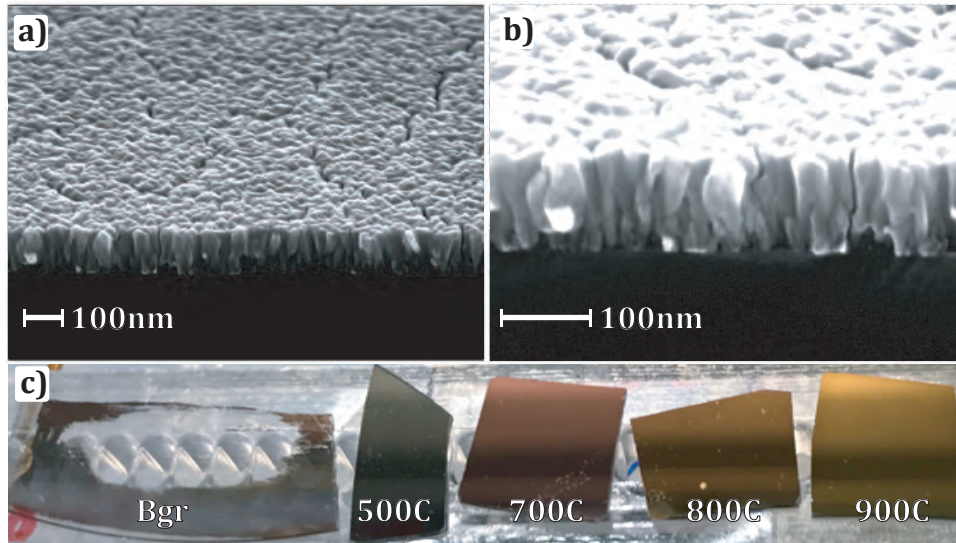
Figure 8.1: a) SEM micrograph of ALD grown TiNx thin films. b) Zoom in onto the interface of a). Grain orientation in the growth direction perpendicular to the surface can be seen. c) Samples of $TiN_x$ films measured for the study. Left to right: reference sample/background, ALD prepared $TiN_x$ film at 500C, film annealed for 1 hour at 700°C, 800°C and 900°C respectively.

the nanoscale. Understanding the structural transformations involved will allow to tailor the optical properties to a given application.

## 8.2 Experimental methods

### TiNx film preparation

TiN films were fabricated in a class 100 cleanroom as described in Shkondin, et. al[251]. The film was deposited in a R-200 Advanced Plasma ALD hot-wall reactor at 500°C from a $TiCl_4$ and $NH_3$ precursors at a growth rate of 0.025nm/cycle. The total film thickness was determined to be 160nm by spectroscopic ellipsometry and SEM cross-sectional measurements.

The films were annealed at 3 different temperatures of 700°C, 800°C and 900°C in PEO-604 furnace from ATV Technologie GMBH. To achieve an oxygen free atmosphere the system went through several pump-purge steps over a course of one hour. The samples were then heated up to the target temperature over the course of 30 minutes and annealed for 1 hour in vacuum with $N_2$ flow rate of 20 sccm. The system was allowed to cool down to room temperature in vacuum with a small flow of nitrogen.

### X-ray diffraction measurements

The x-ray powder diffraction measurements were performed at the beamline ID-11-B at Advanced Photon Source, ANL, Chicago. The diffraction experiments were performed in a transmission geometry and the diffracted signal was collected using a 2D Perkin-
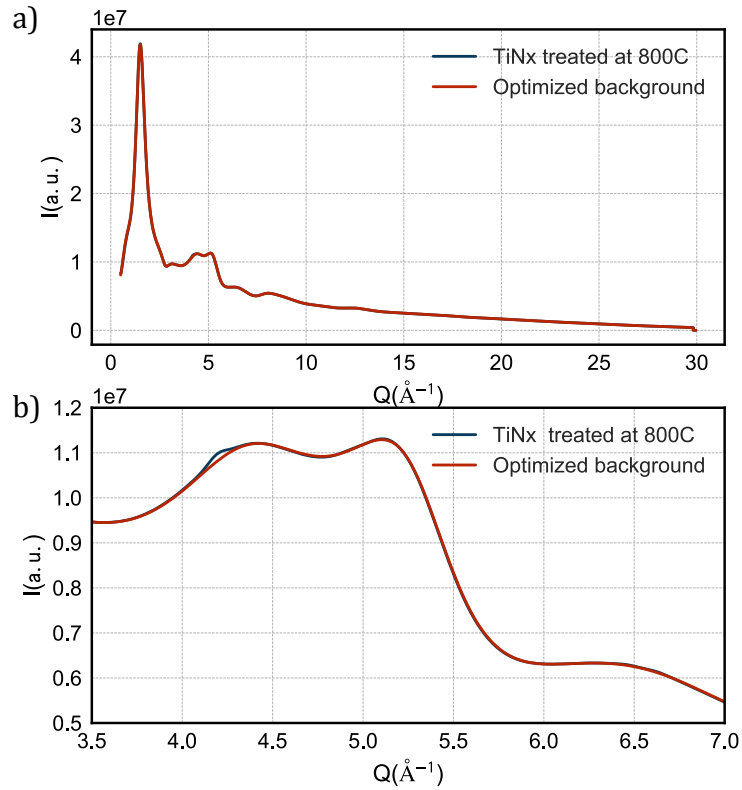
Figure 8.2: a) A diffraction pattern from the TiNx film treated at 800C overlayed with the background measurement. b) Upon closer inspection, the Bragg peaks from the thin film materials can be seen.

Elmer detector at a distance of 166mm. The incidence wavelength of the x-ray beam was 0.2113Å with a beam cross-section at the sample of 0.5mm in the vertical and the horizontal direction. The samples were mounted flat onto a movable sample changer perpendicular to the x-ray beam. A reference background was measured on the same sample changer together with the other samples. The sample-detector distance, and the geometric orientation of the detector were calibrated by measuring a standard $CeO_2$ powder. All measurements were performed at room temperature.

The experimental geometry parameters were calibrated using the Fit2D program [98]. A mask was created to remove outlier pixels and was applied to the 2D diffraction images before azimuthal integration to 1D diffraction patterns.

Instrumental effects like peak profile and peak broadening were calibrated using standard Rietveld refinement techniques on a reference NIST Si powder.

## 8.3   Background subtraction and phase identification

The samples contain approximately 100nm thick layer of material on top of 0.5mm fused silica wafer. As a result the majority of the diffracted signal stems from the substrate. Before any analysis can be performed the substrate signal needs to be removed. Figure 8.2 shows a typical diffraction pattern for the TiNx sample that has been treated at 800C.
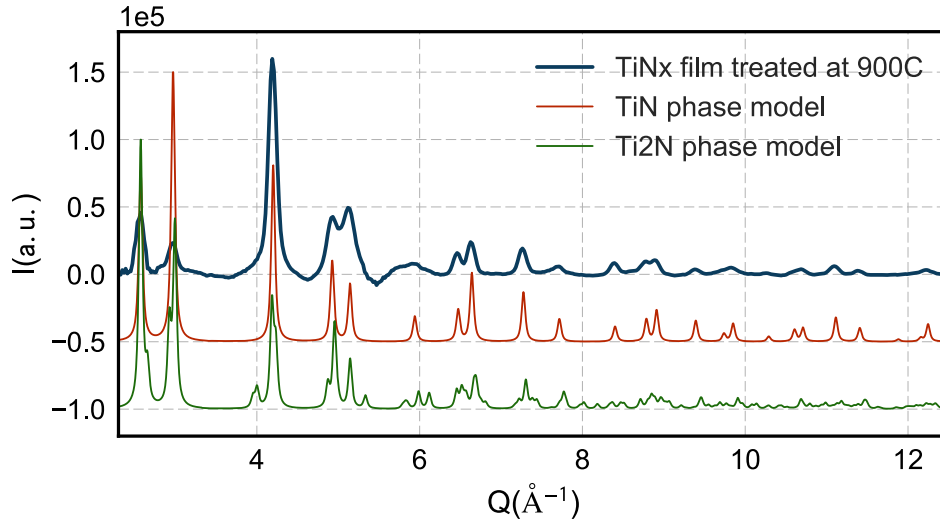
Figure 8.3: Calculated diffraction patterns for TiN and Ti$_2$N overlayed with the optimized background subtracted experimental data. The majority phase is TiN, however presence of Ti$_2$N can not be ruled out.

Upon zooming in weak Bragg peaks coming from the thin film material are seen.

The background can be subtracted from the total diffraction pattern to reveal the thin film material fingerprint. Due to variations within the substrate material, a perfect background subtraction is difficult[123]. A number of optimization steps, such as scaling by a constant factor were used to optimize the difference between the substrate and the full diffraction pattern. Unfortunately, a complete and clean subtraction was impossible due to small misalignments and roughness of the substrate. The decision was made to fit the remaining background signal using a cosine Fourier series in GSASII[88]. This is illustrated in Fig. 8.4, where the residual intensity from incomplete substrate subtraction is seen in Fig. 8.4a) and is removed by fitting a cosine series in Fig. 8.4b). The unfortunate consequence of this process is the removal of diffuse scattering intensity together with the residual from the glass substrate. This means that obtaining a reliable PDF signal becomes impossible.

Since the remaining signal displays clear Bragg reflections the decision was made to focus on the peak pattern alone. A number of related material phases were tested. TiN phase and Ti2N appear to be the best match with the majority phase being TiN after accounting for the instrumental broadening. This is further confirmed by structural refinements. The powder diffraction patterns for TiN and Ti2N overlayed with experimental data are seen in Fig. 8.3.

## 8.4 Structure refinements

To confirm the choice of the majority structural phase the Bragg peaks were indexed using a program GSASII. The most probable space group for the unit cell was $Fm-3m$ which is consistent with TiN. The relative intensities of the Bragg peaks in the data are
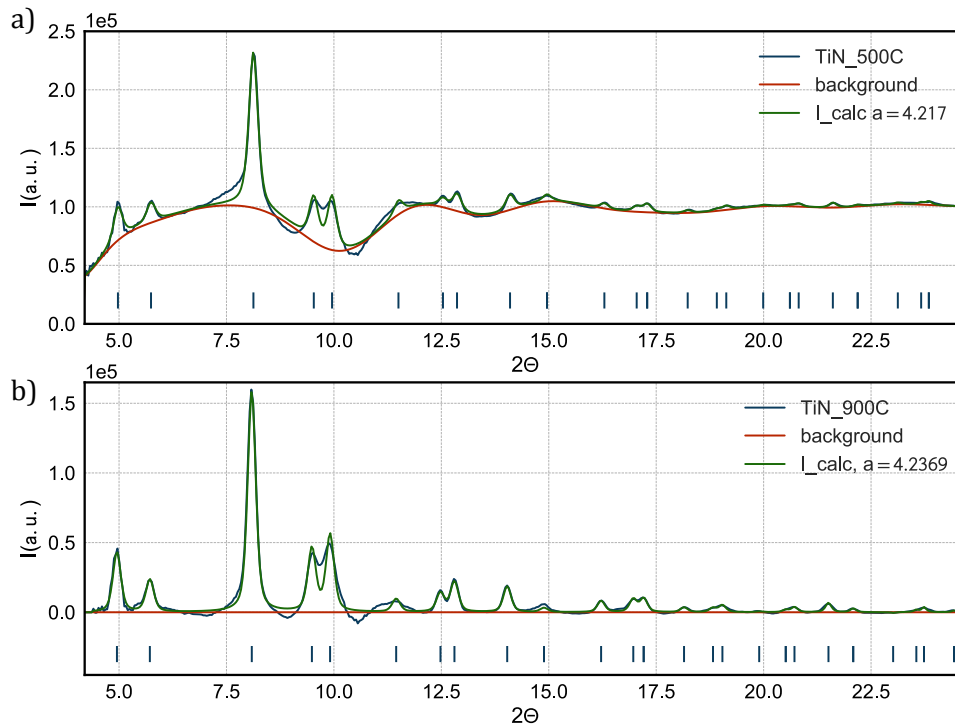
Figure 8.4: Pawley refinements of TiN$_x$ films. a) A single phase Pawley refinement fit to the as-deposited sample. b) The fit to the sample annealed at 900°C. TiN phase peak positions are indicated for reference. The sine background is subtracted in b) for illustration purposes.

not consistent with bulk material, most likely indicating a certain degree of preferred orientation within the film. A degree of elemental substitution of oxygen onto nitrogen sites or nitrogen vacancies is also possible and would contribute to the change in relative Bragg intensity across the pattern.

A Pawley refinement[252] was performed to extract the unit cell lattice parameter, as it allows to ignore the discrepancy in the relative peak intensity. This approach does not constrain the intensities yet still allows for accurate determination of the unit cell parameters without the need for a good model for lattice vacancies or preferred orientation.

A typical structure fit can be seen in Fig. 8.4. The refined parameters were peak intensities, unit cell lattice constant and the Scherrer broadening factor. Using just these parameters the fit results were sufficiently good. As an example, the weighted agreement factor is for the pattern in Fig. 8.4 was $R_{wp} = 4.65\%$.

## 8.5   Results

The structural refinements were performed in a similar way on all datasets, i.e. for 500°C, 700°C, 800°C and 900°C. The lattice parameter appears to be increasing with temperature treatment as seen from the results in Table 8.1.

Estimation of the crystallite sizes from the structural model[253] would be unreliable due to the way the background is modeled and subtracted. It is impossible to know where

| Temperature °C | Lattice Parameter a | Domain size [nm] | Aspect Ratio |
|---|---|---|---|
| 500°C | 4.217 | $37 \pm 8$ | $1.44 \pm 0.29$ |
| 700°C | 4.222 | $40 \pm 9$ | $1.40 \pm 0.26$ |
| 800°C | 4.233 | $45 \pm 11$ | $1.42 \pm 0.27$ |
| 900°C | 4.237 | $49 \pm 11$ | $1.39 \pm 0.26$ |

Table 8.1: Characterization results for TiNx films. Lattice parameters are obtained from Pawley structural refinements, domain sizes and domain aspect ratios are obtained by AFM.
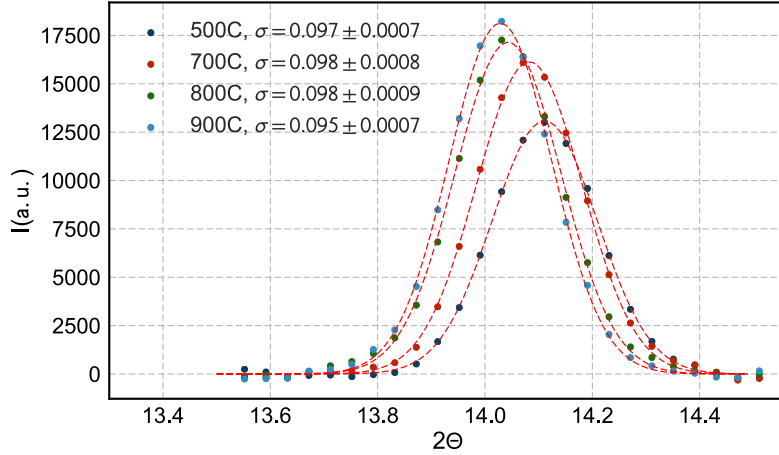


Figure 8.5: Scherrer broadening analysis of a [224] reflection for each treatment temperature. The width of Gaussian fit function does not change significantly indicating roughly the same crystallite size for all samples with a slight growth for the highest temperature. The peak shift is consistent with the lattice expansion.

the base of the peaks is: whether it is preserved or whether the background fitting leads to over-subtraction. A more reliable way would be to examine the change in crystallite size by comparing the peak broadening across the different samples. For this purpose an isolated and well defined Bragg peak was chosen in the high $Q$ region of the diffraction pattern and subsequently fit by a Gaussian function. The analysis on a 224 reflection shows no significant change in crystallite size up to the annealing temperature of 800°C. The crystallites appear to grow only for the annealing temperature of 900°C, which is illustrated in Fig. 8.5. The absolute values for crystallite size could not be extracted with a high degree of accuracy for reasons presented above, however given the instrumental broadening the approximate size would be around $\approx 35$nm growing to around $\approx 45$nm after treatment at 900°C. Notably, the change of this magnitude is right at the resolution limit of the instrument in PDF measurement configuration and complementary information is required to achieve any degree of certainty.

The hypothesis about grain size growth due to annealing at high temperature is further confirmed by the later obtained Atomic Force Microscopy(AFM) and Scanning Electron Microscopy(SEM) data of the samples. This provides a more direct, albeit very local, information about the size distribution compared to the average crystallite size obtained
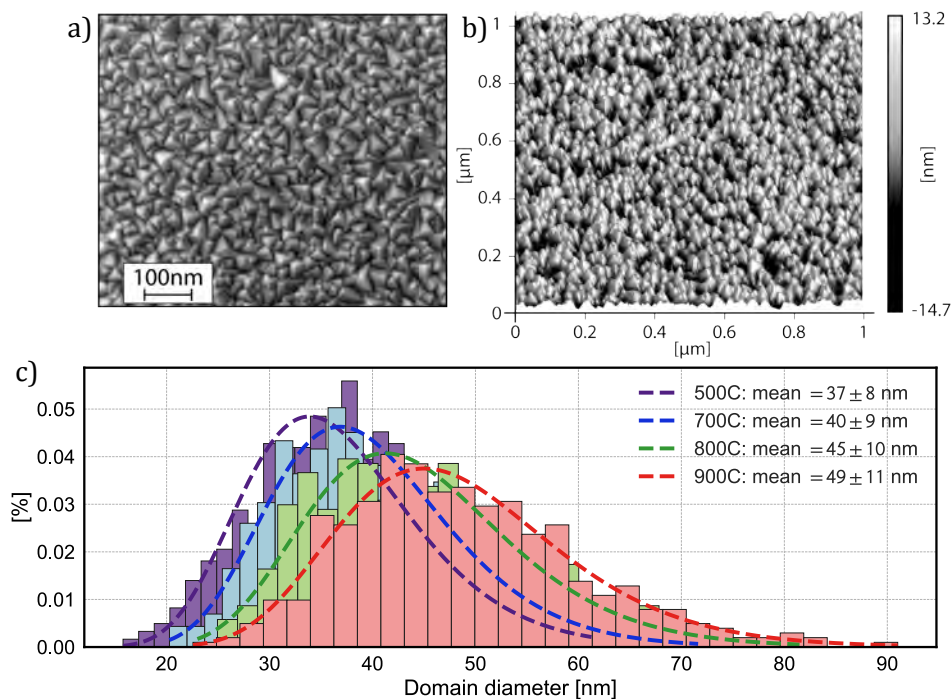
Figure 8.6: a) SEM image of the surface of the sample as prepared at 500°C. b) Height map obtained from an AFM measurement. c) Particle counting histograms for all samples with the corresponding LogNormal distribution fits. The domain size is expressed via a diameter of the circle with the surface area of the domain.

by XRD. The results are presented in Fig 8.6. The domain size increases for all annealing temperatures. The size distributions for the annealed samples are well described by a Log-Normal distribution, while the initially prepared sample is better described by a Gaussian, illustrated in Fig 8.6c) and grows from an average of 37nm up to an average of 49nm for the highest annealing temperature

The crystallites at the surface have a degree of anisotropy as is seen on the height map of the 500°C sample in Fig 8.6b). The aspect ratio here is defined as the longest dimension divided by the orthogonal width, e.g. a square or a circle would have an aspect ratio of 1. The images and the AFM data show elongated triangular grains with an average aspect ratio of 1.4. While the domain size is growing, the aspect ratio appears to stay consistent, indicating that the shape of the crystallites is preserved and that they grow in an isotropic manner. This does not mean that the grains themselves are isotropic and a large part of them is hidden underneath the surface. This is obvious from the image in Fig. 8.1a) and 8.1b) and supports the hypothesis of preferred orientation in a direction perpendicular to the surface of the substrate.

## 8.6   Conclusions

Due to the amount of signal from the deposited material compared to the substrate, a number of trade-offs had to be made to extract structural information with confidence. As the

substrate varies slightly across the surface, the background subtracted powder diffraction patterns cannot provide all of the information of a typical powder diffraction experiment. This includes accurate determination of crystallite sizes and accurate determination of the presence of multiple phases within the sample. Unit cell indexing and the structural refinements are consistent with the majority phase of TiN, however, it is impossible to rule out the presence of $Ti_2N$ or similar phases completely.

The patterns show signs of preferred orientation due to disproportionate intensities from particular reflections, clearly seen in the intensity of the [002] Bragg peak. It would be difficult to produce a model to account for these effects and given the background subtraction quality the effort is not justified.

The main observed effect is the expansion of the lattice for each treatment temperature. One likely cause for this effect is the strain within the material. Thin films are often strained and are known to relax upon heating[92]. The lattice expansion of a sol-gel TiN phase was also reported in a recent study[248]. It was explained by the partial oxidation and substitution of oxygen into the lattice leading to it's compression. This is however unlikely to be the reason in our experiment due to absence of oxygen during the deposition and annealing.

It is important to note that the values for lattice constants obtained from structural refinements in the study are likely offset from the real value due to experimental limitations. They are, however, consistent across all samples within the experiment. For accurate absolute determination of the lattice constant or to determine whether the the values are larger or smaller than bulk TiN a follow up experiment with an internal calibrant would be needed.

A comparative analysis of the peak broadening was performed to examine the patterns for relative changes in crystallinity using the Scherrer broadening equation. The results of this analysis show similar peak profiles across all temperatures with slight change after 900°C treatment. The absolute crystallite sizes could not be determined accurately from XRD analysis with estimated sizes growing from around 35nm to 45nm. The AFM study results show a consistent growth of the crystallites for all annealing temperatures. The domain sizes obtained from AFM were between 37nm and 49nm and are summarized in Table 8.1. This indicates once again, that x-ray diffraction measurements in PDF configuration lack resolution for this type of analysis in this range of crystallite sizes.

Due to the horrendous background mismatch and the inability to properly subtract it, the PDF analysis could not be employed on the available data, but could potentially be of great value to the study. The ability to examine local restructuring of the film would be very valuable, as would be the ability to analyze the presence and potential relaxation of compressive strain[38].

Together with growing domains, the changing lattice parameter could be the key to the changing plasmonic properties of the material, as the permittivity is heavily dependent on domain size and structure[254]. A more rigorous x-ray experiment could be performed in grazing incidence and reflection geometry on a recently realized Grazing Incidence PDF(GI-

PDF) beamline at PetraIII. This will allow to capture more signal from the material and avoid the scattering from the background.

The results outlined in this chapter are ultimately a work in progress. The samples are scheduled for a grazing incidence measurements and are also currently being studied by X-ray Photoelectron Spectroscopy (XPS) to determine the spatial change in elemental composition along the growth direction of the film.

# 9

# Conclusions

Pair distribution function analysis is a great tool for characterization of nanomaterials. It has experienced an incredible growth in the number of users worldwide over the past decade. This success largely owes itself to the development of the new methods and instrumentation. Since the advent of RA-PDF method, it became clear that good quality PDF data could be acquired in minutes instead of hours that it took previously. Today, with the third generation synchrotrons, in many cases this time is reduced to seconds. Every new synchrotron facility built today aims to provide multiple experimental station capable of PDF measurements. As an example, 1-ID-B,C,E, 6-ID-D, 11-ID-B, 11-ID-C and 17-BM-B beamlines at the Advanced Photon Source in Chicago all advertise the capability for PDF measurements. So do P.02-1 and P.07 beamlines at PetraIII in Hamburg. The newly built MAXIV synchrotron is also in the process of constructing its own powder diffraction and PDF end station and the list does not end there.

Today the technique is more relevant than ever. New software makes it more accessible to researchers with different backgrounds and skill sets. Software like PFGui has an easy to use graphical interface and has become the go to analysis tool for small box modeling using PDF analysis. Commercial programs like TOPAS from Bruker and HighScore from PANalytical have also implemented features aimed at total scattering studies. New versions are constantly being released promising more features while being even more accessible, customizable and efficient.

Efficiency is the keyword in the industrial context. The project was successful in developing and using new tools for rapid data reduction and analysis. These tools consist of a software protocol that significantly speeds up the analysis of large sequential datasets. The software mapPDF was designed to integrate seamlessly with the experimental stations, specifically the XPD beamline at NSLSII, reducing the effort required for data reduction and exploratory analysis.

mapPDF software was then used to gain a better understanding of a copper reduction process. The process is aimed at producing large quantities of copper nanoparticles for use in printed electronics such as sensors, solar cells and wearable devices. Using PDF analysis and the specialized flow synthesis measurement setup it was possible to observe

the reduction of copper from an ionic solution to metallic form in-situ. The reduction rate of copper by glucose was determined to be limited by the kinetics of the reactants. It was also determined that glucose is an effective capping agent, able to protect the metallic particles from oxidation without the need for additional surfactants. The analysis of the in-situ datasets benefitted heavily from the existence of the new software. A workflow has been established for the future measurements.

Using synchrotron x-ray PDF analysis it was possible to detect and characterize tiny PtPd and PtPdFe nanoparticles 2nm in diameter comprising just 1wt% of the sample. Despite the presence of highly disordered and strongly scattering support, it was possible to extract the crystallite sizes of these particles and detect a lattice contraction likely responsible for the materials better catalytic activity.

Similarly, it was possible to characterize amorphous molybdenum oxides at the surface of zeolites, a catalyst used for methane valorisation. Using PDF analysis it was possible to understand the difference between the reference catalyst prepared by impregnation and new catalysts prepared by hydrothermal flow method. While the reference catalyst exhibits clear signs of crystallinity, the new materials are mostly amorphous. This in turn leads to a much higher surface area and, as a result, better catalytic activity and selectivity. The amorphous molybdenum oxides consist of arrangements of several octahedrally coordinated molybdenum atoms that are spread around the zeolite surface with higher concentrations around the pores of the zeolite. It was possible to prepare catalysts with higher loadings than the experimentally determined threshold for molybdenum loading before decrease in catalytic activity.

The development of new tools for PDF analysis is crucial for pushing the technique forward. An example of this is the attempt at characterizing a restructuring of TiN film due to thermal annealing. Despite the successes of tf-PDF method, it is still extremely difficult to use and often fails in non-ideal conditions. It was still possible to extract valuable information about the lattice expansion of the film as an effect of the annealing. The films were also found to have high degrees of preferred orientation. The crystallites are growing as the temperature is increased. The lattice expansion together with growing crystallite sizes could be the reason for the changing optical properties of the material.

Industrial research moves at a different pace compared to a typical academic group. It is typically more streamlined and focused on applications, rather than complete understanding of all the aspects of the problem. The labor intensity and the availability, makes PDF analysis much better suited for understanding the studied system, rather than for process development. The discoveries made throughout the project helped understand the material, as in the case for PtPdFe and $MoO_x$. The knowledge gained suggests new avenues of research and new parameter space to explore. A common difficulty throughout the project was staying relevant and not falling behind the development process. In the case of copper reduction study, the new developed tools will significantly help the future studies by allowing rapid characterization of the latest process.

Despite the conclusions being focused at synchrotron pair distribution function analysis,

they apply to all powerful and specialized, yet time consuming techniques. Development of new and more efficient instrumentation and data analysis workflows is key to keeping up with the demand for rapid analysis.

# Bibliography

[1] S. Banerjee, C.-H. Liu, J. D. Lee, A. Kovyakh, V. Grasmik, O. Prymak, C. Koenigs-mann, H. Liu, L. Wang, A. M. M. Abeykoon, S. S. Wong, M. Epple, C. B. Murray, and S. J. L. Billinge, "Improved models for metallic nanoparticle cores from atomic pair distribution function (PDF) analysis ," *Manuscript (submitted)*.

[2] H. Silva, P. Hernandez-Fernandez, A. Baden, H. Hellstern, A. Kovyakh, E. Wisaeus, I. Chorkendorff, L. Christensen, D. Chakraborty, and C. Kallesøe, "Supercritical Flow Synthesis of Cost-effective PtPdFe nanoparticles for Low-temperature Diesel Oxidation," *Manuscript (submitted)*.

[3] F. X. Redl, K. S. Cho, C. B. Murray, and S. O'Brien, "Three-dimensional binary su-perlattices of magnetic nanocrystals and semiconductor quantum dots," *Nat. Mater*, vol. 423, no. 6943, pp. 968–971, 2003.

[4] K. Nomura, H. Ohta, A. Takagi, T. Kamiya, M. Hirano, and H. Hosono, "Room-temperature fabrication of transparent flexible thin-film transistors using amorphous oxide semiconductors," *Nat. Mater*, vol. 432, pp. 488–492, Nov. 2004.

[5] Z. Yi, J. Ye, N. Kikugawa, T. Kako, S. Ouyang, H. Stuart-Williams, H. Yang, J. Cao, W. Luo, Z. Li, Y. Liu, and R. L. Withers, "An orthophosphate semicon-ductor with photooxidation properties under visible-light irradiation," *Nat. Mater*, vol. 9, pp. 559–564, July 2010.

[6] P. Panek, R. P. Socha, G. Putynkowski, and A. Slaoui, "The New Copper Composite of Pastes for Si Solar Cells Front Electrode Application," *Energy Procedia*, vol. 92, pp. 962–970, Aug. 2016.

[7] R. Wagner, G. J. Redhammer, D. Rettenwander, A. Senyshyn, W. Schmidt, M. Wilkening, and G. Amthauer, "Crystal Structure of Garnet-Related Li-Ion Con-ductor Li 7–3 xGa xLa 3Zr 2O 12: Fast Li-Ion Conduction Caused by a Different Cubic Modification?," *Chem. Mater.*, vol. 28, pp. 1861–1871, Mar. 2016.

[8] S. M. Janib, A. S. Moses, and J. A. MacKay, "Imaging and drug delivery using theranostic nanoparticles," *Adv. Drug Deliv. Rev.*, vol. 62, no. 11, pp. 1052–1063, 2010.

[9] A. I. Frenkel, C. W. Hills, and R. G. Nuzzo, "A view from the inside: Complexity in the atomic scale ordering of supported metal nanoparticles," *Journal of Physical Chemistry B*, vol. 105, no. 51, pp. 12689–12703, 2001.

[10] S. E. Hunyadi Murph, K. J. Coopersmith, and G. K. Larsen, *Nanoscale Materials: Fundamentals and Emergent Properties*, vol. 37 of *Nanostructure Science and Technology*. Cham: Springer International Publishing, July 2017.

[11] A. N. Goldstein, C. M. Echer, and A. P. Alivisatos, "Melting in Semiconductor Nanocrystals," *Science*, vol. 256, no. 5062, pp. 1425–1427, 1992.

[12] P. Ball and L. Garwin, "Science at the atomic scale," *Nat. Mater*, vol. 355, pp. 761–766, Feb. 1992.

[13] V. Petkov, S. Shastri, S. Shan, P. Joseph, J. Luo, C.-J. Zhong, T. Nakamura, Y. Herbani, and S. Sato, "Resolving Atomic Ordering Differences in Group 11 Nano-sized Metals and Binary Alloy Catalysts by Resonant High-Energy X-ray Diffraction and Computer Simulations," *J. Phys. Chem. C*, vol. 117, pp. 22131–22141, Oct. 2013.

[14] H. Liu, C. Koenigsmann, R. R. Adzic, and S. S. Wong, "Probing Ultrathin One-Dimensional Pd–Ni Nanostructures As Oxygen Reduction Reaction Catalysts," *ACS Catal.*, vol. 4, pp. 2544–2555, Aug. 2014.

[15] V. Petkov, B. Prasai, S. Shastri, J.-W. Kim, S. Shan, H. R. Kareem, J. Luo, and C.-J. Zhong, "Surface Atomic Structure and Functionality of Metallic Nanoparticles: A Case Study of Au–Pd Nanoalloy Catalysts," *J. Phys. Chem. C*, vol. 121, pp. 7854–7866, Am. Pharm. Rev. 2017.

[16] G. Bergeret and P. Gallezot, *Particle Size and Dispersion Measurements*, vol. 15 of *Online*. Weinheim, Germany: American Cancer Society, 3 ed., Mar. 2008.

[17] I. Chorkendorff and J. W. Niemantsverdriet, "Concepts of Modern Catalysis and Kinetics, Third Edition," 2017.

[18] S. R. S. Rocco, "Peak Silver & Continued Supply Deficits Warn Of Future High Prices."

[19] "European Spallation Source (ESS) synkrotronstråling og andre større infrastruktur-satsninger i et dansk perspektiv."

[20] Haldo Topsøe A/S, "Research principles."

[21] B. E. Warren and N. S. Gingrich, "Fourier Integral Analysis of X-Ray Powder Patterns," *Phys. Rev.*, vol. 46, p. 368, Sept. 1934.

[22] P. J. Chupas, X. Qiu, J. C. Hanson, P. L. Lee, C. P. Grey, and S. J. L. Billinge, "Rapid acquisition pair distribution function analysis (RA-PDF)," *J. Appl. Crystallogr.*, vol. 36, pp. 1342–1347, 2003.

[23] R. Cerny and V. Favre-Nicolin, "Direct space methods of structure determination from powder diffraction: principles, guidelines and perspectives," *Z. Kristallogr. - New Cryst. Struct.*, vol. 222, no. 3-4, pp. 105–113, 2007.

[24] S. J. L. Billinge, T. Dykhne, P. Juhas, E. Božin, R. Taylor, A. J. Florence, and K. Shankland, "Characterisation of amorphous and nanocrystalline molecular materials by total scattering ," *CrystEngComm*, vol. 12, no. 5, pp. 1366–1368, 2010.

[25] M. W. Terban, *Characterizing the atomic structure in low concentrations of weakly ordered, weakly scattering materials using the pair distribution function* . PhD thesis, Sept. 2017.

[26] K. M. Ø. Jensen, C. Tyrsted, M. Bremholm, and B. B. Iversen, "In Situ Studies of Solvothermal Synthesis of Energy Materials," vol. 7, pp. 1594–1611, June 2014.

[27] Y. Wang, M. Klenk, K. Page, and W. Lai, "Local Structure and Dynamics of Lithium Garnet Ionic Conductors: A Model Material Li5La3Ta2O12," *Chem. Mater.*, vol. 26, no. 19, pp. 5613–5624, 2014.

[28] W. H. Bragg, "The reflection of x-rays by crystals," *Nano Lett.*, vol. 91, p. 477, 1913.

[29] P. Debye and P. Scherrer, "Interferenzen an regellos orientierten Teilchen im Röntgenlicht. I.," *Nachrichten von der Gesellschaft der Wissenschaften zu Göttingen, Mathematisch-Physikalische Klasse*, vol. 1916, pp. 1–15, 1916.

[30] W. Paszkowicz, "Ninety years of powder diffraction: From birth to maturity," *Sync. Rad. in Nat. Sci.*, Feb. 2006.

[31] H. M. Rietveld, "Line profiles of neutron powder-diffraction peaks for structure refinement," *Acta Crystallogr.*, vol. 22, pp. 151 – 152, 1967.

[32] M. L. Steigerwald and L. E. Brus, "Synthesis, stabilization, and electronic structure of quantum semiconductor nanoclusters," *Annu. Rev. Mater. Sci*, 1989.

[33] B. Gilbert, F. Huang, H. Zhang, G. A. Waychunas, and J. F. Banfield, "Nanoparticles: Strained and Stiff," *Science*, vol. 305, pp. 651–654, July 2004.

[34] B. E. Warren, "X-ray diffraction study of carbon black," *J. Phys. Chem.*, vol. 2, p. 551, 1934.

[35] B. E. Warren, H. Krutter, and O. Morningstar, "Fourier analysis of x-ray patterns of vitreous $sio_2$ and $b_2o_3$," vol. 19, pp. 202–6, 1936.

[36] C. L. Farrow and S. J. L. Billinge, "Relationship between the atomic pair distribution function and small angle scattering: implications for modeling of nanoparticles," *Acta Crystallogr. A*, vol. 65, no. 3, pp. 232–239, 2009.

[37] R. E. Dinnebier and S. J. L. Billinge, *Powder Diffraction: Theory and Practice*. RSC Publishing, Mar. 2008.

[38] A. S. Masadeh, E. S. Božin, C. L. Farrow, G. Paglia, P. Juhás, A. Karkamkar, M. G. Kanatzidis, and S. J. L. Billinge, "Quantitative size-dependent structure and strain determination of CdSe nanoparticles using atomic pair distribution function analysis," *Phys. Rev. B*, vol. 76, p. 115413, 2007.

[39] H. Ohtaki and M. Maeda, "An X-Ray Diffraction Study of the Structure of Hydrated Copper(II) Ion in a Copper(II) Perchlorate Solution," *BCSJ*, vol. 47, pp. 2197–2199, Sept. 1974.

[40] T. Egami, B. H. Toby, S. J. L. Billinge, C. Janot, J. D. Jorgensen, D. G. Hinks, M. K. Crawford, W. E. Farneth, and E. M. McCarron, "Local structural anomaly at tc observed by neutron scattering," in *High Temperature Superconductivity: Physical Properties, Microscopic Theory and Mechanisms* (J. Ashkenazi *et al.*, eds.), (New York), Plenum, 1992.

[41] T. Proffen, S. J. L. Billinge, and IUCr, "PDFFIT, a program for full profile structural refinement of the atomic pair distribution function," *J. Appl. Crystallogr.*, vol. 32, pp. 572–575, June 1999.

[42] A. Cervellino, R. Frison, N. Masciocchi, and A. Guagliardi, "X-Ray Powder Diffraction Characterization of Nanomaterials," in *X-ray and Neutron Techniques for Nanomaterials Characterization*, pp. 545–608, Springer, Berlin, Heidelberg, 2016.

[43] C. L. Farrow, C. Shi, P. Juhás, X. Peng, and S. J. L. Billinge, "Robust structure and morphology parameters for CdS nanoparticles by combining small angle X-ray scattering and atomic pair distribution function data in a complex modeling framework," *J. Appl. Crystallogr.*, vol. 47, pp. 561–565, 2014. Selected as journal cover.

[44] K. Kodama, S. Iikubo, T. Taguchi, and S. Shamoto, "Finite size effects of nanoparticles on the atomic pair distribution functions," *Acta Crystallogr. A*, vol. 62, pp. 444–453, 2006.

[45] L. Gamez-Mendoza, M. W. Terban, S. J. L. Billinge, and M. Martinez-Inesta, "Modelling and validation of particle size distributions of supported nanoparticles using the pair distribution function technique," *J. Appl. Crystallogr.*, vol. 50, pp. 741–748, June 2017.

[46] C. L. Farrow, P. Juhás, J. Liu, D. Bryndin, E. S. Božin, J. Bloch, T. Proffen, and S. J. L. Billinge, "PDFfit2 and PDFgui: Computer programs for studying nanostructure in crystals," *J. Phys: Condens. Mat.*, vol. 19, p. 335219, 2007.

[47] P. Juhás, C. L. Farrow, X. Yang, K. R. Knox, and S. J. L. Billinge, "Complex modeling: a strategy and software program for combining multiple information sources to solve ill-posed structure and nanostructure inverse problems," *Acta Crystallogr. A*, vol. 71, pp. 562–568, Nov 2015.

[48] X. Yang, A. S. Masadeh, J. R. McBride, E. S. Božin, S. J. Rosenthal, and S. J. L. Billinge, "Confirmation of disordered structure of ultrasmall CdSe nanoparticles from x-ray atomic pair distribution function analysis," *Phys. Chem. Chem. Phys.*, vol. 15, no. 22, pp. 8480–8486, 2013.

[49] B. Gilbert, F. Huang, H. Zhang, G. A. Waychunas, and J. F. Banfield, "Nanoparticles: Strained and stiff," *Science*, vol. 305, pp. 651–654, 2004.

[50] S. Alayoglu, P. Zavalij, B. Eichhorn, Q. Wang, A. I. Frenkel, and P. Chupas, "Structural and Architectural Evaluation of Bimetallic Nanoparticles: A Case Study of Pt−Ru Core−Shell and Alloy Nanoparticles," *J. Phys. Chem. B*, Sept. 2009.

[51] V. Petkov, B. Prasai, S. Shastri, and T.-Y. Chen, "3D Atomic Arrangement at Functional Interfaces Inside Nanoparticles by Resonant High-Energy X-ray Diffraction," *ACS Appl. Mater. Interfaces*, vol. 7, no. 41, pp. 23265–23277, 2015.

[52] M. Zobel, R. B. Neder, and S. A. J. Kimber, "Universal solvent restructuring induced by colloidal nanoparticles," *Science*, vol. 347, no. 6219, pp. 292–294, 2015.

[53] V. V. T. Doan-Nguyen, S. A. J. Kimber, D. Pontoni, D. R. Hickey, B. T. Diroll, X. Yang, M. Miglierini, C. B. Murray, and S. J. L. Billinge, "Bulk metallic glass-like scattering signal in small metallic nanoparticles," *ACS Nano*, vol. 8, no. 6, p. 6163–6170, 2014.

[54] K. M. Ø. Jensen, P. Juhas, M. A. Tofanelli, C. L. Heinecke, G. Vaughan, C. J. Ackerson, and S. J. L. Billinge, "Polymorphism in magic sized $Au_{144}(SR)_{60}$ clusters," *Nat. Commun.*, vol. 7, p. 11859, 2016.

[55] R. E. Franklin, "*," *Acta Crystallogr.*, vol. 3, p. 107, 1950.

[56] A. C. Wright, "Diffraction studies of glass structure: the first 70 years," vol. 24, pp. 148–179, 1998.

[57] A. C. Barnes, H. E. Fischer, and P. S. Salmon, "Structure of disordered systems and liquid metal alloys," vol. 111, pp. 59–96, 2003.

[58] O. Gereben and L. Pusztai, "Structure of amorphous semiconductors: Reverse Monte Carlo studies on $a$-C, $a$-Si, and $a$-Ge," *Phys. Rev. B*, vol. 50, p. 14136, Nov. 1994.

[59] S. J. L. Billinge and I. Levin, "The problem with determining atomic structure at the nanoscale (vol 316, pg 561, 2007)," *Science*, vol. 316, no. 5832, pp. 1698–1698, 2007.

[60] X.-c. Bai, G. McMullan, and S. H. W. Scheres, "How cryo-EM is revolutionizing structural biology," *Trends in Biochemical Sciences*, vol. 40, pp. 49–57, Jan. 2015.

[61] X. Li, P. Mooney, S. Zheng, C. R. Booth, M. B. Braunfeld, S. Gubbens, D. A. Agard, and Y. Cheng, "Electron counting and beam-induced motion correction enable near-atomic-resolution single-particle cryo-EM," *Nat. Method.*, vol. 10, pp. 584–590, June 2013.

[62] W. D. Pyrz and D. J. Buttrey, "Particle Size Determination Using TEM: A Discussion of Image Acquisition and Analysis for the Novice Microscopist," *J. Phys. Chem. B*, Aug. 2008.

[63] C. L. Farrow, S. J. L. Billinge, and IUCr, "Relationship between the atomic pair distribution function and small-angle scattering: implications for modeling of nanoparticles," *Acta Crystallogr A Found Crystallogr*, vol. 65, pp. 232–239, May 2009.

[64] A. Guinier, "La diffraction des rayons X aux très petits angles : application à l'étude de phénomènes ultramicroscopiques," *Ann. Phys.*, vol. 11, pp. 161–237, Apr. 2017.

[65] G. Porod, "Die Röntgenkleinwinkelstreuung von dichtgepackten kolloiden Systemen," *Zeitschrift für Physik*, 1951.

[66] B. R. Pauw, J. S. Pedersen, S. Tardif, M. Takata, and B. B. Iversen, "Improvements and considerations for size distribution retrieval from small-angle scattering data by Monte Carlo methods," *J. Appl. Crystallogr.*, vol. 46, pp. 365–371, Apr. 2013.

[67] H. Schnablegger and Y. Singh, *The SAXS Guide.* Anton Paar GmbH, 2 ed., Oct. 2011.

[68] L. A. Feigin and D. I. Svergun, *Structure Analysis by Small-Angle X-Ray and Neutron Scattering.* Springer, 1 ed., July 1987.

[69] S. J. L. Billinge, "Nanometer scale structure from powder diffraction: Total scattering and atomic pair distribution function analysis," in *International Tables of Crystallography* (C. Gilmore *et al.*, eds.), vol. H, (Buffalo, NY), International Union of Crystallography, 2014. to be published.

[70] J. Becker, M. Bremholm, C. Tyrsted, B. Pauw, K. M. Ø. Jensen, J. Eltzholt, M. Christensen, and B. B. Iversen, "Experimental setup for in situX-ray SAXS/WAXS/PDF studies of the formation and growth of nanoparticles in near- and supercritical fluids," *J. Appl. Crystallogr.*, vol. 43, pp. 729–736, May 2010.

[71] H. Jensen, M. Bremholm, R. P. Nielsen, K. D. Joensen, J. S. Pedersen, H. Birkedal, Y. S. Chen, J. Almer, E. G. Søgaard, S. B. Iversen, and B. B. Iversen, "In Situ High-Energy Synchrotron Radiation Study of Sol–Gel Nanoparticle Formation in Supercritical Fluids," *Angew. Chem.*, vol. 119, no. 7, pp. 1131–1134, 2007.

[72] J. Als-Nielsen and D. McMorrow, *Elements of Modern X-ray Physics.* London, UK: John Wiley & Sons, Inc., second edition ed., Mar. 2011.

[73] A. Guagliardi and N. Masciocchi, *Diffraction at the Nanoscale: Nanocrystals, Defective and Amorphous Materials.* Insubria University Press, 2010.

[74] T. Egami and S. J. L. Billinge, *Underneath the Bragg peaks: structural analysis of complex materials.* Amsterdam: Elsevier, 2nd ed., 2012.

[75] J. Als-Nielsen and D. McMorrow, *Elements of Modern X-ray Physics.* New York: Wiley, 2001.

[76] P. Debye, "Zerstreuung von Röntgenstrahlen," *Ann. Phys.*, vol. 351, pp. 809–823, Jan. 1915.

[77] T. E. Faber and J. M. Ziman, "A theory of the electrical properties of liquid metals iii. the resistivity of binary alloys," *Philos. Mag.*, vol. 11, pp. 153–157, 1965.

[78] D. A. Keen, "A comparison of various commonly used correlation functions for describing total scattering," *J. Appl. Crystallogr.*, vol. 34, pp. 172–177, Apr. 2001.

[79] B. H. Toby and T. Egami, "Accuracy of pair distribution function analysis applied to crystalline and non-crystalline materials," *Acta Crystallogr A Found Crystallogr*, vol. 48, pp. 336–346, May 1992.

[80] R. A. Young, *The Rietveld Method*, vol. 5 of *International Union of Crystallography Monographs on Crystallography.* Oxford: Oxford University Press, 1993.

[81] I. Jeong, T. Proffen, F. Mohiuddin-Jacobs, and S. J. L. Billinge, "Measuring correlated atomic motion using x-ray diffraction," *J. Phys. Chem. A*, vol. 103, pp. 921–924, 1999.

[82] D. A. Keen, "Reverse monte carlo refinement of disordered silica phases," in *Local Structure from Diffraction* (S. J. L. Billinge and M. F. Thorpe, eds.), (New York), p. 101, Plenum, 1998.

[83] R. L. McGreevy and L. Pusztai, "Reverse Monte Carlo simulation: a new technique for the determination of disordered structures.," vol. 1, pp. 359–367, 1988.

[84] A. Guinier, G. Fournet, C. Walker, and K. Yudowitch, *Small-angle scattering of x-rays.* New York: John Wiley & Sons, Inc., 1955.

[85] J. S. Pedersen, *Neutrons, X-rays and Light. Scattering Methods Applied to Soft Condensed Matter, edited by P. Lindner & T. Zemb.* Amsterdam: Elsevier, 2002.

[86] D. S. Young, B. S. Sachais, and L. C. Jefferies, *The Rietveld Method.* 1993.

[87] J. Rodriguez-Carvajal, "Fullprof: A program for rietveld refinement and pattern matching analysis," in *Abstracts of the Satellite Meeting on Powder Diffraction of the XV Congress of the IUCr, Toulouse, France*, 1990.

[88] R. V. Dreele, "Gsas-ii-crystallography data analysis software." https://subversion.xor.aps.anl.gov/trac/pyGSAS, 2013.

[89] L. Lutterotti, H. Wenk, and S. Matthies, "MAUD (Material Analysis Using Diffraction): a user friendly Java program for Rietveld Texture Analysis and more," *iris.unitn.it*, vol. 2, pp. 1599–1604, 1999.

[90] P. Scherrer, "Göttinger Nachrichten," 1918.

[91] C. Y. Yang, "Crystallography of decahedral and icosahedral particles: I. Geometry of twinning," *J. Cryst. Growth*, vol. 47, pp. 274–282, Aug. 1979.

[92] R. E. Dinnebier and S. J. L. Billinge, eds., *Powder diffraction: theory and practice.* London, England: Royal Society of Chemistry, 2008.

[93] S. C. Leemann, "Pulsed sextupole injection for Sweden's new light source MAX IV," *Phys. Rev. ST Accel. Beams*, vol. 15, no. 5, p. 050705, 2012.

[94] S. Kubota, T. Morioka, M. Takesue, H. Hayashi, M. Watanabe, and R. L. Smith Jr, "Continuous supercritical hydrothermal synthesis of dispersible zero-valent copper nanoparticles for ink applications in printed electronics," *J. Supercrit. Fluids*, vol. 86, pp. 33–40, Feb. 2014.

[95] S. Jang, Y. Seo, J. Choi, T. Kim, J. Cho, S. Kim, and D. Kim, "Sintering of inkjet printed copper nanoparticles for flexible electronics," *Scripta Mater.*, vol. 62, no. 5, pp. 258–261.

[96] S. Magdassi, M. Grouchko, and A. Kamyshny, "Copper Nanoparticles for Printed Electronics: Routes Towards Achieving Oxidation Stability," *Materials*, vol. 3, pp. 4626–4638, Sept. 2010.

[97] B. R. Pauw, M. Ohnuma, K. Sakurai, and E. A. Klop, "2D anisotropic scattering pattern fitting using a novel Monte Carlo method: Initial results," *arXiv*, Mar. 2013.

[98] A. P. Hammersley, "Fit2d v12. 012 reference manual v6.0." ESRF Internal Report ESRF98HA01T, 2004.

[99] C. Prescher and V. B. Prakapenka, "DIOPTAS: a program for reduction of two-dimensional X-ray diffraction data and data exploration," *High Pressure Research*, vol. 35, pp. 223–230, July 2015.

[100] J. Kieffer and D. Karkoulis, "Pyfai, a versatile library for azimuthal regrouping," *J. Phys.: Conf. Ser.*, vol. SRI2012, 2013.

[101] P. Juhás, T. Davis, C. L. Farrow, and S. J. L. Billinge, "PDFgetX3: A rapid and highly automatable program for processing powder diffraction data into total scattering pair distribution functions," *J. Appl. Crystallogr.*, vol. 46, pp. 560–566, 2013.

[102] S. J. L. Billinge and C. L. Farrow, "Towards a robust *ad-hoc* data correction approach that yields reliable atomic pair distribution functions from powder diffraction data," *J. Phys: Condens. Mat.*, vol. 25, p. 454202, 2013.

[103] X. Qiu and S. J. L. Billinge, *PDFgetX2 user's guide.* Michigan State University, Department of Physics and Astronomy, v1.0 ed., April 2004.

[104] I. Jeong, J. Thompson, A. M. P. Turner, and S. J. L. Billinge, "PDFgetX: a program for determining the atomic pair distribution function from X-ray powder diffraction data," *J. Appl. Crystallogr.*, vol. 34, p. 536, 2001.

[105] B. H. Toby and R. B. Von Dreele, "*GSAS-II*: the genesis of a modern open-source all purpose crystallography software package," *J. Appl. Crystallogr.*, vol. 46, pp. 544–549, Apr 2013.

[106] M. Jansen and J. C. Schön, "Rational development of new materials — putting the cart before the horse?," *Nat. Mater*, vol. 3, p. 838, Dec. 2004.

[107] R. F. Service, "High-speed materials design," *Science*, vol. 277, no. 5325, pp. 474–475, 1997.

[108] X. D. Xiang, X. D. Sun, G. Briceno, Y. L. Lou, K. A. Wang, H. Y. Chang, W. G. Wallacefreedman, S. W. Chen, and P. G. Schultz, "A Combinatorial Approach to Materials Discovery," *Science*, vol. 268, no. 5218, pp. 1738–1740, 1995.

[109] S. M. Senkan, "High-throughput screening of solid-state catalyst libraries," *Nat. Mater*, vol. 394, no. 6691, pp. 350–353, 1998.

[110] R. Daly, T. S. Harrington, G. D. Martin, and I. M. Hutchings, "Inkjet printing for pharmaceutics - A review of research and manufacturing," *Int. J. Pharm.*, vol. 494, no. 2, pp. 554–567, 2015.

[111] J. Kohn, "New approaches to biomaterials design," *Nat. Mater*, vol. 3, pp. 745–747, Nov. 2004.

[112] E. M. Chan, "Combinatorial approaches for developing upconverting nanomaterials: high-throughput screening, modeling, and applications," *Chem. Soc. Rev.*, vol. 44, no. 6, pp. 1653–1679, 2015.

[113] D. Miracle, B. Majumdar, K. Wertz, and S. Gorsse, "New strategies and tests to accelerate discovery and development of multi-principal element structural alloys," *Scripta Mater.*, vol. 127, pp. 195–200, 2017.

[114] R. Potyrailo, K. Rajan, K. Stoewe, I. Takeuchi, B. Chisholm, and H. Lam, "Combinatorial and High-Throughput Screening of Materials Libraries: Review of State of the Art," *ACS Comb. Sci.*, vol. 13, no. 6, pp. 579–633, 2011.

[115] S. J. L. Billinge, "Pair distribution function technique: principles and methods," in *Uniting Electron Crystallography and Powder Diffraction* (U. Kolb, W. I. F. David, and K. Shankland, eds.), NATO Science for Peace and Security Series B: Physics and Biophysics, (Dordrecht), pp. 179 – 190, Springer Science & Business Media, 2013.

[116] I. Yanase, "Combinatorial study for ceramics powder by X-ray diffraction," *Solid State Ionics*, vol. 154-155, pp. 419–424, Dec. 2002.

[117] T. A. Wilson, A. J. Barlow, M. L. Foster, M. Bravo Sanchez, J. F. Portoles, N. Sano, P. J. Cumpson, and I. W. Fletcher, "In situion beam sputter deposition and X-ray photoelectron spectroscopy (XPS) of multiple thin layers under computer control for combinatorial materials synthesis," *Surf. Interface Anal.*, vol. 49, pp. 18–24, May 2016.

[118] J. Nelson, S. Misra, Y. Yang, A. Jackson, Y. Liu, H. Wang, H. Dai, J. C. Andrews, Y. Cui, and M. F. Toney, "In Operando X-ray Diffraction and Transmission X-ray Microscopy of Lithium Sulfur Batteries," *J. Am. Chem. Soc.*, vol. 134, pp. 6337–6343, Apr. 2012.

[119] J. M. Gregoire, D. G. Van Campen, C. E. Miller, R. J. R. Jones, S. K. Suram, and A. Mehta, "High-throughput synchrotron X-ray diffraction for combinatorial phase mapping," *J. Sync. Rad.*, vol. 21, pp. 1262–1268, Nov. 2014.

[120] E. Reddington, A. Sapienza, B. Gurau, R. Viswanathan, S. Sarangapani, E. S. Smotkin, and T. E. Mallouk, "Combinatorial electrochemistry: A highly parallel, optical screening method for discovery of better electrocatalysts," *Science*, vol. 280, no. 5370, pp. 1735–1737, 1998.

[121] K. M. Ø. Jensen, A. B. Blichfeld, S. R. Bauers, S. R. Wood, E. Dooryhee, D. C. Johnson, B. B. Iversen, and S. J. L. Billinge, "Demonstration of thin film pair distribution function analysis (tfPDF) for the study of local structure in amorphous and crystalline thin films," vol. 2, pp. 481–489, Sept. 2015.

[122] P. J. Chupas, X. Y. Qiu, J. C. Hanson, P. L. Lee, C. P. Grey, and S. Billinge, "Rapid-acquisition pair distribution function (RA-PDF) analysis," *J. Appl. Crystallogr.*, vol. 36, pp. 1342–1347, Dec. 2003.

[123] K. M. O. Jensen, A. B. Blichfeld, S. R. Bauers, S. R. Wood, E. Dooryhée, D. C. Johnson, B. B. Iversen, and S. J. L. Billinge, "Demonstration of thin film pair distribution function analysis (tfPDF) for the study of local structure in amorphous and crystalline thin films," *IUCrJ.*, vol. 2, no. 5, pp. 481–489, 2015.

[124] X. Yang, P. Juhás, C. Farrow, and S. J. L. Billinge, "xPDFsuite: an end-to-end software solution for high throughput pair distribution function transformation, visualization and analysis," *arXiv*, 2015. 1402.3163.

[125] F. Perez and B. E. Granger, "IPython: A system for interactive scientific computing," *Comp. Sci. Eng.*, vol. 9, no. 3, pp. 21–29, 2007.

[126] J. D. Hunter, "Matplotlib: A 2D graphics environment," *Comp. Sci. Eng.*, vol. 9, no. 3, pp. 90–95, 2007.

[127] S. D. M. Jacques, M. D. Michiel, S. A. J. Kimber, X. Yang, R. J. Cernik, A. M. Beale, and S. J. L. Billinge, "Pair distribution function computed tomography," *Nat. Commun.*, vol. 4, p. 2536, 2013.

[128] K. Ghaffarzadeh and Y. Yamamoto, *Conductive Ink Markets 2018-2028: Forecasts, Technologies, Players.* Silver flake, silver nanoparticles, copper inks and pastes, graphene and beyond, Feb. 2018.

[129] P. Harrop and R. Das, *Structural Electronics 2018-2028: Applications, Technologies, Forecasts.* In-mold electronics, smart skin, structural health monitoring, composite smart structures, building integrated photovoltaics (BIPV), Apr. 2018.

[130] P. Hadi, M. Xu, C. S. K. Lin, C.-W. Hui, and G. McKay, "Waste printed circuit board recycling techniques and product utilization," *J. Hazard. Mater.*, vol. 283, pp. 234–243, Feb. 2015.

[131] R. Parashkov, E. Becker, T. Riedl, H.-H. Johannes, and W. Kowalsky, "Large Area Electronics Using Printing Methods ," *J. Mater. Sci. Mater. Electron.*, vol. 93, pp. 1321–1329, July 2005.

[132] D. Rudolph, S. Olibet, J. Hoornstra, A. Weeber, E. Cabrera, A. Carr, M. Koppes, and R. Kopecek, "Replacement of Silver in Silicon Solar Cell Metallization Pastes Containing a Highly Reactive Glass Frit: Is it Possible?," *Energy Procedia*, vol. 43, pp. 44–53, Jan. 2013.

[133] Yuning Li, Y. Wu, , and B. S. Ong, *Facile Synthesis of Silver Nanoparticles Useful for Fabrication of High-Conductivity Elements for Printed Electronics.* American Chemical Society, Feb. 2005.

[134] D. Deng, Y. Jin, Y. Cheng, T. Qi, and F. Xiao, "Copper Nanoparticles: Aqueous Phase Synthesis and Conductive Films Fabrication at Low Sintering Temperature," *ACS Appl. Mater. Interfaces*, vol. 5, no. 9, pp. 3839–3846, 2013.

[135] S. W. Chen and J. M. Sommers, "Alkanethiolate-protected copper nanoparticles: Spectroscopy, electrochemistry, and solid-state morphological evolution," *Journal of Physical Chemistry B*, vol. 105, no. 37, pp. 8816–8820, 2001.

[136] E. Foresti, G. Fracasso, M. Lanzi, I. G. Lesci, L. Paganin, T. Zuccheri, and N. Roveri, "New Thiophene Monolayer-Protected Copper Nanoparticles: Synthesis and Chemical-Physical Characterization," *Journal of Nanomaterials*, vol. 2008, 2008.

[137] J.-g. Yang, Y.-l. Zhou, T. Okamoto, T. Bessho, S. Satake, R. Ichino, and M. Okido, "Preparation of oleic acid-capped copper nanoparticles," *Chem. Lett.*, vol. 35, no. 10, pp. 1190–1191, 2006.

[138] G. Granata, T. Yamaoka, F. Pagnanelli, and A. Fuwa, "Study of the synthesis of copper nanoparticles: the role of capping and kinetic towards control of particle size and stability," *Journal of Nanoparticle Research*, vol. 18, p. 133, May 2016.

[139] Z. Liu and Y. Bando, "A Novel Method for Preparing Copper Nanorods and Nanowires," *Adv. Mater.*, vol. 15, pp. 303–305, Feb. 2003.

[140] C. Qin and S. Coulombe, "Organic layer-coated metal nanoparticles prepared by a combined arc evaporation/condensation and plasma polymerization process," *Plasma Sources Sci. Technol.*, vol. 16, p. 240, May 2007.

[141] J. P. Cason, M. E. Miller, J. B. Thompson, and C. B. Roberts, "Solvent effects on copper nanoparticle growth behavior in AOT reverse micelle systems," *Journal of Physical Chemistry B*, vol. 105, no. 12, pp. 2297–2302, 2001.

[142] B. K. Park, S. Jeong, D. Kim, J. Moon, S. Lim, and J. S. Kim, "Synthesis and size control of monodisperse copper nanoparticles by polyol method," *J. Colloid Interface Sci.*, vol. 311, pp. 417–424, July 2007.

[143] U. S. Shenoy and A. N. Shetty, "Simple glucose reduction route for one-step synthesis of copper nanofluids," *Appl Nanosci*, vol. 4, pp. 47–54, Oct. 2012.

[144] C. Wu, B. P. Mosher, and T. Zeng, "One-step green route to narrowly dispersed copper nanocrystals," *J Nanopart Res*, vol. 8, pp. 965–969, Dec. 2006.

[145] Q.-m. LIU, T. Yasunami, K. Kuruda, and M. Okido, "Preparation of Cu nanoparticles with ascorbic acid by aqueous solution reduction method," *Trans. Nonferrous Met. Soc. China*, vol. 22, pp. 2198–2203, Sept. 2012.

[146] Y. Li, X. Tang, Y. Zhang, J. Li, C. Lv, X. Meng, Y. Huang, C. Hang, and C. Wang, "Cu nanoparticles of low polydispersity synthesized by a double-template method and their stability," *Colloid Polym Sci*, vol. 292, pp. 715–722, Nov. 2013.

[147] J. Xiong, Y. Wang, Q. Xue, and X. Wu, "Synthesis of highly stable dispersions of nanosized copper particles using L-ascorbic acid," *Green Chem.*, vol. 13, no. 4, pp. 900–904, 2011.

[148] S. K. Tam, *Synthesis, Formulation and Application of Copper-Based Conductive Pastes and Inks.* PhD thesis, 2016.

[149] W. Yu, H. Xie, L. Chen, Y. Li, and C. Zhang, "Synthesis and Characterization of Monodispersed Copper Colloids in Polar Solvents," *Nanoscale Res Lett*, vol. 4, p. 465, May 2009.

[150] F. Pagnanelli, E. Moscardini, G. Granata, S. Cerbelli, L. Agosta, A. Fieramosca, and L. Toro, "Acid reducing leaching of cathodic powder from spent lithium ion batteries: Glucose oxidative pathways and particle area evolution," *J. Ind. Eng. Chem.*, vol. 20, pp. 3201–3207, Sept. 2014.

[151] C. L. Farrow, M. Shaw, H.-J. Kim, P. Juhás, and S. J. L. Billinge, "The Nyquist-Shannon sampling theorem and the atomic pair distribution function," *Phys. Rev. B*, vol. 84, p. 134105, 2011.

[152] C. Wu, B. P. Mosher, and T. Zeng, "One-step green route to narrowly dispersed copper nanocrystals," *J Nanopart Res*, vol. 8, pp. 965–969, Dec. 2006.

[153] C. F. Schwenk and B. M. Rode, "New Insights into the Jahn–Teller Effect through ab initio Quantum-Mechanical/Molecular-Mechanical Molecular Dynamics Simulations of CuII in Water," *ChemPhysChem*, vol. 4, pp. 931–943, Sept. 2003.

[154] L. Pauling, "The principles determining the structure of complex ionic crystals," *J. Am. Chem. Soc.*, vol. 51, no. 1-4, pp. 1010–1026, 1929.

[155] R. K. Eby, F. C. Hawthorne, and IUCr, "Structural relations in copper oxysalt minerals. I. Structural hierarchy," *Acta Crystallogr B Struct Sci Cryst Eng Mater*, vol. 49, pp. 28–56, Feb. 1993.

[156] A. Pasquarello, I. Petri, P. S. Salmon, O. Parisel, R. Car, E. Toth, D. H. Powell, H. E. Fischer, L. Helm, and A. E. Merbach, "First solvation shell of the Cu(II) aqua ion: Evidence for fivefold coordination," *Science*, vol. 291, no. 5505, pp. 856–859, 2001.

[157] M. Benfatto, P. D'Angelo, S. Della Longa, and N. V. Pavel, "Evidence of distorted fivefold coordination of the Cu2+ aqua ion from an x-ray-absorption spectroscopy quantitative analysis," *Phys. Rev. B*, vol. 65, p. 174205, May 2002.

[158] J. Blumberger, L. Bernasconi, I. Tavernelli, R. Vuilleumier, and M. Sprik, "Electronic Structure and Solvation of Copper and Silver Ions: A Theoretical Picture of a Model Aqueous Redox Reaction," *J. Am. Chem. Soc.*, vol. 126, pp. 3928–3938, Mar. 2004.

[159] S. Jeong, K. Woo, D. Kim, S. Lim, J. S. Kim, H. Shin, Y. Xia, and J. Moon, "Controlling the Thickness of the Surface Oxide Layer on Cu Nanoparticles for the Fabrication of Conductive Structures by Ink-Jet Printing," *Adv. Funct. Mater.*, vol. 18, pp. 679–686, Mar. 2008.

[160] H.-X. Zhang, U. Siegert, R. Liu, and W.-B. Cai, "Facile Fabrication of Ultrafine Copper Nanoparticles in Organic Solvent," *Nanoscale Res Lett*, vol. 4, p. 705, July 2009.

[161] D. L. Cocke, G. K. Chuah, N. Kruse, and J. H. Block, "Copper oxidation and surface copper oxide stability investigated by pulsed field desorption mass spectrometry," *Applied Surface Science*, vol. 84, pp. 153–161, Feb. 1995.

[162] K. A. Dafforn, J. A. Lewis, and E. L. Johnston, "Antifouling strategies: History and regulation, ecological impacts and mitigation," *Mar Pollut Bull*, vol. 62, pp. 453–465, Mar. 2011.

[163] D. A. Palmer, "Solubility Measurements of Crystalline Cu2O in Aqueous Solution as a Function of Temperature and pH," *J Solution Chem*, vol. 40, pp. 1067–1093, May 2011.

[164] H. Kahlweit, "Ostwald ripening of precipitates," *Adv. Colloid Interface Sci.*, vol. 5, pp. 1–35, Aug. 1975.

[165] I. M. Lifshitz and V. V. Slyozov, "The kinetics of precipitation from supersaturated solid solutions," *J. Phys. Chem. Solids*, vol. 19, pp. 35–50, Apr. 1961.

[166] C. Wagner, "Theorie der Alterung von Niederschlägen durch Umlösen (Ostwald-Reifung)," *Zeitschrift für Elektrochemie*, vol. 65, pp. 581–591, Sept. 1961.

[167] T. H. Fleisch, "Reduction of copper oxides by UV radiation and atomic hydrogen studied by XPS," *Applications of Surface Science*, vol. 10, pp. 51–62, Jan. 1982.

[168] V. Petkov, B. Prasai, S. Shan, Y. Ren, J. Wu, H. Cronk, J. Luo, and C.-J. Zhong, "Structural dynamics and activity of nanocatalysts inside fuel cells by in operando atomic pair distribution studies," *Nanoscale*, vol. 8, no. 20, pp. 10749–10767, 2016.

[169] S. B. Simonsen, I. Chorkendorff, S. Dahl, M. Skoglundh, J. Sehested, and S. Helveg, "Direct Observations of Oxygen-induced Platinum Nanoparticle Ripening Studied by In Situ TEM," *J. Phys. Chem. B*, May 2010.

[170] J. L. Contreras, G. F. S.-M. Products, , and 2012, "Sintering of Supported Metal Catalysts," *intechopen.com*.

[171] T. R. Johns, J. R. Gaudet, E. J. Peterson, J. T. Miller, E. A. Stach, C. H. Kim, M. P. Balogh, and A. K. Datye, "Microstructure of Bimetallic Pt/Pd Catalysts under Oxidizing Conditions," *ChemCatChem*, vol. 5, pp. 2636–2645, Sept. 2013.

[172] M. H. Wiebenga, C. H. Kim, S. J. Schmieg, S. H. Oh, D. B. Brown, D. H. Kim, J.-H. Lee, and C. H. F. Peden, "Deactivation mechanisms of Pt/Pd-based diesel oxidation catalysts," *Catal. Today*, vol. 184, pp. 197–204, Apr. 2012.

[173] A. Russell and W. S. Epling, "Diesel Oxidation Catalysts," *Cat. Rev.*, Oct. 2011.

[174] C. Carrillo, T. R. Johns, H. Xiong, A. DeLaRiva, S. R. Challa, R. S. Goeke, K. Artyushkova, W. Li, C. H. Kim, and A. K. Datye, "Trapping of Mobile Pt Species by PdO Nanoparticles under Oxidizing Conditions," *J. Phys. Chem. B*, May 2014.

[175] H. Xiong, E. J. Peterson, G. Qi, and A. K. Datye, "Trapping mobile Pt species by PdO in diesel oxidation catalysts: Smaller is better," *Catal. Today*, vol. 272, pp. 80–86, Sept. 2016.

[176] T. R. Johns, R. S. Goeke, V. Ashbacher, P. C. Thüne, J. W. Niemantsverdriet, B. Kiefer, C. H. Kim, M. P. Balogh, and A. K. Datye, "Relating adatom emission to improved durability of Pt–Pd diesel oxidation catalysts," *J. Catal.*, vol. 328, pp. 151–164, Aug. 2015.

[177] C. Carrillo, A. DeLaRiva, H. Xiong, E. P. A. C. B, and 2017, "Regenerative trapping: How Pd improves the durability of Pt diesel oxidation catalysts ," *Elsevier*.

[178] M. R. Ward, T. Hyde, E. D. Boyes, and P. L. Gai, "Nanostructural Studies of Fresh and Road-Aged Practical Pt/SiO2 and Pt-Pd/Al2O3 Diesel Oxidation Catalysts by using Aberration-Corrected (Scanning) Transmission Electron Microscopy," *Chem-CatChem*, vol. 4, pp. 1622–1631, Oct. 2012.

[179] R. Ruiz-Rosas, J. M. Rosas, I. G. Loscertales, and J. Rodríguez-Mirasol, "Electro-spinning of silica sub-microtubes mats with platinum nanoparticles for NO catalytic reduction," *Appl. Catal., B*, vol. 156-157, pp. 15–24, Sept. 2014.

[180] M. Khosravi, A. Abedi, R. E. Hayes, W. S. Epling, and M. Votsmeier, "Kinetic modelling of Pt and Pt:Pd diesel oxidation catalysts," *Appl. Catal., B*, vol. 154-155, pp. 16–26, July 2014.

[181] M. Marafi, A. Stanislaus, and E. Furimsky, "Handbook of Spent Hydroprocessing Catalysts," 2017.

[182] A. N. Chigapov, B. P. Carberry, and Ford Global Technologies LLC, "Oxidation catalysts," *Google Patents*, Mar. 2010.

[183] Y.-S. Kim, S. J. Lim, Y. H. Kim, J. H. Lee, and H.-I. Lee, "The role of Fe on PtPd oxidation catalyst prepared by simultaneous and sequential incipient wetnesses," *J. Ind. Eng. Chem.*, vol. 18, pp. 720–725, Mar. 2012.

[184] Y. Sakamoto, K. Higuchi, N. Takahashi, K. Yokota, H. Doi, and M. Sugiura, "Effect of the addition of Fe on catalytic activities of Pt/Fe/γ-Al2O3 catalyst," *Appl. Catal., B*, vol. 23, pp. 159–167, Nov. 1999.

[185] M. Zammit, C. L. DiMaggio, C. H. Kim, C. Lambert, G. G. Muntean, C. H. Peden, J. E. Parks, and K. Howden, "Future Automotive Aftertreatment Solutions: The 150?C Challenge Workshop Report," tech. rep., Pacific Northwest National Laboratory (PNNL), Richland, WA (United States), Oct. 2013.

[186] A. Siani, O. S. Alexeev, B. Captain, G. Lafaye, P. Marecot, R. D. Adams, and M. D. Amiridis, "Synthesis of cluster-derived PtFe/SiO2 catalysts for the oxidation of CO," *J. Catal.*, vol. 255, pp. 162–179, Apr. 2008.

[187] A. Siani, O. S. Alexeev, G. Lafaye, and M. D. Amiridis, "The effect of Fe on SiO2-supported Pt catalysts: Structure, chemisorptive, and catalytic properties," *J. Catal.*, vol. 266, pp. 26–38, Aug. 2009.

[188] H. Chen, Y. Liu, F. Yang, M. Wei, X. Zhao, Y. Ning, Q. Liu, Y. Zhang, Q. Fu, and X. Bao, "Active Phase of FeOx/Pt Catalysts in Low-Temperature CO Oxidation and Preferential Oxidation of CO Reaction," *J. Phys. Chem. B*, May 2017.

[189] J. P. Dunn, H. G. Stenger, and I. E. Wachs, "Oxidation of SO2over Supported Metal Oxide Catalysts," *J. Catal.*, vol. 181, pp. 233–243, Jan. 1999.

[190] Hongbo Fu, Xiao Wang, Hongbo Wu, Y. Yin, , and J. Chen, *Heterogeneous Uptake and Oxidation of SO2 on Iron Oxides.* American Chemical Society, Mar. 2007.

[191] C. Kallesøe, H. F. Clausen, L. H. Christensen, T. Lund-Olesen, M. A. H. Mamakhe, B. B. Iversen, J. Becker-Christensen, D. F. Aarup, J. Hales, and T. Institut, "Method of preparing a catalytic structure," *Google Patents*, July 2015.

[192] P. R. Ellis, C. M. Brown, P. T. Bishop, J. Yin, K. Cooke, W. D. Terry, J. Liu, F. Yin, and R. E. Palmer, "The cluster beam route to model catalysts and beyond," *Faraday Discussions*, vol. 188, no. 0, pp. 39–56, 2016.

[193] T. Imaoka, Y. Akanuma, N. Haruta, S. Tsuchiya, K. Ishihara, T. Okayasu, W.-J. Chun, M. Takahashi, and K. Yamamoto, "Platinum clusters with precise numbers of atoms for preparative-scale catalysis," *Nat. Commun.*, vol. 8, p. 688, Sept. 2017.

[194] S. J. L. Billinge and I. Levin, "The problem with determining atomic structure at the nanoscale," *Science*, vol. 316, pp. 561–565, 2007.

[195] J. M. Cowley, "Stacking faults in $\gamma$-alumina," *Acta Crystallogr.*, vol. 6, pp. 53–54, 1953.

[196] A. Larsson and S. Ruppi, "Microstructure and properties of cvd g-al2o3 coatings," vol. 19, pp. 515–522, 2001.

[197] Gianluca Paglia, E. S. Božin, , and S. J. L. Billinge, "Fine-Scale Nanostructure in $\gamma$-Al2O3," *J. Phys. Chem. B*, June 2006.

[198] G. Paglia, C. E. Buckley, A. L. Rohl, B. A. Hunter, R. D. Hart, J. V. Hanna, and L. T. Byrne, "Tetragonal structure model for boehmite-derived $\gamma$-alumina," *Phys. Rev. B*, vol. 68, p. 144110, 2003.

[199] V. I. Kovalchuk and B. N. Kuznetsov, "Hydrocarbon synthesis from CO and H2 on (Fe + Pt)SiO2 catalysts," *J. Mol. Catal. A: Chem.*, vol. 102, pp. 103–110, Sept. 1995.

[200] S. J. L. Billinge and E. S. Božin, "Pair distribution function technique: principles and methods," in *Diffraction at the Nanoscale: Nanocrystals, Defective and Amorphous Materials* (A. Guagliardi and N. Masciocchi, eds.), (Insubria, Como, Italy), pp. 97–106, Insubria University Press, 2010.

[201] N. V. Ageev and V. S. Shekhtman, "A new compound in the rhenium-iron system," *Dokl. Akad. Nauk SSSR*, vol. 143, no. 5, pp. 1091–1093, 1962.

[202] L. Vegard, "Die konstitution der mischkristalle und die raumfüllung der atome," *Zeitschrift für Physik*, 1921.

[203] W. H. Qi and M. P. Wang, "Size and shape dependent lattice parameters of metallic nanoparticles," *J Nanopart Res*, vol. 7, pp. 51–57, Feb. 2005.

[204] T. J. Schmidt, M. Noeske, H. A. Gasteiger, R. J. Behm, P. Britz, and H. Bonnemann, "PtRu alloy colloids as precursors for fuel cell catalysts - A combined XPS, AFM, HRTEM, and RDE study," *J. Electrochem. Soc.*, vol. 145, pp. 925–931, Mar. 1998.

[205] D. Rickerby and M. Morrison, *Nanotechnology for Sustainable Manufacturing.* CRC Press, 2 ed., May 2014.

[206] E. Antolini, "Carbon supports for low-temperature fuel cell catalysts," *Appl. Catal., B*, vol. 88, pp. 1–24, Apr. 2009.

[207] F. A. Viva, M. M. Bruno, M. Jobbágy, and H. R. Corti, "Electrochemical Characterization of PtRu Nanoparticles Supported on Mesoporous Carbon for Methanol Electrooxidation," *J. Phys. Chem. B*, Feb. 2012.

[208] G. A. Olah, "Beyond Oil and Gas: The Methanol Economy," *Angew. Chem. Int. Ed.*, vol. 44, pp. 2636–2639, Apr. 2005.

[209] IEA, *Renewables Information 2017.* 2017.

[210] R. A. Kerr, "Natural Gas From Shale Bursts Onto the Scene," *Science*, vol. 328, pp. 1624–1626, June 2010.

[211] AFDC, "Alternative Fuels Data Center," tech. rep., AFDC, Oct. 2014.

[212] J. M. Fox III, "The Different Catalytic Routes for Methane Valorization: An Assessment of Processes for Liquid Fuels," *Catalysis Reviews—Science and Engineering*, vol. 35, pp. 169–212, Sept. 2006.

[213] T. V. Choudhary and V. R. Choudhary, "Energy-Efficient Syngas Production through Catalytic Oxy-Methane Reforming Reactions," *Angew. Chem. Int. Ed.*, vol. 47, pp. 1828–1847, Feb. 2008.

[214] E. McFarland, "Unconventional Chemistry for Unconventional Natural Gas," *Science*, vol. 338, pp. 340–342, Oct. 2012.

[215] A. Holmen, "Direct conversion of methane to fuels and chemicals," *Catal. Today*, vol. 142, pp. 2–8, Apr. 2009.

[216] P. Tang, Q. Zhu, Z. Wu, and D. Ma, "Methane activation: the past and future," *Energy Environ. Sci.*, vol. 7, no. 8, pp. 2580–2591, 2014.

[217] A. I. Olivos-Suarez, À. Szécsényi, E. J. M. Hensen, J. Ruiz-Martinez, E. A. Pidko, and J. Gascon, "Strategies for the Direct Catalytic Valorization of Methane Using Heterogeneous Catalysis: Challenges and Opportunities," *J. Phys. Chem. B*, Apr. 2016.

[218] J. Gao, Y. Zheng, J.-M. Jehng, Y. Tang, I. E. Wachs, and S. G. Podkolzin, "Identification of molybdenum oxide nanostructures on zeolites for natural gas conversion," *Science*, p. aaa7048, Apr. 2015.

[219] Y. H. Jang, W. Goddard, and 2002, "Mechanism of Selective Oxidation and Ammoxidation of Propene on Bismuth Molybdates from DFT Calculations on Model Clusters," *J. Phys. Chem. B*.

[220] Gang Fu, Xin Xu, X. Lu, , and H. Wan, *Mechanisms of Methane Activation and Transformation on Molybdenum Oxide Based Catalysts.* American Chemical Society, Feb. 2005.

[221] G. Fu, X. Xu, and H. Wan, "Mechanism of methane oxidation by transition metal oxides: A cluster model study," *Catal. Today*, vol. 117, no. 1-3, pp. 133–137, 2006.

[222] S. Pudar, J. Oxgaard, K. Chenoweth, A. C. T. van Duin, and W. A. Goddard, "Mechanism of Selective Oxidation of Propene to Acrolein on Bismuth Molybdates from Quantum Mechanical Calculations," *J. Phys. Chem. B*, Oct. 2007.

[223] L. Y. Chen, L. W. Lin, Z. S. Xu, X. S. Li, and T. Zhang, "Dehydro-Oligomerization of Methane to Ethylene and Aromatics Over Molybdenum/Hzsm-5 Catalyst," *J. Catal.*, vol. 157, pp. 190–200, Nov. 1995.

[224] D. Ma, Y. Shu, X. Bao, and Y. Xu, "Methane Dehydro-aromatization under Nonoxidative Conditions over Mo/HZSM-5 Catalysts: EPR Study of the Mo Species on/in the HZSM-5 Zeolite," *J. Catal.*, vol. 189, pp. 314–325, Jan. 2000.

[225] C. Kallesoe, C. H. Fano, C. L. Hojslet, T. Lund-Olesen, H. M. M. Aref, I. B. Brummerstedt, J. Becker-Christensen, A. D. Friis, and J. Hales, "Method of preparing a catalytic structure," Jan. 2014.

[226] C. Kallesoe, H. F. Clausen, and L. H. Christensen, "Method of preparing a catalyst structure," Nov. 2016.

[227] M. Brändle, J. Sauer, R. Dovesi, and N. M. Harrison, "Comparison of a combined quantum mechanics/interatomic potential function approach with its periodic quantum-mechanical limit: Proton siting and ammonia adsorption in zeolite chabazite," *J. Chem. Phys.*, vol. 109, p. 10379, Dec. 1998.

[228] R. W. Joyner, A. D. Smith, M. Stockenhuber, and M. W. E. van den Berg, "The local structure of aluminium sites in zeolites," *Phys. Chem. Chem. Phys.*, vol. 6, no. 23, pp. 5435–5439, 2004.

[229] L. B. McCusker and C. Baerlocher, "A re-examination of the structure of SAPO-40," *Microporous Mater.*, vol. 6, pp. 51–54, Mar. 1996.

[230] E. A. Gulbransen, K. F. Andrew, and F. A. Brassart, "Oxidation of Molybdenum 550° to 1700°C," *J. Electrochem. Soc.*, vol. 110, pp. 952–959, Sept. 1963.

[231] J. R. Davis, *Heat-resistant materials.* ASM specialty handbook, Materials Park, OH: ASM International, 1997.

[232] E. R. Braithwaite and J. Haber, *Molybdenum: An Outline of its Chemistry and Uses.* Studies in Inorganic Chemistry, Elsevier Science, 2013.

[233] L. Kihlborg, "The Crystal Chemistry of Molybdenum Oxides," *ACS Adv. Chem.*, vol. 39, pp. 37–45, July 2009.

[234] A. MAGNELI, "Structures of the Reo3-Type with Recurrent Dislocations of Atoms - Homologous Series of Molybdenum and Tungsten Oxides," *Acta Crystallogr A Found Crystallogr*, vol. 6, no. 6, pp. 495–500, 1953.

[235] M. B. Ley, "Mo/ZSM-5 by DTI: internal ADREM characterization report.," tech. rep., Danish Technological Institute, Feb. 2017.

[236] P. Juhás, D. M. Cherba, P. M. Duxbury, W. F. Punch, and S. J. L. Billinge, "Ab initio determination of solid-state nanostructure," *Nature*, vol. 440, no. 7084, pp. 655–658, 2006.

[237] B. Li, S. Li, N. Li, H. Chen, W. Zhang, X. Bao, and B. Lin, "Structure and acidity of Mo/ZSM-5 synthesized by solid state reaction for methane dehydrogenation and aromatization," *Microporous Mesoporous Mater.*, vol. 88, pp. 244–253, Jan. 2006.

[238] S. A. Maier, *Plasmonics: Fundamentals and Applications.* Springer, 2007.

[239] X. Zhang, P. Wang, Z. Zhang, Y. Fang, and M. Sun, "Plasmon-driven sequential chemical reactions in an aqueous environment," *Sci. Rep.*, vol. 4, p. 5407, June 2014.

[240] M. Sandtke and L. Kuipers, "Slow guided surface plasmons at telecom frequencies," *Nature Photonics 2009 3:4*, vol. 1, pp. 573–576, Oct. 2007.

[241] W. L. Barnes, A. Dereux, and T. W. Ebbesen, "Surface plasmon subwavelength optics," *Nat. Mater*, vol. 424, p. 824, Aug. 2003.

[242] D. P. O'Neal, L. R. Hirsch, N. J. Halas, J. D. Payne, and J. L. West, "Photo-thermal tumor ablation in mice using near infrared-absorbing nanoparticles," *Cancer Letters*, vol. 209, pp. 171–176, June 2004.

[243] W. A. Challener, C. Peng, A. V. Itagi, D. Karns, W. Peng, Y. Peng, X. Yang, X. Zhu, N. J. Gokemeijer, Y. T. Hsia, G. Ju, R. E. Rottmayer, M. A. Seigler, and E. C. Gage, "Heat-assisted magnetic recording by a near-field transducer with efficient optical energy transfer," *Nature Photonics 2009 3:4*, vol. 3, pp. 220–224, Apr. 2009.

[244] A. V. Kabashin, P. Evans, S. Pastkovsky, W. Hendren, G. A. Wurtz, R. Atkinson, R. Pollard, V. A. Podolskiy, and A. V. Zayats, "Plasmonic nanorod metamaterials for biosensing," *Nat. Mater*, vol. 8, pp. 867–871, Nov. 2009.

[245] B. Spackova, P. Wrobel, M. Bockova, and J. Homola, "Optical Biosensors Based on Plasmonic Nanostructures: A Review," *J. Mater. Sci. Mater. Electron.*, vol. 104, pp. 2380–2408, Dec. 2016.

[246] H. Inan, M. Poyraz, F. Inci, M. A. Lifson, M. Baday, B. T. Cunningham, and U. Demirci, "Photonic crystals: emerging biosensors and their promise for point-of-care applications," *Chem. Soc. Rev.*, vol. 46, no. 2, pp. 366–388, 2017.

[247] C. Valsecchi and A. G. Brolo, "Periodic Metallic Nanostructures as Plasmonic Chemical Sensors," *J. Phys. Chem. B*, Mar. 2013.

[248] L. Berthod, M. Bichotte, M. Langlet, C. Veillas, D. Jamon, F. Vocanson, I. Verrier, C. Jimenez, O. Parriaux, V. Gâté, and Y. Jourlin, "Direct fabrication of a metal-like TiN-based plasmonic grating using nitridation of a photo-patternable TiO2 sol-gel film," *Opt. Mater. Express, OME*, vol. 6, pp. 2508–2520, Aug. 2016.

[249] G. V. Naik, A. Boltasseva, and J. Kim, "Oxides and nitrides as alternative plasmonic materials in the optical range," *Opt. Mater. Express, OME*, vol. 1, pp. 1090–1099, Oct. 2011.

[250] J. A. Briggs, G. V. Naik, T. A. Petach, B. K. Baum, D. Goldhaber-Gordon, and J. A. Dionne, "Fully CMOS-compatible titanium nitride nanoantennas," *Appl. Phys. Lett.*, vol. 108, p. 051110, Feb. 2016.

[251] E. Shkondin, A. V. Lavrinenko, O. Takayama, and T. Repän, "High aspect ratio titanium nitride trench structures as plasmonic biosensor," *Opt. Mater. Express, OME*, vol. 7, pp. 4171–4182, Nov. 2017.

[252] G. S. Pawley and IUCr, "Unit-cell refinement from powder diffraction scans," *J. Appl. Crystallogr.*, vol. 14, pp. 357–361, Dec. 1981.

[253] R. Delhez, T. H. de Keijser, J. I. Langford, D. Louër, E. J. Mittemeijer, and E. J. Sonneveld, "Crystal imperfection broadening and peak shape in the Rietveld method," *The Rietveld Method*, no. 5, pp. 132–166, 1993.

[254] A. Derkachova, K. Kolwas, and I. Demchenko, "Dielectric Function for Gold in Plasmonics Applications: Size Dependence of Plasmon Resonance Frequencies and Damping Rates for Nanospheres," *Plasmonics*, vol. 11, no. 3, pp. 941–951.

# Supercritical Flow Synthesis of Cost-effective PtPdFe Nanoparticles for Low-temperature Diesel Oxidation

*Hugo Silva[a], Patricia Hernandez-Fernandez[a], Ane K. Baden[a], Henrik L. Hellstern[a], Anton Kovyakh[a,c], Erik Wisaeus[a], Ib Chorkendorff[b], Leif H. Christensen[a], Debasish Chakraborty[b], Christian Kallesøe[a*]*

[a]Danish Technological Institute (DTI), Nano Production and Micro Analysis, Taastrup, 2630, Denmark

[b]SurfCat, Department of Physics, Technical University of Denmark
Fysikvej Building 312, Kgs. Lyngby, 2800, Denmark

[c]Niels Bohr Institute, University of Copenhagen, Universitetsparken 5, DK-2100 Copenhagen, Denmark

**ABSTRACT**

Supercritical flow technology was used for the production of highly active and hydrothermally stable catalysts for diesel exhaust gas treatment. PtPd and PtPdFe nanoparticles were dispersed on a high-surface area $\gamma$-Al$_2$O$_3$ support, with a narrow size-distribution and nanoparticles of 2.3 $\pm$ 0.6 nm and 2.4 $\pm$ 0.6 nm, respectively, as confirmed by HAADF-STEM imaging. Fe addition improved the activity of the fresh catalysts for propene oxidation, with a turn over frequency of 0.06 s$^{-1}$ at 120 °C for a catalyst with 0.12 wt.% Fe, three times higher than the analogous PtPd catalyst. Fe was also added while replacing PtPd precious metal content ((PtPd)$_{x-y}$Fe$_y$, $x$=0.75 wt.% and $y$=0-0.25 wt.%), and a relation between the activity for propene oxidation and the atomic ratio of Fe to PtPd was found. Synchrotron x-ray powder diffraction showed that as the Fe amount increases the lattice constant related to PtPd decreases, implying that PtPdFe alloy formation is accountable for the improved activity for propene oxidation. Not just as fresh, but also after aging, all the Fe containing catalysts overcame the so-called 150 °C challenge from DOE that targets emission regulations for new engines with higher fuel efficiency. Another beneficial effect of Fe was on the hydrothermal stability of the PtPd nanoparticles. XRD of the aged catalysts showed that Fe has a role on inhibiting the sintering of the PtPd crystalline phase, which was verified with HAADF-STEM. Finally, replacing PtPd with Fe, allows savings of up to 33 % when tuning the Fe to precious metal ratio, while maintaining higher activity levels than bimetallic PtPd catalyst. Thus, the invented PtPdFe catalysts not only have higher activity and stability than the presently used PtPd, it also reduces the price significantly by replacing expensive and scarce precious metal with equal amount of inexpensive iron.

**INTRODUCTION**

Emissions standards for diesel vehicles are imposing stricter limits on nitrogen oxides ($NO_x$), carbon monoxide (CO), unburned hydrocarbons (HC, e.g. propene) and particulate matter concentration levels, driving the automotive industry to enhance catalytic converter devices efficiency [1,2]. One of the foreseen strategies is to improve the performance of the diesel oxidation catalyst (DOC) that needs to fulfil a wide range of operating conditions, from low-temperature activity (< 200 °C), especially during cold-start phase where emissions are higher, to high-temperature stability, for instance, during particulate matter regeneration cycles (e.g. 750 °C). The challenge is even higher when considering the presence of water in the exhaust stream and the oxygen-rich environments (up to 10 vol.%) that accelerate the sintering rate of the highly dispersed active-phase nanoparticles through Ostwald ripening mechanism at higher temperatures (> 300 °C) [3,4]. These extreme conditions narrow the suitable metal elements for active-phase composition. Noble metals are envisioned as ideal candidates due to their thermal stability and resistance to oxidation, which are key aspects for the design of a DOC with long-term durability.

Platinum (Pt) or bimetallic combinations with palladium (Pd)[5,6] represent the commercially available catalysts, typically supported as fine nanoparticles on a high surface area metal oxide washcoat, such as $\gamma$-$Al_2O_3$[7]. It has been reported that the addition of Pd supresses the sintering of Pt nanoparticles on model catalysts, as PdO species formed in oxygen-rich environments could trap mobile Pt atomic species, leading to the formation of PtPd alloys[8-11]. Ward *et al*[12] reported on a real road-aged DOC, the formation of PtPd alloyed nanoparticles with random composition and a minor fraction with core-shell structures. Another positive effect of Pd is the improved activity for HC and CO oxidation compared to a monometallic Pt system, even before aging[5,13,14]. From an economic perspective, the advantages of using Pd has previously been a decrease of Pt costs.

However, nowadays the price of both metals is approximately the same due to the increase in the demand of Pd for catalytic converters[15]. Thus, the discovery of novel catalytic systems that can reduce the costs and at the same time fulfil the demanding levels of performance is both of technological and economical significance.

Cost-wise, iron (Fe) is an attractive element that has previously been reported for DOC technology[16-18]. Sakamoto *et al.*[17] tested $Pt/Fe/\gamma-Al_2O_3$ catalysts, but despite the improved thermal stability attributed to the coverage of Pt nanoparticles by $Fe_2O_3$ layers, the activity in lean-conditions was lower than the $Pt/Al_2O_3$ catalyst used for comparison. Accordingly, the temperature at HC half conversion (T50) of a catalyst with 1.1 wt.% Fe and 3.7 wt.% Pt was *ca.* 300 °C, after aging in 7.5 % $O_2$ at 800 °C/5 h, far from the low-temperature targets recommended by the U.S. department of energy (DOE): T50 < 150 °C[19]. Another reported scenario is the use of two types of DOCs, one conventional Pt catalyst combined with an iron-doped zeolite (HZS-5) that initially works as a HC adsorber at colder stages, and subsequently desorbs at hotter stages when higher conversion is attained[20]. However, the hydrothermal stability of HZS-5 zeolites is an issue during DOC reaction conditions, which can lead to surface changes and eventually the collapse of the 3D framework[21-23]. Outside the DOC applications, the use of PtFe alloys has been reported for single CO oxidation reaction, which compared to HC is much easier to oxidize[24-26]. Furthermore, $Fe_2O_3$ helps to oxidize $SO_2$ that acts as a poison of active metal sites[27,28].

In this work, continuous supercritical flow technology was used to synthesize highly active and hydrothermal stable $PtPd/\gamma-Al_2O_3$ and $PtPdFe/\gamma-Al_2O_3$ catalysts for diesel oxidation applications. The patented technology[29,30] allows the production of finely divided nanoparticles (e.g. 2-3 nm) with a very narrow size distribution, high crystallinity, and high throughput rate, up to 0.5 kg·h$^{-1}$. It is well-known that the design of nanoparticulate catalysts with a precise size-control represents a strategy to achieve higher resistance to sintering, due to suppression of the Ostwald ripening[31].

However, the former desired properties are extremely difficult to attain with conventional laboratorial methods such as impregnation. Other methods such as cluster-sources offer the desired size-control of nanoparticles and while giving deep scientific insight suffers disadvantages for real-life applications, including high-cost and low-production rate (e.g. 1 µg·h^{-1})[32,33]. The supercritical synthesized catalysts were studied for HC oxidation, both as fresh and after aging at 750 °C for 3h (10% $O_2$, 10% $H_2O$). Noteworthy is the effect of replacing PtPd content with Fe, allowing savings of precious metals up to ca. 33%, while having better activity levels than the bimetallic PtPd catalyst.

## MATERIALS AND METHODS

Propene oxidation reaction was performed in a tubular quartz reactor (4 mm, ID) placed inside a temperature controlled furnace (Carbolite, MTF 12/25/250). 15 mg of catalyst sample was diluted with inert γ-$Al_2O_3$ (100 mg) powder support (Sasol, Puralox TM 100/150), defining the packed-bed dimensions for the same grain size-distribution ($d_{50}$ of *ca.* 2 µm). Plug flow conditions were assumed since the reactor length to catalyst diameter ratio was higher than 50 ($L_{reactor}/d_{particle} > 50$) and the reactor to catalyst diameter ratio was higher than 30 ($d_{reactor}/d_{particle} > 30$)[34]. The feedstream composition was 10% $O_2$, 400 ppm $C_3H_6$ and the balance nitrogen, for a total flow-rate of 100 Nml·min^{-1} (GSHV of *ca.* 30000 h^{-1}). Gas flow rates were controlled using mass flow controllers (Brooks Instruments 5850 EM, 1.5% F.S.). The reaction stages were defined by ramping up at 6 °C·min^{-1} in step intervals of 10 °C, and isothermal conditions were maintained for ca. 45 min at each temperature stage. Thermocouples were placed on the top and bottom of the packed-bed for a more precise monitoring of temperature. The outlet stream from the reactor was analysed using a gas chromatograph (Agilent 7890a), equipped with a flame ionization detector (FID). After

measuring the light-off curve the reactor was cooled down to room temperature while under nitrogen flow, and a calibration curve for the detector was acquired for compositions of propene up to 400 ppm. The aging procedure of the catalysts was performed in the activity set-up at 750 °C for 3h, where the injection of water was done using a syringe pump (ISCO 100 DM), for a mixture composition of 10% $H_2O$ and 10% $O_2$, balanced in nitrogen.

PtPd and PtPdFe nanoparticles were synthesized by reducing the metal salt precursors (Sigma-Aldrich $FeCl_3 \cdot 6H_2O$, Alfa Aesar $PdCl_2$, Alfa Aesar $H_2PtCl_2 \cdot 6H_2O$) on γ-$Al_2O_3$ support (Sasol, Puralox TM 100/150) using supercritical ethanol both as the solvent and reductant in a continuous flow reactor. Figure 1 shows a sketch of the custom-designed reactor, composed of two pumps, a heated reactor block, a pressure relief valve, a manometer, and a temperature control and cooling system. The automated system allows for accurate control of the reaction conditions, including temperature, pressure and residence time (flow rate). During synthesis, the solution containing the reactants, i.e. Pt, Pd and Fe precursors and γ-$Al_2O_3$ support in suspension, is continuously stirred in a vessel. The reactant suspension is pumped at ambient temperature into the pressurized reactor and continuously mixed with a stream of ethanol that has been heated up to the desired temperature, above the critical point. Because of the rapid mixing of the supercritical fluid and hence rapid heating of the reactants, an instantaneous homogeneous nucleation occurs, producing a nanomaterial with narrow particle size distribution and high crystallinity. The reaction mixture is kept at supercritical conditions as it passes through the reactor maturing the nanoparticles. The residence time can be easily controlled through the reactant and solvent flow. The reaction is terminated by cooling the process flow, and subsequent depressurizing the product solution. The synthesis parameters are visualized in real time to ease interpretation and allow proper readout/control. All experiments were performed at 280 bar and 300 °C (reactor conditions). The products were washed with distilled water and collected by centrifugation. Table 1 compiles the

metallic loadings of the prepared catalysts determined by scanning electron microscopy with energy dispersive x-ray spectroscopy (SEM-EDX), showing the elemental composition and the combined precious metal (PtPd) loading in wt.%. For each sample, three different areas were analysed for the metallic loading determination.

**Table 1** – Metallic composition of the catalysts prepared by supercritical synthesis method, determined by SEM-EDX.

| Catalyst name | Elemental Composition (wt%) | | | PtPd total loading (wt%) |
|---|---|---|---|---|
| | (Pt) | (Pd) | (Fe) | |
| $(PtPd)_1/\gamma\text{-}Al_2O_3$ | 0.78±0.03 | 0.17±0.02 | - | 0.95±0.04 |
| $(PtPd)_1Fe_{0.3}/\gamma\text{-}Al_2O_3$ | 0.73±0.03 | 0.13±0.01 | 0.12±0.02 | 0.86±0.03 |
| $(PtPd)_{0.75}/\gamma\text{-}Al_2O_3$ | 0.65±0.07 | 0.10±0.01 | - | 0.75±0.07 |
| $(PtPd)_{0.70}Fe_{0.05}/\gamma\text{-}Al_2O_3$ | 0.58±0.02 | 0.13±0.03 | 0.06±0.02 | 0.71±0.04 |
| $(PtPd)_{0.65}Fe_{0.10}/\gamma\text{-}Al_2O_3$ | 0.51±0.02 | 0.13±0.03 | 0.11±0.01 | 0.64±0.04 |
| $(PtPd)_{0.55}Fe_{0.20}/\gamma\text{-}Al_2O_3$ | 0.45±0.05 | 0.11±0.03 | 0.18±0.02 | 0.56±0.06 |
| $(PtPd)_{0.50}Fe_{0.25}/\gamma\text{-}Al_2O_3$ | 0.40±0.02 | 0.05±0.02 | 0.19±0.02 | 0.45±0.03 |
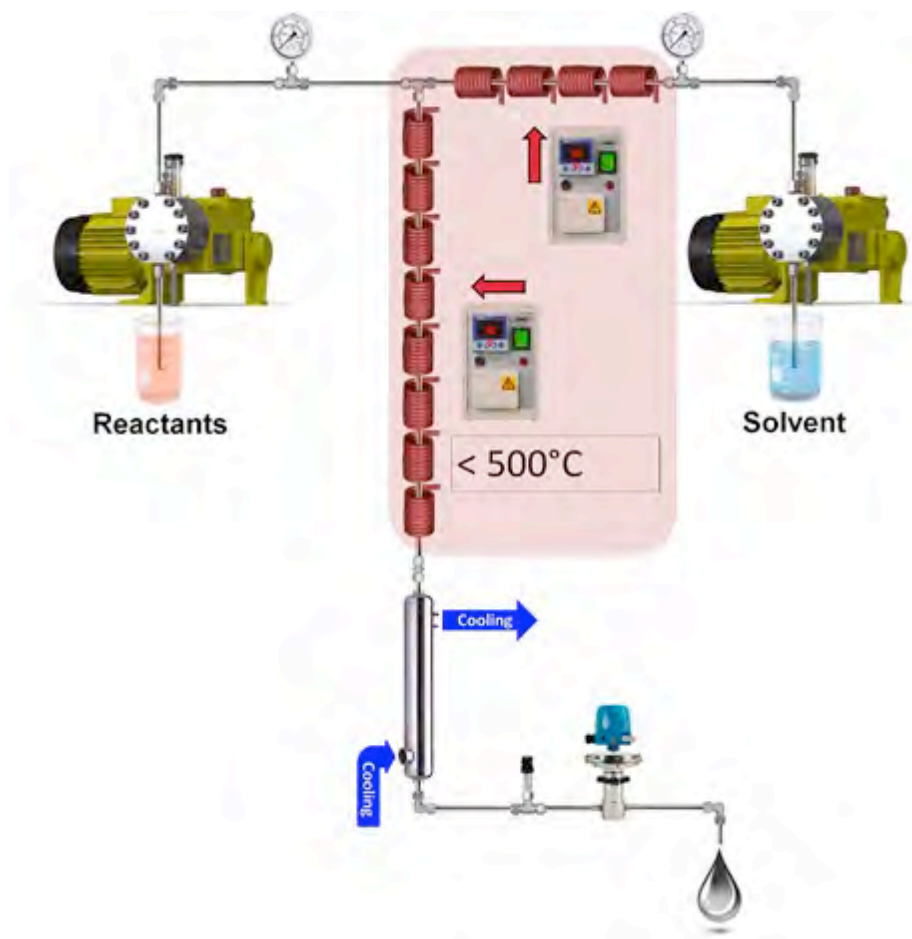
**Figure 1 –** Schematic of the custom-designed continuous flow reactor used for the supercritical synthesis of the PtPd and PtPdFe nanoparticles supported on $\gamma$-$Al_2O_3$. The reactant suspension (precursors and support), and solvent are pumped into the pressurized reactor and subjected to heat for the syntheses of the catalysts nanoparticles.

Powder X-ray diffraction (XRD) measurements were carried out on a PANalytical X'Pert PRO diffractometer, operating in a Bragg–Brentano focusing geometry and using Cu $K\alpha$ radiation at wavelengths Cu $K\alpha_1 = 1.54060$ Å and Cu $K\alpha_2 = 1.54443$ Å. The data was recorded between $2\theta = 10$–$100°$, with a step size of $0.007°$ and step speed of $0.42°$ $min^{-1}$.

Scanning Transmission Electron Microscopy (STEM) was carried out using a FEI TALOS F220A including Energy Dispersive X-ray Spectroscopy (EDX) and High Angle Annular Dark Field (HAADF) at 200kV.

Elemental composition of the samples was quantified by field emission scanning electron microscopy (SEM) (Zeiss XB-1540, Carl Zeiss NTS GmbH, Oberkochen, Germany) equipped with an EDX spectroscopy system (Oxford X-Max 50 mm$^2$, Oxford Instruments, Oxfordshire, UK). Samples were prepared for SEM-EDX analysis by mounting and gentle compacting on double-adhesive carbon tabs. Three X-ray spectra at 20 kV were acquired for each sample in different areas at a magnification of 250X, corresponding to approximately 200x300 µm.

The synchrotron x-ray powder diffraction measurements were performed at the P02.1 beamline at PETRAIII, DESY, Germany. The diffraction experiments were performed in transmission geometry using the Rapid Acquisition Pair Distribution Function (PDF) method[35], where the diffracted signal was collected using a 2D Perkin-Elmer detector at a distance of 200 mm. The incidence wavelength of the x-ray beam was 0.2072 Å with a beam cross-section at the sample of 0.5 mm in the vertical and the horizontal direction. A reference background measurement was collected alongside the other samples in the series. All measurements were performed at room temperature. The experimental geometry parameters were calibrated before data reduction using LaB6 powder diffraction standard.

**RESULTS AND DISCUSSION**

**The effect of Fe addition: catalytic activity and characterization**

The effect of Fe addition to 1 wt.% PtPd catalyst prepared by supercritical synthesis was evaluated considering the activity for $C_3H_6$ oxidation as a probe reaction of the DOC performance. Figure 2 shows the obtained results before and after aging at 750 °C/3h (10% $O_2$, 10% $H_2O$). The T50 is the reaction temperature where 50% of $C_3H_6$ is converted and is a common criterion to compare DOCs[36,37]. The lower the T50, the higher the activity for the reaction. Figure 2a) shows the light-off curve of the $(PtPd)_1Fe_{0.3}/\gamma-Al_2O_3$ catalyst, where T50 for samples before and after aging is 112 °C and 133 °C, respectively. The comparison of the obtained T50 results is presented in Figure 2b), demonstrating that the addition of a low amount of Fe enhances the activity of the bimetallic $(PtPd)_1/\gamma-Al_2O_3$, for which T50 is 126 °C as fresh. Though both catalysts decay in activity after aging the $(PtPd)_1Fe_{0.3}/\gamma-Al_2O_3$ was still the one with the lowest T50, 133 °C, whereas the T50 of the $(PtPd)_1/\gamma-Al_2O_3$ increased to 143 °C. This suggests that the incorporation of Fe not only has a beneficial effect on the activity of the fresh catalyst, but also on the activity after exposing the catalyst to the harsh aging conditions.
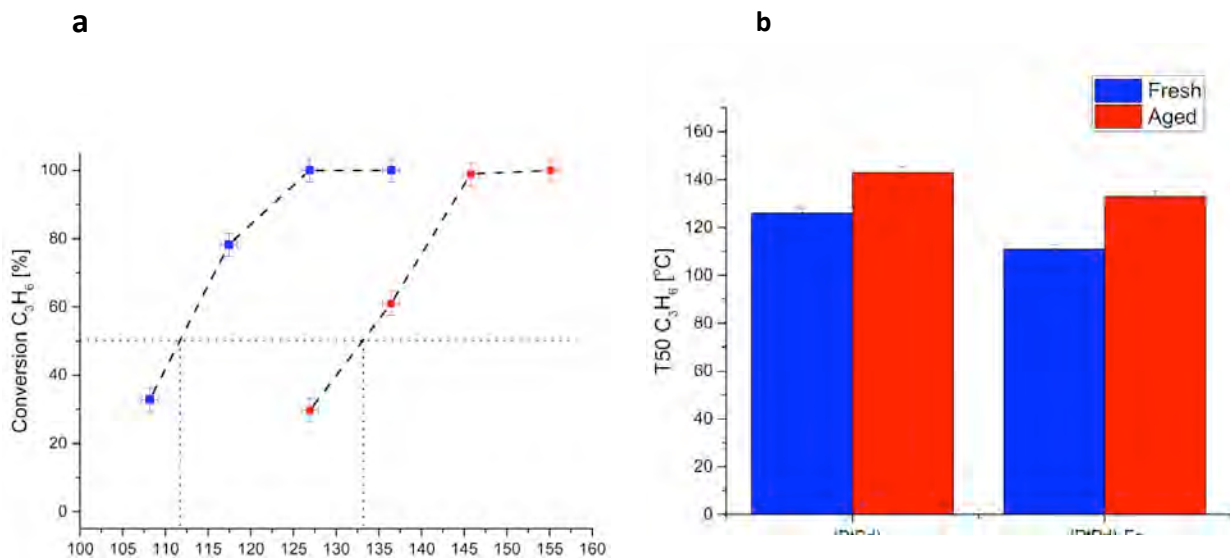
**Figure 2**– a) Light-off curves of the $(PtPd)_iFe_{03}/\gamma\text{-}Al_2O_3$ catalyst prepared by supercritical synthesis fresh (blue) and after aging at 750 °C/3h (10% $O_2$, 10% $H_2O$) (red). The T50 for $C_3H_6$ oxidation is indicated with a dot line; b) Light-off temperatures for $C_3H_6$ oxidation, fresh (blue) and after aging (red), of the $(PtPd)_i/\gamma\text{-}Al_2O_3$ and $(PtPd)_iFe_{03}/\gamma\text{-}Al_2O_3$ catalysts prepared by supercritical synthesis.

The role of Fe on the PtPd phase was further investigated using XRD to gain insight on the crystal structure and crystallite size of the fresh and aged catalysts. The diffraction patterns of the fresh samples showed only the peaks from $\gamma\text{-}Al_2O_3$ support (Figure not showed), indicating that the crystallite size of the active-phase nanoparticles was below the detection limit of the technique (less than 3 nm)[38]. The diffraction peaks attributed to the active-phase nanoparticles are detected for the aged samples (Figure 3).
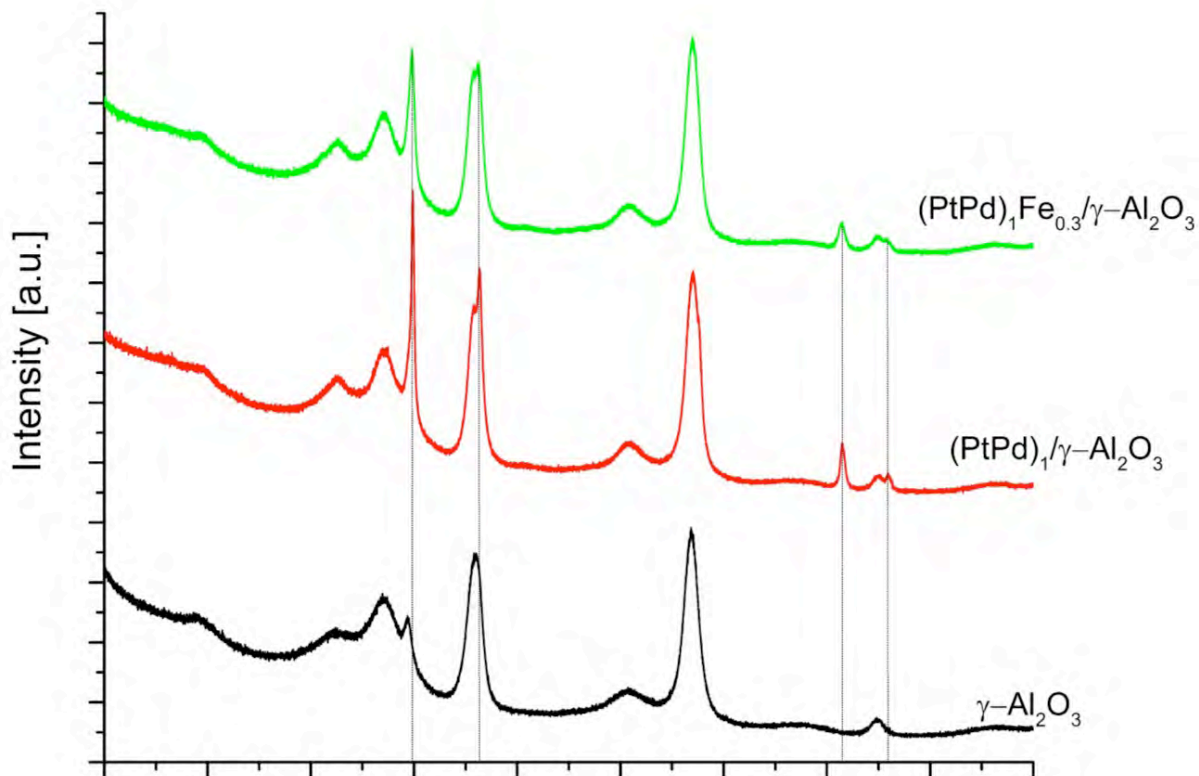
**Figure 3** – XRD patterns of the γ-Al₂O₃ support (black) and the catalysts prepared by supercritical synthesis method, after aging at 750 °C/3h in static conditions: (PtPd)₁/γ-Al₂O₃ (red) and (PtPd)₁Fe₀.₃/γ-Al₂O₃ (green). The vertical dotted lines indicate the 2θ position of the diffraction peaks ascribed to the active-phase nanoparticles.

As seen in Figure 3, the diffraction peak displaying the highest intensity in both catalysts at 2θ = 39.9° is ascribed to PtPd alloyed nanoparticles with fcc structure, and is slightly shifted compared to the Pt(111) crystalline plane that is situated at 39.6° (ICSD 98-018-0881). The shift towards higher angles indicates compression of the Pt fcc lattice, meaning that the lattice constant is smaller for PtPd alloy than for Pt metallic phase, which is ascribed to Pd incorporation. Figure 3 also shows diffraction peaks at the following 2θ angles: 46.1°, 81.4° and 85.9°, which corresponds to the

PtPd(002), PtPd(113) and PtPd(222) crystalline planes, respectively. Even though the samples were aged at high-temperatures in an oxygen-rich environment, no precious metal oxide phases were detected. Pd has a lower resistance to oxidation than Pt but no PdO was detected[8]. Moreover, there is no detection of iron-based crystalline phases for the $(PtPd)_1Fe_{0.3}/\gamma-Al_2O_3$ catalyst. Despite this, after aging, the $(PtPd)_1Fe_{0.3}/\gamma-Al_2O_3$ catalyst had broader diffraction peaks, ascribed to PtPd crystalline phase, than the $(PtPd)_1/\gamma-Al_2O_3$, suggesting that Fe had a role on inhibiting the sintering of PtPd alloyed nanoparticles. In fact, the average crystallite size determined by Debye-Scherrer equation for $(PtPd)_1Fe_{0.3}/\gamma-Al_2O_3$ catalyst using the PtPd(222) crystalline plane at 81.4° was 15.6 nm, whereas it was 26.0 nm for the $(PtPd)_1/\gamma-Al_2O_3$. This size-effect of Fe can also be related to the improved activity of the Fe containing catalyst after aging when comparing to the bimetallic PtPd, as shown in Figure 2b).

In-house XRD was helpful to understand the composition and size of the active-phase nanoparticles after aging; however, no insight was obtained regarding the fresh samples. Therefore, STEM and HR-TEM microscopy studies were conducted on the $(PtPd)_1/\gamma-Al_2O_3$ and $(PtPd)_1Fe_{0.3}/\gamma-Al_2O_3$ fresh catalysts. Figure 5 shows representative HAADF-STEM images and particle size histograms for both catalysts before and after aging. Since the mean atomic number of Pt–Pd–Fe compounds is higher than that of alumina, the active-phase nanoparticles in HAADF-STEM images will scatter more strongly and appear brighter compared to the support. As can be seen from the HAADF-STEM images the supercritical synthesis method was capable of producing finely divided nanoparticles on the $\gamma-Al_2O_3$ support. The average particle size for the fresh samples was approximately the same for both catalysts 2.3 ± 0.6 nm and 2.4 ± 0.6 nm for $(PtPd)_1/\gamma-Al_2O_3$ and $(PtPd)_1Fe_{0.3}/\gamma-Al_2O_3$, respectively. Elemental mapping and line-scan analysis confirmed the presence of nanoparticles composed of PtPd (Figure S01) or PtPdFe (Figure S02). Furthermore, the presence of Fe on the $(PtPd)_1Fe_{0.3}/\gamma-Al_2O_3$ nanoparticles was also observed by SEM-EDX. An Fe

amount of 0.12 wt.% was determined during elemental analysis at low-magnification. The narrow size distribution of both (PtPd)$_1$/γ-Al$_2$O$_3$ and (PtPd)$_1$Fe$_{0.3}$/γ-Al$_2$O$_3$ catalysts shows the strength of the supercritical flow synthesis method and its fast nucleation. For other traditional synthesis methods, such as impregnation on oxide supports, Pt-based nanoparticle sizes are frequently reported to be between 5-10 nm[39-41]. The high surface-to-volume ratio of the prepared catalysts is an important feature in the design of DOCs, known for promoting high-levels of conversion at low-temperature stages, in this case below the low-temperature target recommend by the DOE (T50 for HC < 150 °C)[19]. Moreover, the addition of a low-amount of Fe to the (PtPd)$_1$/γ-Al$_2$O$_3$ improved the activity by increasing the turn over frequency (TOF) from 0.02 s$^{-1}$ to 0.06 s$^{-1}$ at 120° C (Figure 4).
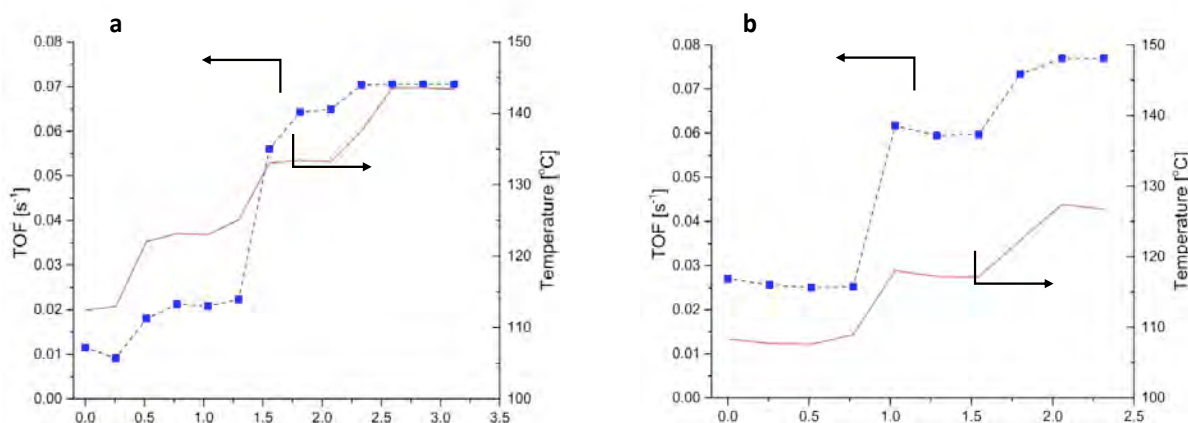


**Figure 4** – TOF of a) (PtPd)$_1$/γ-Al$_2$O$_3$ and b) (PtPd)$_1$Fe$_{0.3}$/γ-Al$_2$O$_3$ catalysts for propene oxidation.

The effect of Fe on the aged samples was also analysed by HAADF-STEM. As seen on Figure 5, the PtPd and PtPdFe nanoparticles have similar sizes as fresh around 2 nm. However, after aging, the fraction of small nanoparticles is higher on the (PtPd)$_1$Fe$_{0.3}$/γ-Al$_2$O$_3$ catalyst, with an average size of 15.1 ± 6.8 nm, whereas the (PtPd)$_1$/γ-Al$_2$O$_3$ average size is 17.8 ± 7.2 nm. Thus, the obtained results along with the XRD data confirm the role of Fe on preventing the growth of the active-

phase nanoparticles. In terms of composition, elemental mapping (Figure S03) show nanoparticles composed by PtPd on the aged $(PtPd)_1/\gamma$-$Al_2O_3$ catalyst, without any oxide species. Accordingly, O signal shows identical concentration in the total area analysed, matching with the Al signal from the $\gamma$-$Al_2O_3$ support and not specifically with the nanoparticle region. Additionally, PdO was not visible on the HAADF-STEM images at higher magnification, which would show up as particles of lower contrast relative to metallic PtPd. For the $(PtPd)_1Fe_{0.3}/\gamma$-$Al_2O_3$ catalyst, the aged nanoparticles are composed of PtPdFe with no oxide formation, and similarly to the $(PtPd)_1/\gamma$-$Al_2O_3$ catalyst (Figure S04 and Figure S05). Along with the Pt and Pd elemental signals, Fe signal was detected on the line scan and elemental mapping, along with an O signal that was attributed to the $\gamma$-$Al_2O_3$ support contribution.
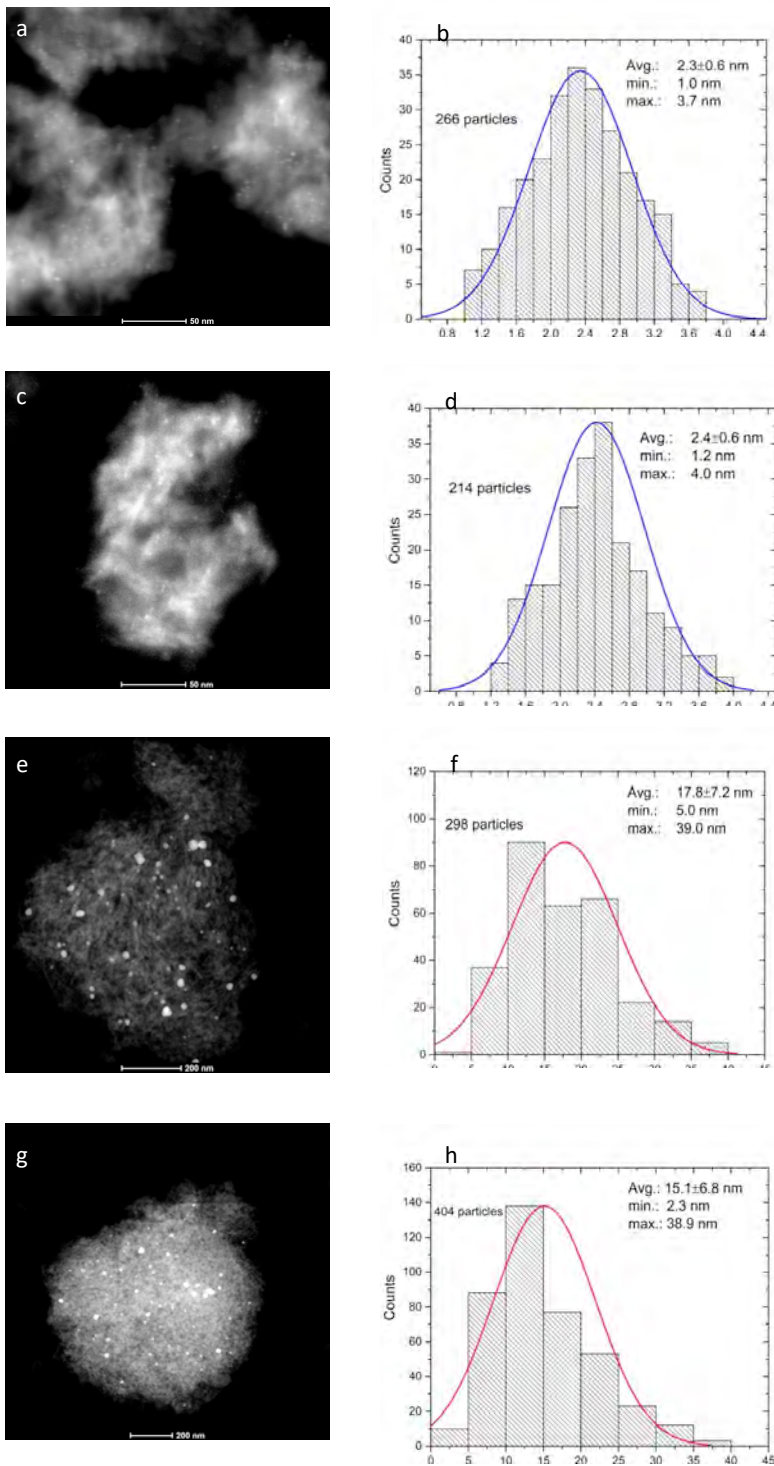
**Figure 5** – HAADF-STEM images and particle size distribution with fitted normal distribution curve of the a,b) $(PtPd)_1/\gamma-Al_2O_3$ and c, d) $(PtPd)_1Fe_{0.3}/\gamma-Al_2O_3$ fresh catalysts; e,f) $(PtPd)_1/\gamma-Al_2O_3$ and g, h) $(PtPd)_1Fe_{0.3}/\gamma-Al_2O_3$ aged catalysts.

**Replacing PtPd precious metal content by Fe**

The effect of Fe addition to PtPd alloyed nanoparticles was further studied by tuning the Fe to precious metal ratio, for the same total metal loading: $x=0.75$ wt.%. Figure 6 shows the activity results expressed as T50 of a series of $(PtPd)_{x-y}Fe_y/\gamma-Al_2O_3$ catalysts with increasing amount of inexpensive Fe, which was added to replace the precious PtPd content. To express the precious metal savings for each measured sample, Figure 6 also depicts the range of PtPd savings in relation with the atomic ratio of Fe to PtPd.
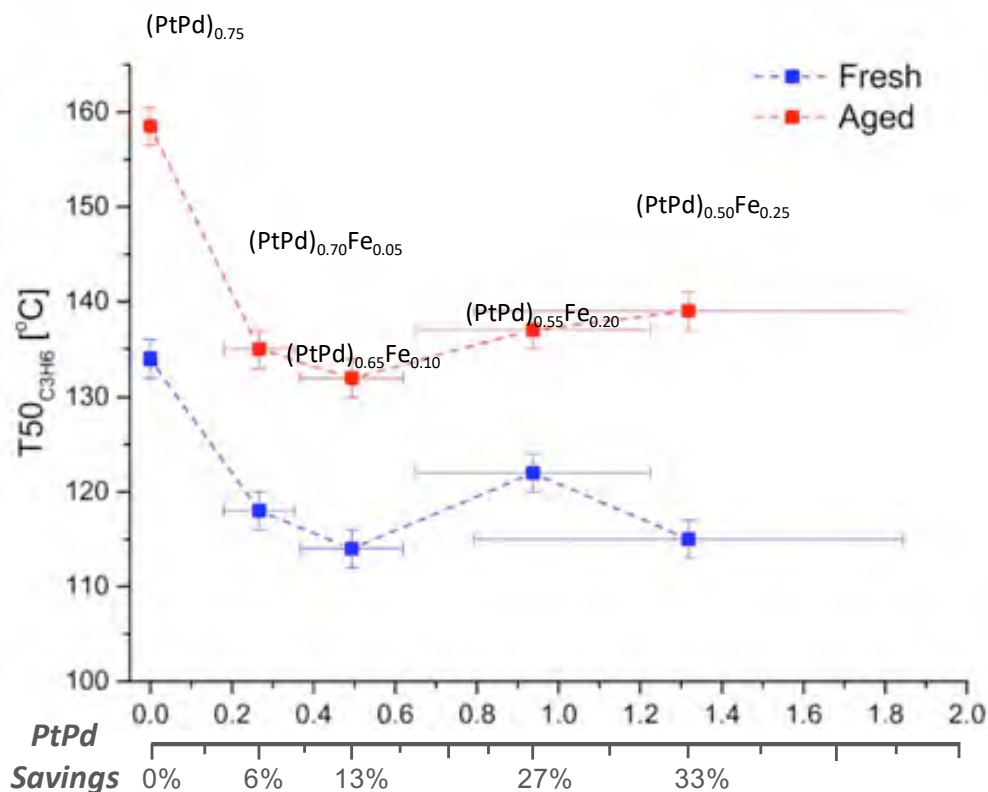


**Figure 6** – Propene oxidation activity, before and after aging at 750 °C/3h (10% $O_2$, 10% $H_2O$), of the supercritical synthesized $(PtPd)_{x-y}Fe_y/\gamma-Al_2O_3$ catalysts, where $x$ is the total catalyst metal

loading in wt.% ($x$=0.75 wt.%) and $y$ is the amount of PtPd substituted by Fe in wt.%. The atomic ratio of Fe to PtPd shown on the x-axis was determined using the atomic compositions measured on SEM-EDX. The range of PtPd savings is shown below the x-axis.

As shown in Figure 6 the T50 is dependent on the atomic ratio of Fe to precious metal. The lowest T50 measured for propene oxidation, ca. 114 °C as fresh and 133 °C after aging, was for a $(PtPd)_{0.65}Fe_{0.10}$/γ-Al$_2$O$_3$ catalyst with atomic ratio of Fe to PtPd of ca. 0.5. This optimized catalyst not only had the best performance for HC oxidation, but also enables savings of ca. 13% of the precious metal amount. Additionally, the $(PtPd)_{0.50}Fe_{0.25}$/γ-Al$_2$O$_3$ uses 33% less of precious metal loading and still displays a superior activity than the bimetallic $(PtPd)_{0.75}$/γ-Al$_2$O$_3$ catalyst. The hydrothermal stability of the catalysts was also evaluated after *in-situ* aging at 750°C/3h (10% O$_2$, 10% H$_2$O). As result, the T50 difference between the bimetallic PtPd sample and the Fe-containing samples is accentuated after aging, being ca. 25 °C for the optimum $(PtPd)_{0.65}Fe_{0.10}$/γ-Al$_2$O$_3$ catalyst, whereas as fresh it was 18 °C. This is a remarkable result, showing that the PtPdFe nanoparticles have allied both to an enhanced fresh activity, a notable durability that reinforces the positive role of Fe in the full life span of the catalyst.

The fresh $(PtPd)_{x-y}Fe_y$/γ-Al$_2$O$_3$ catalysts were further analysed using synchrotron PDF analysis[42]. The diffraction signal from γ-Al$_2$O$_3$ was subtracted from the total scattering pattern leaving only the scattering intensity from the catalytic nanoparticles. Azimuthally integrated intensity data were transformed to G(r) with $Q_{min}$= 0.46 and $Q_{max}$= 20 for the data obtained at P02.1, PETRA III ensuring the best compromise between resolution and noise. A spherically attenuated fcc bulk model for PtPd alloy was refined constraining the chemical composition to the stoichiometry obtained by SEM-EDX.
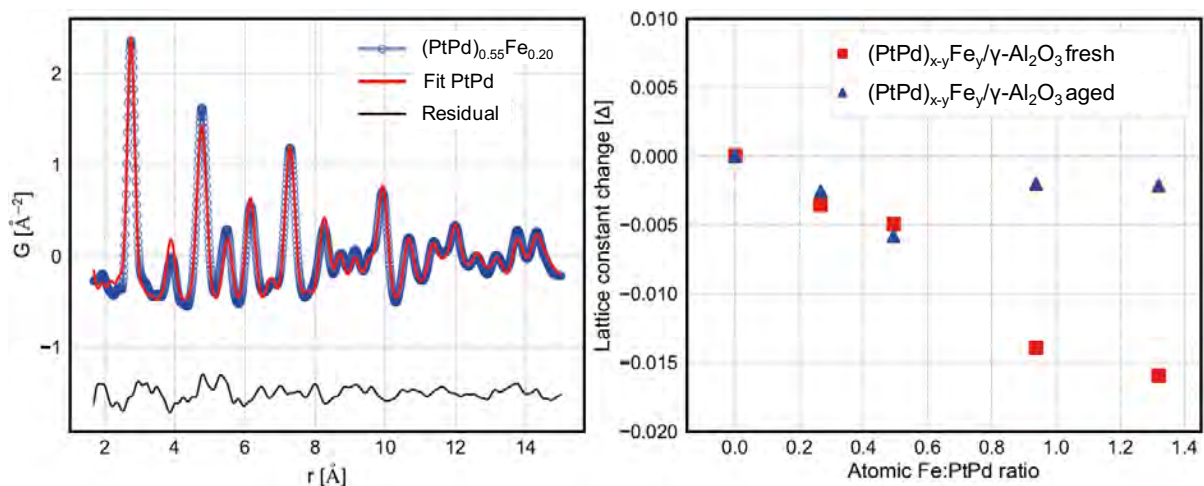
**Figure 7** – a) PDF fitting of a spherically attenuated fcc model with agreement factor R$w$=17%. b) Lattice parameters from the background subtracted datasets for PtPd and PtPdFe revealing a trend of lattice contraction as result of Fe incorporation.

The refinement results show that the simple model was sufficient to describe all of the major features present in the data as shown in Figure 7a). Lattice parameters were extracted from the refined models as shown in Figure 7b), and for the fresh catalysts reveal a decreasing trend as the amount of Fe in the system increases. As no features indicating oxide phases were observed, the decreasing lattice parameter trend is consistent with alloying of Fe into the PtPd lattice. Due to difficulties when examining highly scattering supported nanomaterial with x-rays the presence of an additional Fe phase cannot be completely ruled out, yet the findings indicate that the nanoparticles consist mainly of a nanocrystalline fcc phase. Nanoparticle crystallite sizes were extracted from the spherical particle attenuation function and were 2.0 ± 0.2 nm, which is consistent with HAADF-STEM results (see Figure S06). After aging, the lattice constant matches the measured values of the fresh state until a Fe:PtPd atomic ratio of 0.5, indicating that Fe remains alloyed with PtPd, even after the harsh aging conditions. However, the aged lattice constant increases when compared with the fresh state for ratios higher than 0.5, suggesting partial

segregation of Fe from the PtPd lattice. Sakamoto *et. al.*, reports the segregation of Fe to $Fe_2O_3$ phase on PtFe nanoparticulate system, but for catalysts prepared by impregnation with higher Pt loadings (i.e. 3.5 wt.%), and larger Fe addition of 1.10 wt.% and 5.16 wt.%[43].

Overall, the combined results from synchrotron XRD and HAADF-STEM show that Fe is alloyed with PtPd, which can be related to the activity enhancement according to the d-band theory[44–46]. Thus, Fe-alloying lowers the d-band center in comparison with PtPd alloy and this way oxygen adsorbs more weakly on the PtPdFe nanoparticles surface.

These results demonstrate how low-temperature activity can be achieved with improved durability in a catalysis field where the material demand for precious Pt and Pd has been growing at a fast pace to answer the stricter legislations limits. Furthermore, the supercritical flow synthesis method was shown to be highly effective in the preparation of size-controlled nanoparticles, displaying distinct properties responsible for their superior catalytic performance.

**CONCLUSIONS**

Supercritical flow technology, with throughput rate up to 0.5 kg·h^{-1} was effectively used on the synthesis of highly dispersed PtPd and PtPdFe nanoparticles on a high surface area $\gamma$-$Al_2O_3$ support. The addition of a low-amount of Fe, 0.12 wt.%, enhanced the HC activity of the (PtPd)$_1$/$\gamma$-$Al_2O_3$ fresh catalyst, increasing the TOF from 0.02 s^{-1} to 0.06 s^{-1}, at the low-temperature stage of ca. 120 °C. Additionally, Fe constrained sintering of PtPd alloyed nanoparticles when exposed to aging conditions, as shown on XRD and HAADF-STEM. Noteworthy, is also the possibility of replacing precious metal amount by Fe, which allows less usage of PtPd while leading to an optimization of the catalytic activity and stability. Synchrotron x-ray powder diffraction showed that by increasing the Fe amount there is a decreasing trend to the PtPd associated lattice, suggesting that PtPdFe

alloyed nanoparticles are formed, promoting a higher activity of the fresh catalysts when compared to the bimetallic PtPd system. A $(PtPd)_{0.65}Fe_{0.10}/\gamma\text{-}Al_2O_3$ catalyst exhibited the lowest T50 for $C_3H_6$ oxidation, being significantly better than the $(PtPd)_{0.75}/\gamma\text{-}Al_2O_3$ catalyst, both as fresh and after aging. This optimum catalyst led to 13 % savings of precious metals, which can go up to 33 % by increasing the amount of Fe, and still exhibit a better performance than the bimetallic PtPd catalyst, extensively used on commercial catalytic converters.

**Corresponding Author**

*Christian Kallesøe (e-mail: chkl@teknologisk.dk).

**ABBREVIATIONS**

DOC, diesel oxidation catalyst; TOF, turn over frequency.

**REFERENCES**

(1)     Fino, D.; Bensaid, S.; Piumetti, M.; Russo, N. A Review on the Catalytic Combustion of Soot in Diesel Particulate Filters for Automotive Applications: From Powder Catalysts to Structured Reactors. *Appl. Catal. A Gen.* **2016**, *509*, 75–96.

(2)     Weiss, M.; Bonnel, P.; Kühlwein, J.; Provenza, A.; Lambrecht, U.; Alessandrini, S.; Carriero, M.; Colombo, R.; Forni, F.; Lanappe, G.; et al. Will Euro 6 Reduce the NOx Emissions of New Diesel Cars? – Insights from on-Road Tests with Portable Emissions Measurement Systems (PEMS). *Atmos. Environ.* **2012**, *62*, 657–665.

(3)     Simonsen, S. B.; Chorkendorff, I.; Dahl, S.; Skoglundh, M.; Sehested, J.; Helveg, S. Direct Observations of Oxygen-Induced Platinum Nanoparticle Ripening Studied by In Situ TEM. *J. Am. Chem. Soc.* **2010**, *132* (23), 7968–7975.

(4)     Contreras, J. L.; Fuentes, G. A. Sintering of Supported Metal Catalysts. In *Sintering-Methods and Products*; InTech, 2012.

(5)     Johns, T. R.; Gaudet, J. R.; Peterson, E. J.; Miller, J. T.; Stach, E. A.; Kim, C. H.; Balogh, M. P.; Datye, A. K. Microstructure of Bimetallic Pt🍎Pd Catalysts under Oxidizing Conditions. *ChemCatChem* **2013**, *5* (9), 2636–2645.

(6)     Wiebenga, M. H.; Kim, C. H.; Schmieg, S. J.; Oh, S. H.; Brown, D. B.; Kim, D. H.; Lee, J.-H.; Peden, C. H. F. Deactivation Mechanisms of Pt/Pd-Based Diesel Oxidation Catalysts. *Catal. Today* **2012**, *184* (1), 197–204.

(7)     Russell, A.; Epling, W. S. Diesel Oxidation Catalysts. *Catal. Rev.* **2011**, *53* (4), 337–423.

(8)     Carrillo, C.; Johns, T. R.; Xiong, H.; DeLaRiva, A.; Challa, S. R.; Goeke, R. S.; Artyushkova, K.; Li, W.; Kim, C. H.; Datye, A. K. Trapping of Mobile Pt Species by PdO

Nanoparticles under Oxidizing Conditions. *J. Phys. Chem. Lett.* **2014**, *5* (12), 2089–2093.

(9)    Johns, T. R.; Goeke, R. S.; Ashbacher, V.; Thüne, P. C.; Niemantsverdriet, J. W.; Kiefer, B.; Kim, C. H.; Balogh, M. P.; Datye, A. K. Relating Adatom Emission to Improved Durability of Pt–Pd Diesel Oxidation Catalysts. *J. Catal.* **2015**, *328*, 151–164.

(10)   Xiong, H.; Peterson, E.; Qi, G.; Datye, A. K. Trapping Mobile Pt Species by PdO in Diesel Oxidation Catalysts: Smaller Is Better. *Catal. Today* **2016**, *272* (Supplement C), 80–86.

(11)   Carrillo, C.; DeLaRiva, A.; Xiong, H.; Peterson, E. J.; Spilde, M. N.; Kunwar, D.; Goeke, R. S.; Wiebenga, M.; Oh, S. H.; Qi, G.; et al. Regenerative Trapping: How Pd Improves the Durability of Pt Diesel Oxidation Catalysts. *Appl. Catal. B Environ.* **2017**, *218* (Supplement C), 581–590.

(12)   Ward, M. R.; Hyde, T.; Boyes, E. D.; Gai, P. L. Nanostructural Studies of Fresh and Road-Aged Practical Pt/SiO2 and Pt-Pd/Al2O3 Diesel Oxidation Catalysts by Using Aberration-Corrected (Scanning) Transmission Electron Microscopy. *ChemCatChem* **2012**, *4* (10), 1622–1631.

(13)   Khosravi, M.; Sola, C.; Abedi, A.; Hayes, R. E.; Epling, W. S.; Votsmeier, M. Oxidation and Selective Catalytic Reduction of NO by Propene over Pt and Pt:Pd Diesel Oxidation Catalysts. *Appl. Catal. B Environ.* **2014**, *147*, 264–274.

(14)   Khosravi, M.; Abedi, A.; Hayes, R. E.; Epling, W. S.; Votsmeier, M. Kinetic Modelling of Pt and Pt:Pd Diesel Oxidation Catalysts. *Appl. Catal. B Environ.* **2014**, *154* (Supplement C), 16–26.

(15)   Marafi, M.; Stanislaus, A.; Furimsky, E. Chapter 14 - Markets and Price Trends for Metals

in Spent Hydroprocessing Catalysts BT - Handbook of Spent Hydroprocessing Catalysts (Second Edition); Elsevier, 2017; pp 405–411.

(16)    Chigapov, A. N.; Carberry, B. P. Oxidation Catalysts. Google Patents March 2010.

(17)    Sakamoto, Y.; Higuchi, K.; Takahashi, N.; Yokota, K.; Doi, H.; Sugiura, M. Effect of the Addition of Fe on Catalytic Activities of Pt/Fe/γ-Al2O3 Catalyst. *Appl. Catal. B Environ.* **1999**, *23* (2), 159–167.

(18)    Kim, Y.-S.; Lim, S. J.; Kim, Y. H.; Lee, J. H.; Lee, H.-I. The Role of Fe on PtPd Oxidation Catalyst Prepared by Simultaneous and Sequential Incipient Wetnesses. *J. Ind. Eng. Chem.* **2012**, *18* (2), 720–725.

(19)    Zammit, M.; DiMaggio, C.; GM, C. K.; Lambert, C.; Muntean, G.; Peden, C.; Parks, J.; DOE, K. H. Future Automotive Aftertreatment Solutions: The 150 C Challenge Workshop Report.

(20)    Maletz, G.; Kurth, V.; Bentele, A.; Wanninger, K.; Tissler, A. Coating Composition for Diesel Oxidation Catalysts. Google Patents April 2013.

(21)    Hoff, T. C.; Thilakaratne, R.; Gardner, D. W.; Brown, R. C.; Tessonnier, J.-P. Thermal Stability of Aluminum-Rich ZSM-5 Zeolites and Consequences on Aromatization Reactions. *J. Phys. Chem. C* **2016**, *120* (36), 20103–20113.

(22)    Valle, B.; Gayubo, A. G.; Alonso, A.; Aguayo, A. T.; Bilbao, J. Hydrothermally Stable HZSM-5 Zeolite Catalysts for the Transformation of Crude Bio-Oil into Hydrocarbons. *Appl. Catal. B Environ.* **2010**, *100* (1), 318–327.

(23)    Gayubo, A. G.; Alonso, A.; Valle, B.; Aguayo, A. T.; Olazar, M.; Bilbao, J. Hydrothermal

Stability of HZSM-5 Catalysts Modified with Ni for the Transformation of Bioethanol into Hydrocarbons. *Fuel* **2010**, *89* (11), 3365–3372.

(24) Siani, A.; Alexeev, O.; Captain, B.; Lafaye, G.; Marecot, P.; Adams, R.; Amiridis, M. Synthesis of Cluster-Derived PtFe/SiO2 Catalysts for the Oxidation of CO. *J. Catal.* **2008**, *255* (2), 162–179.

(25) Siani, A.; Alexeev, O. S.; Lafaye, G.; Amiridis, M. D. The Effect of Fe on SiO2-Supported Pt Catalysts: Structure, Chemisorptive, and Catalytic Properties. *J. Catal.* **2009**, *266* (1), 26–38.

(26) Chen, H.; Liu, Y.; Yang, F.; Wei, M.; Zhao, X.; Ning, Y.; Liu, Q.; Zhang, Y.; Fu, Q.; Bao, X. Active Phase of FeOx/Pt Catalysts in Low-Temperature CO Oxidation and Preferential Oxidation of CO Reaction. *J. Phys. Chem. C* **2017**, *121* (19), 10398–10405.

(27) Dunn, J. P.; Stenger, H. G.; Wachs, I. E. Oxidation of SO 2 over Supported Metal Oxide Catalysts. *J. Catal.* **1999**, *181* (2), 233–243.

(28) Fu, H.; Wang, X.; Wu, H.; Yin, Y.; Chen, J. Heterogeneous Uptake and Oxidation of SO2 on Iron Oxides. *J. Phys. Chem. C* **2007**, *111* (16), 6077–6085.

(29) Kallesøe, C.; Clausen, H. F.; Christensen, L. H. Method of Preparing a Catalyst Structure. Google Patents July 2015.

(30) Kallesøe, C.; Fanø, C. H.; Højslet, C. L.; Lund-Olesen, T.; Aref, H. M. M.; Brummerstedt, I. B.; Becker-Christensen, J.; Friis, A. D.; Hales, J. Method of Preparing a Catalytic Structure. Google Patents January 2014.

(31) Wettergren, K.; Schweinberger, F. F.; Deiana, D.; Ridge, C. J.; Crampton, A. S.; Rötzer, M.

D.; Hansen, T. W.; Zhdanov, V. P.; Heiz, U.; Langhammer, C. High Sintering Resistance of Size-Selected Platinum Cluster Catalysts by Suppressed Ostwald Ripening. *Nano Lett.* **2014**, *14* (10), 5803–5809.

(32)   Ellis, P. R.; Brown, C. M.; Bishop, P. T.; Yin, J.; Cooke, K.; Terry, W. D.; Liu, J.; Yin, F.; Palmer, R. E. The Cluster Beam Route to Model Catalysts and Beyond. *Faraday Discuss.* **2016**, *188* (0), 39–56.

(33)   Imaoka, T.; Akanuma, Y.; Haruta, N.; Tsuchiya, S.; Ishihara, K.; Okayasu, T.; Chun, W.-J.; Takahashi, M.; Yamamoto, K. Platinum Clusters with Precise Numbers of Atoms for Preparative-Scale Catalysis. *Nat. Commun.* **2017**, *8*, 688.

(34)   Froment, G. F. *Chemical Reactor Analysis and Design*; Wiley, 1990.

(35)   Chupas, P. J.; Qiu, X.; Hanson, J. C.; Lee, P. L.; Grey, C. P.; Billinge, S. J. L. Rapid-Acquisition Pair Distribution Function (RA-PDF) Analysis. *J. Appl. Crystallogr.* **2003**, *36* (6), 1342–1347.

(36)   Herreros, J. M.; Gill, S. S.; Lefort, I.; Tsolakis, A.; Millington, P.; Moss, E. Enhancing the Low Temperature Oxidation Performance over a Pt and a Pt–Pd Diesel Oxidation Catalyst. *Appl. Catal. B Environ.* **2014**, *147* (Supplement C), 835–841.

(37)   Kim, M.-Y.; Kyriakidou, E. A.; Choi, J.-S.; Toops, T. J.; Binder, A. J.; Thomas, C.; Parks II, J. E.; Schwartz, V.; Chen, J.; Hensley, D. K. Enhancing Low-Temperature Activity and Durability of Pd-Based Diesel Oxidation Catalysts Using ZrO2 Supports. *Appl. Catal. B Environ.* **2016**, *187*, 181–194.

(38)   Li, W.-Z.; Kovarik, L.; Mei, D.; Liu, J.; Wang, Y.; Peden, C. H. F. Stable Platinum

Nanoparticles on Specific MgAl2O4 Spinel Facets at High Temperatures in Oxidizing Atmospheres. *Nat Commun* **2013**, *4*.

(39)     Valdez, R.; Pawelec, B.; Quintana, J. M.; Olivas, A. Effect of the Acidity of Alumina over Pt, Pd, and Pt–Pd (1:1) Based Catalysts for 2-Propanol Dehydration Reactions. *Fuel* **2013**, *105* (Supplement C), 688–694.

(40)     Graham, G. W.; Jen, H.-W.; Ezekoye, O.; Kudla, R. J.; Chun, W.; Pan, X. Q.; McCabe, R. W. Effect of Alloy Composition on Dispersion Stability and Catalytic Activity for NO Oxidation over Alumina-Supported Pt--Pd Catalysts. *Catal. Letters* **2007**, *116* (1), 1–8.

(41)     Ikeda, M.; Takeshima, S.; Tago, T.; Kishida, M.; Wakabayashi, K. Preparation of Size-Controlled Pt Catalysts Supported on Alumina. *Catal. Letters* **1999**, *58* (4), 195–197.

(42)     Guagliardi, A.; Masciocchi, N. *Diffraction at the Nanoscale: Nanocrystals, Defective & Amorphous Materials*; Insubria University Press, 2010.

(43)     Sakamoto, Y. Effect of the Addition of Fe on Catalytic Activities of Pt/Fe/γ-Al2O3 Catalyst. *Appl. Catal. B Environ.* **1999**, *23* (2–3), 159–167.

(44)     Stamenkovic, V.; Mun, B. S.; Mayrhofer, K. J. J.; Ross, P. N.; Markovic, N. M.; Rossmeisl, J.; Greeley, J.; Nørskov, J. K. Changing the Activity of Electrocatalysts for Oxygen Reduction by Tuning the Surface Electronic Structure. *Angew. Chemie-International Ed.* **2006**, *45* (18), 2897–2901.

(45)     Nørskov, J. K.; Studt, F.; Abild-Pedersen, F.; Bligaard, T. The Electronic Factor in Heterogeneous Catalysis. *Fundam. Concepts Heterog. Catal.* 114–137.

(46)     Nørskov, J. K.; Abild-Pedersen, F.; Studt, F.; Bligaard, T. Density Functional Theory in

*Low-temperature and hydrothermal stability are key performance indicators of DOCs. PtPd precious metal nanoparticles are the state of the art catalysts to answer the stricter legislation. PtPdFe nanoparticles prepared by supercritical synthesis not only outperform PtPd catalyst, but also allow savings of precious metal up to 33 %.*
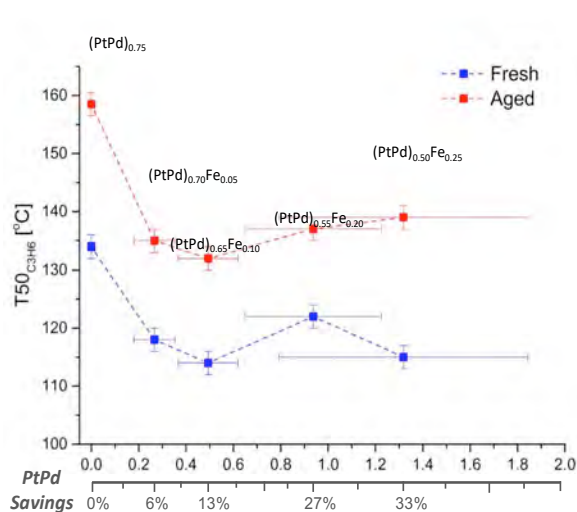


Hugo Silva[a], Patricia Hernandez-Fernandez[a], Ane K. Baden[a], Henrik L. Hellstern[a], Anton Kovyakh[a,c], Erik Wisaeus[a], Ib Chorkendorff[b], Leif H. Christensen[a], Debasish Chakraborty[b], Christian Kallesøe[a*]

**Page 1 – Page 28**

*Supercritical Flow Synthesis of Cost-effective PtPdFe Nanoparticles for Low-temperature Diesel Oxidation*

# Streamlining data analysis and modelling for high-throughput synchrotron datasets

Anton Kovyakh,[1,2] Soham Banerjee,[2] Chia-Hao Liu,[2] Christopher J. Wright,[2] Yuguang
C. Li,[3] Thomas E. Mallouk,[3] Robert Feidenhans'l,[1] and Simon J. L. Billinge[2,4]

[1] *Niels Bohr Institute, University of Copenhagen,*
*Universitetsparken 5, DK-2100 Copenhagen, Denmark*
[2] *Department of Applied Physics and Applied Mathematics, Columbia University, New York, NY 10027*
[3] *Department of Engineering Science and Mechanics, Department of Chemistry,*
*and Department of Biochemistry and Molecular Biology and Department of Physics,*
*The Pennsylvania State University, University Park, Pennsylvania 16802, United States*
[4] *Condensed Matter Physics and Materials Science Department,*
*Brookhaven National Laboratory, Upton, NY 11973*
(Dated: April 30, 2018)

Obtaining quantitative structural information efficiently is essential to studying materials synthesized from combinatorial methods. To address this we propose a protocol for measuring and analyzing data from high-throughput experiments. A combinatorial array containing catalytic nanoparticles was prepared directly on-chip from liquid precursors using an ink-jet liquid handling system. The array was then measured at the X-ray powder diffraction beamline (NSLS-II) and analyzed by the pair distribution function (PDF) technique using a software implementation of the protocol. The protocol software can handle semi-automated data reduction, normalization and modelling, with user-defined recipes generating a comprehensive collection of metadata and analysis results. By slicing the collection using included functions it was possible to determine the distribution of material on the array, highlight regions with heterogeneity, and visualize spatially varying structural parameters. The modular design of the software is intended to be transparent and extensible, with potential applications to other experimental techniques.

## INTRODUCTION

Several strategies exist for increasing the throughput of x-ray diffraction measurements like employing robotic sample makers[1], *in-situ* ion beam sputtering deposition[2] or by operando studies[3]. One of the more promising methods is analyzing combinatorial arrays of thin film libraries on a chip, a synthesis method which has become a widely accepted industry standard[4, 5] in many fields including heterogeneous catalysis, pharmaceuticals, biomaterials, optics and multi-principal element alloys[6–11]

Advances in ink-jet printing technologies allow for deposition of hundreds to thousands of distinct compositions on a single substrate[12]. Analysis of such arrays is possible using the recently demonstrated normal incidence thin film diffraction method and PDF analysis[13].

Such high throughput (HT) measurements challenge existing powder diffraction workflows at synchrotron sources. Even when the data may be collected rapidly using large area 2D detectors [14] the complex data reduction and modelling steps are not currently automated resulting in many datasets that must be processed manually, which is time-consuming and error-prone. This becomes extremely challenging when the library sizes increase past $\sim 10^2$ measurement points. In the lab-on-a-chip experiment one of the key steps is to relate positional information (where the beam hits the sample) with measured data in the form of diffraction images and any prior information from the sample preparation such as target composition. Automation is a priority at modern x-ray synchrotron beamlines where metadata about the instrument configuration, such as motor positions, is available electronically.

Here we describe a protocol for handling this type of analysis, including data acquisition at the XPD powder diffraction instrument at NSLS-II, data reduction that tolerates sample heterogeneity, and subsequent data analysis using the pair distribution function (PDF) technique. The accompanying software allows the data to be reduced and analyzed in a highly automated fashion, and the extracted material specific properties to be easily visualized as 2D parameter maps. As a demonstration we consider an array of catalytic nanoparticles. This supports a major goal in HT nanostructure characterization for situations with hundreds of measurements per hour and analysis times on the same order of magnitude as the measurement time [11].

The protocol is developed for screening spatially resolved PDF data and is modular in design. This allows the protocol to be extended to a wide variety high throughput experiments, such as in-situ synthesis experiments, as well as other experimental techniques.

## THE PDF METHOD

The experimental PDF, denoted $G(r)$, is the truncated Fourier transform of the total scattering structure function, $F(Q) = Q[S(Q) - 1]$:[15]

$$G(r) = \frac{2}{\pi} \int_{Q_{\min}}^{Q_{\max}} F(Q) \sin(Qr)\, \mathrm{d}Q, \qquad (1)$$

where $Q$ is the magnitude of the scattering momentum. The structure function, $S(Q)$, is extracted from the Bragg and diffuse components of x-ray, neutron or electron powder diffraction intensity.

The PDF gives the scaled probability of finding two atoms in a material a distance $r$ apart and is related to the density of atom pairs in the material.[16] For a
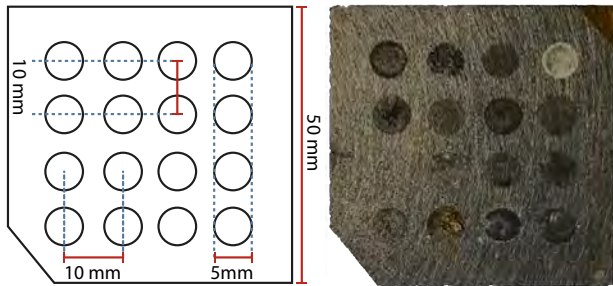
FIG. 1. A typical sample layout for combinatorial studies (left) and the tested array or catalytic material(right). A square piece of carbon paper was used as a substrate for the ink-jet printed material in a 4x4 configuration



FIG. 2. The combinatorial library mounted on a 3D printed bracket in front of the x-ray beam. The array is mounted to the goniometer which allows measurement access to all deposition sites.

macroscopic scatterer, $G(r)$ can be calculated from a known structure model according to

$$G(r) = 4\pi r \left[\rho(r) - \rho_0\right],\qquad(2)$$

$$\rho(r) = \frac{1}{4\pi r^2 N} \sum_i \sum_{j \neq i} \frac{b_i b_j}{\langle b\rangle^2} \delta(r - r_{ij}).$$

Here, $\rho_0$ is the atomic number density of the material and $\rho(r)$ is the atomic pair density, which is the mean weighted density of neighbor atoms at distance $r$ from an atom at the origin. The sums in $\rho(r)$ run over all atoms in the sample, $b_i$ is the scattering factor of atom $i$, $\langle b\rangle$ is the average scattering factor and $r_{ij}$ is the distance between atoms $i$ and $j$.

Eqs. 2 is used to fit the PDF generated from a structure model to a PDF determined from experiment. For this purpose, the delta functions in Eqs. 2 are Gaussian-broadened and the equation is modified to account for experimental effects. PDF modelling is performed by adjusting the parameters of the structure model to maximize the agreement between the theoretical and an experimental PDF, described by the weighted agreement factor parameter $R_w$.

## EXPERIMENT

The combinatorial catalyst library was deposited using a Pipetmax automated liquid handling system on semicrystalline carbon paper (Toray 120, from FuelCellStore) in a $4 \times 4$ grid giving 16 circular deposition sites ("wells") 5 mm in diameter and with a center to center spacing of 10 mm. Transition metal nitrate solutions at 0.1 M were used for deposition, except for the Au well where $HAuCl_4$ was used. The precursor solutions were mixed onto the carbon paper and reduced with excess hydrazine solution. The sample was then vacuum dried over night in a 60 degree oven and washed with DI water to create the different alloyed metal samples as shown in Fig. 1. The choice of chemicals, size, number of samples and pattern are programmable from the liquid handling system for future implementations of this protocol.
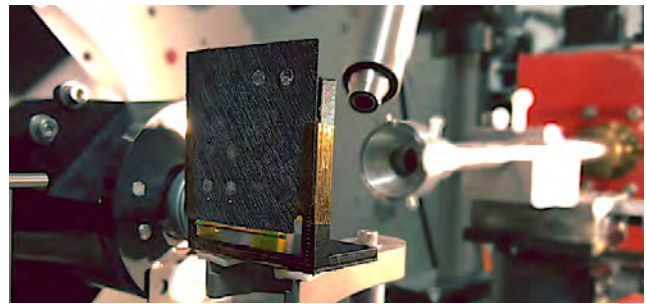
The experiments were carried out at the 28-ID-II (XPD) beamline (NSLS-II; Brookhaven National Lab-

oratory) using the normal incidence thin film PDF (tfPDF) method [13]. The combinatorial array was mounted perpendicular to the x-ray beam direction using a 3D printed bracket. The measurements were performed in a transmission geometry as shown in Fig. 2. The array was moved relative to the beam position using goniometer motors in an $xy$-plane perpendicular to the incident beam direction, with a fixed sample to detector distance. A 2D detector was placed behind the sample at a distance of 203.4 mm, which gave an effective instrumental $Q$ range, where $Q = 4\pi \sin\theta/\lambda$, of $0.12 \leq Q \leq 32$ Å$^{-1}$. The incident wavelength of the x-rays was $\lambda = 0.183983$ Å with a beam cross section at the sample of $250 \times 300$ $\mu m$ in the vertical and horizontal directions, respectively.

The sample wells are much larger than the beam, and the sample distribution within the wells is not uniform (see the Results section). We therefore sought a measurement protocol that scanned over large areas of the sample in order to find both the best measurement conditions for sample determination, and also to assess the heterogeneity of the sample. A zoomed-in measurement area of 9 mm by 15 mm was chosen over which the beam was scanned in a meandering array of points. The chosen scan pattern encompassed two catalyst "wells" containing AuAg and AgCu nanocrystalline material, respectively, as shown in Fig. 1.

A coarse alignment was done to set the position of the first measurement point by using a laser coaxially aligned with the incoming x-ray beam. The meandering measurement pattern was then executed with a series of 1 mm steps vertically followed by 1 mm horizontal offsets rastering back in the vertical direction, repeated to cover the full measurement area. Exposure time was selected, based on signal quality, and set to $5s$ per point achieving measurement throughput of over 6000 measurements per hour.

The sample-detector distance, $Q$ range and the geometric orientation of the detector were calibrated by measuring a crystalline Ni powder mounted on the same bracket that holds the sample chip prior to data collection. The experimental geometry parameters were refined using the Fit2D program [17]. A mask was created to remove outlier pixels and applied to the 2D images from the measurement series before azimuthal

integration to 1D diffraction patterns.

The carbon sheet produces a significant background in this experimental geometry, but the background signal can be subtracted from the data leaving only the structural information of the deposited material. Background subtraction is not trivial for these samples and is described in greater detail in the results section. The total scattering structure function, $F(Q)$, was then obtained after standard corrections and normalizations of the data and Fourier transformed to obtain the PDF, using PDFgetX3 [18] within xPDFsuite [19]. The maximum range of data used in the Fourier transform ($Q_{max}$) was chosen to be 21 Å$^{-1}$ in the current case, which was the best compromise between resolution and noise.

## RESULTS

### Protocol automation software

The main goal of the protocol is to address the large number of measured data-points that are generated during high throughput experiments. We have written a set of Python scripts that are intended to be highly flexible and customizable allowing for efficient data collection, curation, reduction and analysis. The software is intended to be accessible and user friendly. The code can be executed using IPython[20] and Jupyter notebook.

The overall approach builds a collection of information about the experiment, associating reduced data, user inputs based on prior knowledge of the material, and analysis results. The collection can then be sliced and visualized easily by the user to interrogate and draw conclusions from the entire dataset. A schematic of the overall layout is shown in Fig. 3 showing all of the modules and the general workflow.

The data analysis protocol is currently optimized for the XPD beamline at NSLS-II. After a measurement, the acquisition software at the beamline outputs a log file containing the metadata, such as motor positions, measurement times and unique identifiers for each diffraction image.

In the first step the protocol software interrogates the log file and converts each measurement entry into an event. Each event then contains links to positional and other measurement metadata and the corresponding image files. The main benefit of the approach is manageability of the contents of the collection which are easy to visualize for the user using standard python plotting packages such as matplotlib[21] in conventional 1D or heatmap plots by simple iteration and filtering of the corresponding keywords. In addition we have prepared a few custom plotting functions that produce the figures presented.

Any pre existing knowledge can be appended to the corresponding event entries using simple macros, such as python for loops and conditional statements. For example, we can add composition information based on our prior knowledge of the layout of the sample:
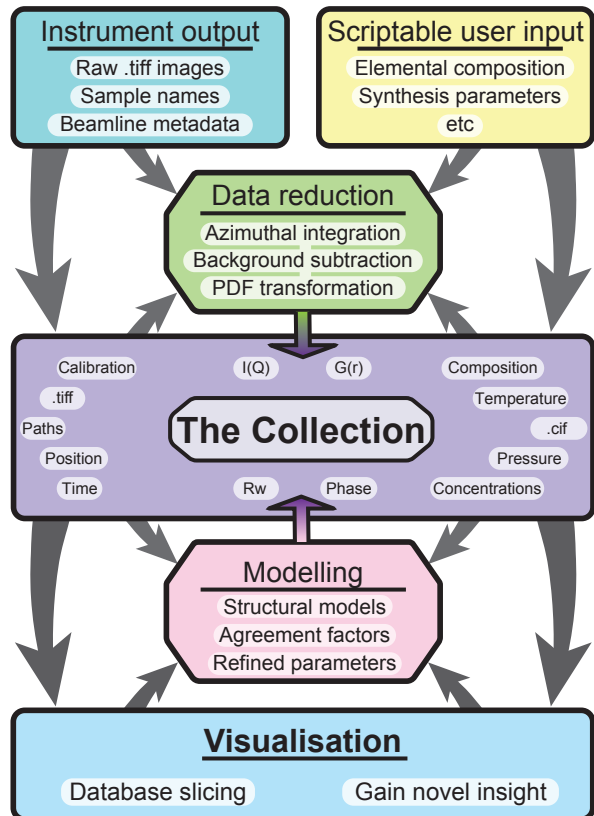


FIG. 3. A flowchart illustrating the core of the mapPDF protocol and current implementation. Instrumental output is combined with user created metadata to perform data reduction. Every step of the process is saved in the collection which can be sliced and visualized for screening and advanced analysis.

```
i = collection['x_motor'] < 1
collection[i]['composition'] = 'AgCu'
```

This way, any useful information which is absent in the metadata can be added on a per entry basis.

Experimental geometry calibration information is obtained from a Ni standard material measured at the same time as the array (Fig. 2). Calibration parameters are used when the images are azimuthally integrated to one dimensional $I(Q)$ patterns using Fit2D. The integrated patterns are then linked alongside the other information in the collection to the correct events as data arrays.

### Background subtraction

The tfPDF measurement requires careful subtraction of the substrate scattering because the substrate signal (background) was significant compared to the small signal from the deposited nanoparticles.

Background images were acquired from a sample region with no nanomaterial and integrated to $I(Q)$ in the same way as the images containing the material. A different background measurement can be assigned to each entry in the collection. This is particularly useful when substrate properties vary as a function of position

and a background measurement in proximity to the material of interest is optimal for signal extraction. In the present case a single background dataset was collected from the center of the array and assigned to all images.

The background subtraction is performed after interpolating the background dataset onto the $Q$ grid of the target pattern. In most cases a scaling factor of 1 is used for all backgrounds in a dataset, but a global scale factor may be defined by the user if needed. Additionally, a utility function has been provided to optimize the background subtraction per entry in the collection, by minimizing the difference between sample and background signal intensity, over a user defined $Q$-range[22]. The background subtracted diffraction patterns are then appended to the collection as data arrays.

### PDF transformation and model fitting

The background subtracted $I(Q)$ data is Fourier transformed to the PDF using PDFgetX3 [18] using parameters such as $Q_{max}$ and elemental compositions that are stored in the collection. The output PDF data, $G(r)$, is again appended to the main collection. A representative example of data at each step of the process is shown in Fig. 4. These transformation steps can be performed on all database entries or a subset.

In the combinatorial array experiment presented, each well contained different metallic nanoparticles. We used an fcc model to refine the experimental PDFs and extract structural parameters for each event in the collection. The PDFs, relevant metadata entries and initial guesses for the structural parameters are fed into the model to perform structural refinement using the DIFFPY-CMI [23] - Complex modelling Infrastructure software available at diffpy.org. A representative example from the combinatorial array experiment may be seen in Fig. 5. The primary parameters of interest from the output of the refinement for this dataset, namely the crystallite size and lattice parameter, and weighted agreement factor $R_w$, are associated with the correct event in the collection, as shown in Fig. 3.

### Visualizing combinatorial data

Good visualization tools are essential for HT experiments. The approach outlined above results in a comprehensive collection of measured data and data analysis results. Presenting this data in a manageable way is usually a major challenge. The main philosophy we have taken is to make spatial maps of scalar quantities that are associated with some aspect of the components in the collection, for example, goodness of fit or lattice parameter. Figure 6 illustrates a usecase where position of the quantity on the plot corresponds to the physical position on the chip where the data were measured, as viewed along the direction of travel of the x-rays. Fig. 6(a) shows the $R_w$ from fits of the fcc model to the background subtracted data from our array of catalytic material as a function of position on the array.
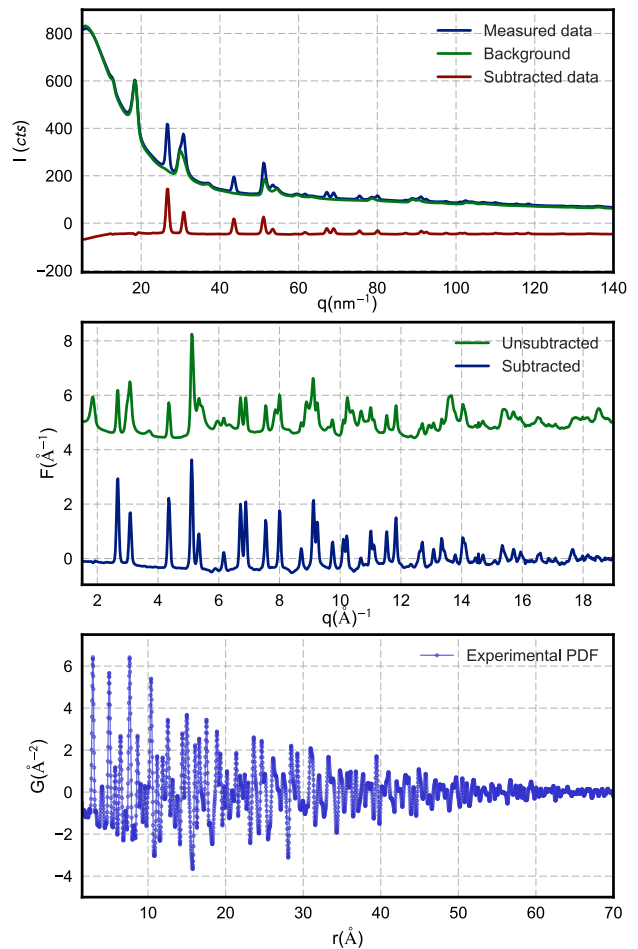


FIG. 4. An example of data processing from a single event in the collection. The background signal is subtracted following normalization in order to better resolve scattered intensity from the nanoparticle sample.
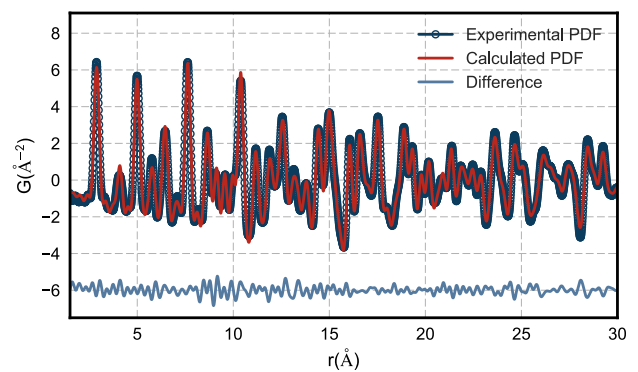


FIG. 5. An example of a single PDF fit using a bimetallic FCC model to one of the datafiles in the collection. Blue illustrate the experimental data. The refinement score ($R_w$) is 12.3%.

The plot can be generated from a complete collection using a simple plotting function:

```
slice_2D('x_motor','y_motor','rw')
```

this function loops over the collection, extracts the parameter of interest, sets the correct boundaries, and provides colorscale. The color of the squares indicates

(a)



(b)
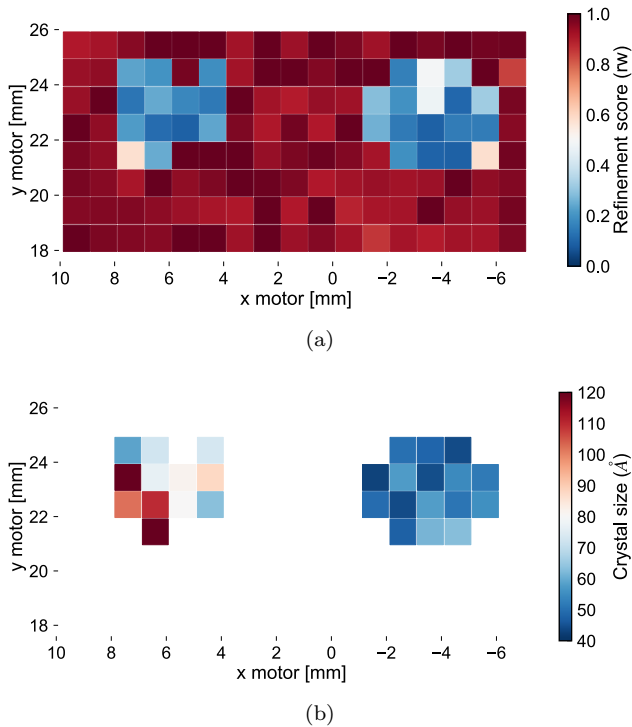
FIG. 6. 6(a) Map of refinement scores vs. position for the array. Red squares indicate a measurement area with a poor refinement score, while blue squares indicate areas with good refinement scores, and thus presence of the fcc phase. There are two distinct regions with nanomaterial surrounded by measurements of nothing but the background. The refinement scores for this dataset are highly correlated with signal to noise ratio and give an indirect metric for the amount of material in a given area. 6(b) Map of particle size vs. position on the array filtered to only display good model refinement scores. The colorscale indicates spherical particle diameter parameter from smaller (blue) to larger (red) crystallite size estimates. The figures are generated using simple conditional statements to slice the collection.

the model fit quality at the measured position, where dark red indicates minimal or no agreement to the candidate structure, and dark blue for good agreement. After the background subtraction step, the areas where all of the signal is from the substrate would contain nothing but noise. Since we are fitting the fcc model, these regions will result in poor $R_w$ values and good fits are an indication of where the catalytic material is located, and how much is there. We can then return to the locations with the material to do more careful structural analyses.

In a similar fashion to the figure above, it is possible to generate maps of any quantity in the collection with multiple filters by using simple python syntax, conditional statements and built in matplotlib functions like the one presented in Figure. 6(b):

```
i = d['rw']<0.3
plt.scatter(d['x'][i], d['y'][i], c=d['psize'][i])
```

The code snippet above generates the spatial map of nanoparticle size vs. position, refined from the fcc model after filtering for acceptable $R_w$. From the figure it becomes clear that the particle size distributions differ within the wells with the AgAu well being much more uniform and smaller on average.

**Software flexibility, modularity and availability**

The software that implements the protocol can be divided into several key parts as presented in figure 3 are initial data treatment, transformation of the data and model fitting and refinement. All three can be modified, replaced or omitted by the user depending on the use-case and user preferences.

Although originally intended for tracking positional information about the sample, the protocol can be extended to keeping track of any scalar quantity and has been found extremely useful for time-series datasets. Structural parameter evolution as a function of time, instead of being a function of motor positions, can be visualized using the protocol software and helps streamline systematic analyses of large in-situ datasets. The methodology is currently being extended for studying nanocluster formation in a wet synthesis environment measured at the P.02 beamline at PetraIII, Hamburg, Germany.

The software, mapPDF, is free and distributed under a BSD license at https://github.com/diffpy/mappdf as well as an example dataset used to generate the figures above.

**CONCLUSION**

An analysis protocol and a set of scripts for treating a wide variety of combinatorial high-throughput materials characterization data is presented. The protocol software is flexible and can be modified and expanded by the user. An example of a combinatorial catalyst library analyzed using the PDF technique has been demonstrated, highlighting the power of the approach. The ability keep track of and analyze large volumes of data and additionally parametrize the dataset allow for quick analysis that is necessary for high throughput experiments.

**ACKNOWLEDGEMENTS**

––––––––––––

[1] I. Yanase, Solid State Ion. **154-155**, 419 (2002).

[2] T. A. Wilson, A. J. Barlow, M. L. Foster, M. Bravo Sanchez, J. F. Portoles, N. Sano, P. J. Cumpson, and I. W. Fletcher, Surf. Interface Anal. **49**, 18 (2016).

[3] J. Nelson, S. Misra, Y. Yang, A. Jackson, Y. Liu, H. Wang, H. Dai, J. C. Andrews, Y. Cui, and M. F. Toney, J. Am. Chem. Soc. **134**, 6337 (2012).

[4] R. F. Service, Science **277**, 474 (1997).

[5] X. D. Xiang, X. D. Sun, G. Briceno, Y. L. Lou, K. A. Wang, H. Y. Chang, W. G. Wallacefreedman, S. W. Chen, and P. G. Schultz, Science **268**, 1738 (1995).

[6] S. M. Senkan, Nat. Mater. **394**, 350 (1998).

[7] R. Daly, T. S. Harrington, G. D. Martin, and I. M. Hutchings, Int. J. Pharm. **494**, 554 (2015).

[8] J. Kohn, Nat. Mater. **3**, 745 (2004).

[9] E. M. Chan, Chem. Soc. Rev. **44**, 1653 (2015).

[10] D. Miracle, B. Majumdar, K. Wertz, and S. Gorsse, Scr. Mater. **127**, 195 (2017).

[11] R. Potyrailo, K. Rajan, K. Stoewe, I. Takeuchi, B. Chisholm, and H. Lam, ACS Comb. Sci. **13**, 579 (2011).

[12] E. Reddington, A. Sapienza, B. Gurau, R. Viswanathan, S. Sarangapani, E. S. Smotkin, and T. E. Mallouk, Science **280**, 1735 (1998).

[13] K. M. O. Jensen, A. B. Blichfeld, S. R. Bauers, S. R. Wood, E. Dooryhée, D. C. Johnson, B. B. Iversen, and S. J. L. Billinge, IUCrJ. **2**, 481 (2015).

[14] P. J. Chupas, X. Qiu, J. C. Hanson, P. L. Lee, C. P. Grey, and S. J. L. Billinge, J. Appl. Crystallogr. **36**, 1342 (2003).

[15] C. L. Farrow and S. J. L. Billinge, Acta Crystallogr. A **65**, 232 (2009).

[16] T. Egami and S. J. L. Billinge, Underneath the Bragg peaks: structural analysis of complex materials, Elsevier, Amsterdam, 2nd edition, 2012.

[17] A. P. Hammersley, Fit2d v12. 012 reference manual v6.0, ESRF Internal Report ESRF98HA01T, 2004.

[18] P. Juhás, T. Davis, C. L. Farrow, and S. J. L. Billinge, J. Appl. Crystallogr. **46**, 560 (2013).

[19] X. Yang, P. Juhás, C. Farrow, and S. J. L. Billinge, arXiv (2015), 1402.3163.

[20] F. Perez and B. E. Granger, Comput. Sci. Eng. **9**, 21 (2007).

[21] J. D. Hunter, Comput. Sci. Eng. **9**, 90 (2007).

[22] S. D. M. Jacques, M. D. Michiel, S. A. J. Kimber, X. Yang, R. J. Cernik, A. M. Beale, and S. J. L. Billinge, Nat. Commun. **4**, 2536 (2013).

[23] P. Juhás, C. L. Farrow, X. Yang, K. R. Knox, and S. J. L. Billinge, Acta Crystallogr. A **71**, 562 (2015).

# Improved models for metallic nanoparticle cores from atomic pair distribution function (PDF) analysis

Soham Banerjee,[†] Chia-Hao Liu,[†] Jennifer D. Lee,[‡] Anton Kovyakh,[¶] Viktoria Grasmik,[§] Oleg Prymak,[§] Christopher Koenigsmann ,[a][‖] Haiqing Liu,[‖] Lei Wang ,[b][‖] A. M. Milinda Abeykoon,[⊥] Stanislaus S. Wong,[‖] Matthias Epple,[§] Christopher B. Murray,[‡][#] and Simon J. L. Billinge[*][†][⊥]

[†]Department of Applied Physics and Applied Mathematics, Columbia University, New York, NY 10027, USA

[‡]Department of Chemistry, University of Pennsylvania, Philadelphia, PA 19104, USA

[¶]Niels Bohr Institute, University of Copenhagen, Universitetsparken 5, DK-2100, Copenhagen, Denmark

[§]Inorganic Chemistry and Center for NanoIntegration Duisburg-Essen (CENIDE), University of Duisburg-Essen, Universitaetsstr. 7, 45141, Essen, Germany

[‖]Department of Chemistry, State University of New York at Stony Brook, Stony Brook, NY 11794, USA

[⊥]Condensed Matter Physics and Materials Science Department, Brookhaven National Laboratory, Upton, NY 11973, USA

[#]Department of Materials Science and Engineering, University of Pennsylvania, Philadelphia, PA 19104, USA

E-mail: sb2896@columbia.edu

---

[a]Current Address: Department of Chemistry, Fordham University, 441 East Fordham Road, Bronx, NY 10548, USA

[b]Current Address: Department of Materials Science and Chemical Engineering, State University of New York at Stony Brook, Stony Brook, NY 11794, USA

**Abstract**

X-ray atomic pair distribution functions (PDFs) were collected from a range of canonical metallic nanomaterials, both elemental and alloyed, prepared using different synthesis methods and exhibiting drastically different morphological properties. Widely applied shape-tuned virtual crystal (VC) fcc models proved inadequate, yielding structured, coherent, and correlated fit residuals. However, equally simple discrete cluster models could account for the largest amplitude features in these difference signals. A hypothesis testing based approach to nanoparticle structure modelling systematically ruled out effects from crystallite size, composition, shape, and surface faceting as primary factors contributing to the VC misfit. On the other hand, decahedrally twinned cluster cores were found to be the origin of the VC structure misfits for a majority of the nanomaterials reported here. It is further motivated that the PDF can readily differentiate between the arrangement of domains in these multiply-twinned motifs. Most of the nanomaterials surveyed also fall within the sub-5 nm size regime where traditional electron microscopy cannot easily detect and quantify domain structures, with sampling representative of the average nanocrystal synthesized. The results demonstrate that PDF analysis is a powerful method for understanding internal atomic interfaces in small noble metallic nanomaterials. Such core cluster models, easily built algorithmically, should serve as starting structures for more advanced models able to capture atomic positional disorder, ligand induced or otherwise, near nanocrystal surfaces.

# Keywords

Determining the three-dimensional arrangement of atoms inside metallic nanocrystals is important in a diversity of scientific and technological areas.[1–9] This is challenging because of the nanostructure problem.[10] In rare cases, metallic nanoclusters can be crystallized and single crystal x-ray methods used to solve their structures,[11–15] or atomic resolution tomographic images of individual nanoparticles obtained.[16] However in general, additional methods for quantitative and rapid structural characterization of nanomaterials are needed.

A good alternative approach, is to use PDF analysis. It is possible to get information-rich PDFs of many different metallic nanomaterials, from $\sim 1$ nm atomically precise clusters to nanocrystals with different sizes and morphologies, synthesized under different conditions, prepared with or without surfactants, and measured down to low concentrations within industry-relevant sample environments and supports. Quantitative information may be extracted from these PDFs using modelling. The simplest, but still very powerful approach to modelling nanoparticles is based on a virtual crystal (VC) approximation. VC models are built by applying crystallographic symmetry and periodic boundary conditions to a small unit cell. Nanocrystals are finite sized, and this is accounted for by attenuating the calculated PDFs with shape functions that encode the nanoparticle morphology. The most widely used software for this kind of analysis is PDFGUI.[17] VC modelling of nanoparticles using highly constrained refinements in PDFGUI is simple, rapid, and less susceptible to over-fitting. The ability to independently refine local, intermediate, and long-range structure, simply by specifying an interatomic range, is also an intuitive means of understanding structure and heterogeneity originating from different length-scales. The PDFGUI approach has been used to characterize critically important structural properties of nanoparticles such as stacking faults,[18,19] strain,[20] size,[21] shape,[22,23] segregation,[24] and broken symmetries.[25,26]

An often overlooked benefit of calculating PDFs from simple VC models and refining them with a few parameters to high resolution experimental PDFs is that fit residuals become a critical part of data analysis, and give a trustworthy measure of how well the VC model alone can describe the data. Sinusoidal oscillations observed in PDF fit residuals from

VC refinements of nanoparticles have been used to identify solvent restructuring in ZnO NPs[27] and the size-dependent emergence of amorphous-like scattering in nickel NPs, closely resembling the scattering from bulk metallic glasses.[28] In this paper, we isolate and compare seemingly benign, but in fact highly structured residuals that can be extracted reproducibly from nanostructured noble metals after fitting them to close packed VC models. We show that these may be explained by simple discrete but rational cluster structure models. We argue that any more complicated models such as highly defected,[29,30] multi-phase[31,32] and heterogeneous core-shell models[33–39] should only be attempted to explain signal in the PDF difference curve that is not captured by the finite clusters described here.

## Results

X-ray PDFs were measured for a set of noble metallic nanocrystals, listed in Table 1. The data collection, analysis and modelling are described in the Methods section. We first compare fits of an fcc VC model to a representative nanoparticle dataset, Pd ($Pd^P$ in Table 1). The results are shown in Fig. 1(b). For comparison, in Fig. 1(a) we show a fit to a well-ordered crystalline material, bulk nickel. The fit is excellent as evidenced by the low agreement factor, $R_w = 0.019$, and the very small fluctuations in the difference curve. The fit to the 3 nm diameter nanoparticle sample is also quite good, with an $R_w = 0.253$ that is generally considered an acceptable fit to nanoparticle data in the literature.[18,24,34,40–47] The calculated and measured peaks line up well, suggesting the structural model appropriately captures a majority of the PDF signal. However, the nanoparticle fit is worse than the fit of the crystalline material, with an $R_w$ thirteen times larger, and the difference curve contains well-resolved, structured features, for example, around 5, 6, 8.5, and 10 Å highlighted with arrows in the figure.

If we assume that this signature in the difference curve is coming from a well defined structural motif in the nanoparticle that is not captured in the VC modelling, we would like

4

Table 1: Metallic nanocrystalline samples used in this study. D: Particle or wire diameter, Surfact: Surfactant, Morph: particle morphology. Morphologies are nanoparticle ($P$), nanowire ($W$), nanocluster ($Cl$), bulk ($B$). $C$ indicates the sample was on a carbon support. Primary capping agents are specified in the surfactant column, OAm: Oleylamine, TOP: Trioctylphosphine, PVP: Polyvinylpyrrolidone, ODA: Octadecylamine, PFSA: Perfluorosulfonic acid, p-MBA: *para*-Mercaptobenzoic Acid, SC6: Hexanethiol. For more information on sample preparation and characterization using TEM please see the Synthesis Methods section in the Supporting Information.

| Name | Composition | D (nm) | Surfact. | Beamline | Morph. |
|------|-------------|--------|----------|----------|--------|
| $Pd^P$ | Pd | 3.0 [a] | OAm | XPD | P |
| $CoPd^P$ | $Co_{0.2}Pd_{0.8}$ | 8.6 [a] | OAm, TOP | XPD | P |
| $PdNi^W$ | $Pd_{0.83}Ni_{0.17}$ | 2.3 [a] | ODA | X17A | W |
| $Ag^P$ | Ag | 38.0 [b] | PVP | XPD | P |
| $AgAu^P$ | $Ag_{0.5}Au_{0.5}$ | 5.0 [b] | PVP | PDF | P |
| $PdAu^W$ | $Pd_{0.9}Au_{0.1}$ | 2.1 [a] | ODA | X17A | W |
| $Pd^W$ | Pd | 2.0 [a] | ODA | X17A | W |
| $Au^P$ | Au | 9.0 [b] | PVP | XPD | P |
| $PtRu^{P,C}$ | $Pt_{0.5}Ru_{0.5}$ | 3.5 [a] | PFSA | XPD | P,C |
| $Pt^P$ | Pt | 3.0 [a] | OAm, TOP | XPD | P |
| $Au^{Cl1}$ | Au | 1-2 | p-MBA | ID11 | Cl1 |
| $Au^{Cl2}$ | Au | 1-2 | SC6 | 11IDB | Cl2 |
| $Ni^B$ | Ni | Bulk | None | XPD | B |

[a] Average size by transmission electron microscopy (TEM)
[b] Average size by differential centrifugal sedimentation (DCS)
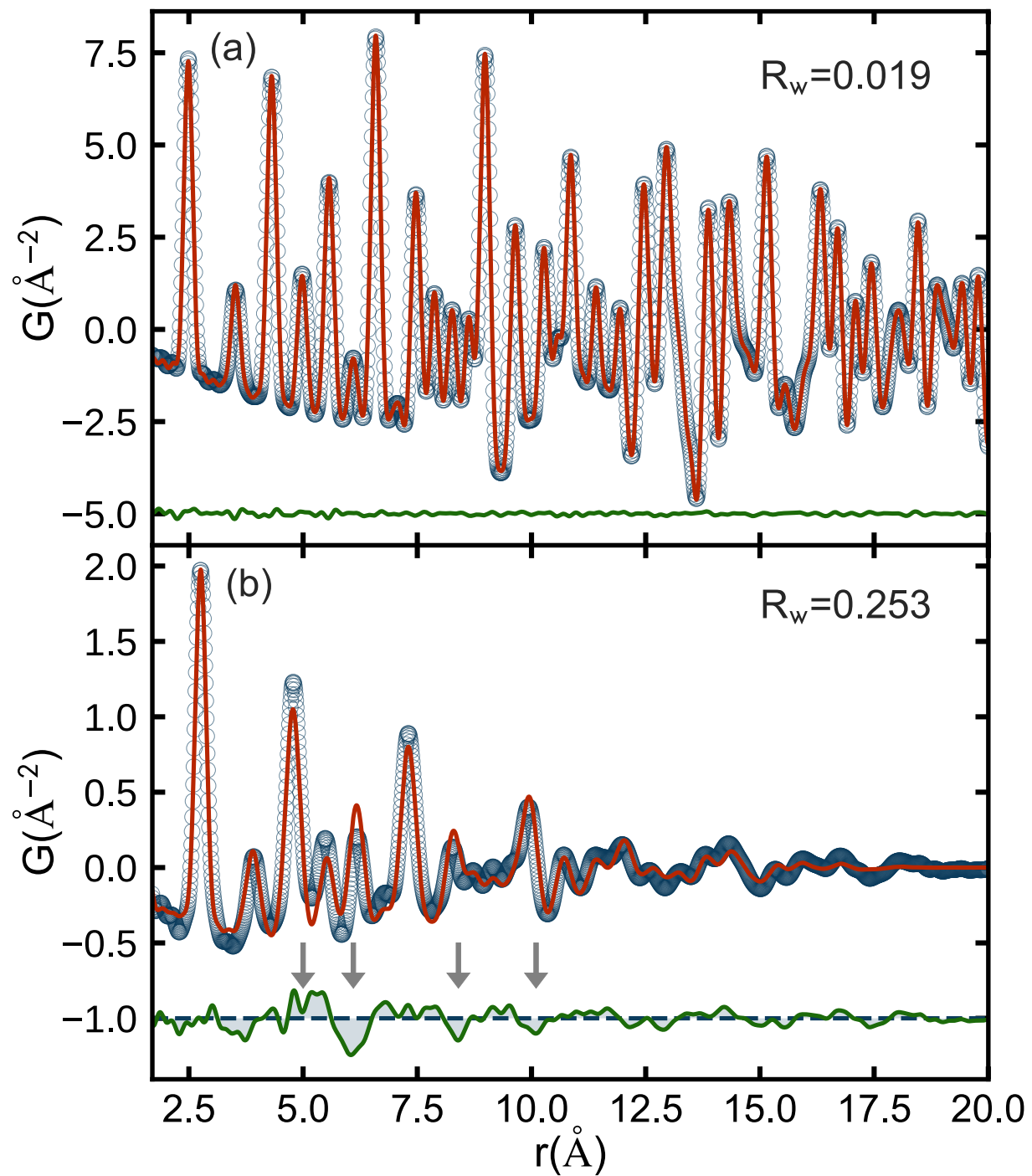
Figure 1: Measured (open circles) and calculated (red solid lines) PDFs with difference curves shown offset below (green) for (a) bulk nickel and (b) 3 nm diameter palladium nanoparticles.

to know how ubiquitous this structural relaxation is. To do this we look at the difference curves between best-fit fcc VC models and the wide array of nanocrystalline samples listed in Table 1. If the difference curves are similar, it indicates that the materials surveyed share a common underlying structural modification, whereas if they are not similar, it will indicate more than one modification type, or even non-transferable structural relaxations might exist that depend on nanocrystal composition, size, dispersity, ligand coverage, or other factors. The results are shown in Fig. 2. Each curve in this plot is a difference curve, like the one shown offset below the Pd nanoparticle data in Fig. 1(b), but here they are the differences between the best-fit fcc VC models and the data from the different samples in Table 1. We immediately see a high degree of similarity, at least among the top 7 curves in the plot. There are some similarities, but the agreement is less clear for the curves below this. However, the most striking result is that multiple samples, made from different materials and in different morphologies, as disparate as 40 nm particles and 2 nm wires, result in highly similar difference curves when fit with fcc VC nanoparticle models. In addition, we note that this characteristic difference curve is apparent in other studies in the literature.[21,28,46,48,49] This strongly suggests that a variety of noble metallic nanomaterials share a common structural modification. We next turn to investigating the structural origin of these features.

We sought simple models to explain these difference signals. Inspired by the structures of small atomic clusters, we looked at spherical, octahedral, icosahedral, and decahedral models. As a representative dataset, we fit these cluster structures to the 3 nm Pd nanoparticle PDF. The results are shown in Fig. 3. In this figure we show the difference curves that are obtained after each of these discrete cluster models are refined to their best-fit values, while varying an expansion coefficient, a scale factor, an isotropic atomic displacement parameter ($U_{iso}$), and a parameter for correlated motion effects ($\delta_2$). The top curve is the residual from the best-fit fcc VC model, yielding a refined spherical particle diameter, or fcc coherence length, of 1.9 nm. This is the first difference curve in Fig. 2 labeled $Pd^P$. Next we assess whether keeping
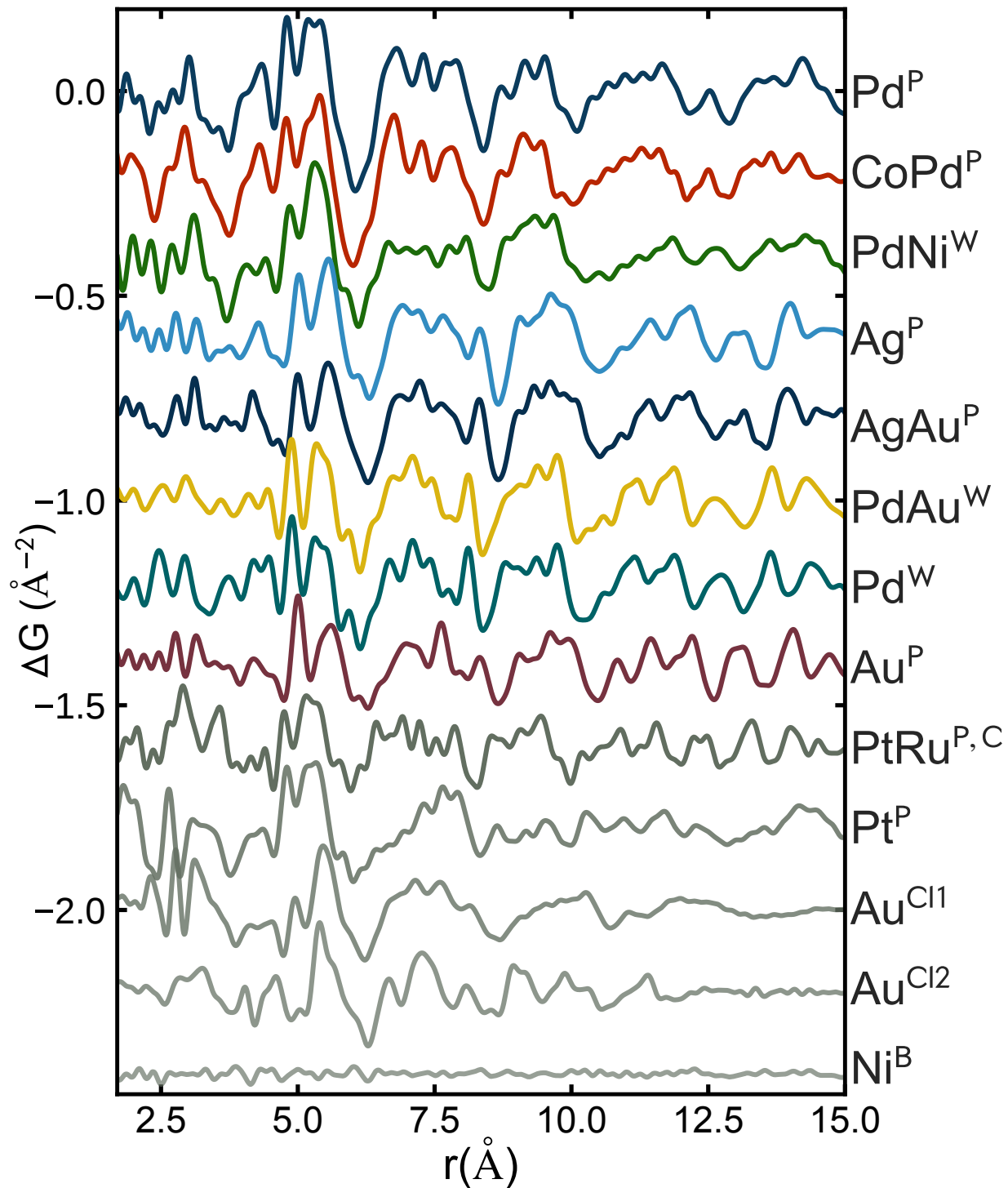
Figure 2: Difference curves from fcc VC refinements for samples listed in Table 1. The residual curves are normalized to place them on the same scale as the Pd curve for easier visual comparison. Bulk nickel is shown at the bottom, unscaled, for comparison. See Table 1 for the meaning of the curve labels.
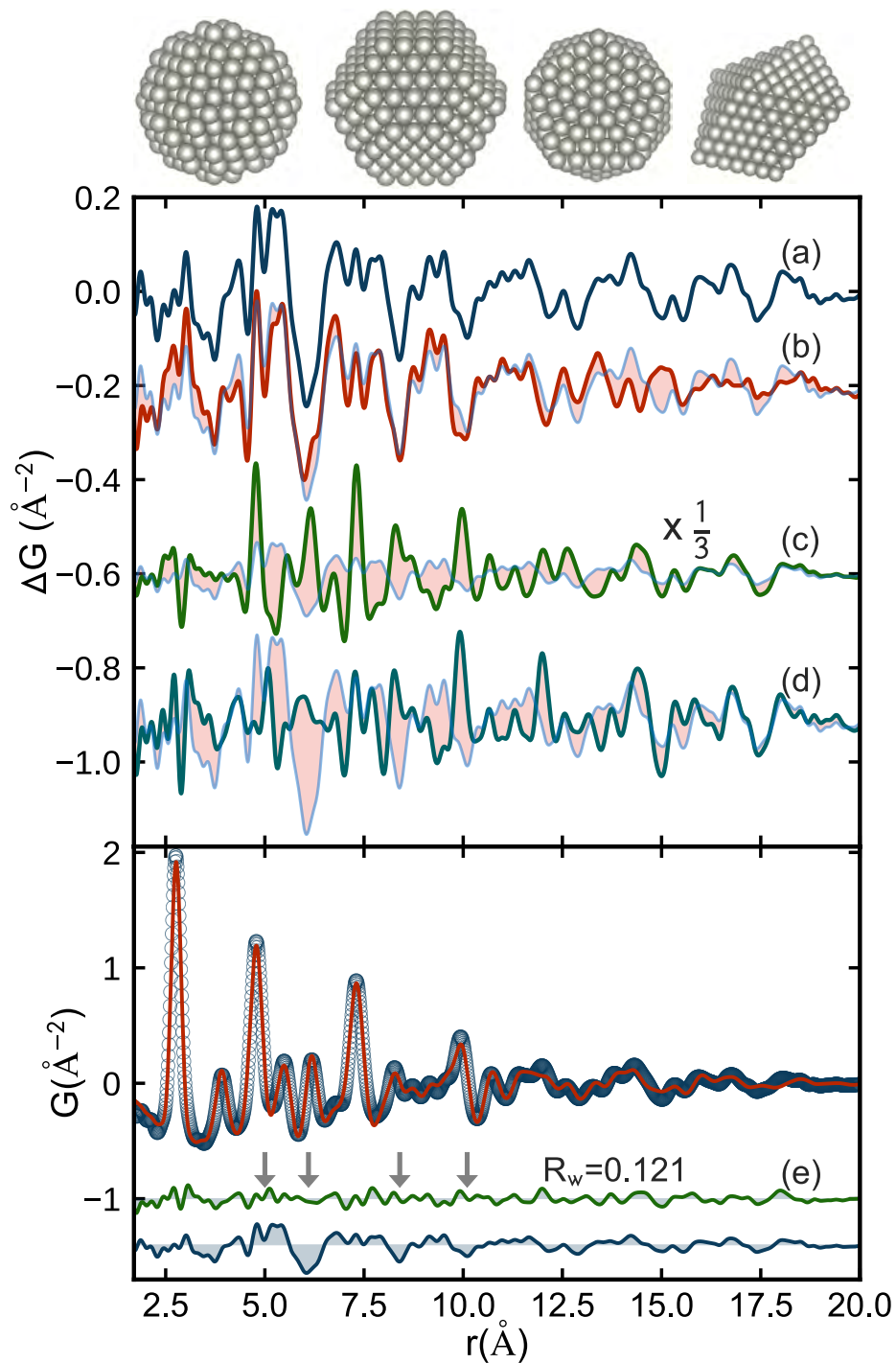
Figure 3: Top panel: Best-fit difference curves for different cluster models and the measured PDF of Pd$^P$. The cluster structures are shown above the panel in the same order from left to right. (a) fcc VC sphere (same curve as the top curve in Fig. 2) (b) truncated fcc octahedron (Wulff) (c) Mackay icosahedron (scaled by factor $\frac{1}{3}$) (d) regular decahedron. The difference curve from the VC model fit is shown as pale blue on each of the plots for comparison. Bottom panel: the measured PDF (open circles) and calculated (red solid line) from a 3.6 nm decahedron. Offset below in green is the difference curve, with again the VC residual curve reproduced below in blue. Arrows are positioned over characteristic features in the VC residual, as shown in Fig. 1.

9

the underlying fcc structure, but changing the shape of the cluster, in this case to a faceted truncated octahedron (suggested from a Wulff analysis) can explain the VC misfit. The best-fit difference curve of the octahedral model is shown in Fig. 3(b). It is largely unchanged from the fcc VC residual in Fig. 3(a). The prominent local structural features in the difference curve are not due to changes in nanoparticle shape. In Fig. 3(c) we show the best-fit difference curve for an icosahedral model. This is the closest magic sized icosahedron to a 2 nm sphere, consisting of 309 atoms. The difference curve is now considerably modified, which shows that changing from an underlying fcc basis to an icosahedral motif has a significant effect on the PDF. However, the agreement is substantially worse than the fcc VC misfit (in the figure the resulting difference curve had to be scaled down by a factor of 3), suggesting that the icosahedral structural modification is not a dominant property of the Pd nanoparticle. Next we consider a decahedral model with a particle diameter, or maximum intervertex distance, of 2.7 nm. This model's best-fit difference curve is shown in Fig. 3(d). This also results in a significant change to the fit residual, suggesting that the PDF is sensitive to a decahedral structure modification, but the overall agreement is still not ideal. However, close inspection of the difference curve suggests that many of the large amplitude features in the VC residual in the low-$r$ region, below 10 Å, *are* corrected by this model, at the expense of large amplitude misfit features appearing at high-$r$. This may suggest that the decahedral structural modification is in the right direction, but a different sized cluster core is needed to fully explain the residual. We therefore tried different sized decahedra to see if we could improve the fit from $1.5 < r < 20$ Å, where the core structural misfit is most pronounced. The best-fit difference curve for a 3.6 nm diameter decahedron is shown in the lower panel of Fig. 3 labeled (e). This leads to a significant improvement in the agreement over the $r$-range capturing a majority of the experimental PDF signal, with the $R_w$ decreasing by more than a factor of 2, from 0.253 to 0.121. All the large amplitude features in the difference curve are removed with this model. This analysis shows that the PDF can differentiate between different clusters, and that there are cluster models that can sufficiently explain the

widely seen fcc VC residuals. We fit this same 3.6 nm decahedron to the samples generating residuals that appear to be highly correlated to the Pd difference curve in Fig. 2. The refined agreement factors and ADPs are given in Table 2, showing substantial improvements in both parameters for most of these samples, while also indicating that other sources of structural misfit exist that cannot be remedied by a single regular decahedral cluster, with a fixed number of atoms.

Table 2: Comparison of fit results for virtual crystal (VC) and decahedral (D) models to the samples that exhibit highly correlated difference curves in Fig. 2. $R_w$ in the subscript indicates the refined agreement factor, and $U_{iso}$ the refined ADP values. All decahedral fits indicated by D use a single 3.6 nm (609 atom) regular decahedron, as shown in Fig. 3

| Name | $VC_{R_w}$ | $D_{R_w}$ | $\Delta R_w$ (%) | $VC_{U_{iso}}$ (Å$^{-2}$) | $D_{U_{iso}}$ (Å$^{-2}$) | $\Delta U_{iso}$ (%) |
|---|---|---|---|---|---|---|
| Pd$^P$ | 0.253 | 0.121 | -52.1 | 0.016 | 0.012 | -22.5 |
| CoPd$^P$ | 0.322 | 0.199 | -38.1 | 0.020 | 0.014 | -27.5 |
| PdNi$^W$ | 0.281 | 0.173 | -38.6 | 0.014 | 0.005 | -64.4 |
| Ag$^P$ | 0.229 | 0.156 | -31.9 | 0.016 | 0.010 | -35.7 |
| AgAu$^P$ | 0.237 | 0.162 | -31.9 | 0.016 | 0.010 | -37.2 |
| PdAu$^W$ | 0.189 | 0.127 | -33.1 | 0.012 | 0.007 | -40.6 |
| Pd$^W$ | 0.165 | 0.173 | +4.90 | 0.009 | 0.005 | -45.1 |

We now turn our attention to the difference curves at the bottom of Fig. 2 which appear slightly different to those from the decahedral samples that have been discussed previously. For a sample that is representative of this behavior we pick Au$^{Cl2}$ whose difference curve, when fit with the VC model, is shown in grey at the bottom of Fig. 2 and reproduced as the top grey curve in Fig. 4. We carry out the same analysis that was done for the Pd$^P$ decahedron, by comparing the difference curves of various discrete cluster models. As before, the Wulff-shaped discrete fcc cluster (Fig. 4b) does little to affect the VC difference curve (Fig. 4a). However, this time the decahedral model (Fig. 4d) also does little to reduce the signal in the residual. On the other hand, an icosahedral model does a significantly better job, at least in the low-$r$ region (Fig. 4c). This suggests that the core of the underlying metallic cluster is icosahedral in nature rather than decahedral and that the PDF is again able to differentiate between these possibilities, as demonstrated for Pd$^P$.

11
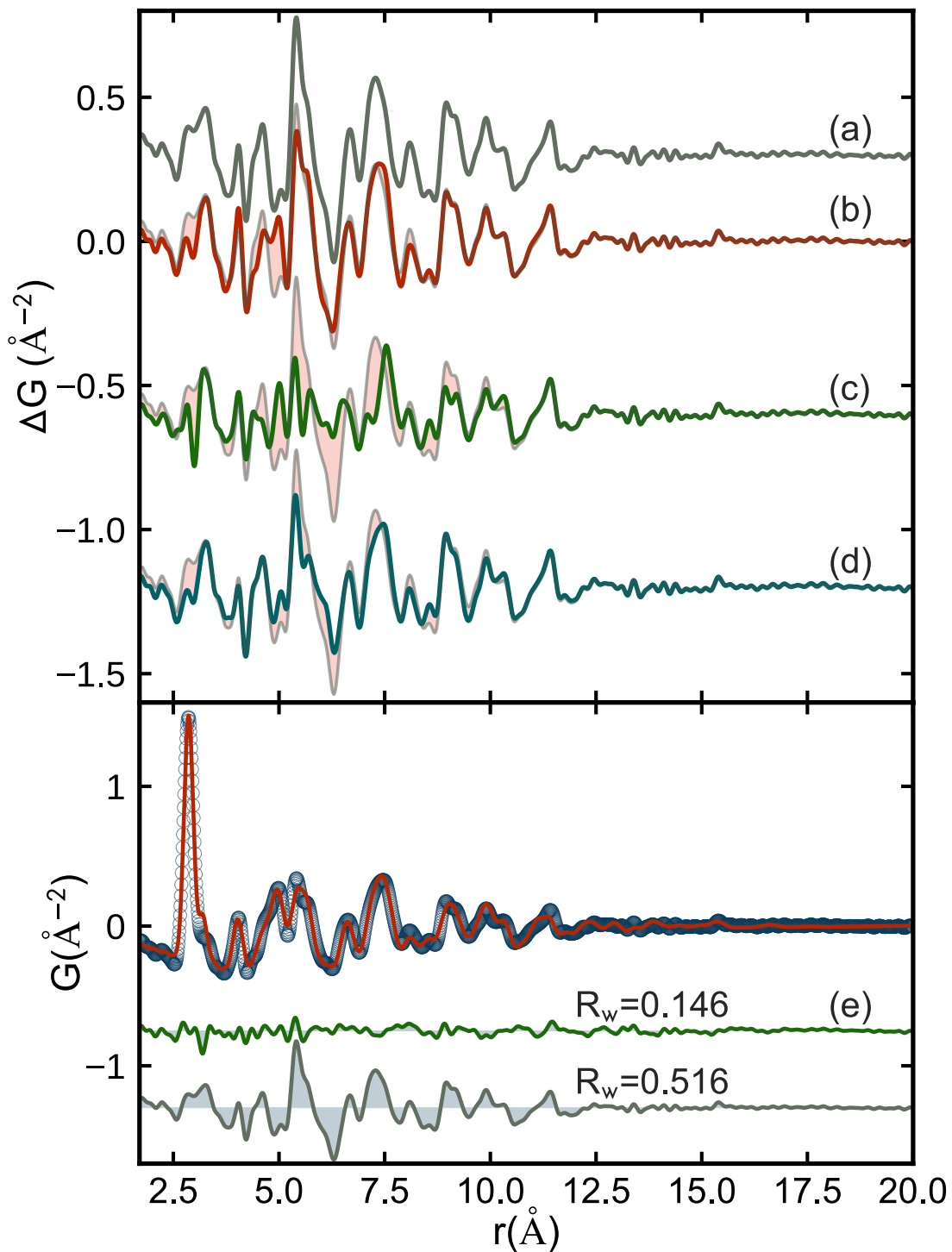
Figure 4: Top panel: Best-fit difference curves for different cluster models and the measured PDF of Au$^{Cl2}$. (a) fcc VC model (same curve as the second to bottom curve in Fig. 2) (b) truncated fcc octahedron (Wulff) (c) Mackay icosahedron (d) truncated decahedron. The difference curve from the VC model fit is shown as pale grey and overlaid on each of the plots for comparison. Cluster models (b-d) each contain exactly 55 atoms. Bottom panel: the measured PDF (open circles) and calculated (red solid line) from the Lopez-Acevedo 144 atom structure containing an icosahedral core. Offset below are the discrete (green) and VC (grey) difference curves.

12

Although the signal in the difference curve is greatly reduced by the icosahedral cluster, from $R_w = 0.516$ for the VC model to $R_w = 0.289$, the agreement factor is still much larger than the best-fit decahedron in Fig. 3(e). In fact, there is an established DFT-derived structure solution for $Au^{Cl2}$ cluster[50] which was corroborated by STEM and PDF studies.[51,52] We computed the PDF directly from this 144 atom model and compared it to the experimental $Au^{Cl2}$ PDF in the lower panel of Fig. 4. It gives an even better agreement to the measured PDF, reducing the $R_w$ to 0.146. It also results in much smaller refined ADPs, with $U_{iso}$'s reduced by a factor of $\sim 5$ versus the VC model, from 0.034 to 0.0066. The refined parameters are comparable to the best-fit decahedral models and approach those obtained from crystalline materials. It is interesting to investigate the differences between the Lopez-Acevedo structure (LA model) and the simple ASE generated 55 atom icosahedral core cluster that we used. The LA model has a 54 atom icosahedral core consisting of two Mackay shells with 20 tetrahedral faces, which is nearly identical to the ASE generated 55 atom icosahedron, the difference being the absence of one central atom (the first Mackay "shell"). However, in the LA model the layers surrounding this core do not follow the Mackay packing at all. Instead, they are generated by placing 60 atoms at hcp sites on the surface of the 54 atom icosahedral core, 3 per {111} faceted tetrahedral face. There is also an outermost shell protecting the 114 atom cluster with 30 thiolate-gold staples. This explains why the fit of the 55 atom icosahedral core model does well in the low-$r$ region of the PDF, which is dominated by signal from the core, but not at high-$r$, which contains only information about the outer-layers of the cluster.

## Discussion

A striking aspect of these results is the robustness of the difference curve signal from the decahedral samples. Highly reproducible residuals were collected at four different synchrotron sources on single element and alloyed nanocrystals, prepared using different synthesis meth-

ods, and with markedly different morphologies. This underscores the fact that the structural information contained in the difference curves does not depend sensitively on experimental conditions, particle shape, composition, or even size. This is further borne out by the observation that the standard Wulff models did nothing to fit those signals. The fact that decahedral cluster models could be found that removed the signature features in the residual shows that the structural origins of the fcc VC misfit are in the details of the nanocrystal cores. Again, we note that it is not the morphology of the decahedral models that improves the fit.

The decahedral cluster models used here are made up of 5 tetrahedral sub-units of fcc close-packed material arranged in a star shape with a common aligned $\langle 110 \rangle$ tetrahedral edge, and a slight elongation to the 5 pentagonal edges. We believe that the primary modification to the fcc structure captured in many fit residuals is due to the presence of {111} type contact twins at the boundaries between the tetrahedra in the decahedron. The presence of twin boundaries introduces new interatomic distances into the model that are not present in the unfaulted structure but are needed to explain the measured PDFs. It is also important to note that the diameter of the decahedral model that had the best agreement with the $Pd^P$ data was nearly double that of the best-fit spherical model (3.6 nm rather than $\sim 2$ nm for the VC model). Actually, in a 3.6 nm regular decahedron the characteristic dimension of the fcc tetrahedral sub-unit is 1.9 nm. The somewhat low symmetry of the multi-domain structures lead to a rather large number of similar but different inter-domain interatomic distances which overlap and reduce the number of distinct PDF peaks in the high-$r$ region. [sjb:not sure what was added here, if anything][sob:Simon, added sentences discussing particle vs cluster size and some other things starts here]While the best choice decahedral model for $Pd^P$ is perhaps an overestimation of the TEM determined particle size, an estimate which may not be representative of the sample measured by PDF where many orders of magnitude more particles are averaged, we do not claim that the core structure refinements over $1.5 < r < 20$ Å are sensitive to particle size nor should they be compared to TEM

data. For some of the nanoparticles and nanowires studied, there is considerable signal in the PDF past 20 Å(see Fig. S4 in the supporting info for experimental PDFs over a wider $r$-range). The candidate cluster cores may over/under-estimate the full coherence of the measured PDF, however the strength of the method is in differentiating between structural motifs, not determining average particle size or size distributions. Additionally, as shown for $Au^{Cl2}$ sample, nanoparticle cores are rarely identical to their surfaces, though in this case the subtle rearrangement of the outer-layers could only occur because of atomic planes made available by the core. An extension of this methodology, in order to differentiate atomic packing and other rearrangements as a function of $r$-range, also using simple faulted clusters, is underway.[sob:Addition ends here.]

It is interesting that we also observe a robust decahedral signal in the difference curves from the metallic nanowire samples. This clearly shows that these samples must also contain significant numbers of twin boundaries. The importance of decahedral-like twinning in large 50-100 nm wires has been widely noted in the literature.[53–56] Here we also find them in very thin $\sim$ 2 nm diameter wires, previously thought to consist of single crystalline fcc segments,[57–59] and show that PDF can be a powerful method for establishing the presence of domains in highly anisotropic morphologies.

This work also suggests that caution should be exercised when introducing more complex models to explain nanocrystal data. We have obtained fits to both elemental and alloyed PDFs from metallic nanoparticles and nanowires that have $R_w$ values well below 0.2 with a single decahedral cluster structure that contains only 4 refinable parameters. That is not to say that better fits cannot be obtained with more complicated models, such as heterogeneous core shell structures including models with surface oxide phases and nanoparticle-ligand correlations, but there is a very small signal in the difference curve that is left to be fit by the additional degrees of freedom in these models. As an example, the difference curve below the data in the lower panel of Fig. 3 illustrates the amplitude of the unfit signal that is left after fitting the 4-parameter decahedral cluster. This is representative of the signal left over

that would be available to constrain additional parameters in other models.

Finally, we would like to emphasize the value of interrogating fit residuals carefully. While this may seem obvious, it is oftentimes forgotten in PDF studies of nanomaterials where poor fits are accepted as a *de facto* limitation of nanoparticle studies, or comparisons of simulated PDFs are used to glean understanding from experimental data without refinements.[24,38,44,46,48,60? –62]

# Methods

## Pair distribution function measurements

Total scattering measurements were performed at four synchrotron x-ray facilities and five beamlines NSLS-I (X17A), NSLS-II (XPD, PDF), ESRF (ID11), and APS (11-ID-B) across various beamtimes with hard x-rays in the range of 66.7-86.5 keV. Nanocrystals were loaded in, or deposited on, standard sample supports such as polyimide tubes/tape and carbon paper. Experimental conditions differed slightly between measurements, but all diffraction patterns were collected in a wide-angle transmission geometry with area detectors placed in close proximity to the sample. Sample information is given in Table 1 and measurement/PDF specific details are provided in SI Table 1.

FIT2D,,[63] PYFAI,[64] or DIOPTAS[65] was used to calibrate experimental geometries and azimuthally integrate diffraction intensities to 1D diffraction patterns. Standardized corrections are then made to the data to obtain the total scattering structure function $F(Q)$, which is then sine Fourier transformed to the PDF using PDFGETX3[66] and XPDFSUITE.[67]

## Modelling

VC modelling for samples listed in Table 1 was carried out in PDFGUI using a close-packed fcc ($Fm\bar{3}m$) model. An isotropic gaussian atomic displacement parameter ($U_{iso}$), cubic lattice constant ($a$), global scale, and $\delta_2$, a parameter for correlated motion effects,[68] were

refined. Parameters that describe the resolution of the measurement ($Q_{damp}$, $Q_{broad}$) were obtained by independently refining a bulk calibrant measured in the same geometry as the nanocrystalline sample. The experimental PDFs were fit over a wide $r$-range, $1.5 < r < 70$ Å, with an additional spherical shape function that damps PDF peak intensities with increasing $r$ due to the finite size or structural coherence of the nanoparticle crystallites.[69]

Discrete structure refinements were done within the CMI software framework.[70] The PDFs are calculated from discrete models expressed in cartesian coordinates using the Debye scattering equation,[71] implemented in DIFFPY's DEBYEPDFCALCULATOR. The atomic coordinates in space were held constant in the refinements but four parameters were allowed to vary and obtain good agreement between the calculated and measured PDFs: an expansion coefficient to account for differences in nearest neighbor distances, $U_{iso}$, a single scale factor, and $\delta_2$. PDF refinements were carried out over the range $1.5 < r < 20$ Å. Discrete models were built using the Python atomic simulation environment ASE.[72] Details are provided in the SI, including instructions needed to reproduce all core cluster models tested in this study.

# Acknowledgement

## Supporting Information Available

- supportingInformation.pdf: Synthesis methods, select microscopy, details on the total scattering measurements, and code snippets to reproduce discrete clusters described in this article.

This material is available free of charge via the Internet at `http://pubs.acs.org/`.

# References

(1) Murray, C. B.; Kagan, C. R.; Bawendi, M. G. Synthesis and Characterization of Monodisperse Nanocrystals and Close-Packed Nanocrystal Assemblies. *Annu. Rev. Mater. Sci.* **2000**, *30*, 545–610.

(2) Xia, Y.; Yang, H.; Campbell, C. T. Nanoparticles for Catalysis. *Acc. Chem. Res.* **2013**, *46*, 1671–1672.

(3) Rosi, N. L.; Mirkin, C. A. Nanostructures in Biodiagnostics. *Chem. Rev.* **2005**, *105*, 1547–1562.

(4) Sokolova, V.; Epple, M. Inorganic Nanoparticles as Carriers of Nucleic Acids into Cells. *Angewandte Chemie International Edition* **2008**, *47*, 1382–1395.

(5) Koenigsmann, C.; Santulli, A. C.; Gong, K.; Vukmirovic, M. B.; Zhou, W.-p.; Sutter, E.; Wong, S. S.; Adzic, R. R. Enhanced Electrocatalytic Performance of Processed, Ultrathin, Supported Pd–Pt Core–Shell Nanowire Catalysts for the Oxygen Reduction Reaction. *J. Am. Chem. Soc.* **2011**, *133*, 9783–9795.

(6) Alivisatos, A. P. Semiconductor Clusters, Nanocrystals, and Quantum Dots. *Science* **1996**, *271*, 933–937.

(7) Aricò, A. S.; Bruce, P.; Scrosati, B.; Tarascon, J.-M.; van Schalkwijk, W. Nanostructured Materials for Advanced Energy Conversion and Storage Devices. *Nat. Mater.* **2005**, *4*, 366–377.

(8) Daniel, M.-C.; Astruc, D. Gold Nanoparticles: Assembly, Supramolecular Chemistry, Quantum-Size-Related Properties, and Applications toward Biology, Catalysis, and Nanotechnology. *Chem. Rev.* **2004**, *104*, 293–346.

(9) Lee, J.; Yang, J.; Kwon, S. G.; Hyeon, T. Nonclassical Nucleation and Growth of Inorganic Nanoparticles. *Nat. Rev. Mater.* **2016**, *1*, 16034.

(10) Billinge, S. J. L.; Levin, I. The problem with determining atomic structure at the nanoscale. *Science* **2007**, *316*, 561–565.

(11) Tran, N. T.; Powell, D. R.; Dahl, L. F. Nanosized Pd145(CO)x(PEt3)30 Containing a Capped Three-Shell 145-Atom Metal-Core Geometry of Pseudo Icosahedral Symmetry. *Angewandte Chemie International Edition* **2000**, *39*, 4121–4125.

(12) Yang, H. et al. Plasmonic Twinned Silver Nanoparticles with Molecular Precision. *Nat. Commun.* **2016**, *7*, 12809.

(13) Jadzinsky, P. D.; Calero, G.; Ackerson, C. J.; Bushnell, D. A.; Kornberg, R. D. Structure of a Thiol Monolayer-Protected Gold Nanoparticle at 1.1 Å Resolution. *Science* **2007**, *318*, 430–433.

(14) Sakthivel, N. A.; Theivendran, S.; Ganeshraj, V.; Oliver, A. G.; Dass, A. Crystal Structure of Faradaurate-279: Au279(SPh-tBu)84 Plasmonic Nanocrystal Molecules. *J. Am. Chem. Soc.* **2017**, *139*, 15450–15459.

(15) Vergara, S. et al. MicroED Structure of Au146(p-MBA)57 at Subatomic Resolution Reveals a Twinned FCC Cluster. *J. Phys. Chem. Lett.* **2017**, *8*, 5523–5530.

(16) Miao, J.; Ercius, P.; Billinge, S. J. L. Atomic electron tomography: 3D structures without crystals. *Science* **2016**, *353*, aaf2157.

(17) Farrow, C. L.; Juhás, P.; Liu, J.; Bryndin, D.; Božin, E. S.; Bloch, J.; Proffen, T.; Billinge, S. J. L. PDFfit2 and PDFgui: Computer programs for studying nanostructure in crystals. *J. Phys: Condens. Mat.* **2007**, *19*, 335219.

(18) Masadeh, A. S.; Božin, E. S.; Farrow, C. L.; Paglia, G.; Juhás, P.; Karkamkar, A.; Kanatzidis, M. G.; Billinge, S. J. L. Quantitative size-dependent structure and strain determination of CdSe nanoparticles using atomic pair distribution function analysis. *Phys. Rev. B* **2007**, *76*, 115413.

(19) Yang, X.; Masadeh, A. S.; McBride, J. R.; Božin, E. S.; Rosenthal, S. J.; Billinge, S. J. L. Confirmation of disordered structure of ultrasmall CdSe nanoparticles from X-ray atomic pair distribution function analysis. *Phys. Chem. Chem. Phys.* **2013**, *15*, 8480–8486.

(20) Gilbert, B.; Huang, F.; Zhang, H.; Waychunas, G. A.; Banfield, J. F. Nanoparticles: Strained and Stiff. *Science* **2004**, *305*, 651–654.

(21) Shi, C.; Redmond, E. L.; Mazaheripour, A.; Juhás, P.; Fuller, T. F.; Billinge, S. J. L. Evidence for anomalous bond softening and disorder below 2 nm diameter in carbon supported platinum nanoparticles from the temperature dependent peak width of the atomic pair distribution function. *J. Phys. Chem. C* **2013**, *117*, 7226–7230.

(22) Farrow, C. L.; Shi, C.; Juhás, P.; Peng, X.; Billinge, S. J. L. Robust structure and morphology parameters for CdS nanoparticles by combining small angle X-ray scattering and atomic pair distribution function data in a complex modeling framework. *J. Appl. Crystallogr.* **2014**, *47*, 561–565, Selected as journal cover.

(23) Kodama, K.; Iikubo, S.; Taguchi, T.; Shamoto, S. Finite size effects of nanoparticles on the atomic pair distribution functions. *Acta Crystallogr. A* **2006**, *62*, 444–453.

(24) Alayoglu, S.; Zavalij, P.; Eichhorn, B.; Wang, Q.; Frenkel, A. I.; Chupas, P. Structural and Architectural Evaluation of Bimetallic Nanoparticles: A Case Study of Pt-Ru Core-Shell and Alloy Nanoparticles. *ACS Nano* **2009**, *3*, 3127–3137.

(25) Smith, M. B.; Page, K.; Siegrist, T.; Redmond, P. L.; Walter, E. C.; Seshadri, R.; Brus, L. E.; Steigerwald, M. L. Crystal Structure and the Paraelectric-to-Ferroelectric Phase Transition of Nanoscale BaTiO3. *J. Am. Chem. Soc.* **2008**, *130*, 6955–6963.

(26) Page, K.; Proffen, T.; Niederberger, M.; Seshadri, R. Probing Local Dipoles and Ligand Structure in BaTiO3 Nanoparticles. *Chem. Mater.* **2010**, *22*, 4386–4391.

(27) Zobel, M.; Neder, R. B.; Kimber, S. A. J. Universal solvent restructuring induced by colloidal nanoparticles. *Science* **2015**, *347*, 292–294.

(28) Doan-Nguyen, V. V. T.; Kimber, S. A. J.; Pontoni, D.; Hickey, D. R.; Diroll, B. T.; Yang, X.; Miglierini, M.; Murray, C. B.; Billinge, S. J. L. Bulk metallic glass-like scattering signal in small metallic nanoparticles. *ACS Nano* **2014**, *8*, 6163–6170.

(29) Longo, A.; Martorana, A. Distorted f.c.c. Arrangement of Gold Nanoclusters: A Model of Spherical Particles with Microstrains and Stacking Faults. *J. Appl. Crystallogr.* **2008**, *41*, 446–455.

(30) Beyerlein, K. R.; Snyder, R. L.; Scardi, P. Faulting in Finite Face-Centered-Cubic Crystallites. *Acta Crystallogr. A* **2011**, *67*, 252–263.

(31) Cervellino, A.; Giannini, C.; Guagliardi, A. Determination of Nanoparticle Structure Type, Size and Strain Distribution from X-Ray Data for Monatomic f.c.c.-Derived Non-Crystallographic Nanoclusters. *J. Appl. Crystallogr.* **2003**, *36*, 1148–1158.

(32) Cervellino, A.; Giannini, C.; Guagliardi, A.; Zanchet, D. Quantitative Analysis of Gold Nanoparticles from Synchrotron Data by Means of Least-Squares Techniques. *Eur. Phys. J. B* **2004**, *41*, 485–493.

(33) Petkov, V.; Shastri, S. D. Element-Specific Structure of Materials with Intrinsic Disorder by High-Energy Resonant x-Ray Diffraction and Differential Atomic Pair-Distribution Functions: A Study of PtPd Nanosized Catalysts. *Phys. Rev. B* **2010**, *81*, 165428.

(34) Wu, J.; Shan, S.; Petkov, V.; Prasai, B.; Cronk, H.; Joseph, P.; Luo, J.; Zhong, C.-J. Composition–Structure–Activity Relationships for Palladium-Alloyed Nanocatalysts in Oxygen Reduction Reaction: An Ex-Situ/In-Situ High Energy X-Ray Diffraction Study. *ACS Catal.* **2015**, *5*, 5317–5327.

(35) Petkov, V.; Wanjala, B. N.; Loukrakpam, R.; Luo, J.; Yang, L.; Zhong, C.-J.; Shastri, S. Pt–Au Alloying at the Nanoscale. *Nano Lett.* **2012**, *12*, 4289–4299.

(36) Petkov, V.; Shastri, S.; Shan, S.; Joseph, P.; Luo, J.; Zhong, C.-J.; Nakamura, T.; Herbani, Y.; Sato, S. Resolving Atomic Ordering Differences in Group 11 Nanosized Metals and Binary Alloy Catalysts by Resonant High-Energy X-Ray Diffraction and Computer Simulations. *J. Phys. Chem. C* **2013**, *117*, 22131–22141.

(37) Merrill, N. A.; McKee, E. M.; Merino, K. C.; Drummy, L. F.; Lee, S.; Reinhart, B.; Ren, Y.; Frenkel, A. I.; Naik, R. R.; Bedford, N. M.; Knecht, M. R. Identifying the Atomic-Level Effects of Metal Composition on the Structure and Catalytic Activity of Peptide-Templated Materials. *ACS Nano* **2015**, *9*, 11968–11979.

(38) Prasai, B.; R. Wilson, A.; J. Wiley, B.; Ren, Y.; Petkov, V. On the Road to Metallic Nanoparticles by Rational Design: Bridging the Gap between Atomic-Level Theoretical Modeling and Reality by Total Scattering Experiments. *Nanoscale* **2015**, *7*, 17902–17922.

(39) Petkov, V.; Prasai, B.; Shastri, S.; Kim, J.-W.; Shan, S.; Kareem, H. R.; Luo, J.; Zhong, C.-J. Surface Atomic Structure and Functionality of Metallic Nanoparticles: A Case Study of Au–Pd Nanoalloy Catalysts. *J. Phys. Chem. C* **2017**, *121*, 7854–7866.

(40) Petkov, V.; Peng, Y.; Williams, G.; Huang, B.; Tomalia, D.; Ren, Y. Structure of gold nanoparticles in water by x-ray diffraction and computer simulations. *Phys. Rev. B* **2005**, *72*, 195402.

(41) Petkov, V.; Shastri, S. D. Element-specific structure of materials with intrinsic disorder by high-energy resonant x-ray diffraction and differential atomic pair-distribution functions: A study of PtPd nanosized catalysts. *Phys. Rev. B* **2010**, *81*, 165428.

(42) Page, K.; Hood, T. C.; Proffen, T.; Neder, R. B. Building and refining complete

nanoparticle structures with total scattering data. *J. Appl. Crystallogr.* **2011**, *44*, 327–336.

(43) Newton, M. A.; Chapman, K. W.; Thompsett, D.; Chupas, P. J. Chasing Changing Nanoparticles with Time-Resolved Pair Distribution Function Methods. *J. Am. Chem. Soc.* **2012**, *134*, 5036–5039.

(44) Kumara, C.; Zuo, X.; Ilavsky, J.; Chapman, K. W.; Cullen, D. A.; Dass, A. Super-Stable, Highly Monodisperse Plasmonic Faradaurate-500 Nanocrystals with 500 Gold Atoms: $Au_{\sim500}(SR)_{\sim120}$. *J. Am. Chem. Soc.* **2014**, *136*, 7410–7417.

(45) Fleury, B.; Cortes-Huerto, R.; Taché, O.; Testard, F.; Menguy, N.; Spalla, O. Gold Nanoparticle Internal Structure and Symmetry Probed by Unified Small-Angle X-Ray Scattering and X-Ray Diffraction Coupled with Molecular Dynamics Analysis. *Nano Lett.* **2015**, *15*, 6088–6094.

(46) Poulain, A.; Sobczak, I.; Ziolek, M. Size of Au-Nanoparticles Supported on Mesostructural Cellular Foams Studied by the Pair Distribution Function Technique. *Crystal Growth & Design* **2016**, *16*, 5985–5993.

(47) Gamez-Mendoza, L.; Terban, M. W.; Billinge, S. J. L.; Martinez-Inesta, M. Modelling and Validation of Particle Size Distributions of Supported Nanoparticles Using the Pair Distribution Function Technique. *J. Appl. Crystallogr.* **2017**, *50*, 741–748.

(48) Kumara, C.; Zuo, X.; Cullen, D. A.; Dass, A. Faradaurate-940: Synthesis, Mass Spectrometry, Electron Microscopy, High-Energy X-ray Diffraction, and X-ray Scattering Study of $Au_{\sim940}(SR)_{\sim160}$ Nanocrystals. *ACS Nano* **2014**, doi: 10.1021/nn501970v.

(49) Sanchez, S. I.; Small, M. W.; Bozin, E. S.; Wen, J.-G.; Zuo, J.-M.; Nuzzo, R. G. Metastability and Structural Polymorphism in Noble Metals: The Role of Composition and Metal Atom Coordination in Mono- and Bimetallic Nanoclusters. *ACS Nano* **2013**, *7*, 1542.

(50) Lopez-Acevedo, O.; Akola, J.; Whetten, R. L.; Grönbeck, H.; Häkkinen, H. Structure and Bonding in the Ubiquitous Icosahedral Metallic Gold Cluster $Au_{144}(SR)_{60}$. *The Journal of Physical Chemistry C* **2009**, *113*, 5035–5038.

(51) Bahena, D.; Bhattarai, N.; Santiago, U.; Tlahuice, A.; Ponce, A.; Bach, S. B. H.; Yoon, B.; Whetten, R. L.; Landman, U.; Jose-Yacaman, M. STEM Electron Diffraction and High-Resolution Images Used in the Determination of the Crystal Structure of the $Au_{144}(SR)_{60}$ Cluster. *J. Phys. Chem. Lett.* **2013**, *4*, 975–981.

(52) Jensen, K. M. Ø.; Juhás, P.; Tofanelli, M. A.; Heinecke, C. L.; Vaughan, G.; Ackerson, C. J.; Billinge, S. J. L. Polymorphism in magic sized $Au_{144}(SR)_{60}$ clusters. *Nat. Commun.* **2016**, *7*, 11859.

(53) Sun, Y.; Mayers, B.; Herricks, T.; Xia, Y. Polyol Synthesis of Uniform Silver Nanowires: A Plausible Growth Mechanism and the Supporting Evidence. *Nano Lett.* **2003**, *3*, 955–960.

(54) Zhang, S.-H.; Jiang, Z.-Y.; Xie, Z.-X.; Xu, X.; Huang, R.-B.; Zheng, L.-S. Growth of Silver Nanowires from Solutions: A Cyclic Penta-Twinned-Crystal Growth Mechanism. *J. Phys. Chem. B* **2005**, *109*, 9416–9421.

(55) Luis Elechiguerra, J.; Reyes-Gasga, J.; Jose Yacaman, M. The Role of Twinning in Shape Evolution of Anisotropic Noble Metal Nanostructures. *J. Mater. Chem.* **2006**, *16*, 3906–3919.

(56) Huang, X.; Zheng, N. One-Pot, High-Yield Synthesis of 5-Fold Twinned Pd Nanowires and Nanorods. *J. Am. Chem. Soc.* **2009**, *131*, 4602–4603.

(57) Koenigsmann, C.; Santulli, A. C.; Gong, K.; Vukmirovic, M. B.; Zhou, W.-p.; Sutter, E.; Wong, S. S.; Adzic, R. R. Enhanced Electrocatalytic Performance of Processed, Ultrathin, Supported Pd–Pt Core–Shell Nanowire Catalysts for the Oxygen Reduction Reaction. *J. Am. Chem. Soc.* **2011**, *133*, 9783–9795.

(58) Koenigsmann, C.; Sutter, E.; Adzic, R. R.; Wong, S. S. Size- and Composition-Dependent Enhancement of Electrocatalytic Oxygen Reduction Performance in Ultrathin Palladium–Gold (Pd1–xAux) Nanowires. *J. Phys. Chem. C* **2012**, *116*, 15297–15306.

(59) Liu, H.; Koenigsmann, C.; Adzic, R. R.; Wong, S. S. Probing Ultrathin One-Dimensional Pd–Ni Nanostructures As Oxygen Reduction Reaction Catalysts. *ACS Catal.* **2014**, *4*, 2544–2555.

(60) Sanchez, S. I.; Small, M. W.; Bozin, E. S.; Wen, J.-G.; Zuo, J.-M.; Nuzzo, R. G. Metastability and Structural Polymorphism in Noble Metals: The Role of Composition and Metal Atom Coordination in Mono- and Bimetallic Nanoclusters. *ACS Nano* **2013**, *7*, 1542–1557.

(61) Nakotte, H.; Silkwood, C.; Page, K.; Wang, H.-W.; Olds, D.; Kiefer, B.; Manna, S.; Karpov, D.; Fohtung, E.; Fullerton, E. E. Pair Distribution Function Analysis Applied to Decahedral Gold Nanoparticles. *Phys. Scr.* **2017**, *92*, 114002.

(62) Page, K.; Proffen, T.; Terrones, H.; Terrones, M.; Lee, L.; Yang, Y.; Stemmer, S.; Seshadri, R.; Cheetham, A. K. Direct Observation of the Structure of Gold Nanoparticles by Total Scattering Powder Neutron Diffraction. *Chemical Physics Letters* **2004**, *393*, 385–388.

(63) Hammersley, A. P.; Svenson, S. O.; Hanfland, M.; Hauserman, D. Two-dimensional detector software: from real detector to idealised image or two-theta scan. *High Pressure Res.* **1996**, *14*, 235–248.

(64) Kieffer, J.; Karkoulis, D. PyFAI, a versatile library for azimuthal regrouping. *J. Phys.: Conf. Ser.* **2013**, *SRI2012*.

(65) Prescher, C.; Prakapenka, V. B. DIOPTAS: A Program for Reduction of Two-

Dimensional X-Ray Diffraction Data and Data Exploration. *High Press. Res.* **2015**, *35*, 223–230.

(66) Juhás, P.; Davis, T.; Farrow, C. L.; Billinge, S. J. L. PDFgetX3: A rapid and highly automatable program for processing powder diffraction data into total scattering pair distribution functions. *J. Appl. Crystallogr.* **2013**, *46*, 560–566.

(67) Yang, X.; Juhás, P.; Farrow, C.; Billinge, S. J. L. xPDFsuite: an end-to-end software solution for high throughput pair distribution function transformation, visualization and analysis. *arXiv* **2015**, 1402.3163.

(68) Proffen, T.; Billinge, S. J. L. PDFFIT, a program for full profile structural refinement of the atomic pair distribution function. *J. Appl. Crystallogr.* **1999**, *32*, 572–575.

(69) Egami, T.; Billinge, S. J. L. *Underneath the Bragg peaks: structural analysis of complex materials*, 2nd ed.; Elsevier: Amsterdam, 2012.

(70) Juhás, P.; Farrow, C. L.; Yang, X.; Knox, K. R.; Billinge, S. J. L. Complex Modeling: a strategy and software program for combining multiple information sources to solve ill-posed structure and nanostructure inverse problems. *Acta Crystallogr. A* **2015**, *71*, 562–568.

(71) Debye, P. Dispersion of Röntgen rays. *Annalen der Physik (Berlin, Germany)* **1915**, *351*, 809–823.

(72) Larsen, A. H. et al. The Atomic Simulation Environment—a Python Library for Working with Atoms. *J. Phys.: Condens. Matter* **2017**, *29*, 273002.